UNIVERSITY OF NAPLES FEDERICO II

Department of Structures
for Engineering and Architecture

PH.D. COURSE IN
STRUCTURAL, GEOTECHNICAL AND SEISMIC ENGINEERING
COORDINATOR PROF. LUCIANO ROSATI
XXIX CYCLE

PAOLINO CASSESE

PH.D. THESIS

SEISMIC PERFORMANCE OF EXISTING HOLLOW REINFORCED CONCRETE BRIDGE COLUMNS

TUTOR:
PROF. ING. GERARDO M. VERDERAME
PROF. ING. ANTONIO OCCHIUZZI

2017

To my mother, my father and my little great brother.
To Fortuna, my force and my serenity.

Acknowledgements

I hereby express my gratitude and appreciation to my supervisor Professor Gerardo Mario Verderame. He provided me with invaluable advice throughout the years of this study. His knowledge and friendly approach towards me was impressive to say at the least. I will remember forever the shared successes, but, even more, our intense discussions and disputes, which helped me to overcome all the difficulties which have some-what characterized these years.

I express my gratitude to Professor Gaetano Manfredi for the opportunity given to me to be part of the Department of Structures for Engineering and Architecture of the University of Naples Federico II and of his research group.

My deepest thanks to my team-colleague Maria Teresa De Risi. Her advice, encouragement, and guidance, made the completion of this research possible.

Sincere gratitude to Paolo Ricci for sharing with me his experience and knowledge, essential for the success of the experimental activity of this study.

A special thanks to the other research-team members, my friends, Carlo and Mariano: they provided, in different ways, a great support to my research.

The experimental work described in this thesis would not have been possible without the assistance of laboratory personnel, in particular Emanuele, Luigi, and Giovanni.

Thanks to all my colleagues, because they had given me the opportunity to work in a very pleasant and cooperative environment. Among my colleagues I would like to thank especially Orsola, Costantino, Stefano, Andrea, Marco, Raffaele, Mariapia, Maddalena, for their friendship and support, everyday.

I am above-all thankful to my mother, my father and my "little great" brother for their patient, understanding and support, without which I would not have reached my objective today. No words can explain how grateful I am.

Finally, I say "thank you", Fortuna, for your unconditional love. Thanks, because you enjoyed and suffered with me throughout all these years of hard study. Thanks, because you offered me the most precious thing you have, your time.

Naples, April 2017

Abstract

Highway bridges can be considered as crucial civil structures for economic and social progress of urban areas. The damages to highway bridges due to earthquake events may have dramatic impact on the interested area, with or without life threatening consequences, since bridges are essential for relief operations. For these reasons, the assessment of seismic performance of existing bridge structures is a paramount issue, especially in those countries, such as Italy, where most of existing bridges was constructed before the advancement in earthquake engineering principles and seismic design codes.

Several major earthquakes occurred throughout the world highlighted the seismic vulnerability of the bridge piers, due to obsolete design. If, for ordinary shaped reinforced concrete (RC) bridge columns the seismic assessment issue can be considered as almost solved, due to several analytical assessment formulations available in literature, and adopted by codes, the same cannot be said for columns with hollow-core cross section, despite their widespread use. None of the current codes addresses specialized attention to RC hollow core members, and only quite recently, attention has been paid to experimental cyclic response of hollow columns. Some critical issues for hollow RC columns are related to the assessment of their shear capacity, special focusing on degradation mechanisms, and the high shear deformation characterizing the seismic response of such elements.

In the above outlined contest, a contribution in the seismic assessment of hollow bridges piers is provided by the present work: the investigation of cyclic lateral response of RC existing bridge piers with hollow rectangular and hollow circular cross-section is performed. Special attention has been focused on failure mode prediction and shear capacity assessment.

A critical review of the state-of-the-art and of the theoretical background is firstly carried out: the review process has been focused on the past experimental and analytical research on seismic performance of hollow reinforced concrete bridge piers, both for hollow rectangular and hollow circular cross sections.

The experimental campaign, conducted at Laboratory of the Department of Structures for Engineering and Architecture, University of Naples "Federico II", is presented. The experimental program comprised tests on six reduced-scale RC bridge piers with hollow cross-section (four rectangular shaped and two circular shaped). The specimens were ad hoc designed in order to be representative of the existing bridge columns typical of the Italian transport infrastructures realized before 1980, by using a scaling factor equal to 1:4. The construction procedure is detailed, too. All the tests were performed in quasi-static way by applying increasing horizontal displacement cycles with constant axial load (equal to 5% of the axial compressive capacity) until collapse. The monitoring system is accurately explained: it was composed of two sub-systems, one used for global measures (forces and displacement), and the other to deeply investigate about local deformation.

Experimental results for both hollow rectangular and hollow circular specimens are reported: for each specimen the results in terms of lateral load versus drift are shown and the evolution of observed damage with increasing displacement is described and related to the lateral load-drift response. An experimental analysis of deformability contributions to the top displacement is performed, mainly in order to better understand the relevance of taking into account shear deformations for bridge piers assessment. The energy dissipation capacity is also analyzed, evaluating the equivalent damping ratio and its evolution with ductility. For hollow rectangular specimens, the global response is modelled through a three-component numerical model, in which flexure, shear and bar slip are considered separately. The main goal of the numerical analysis is to reproduce the experimental deformability contributions.

The last part of the work focuses on the definition of proper shear strength models for both hollow rectangular and hollow circular cross sections, and the definition of a deformability capacity model for hollow rectangular cross section. To this aim, two different experimental databases are collected and critically analyzed. The effectiveness in shear capacity and failure mode

prediction of main existing shear capacity models is investigated, by applying these models to the database columns. Based on the obtained results, some modifications to existing shear strength models are discussed and proposed in order to improve their reliability for hollow columns. Finally, a new drift capacity model is developed and proposed to assess drift at shear failure of hollow rectangular columns.

Keywords: Reinforced concrete bridge piers; Hollow rectangular cross-section; Hollow circular cross-section; Experimental tests; Failure mode; Deformability contribution; Seismic assessment; Shear strength assessment; Drift-capacity model.

Tables of contents

List of figures

List of tables

Chapter 1
INTRODUCTION

1.1 Motivation and research objectives

Among the natural hazards, earthquakes are paramount due to their impact on civil structures worldwide. The considerable direct and indirect losses due to earthquakes for vulnerable existing structures have prompted a great interest in performance assessment to future seismic events. Seismic performance evaluations, beyond the traditional goal of life safety, are today required to rightly estimate expected losses. Realistic losses evaluations require more accurate seismic risk assessment tools, in order to help decision and policy-makers both in pre-earthquake planning to mitigate probable losses and in post-earthquake planning to develop emergency response and recovery strategies. According to a performance-based approach, modern seismic codes worldwide define performance levels aimed at avoiding collapse under major earthquakes and ensuring control and limitation of damage under more frequent but less severe earthquakes, in order to minimize economic and functionality losses. In this framework, seismic vulnerability and risk assessment of civil structures are essential, starting from the characterization of earthquake hazard, and going on with determination of structural response (structural demand), identification of performance limits (structural capacity), and degrees of structural damage and losses associated with specific damage states.

Among civil structures, highway bridges can be considered as crucial for economic and social progress of urban areas. Moreover, after seismic events

occurrence, bridges are essential for relief operations. For these reasons, damages to highway bridges due to earthquake events, even if not particularly intense, may have dramatic impact on the interested area, with or without life threatening consequences. The assessment of seismic performance of existing bridge structures is a paramount issue, especially in those countries, such as Italy, where most of existing bridges was constructed before the advancement in earthquake engineering principles and seismic design codes.

The majority of the current Italian highway infrastructures was constructed following the rapid economic growth of the 1950s (the so-called ''Italian miracle''). In particular, a great part of the bridges stock on Italian highways was built during the two decades from 1955–1975. In the late 1980s, construction resumed to fill some important gaps that had emerged in the meantime. Except some major bridges of architectural value, representing only a minor portion of the bridge stock, the rest of the highway bridges is of rather uniform typology, with simply supported spans and piers of single stem or frame types (Figure 1.1). The bridge typologies of that period were substantially unchanged, although the quality of construction has considerably been improved. Throughout that period, the national design code did not evolve significantly. The safety format remained firmly anchored to the allowable stress design until the early 2000s, and changes, as it regards bridges, were mainly in terms of traffic loads, whose intensity increased over time. In particular, one aspect completely missed was the design criteria against seismic actions. The seismic design consisted in the application of nominal ''equivalent'' static horizontal forces with no other considerations regarding ductile behavior. The maximum value of these forces, in the area of higher seismicity, was 10% of the weight (Pinto and Franchin, 2010).

Figure 1.1. Typical Italian simply supported viaducts

The perception of the risk associated to the seismic vulnerability of the transportation infrastructure, and in particular to that of bridge structures, is a quite recent acquisition in Italy, on the part of both the relevant authorities and the experts. This is possibly because in the last major earthquakes, the transportation infrastructure has not suffered significant distress (Pinto and Mancini, 2005). Even if it is to be noted, that these seismic events (Friuli 1976, Irpinia1980, L'Aquila 2009) occurred in periods when the presence of highway viaduct was not so intense in the interested areas. However, it can be observed that the delay in the seismic risk recognize is not exclusive of Italy. For example, it took twelve years after the failures of quite modern bridges during the San Fernando earthquake (1971), for the Federal Highway Administration (FHWA) to publish a first document titled "Retrofitting guidelines for Highway Bridges" (FHWA-ATC, 1983). Still, in 1989, despite of the large retrofit program set up, the Loma Prieta earthquake exposed substantial deficiencies in bridges in California (Pinto et al., 2009). The seismic vulnerability of existing highway bridges, and in particular of the bridge piers, principally due to obsolete design, has been highlighted by several major earthquakes occurred throughout the world. Various failure modes of bridge columns have been identified during post-earthquake reconnaissance operations on transportation infrastructures. Generally, failure is related to a displacement-ductility capacity not adequate to the seismic demand, caused by not sufficient reinforcement details. In some cases, generally for columns with high aspect ratio (namely, columns height-to-section depth ratio), this led to collapse for combined axial load and bending moment of the plastic regions located at the basis of the piers, with spalling and crushing of the compressed concrete, and longitudinal bars buckling (see Figure 1.2). In other cases, especially for medium-low aspect ratio columns, the premature collapse is to assign to a not sufficient not-degraded shear capacity (see Figure 1.3), or to degradation of shear capacity caused by flexural damages during non-linear response, namely, the so called "flexure-shear" failure mode (see Figure 1.4).

Seismic performance of bridges substantially depends on lateral behavior of vertical structural sub-systems, in particular of the piers. The modern seismic design philosophy for bridge structure is to pursue energy dissipation by ductile flexural hinges at the piers base (Priestley et al., 1996), unlike columns used in building frames that are typically designed following the weak beam-strong column philosophy for seismic resistance (Paulay and

Priestley, 1992). Brittle shear failure of bridge piers clearly has to be prevented to avoid disastrous collapse, and special attention has to be paid also to shear strength degradation with increasing flexural ductility demand. If for ordinary shaped reinforced concrete (RC) bridge columns (namely, with solid rectangular or circular cross-section) the seismic assessment issue can be considered as almost resolved, since many experimental and analytical studies are available in literature (Priestley and Park, 1987; Priestley et al., 1994, Xiao and Ma, 1997, among many others), the same cannot be said for columns with hollow-core cross section.

RC hollow section piers are a widespread structural solution for bridge structures, economically attractive because of several reasons including the larger moment-of-inertia than solid sections with a similar area, reduced inertia masses, saving of materials and equipment during construction, reduced problems related to the hydration of massive concrete. In particular, circular shape of the RC hollow section piers is very used for highway bridges, because its lateral response under wind and seismic loads is similar in any direction.

Figure 1.2. Plastic hinge collapse: Gothic Avenue viaduct (Northridge earthquake, California, 1994)

Figure 1.3. Piers shear failure: Wu-Shi bridge (Chi-Chi earthquake, Taiwan, 1999)

Figure 1.4. Flexure-shear failure: Hanshin viaduct (Kobe earthquake, Japan, 1995)

Despite their widespread use, none of the current codes addresses specialized attention to RC hollow core members, both for design and assessment (Turmo et al. 2009). Only quite recently, attention has been paid to experimental cyclic response of hollow columns: relatively few experimental studies, especially if compared with columns with solid cross section, are available in literature. Recent principal earthquakes around the world have highlighted the inadequate seismic performance of existing hollow piers, generally characterized by poor structural detailing and small web thickness. A critical, and still open, issue is the assessment of shear capacity of hollow RC columns (Calvi et al., 2005), special focusing on degradation mechanisms. In fact, shear-resisting mechanisms typical of this structural typology are very similar to those characterizing tube sections, depending mainly on webs aspect ratio and transverse reinforcement details. Small thickness together with not sufficient reinforcement details limit the confined concrete core, crucial to seismic energy dissipation (Kim et al., 2012). Another important issue related to existing hollow RC piers is that their seismic response is characterized by high shear deformations, comparable to ones typical of RC walls, which may represent also a considerable portion of global top displacement as highlighted by Delgado et al., (2008).

The situation outlined above is sufficient to understand that the state of the art on seismic assessment of hollow bridges piers still needs to be advanced in several areas. In particular, proper predictions of nonlinear behavior, failure modes, and shear capacity, are essential prerequisites for a reliable evaluation of structural fragility and, then, of seismic performance and risk assessment of RC bridges.

This work aims at contributing to the investigation of cyclic lateral

response of RC existing bridge piers with hollow rectangular and hollow circular cross-section, characterized by not sufficient seismic reinforcement details, therefore susceptible to high shear deformations and, eventually, shear failure. Special attention is focused on failure mode prediction and shear capacity assessment. For these purposes, both experimental and analytical studies are carried out and presented. To define and develop these studies, a critical literature review of the available experimental and analytical works is carried out.

The experimental study is performed on reduced-scale hollow RC columns, with rectangular and circular shape, different for aspect ratio, tested under cyclic increasing loading and constant axial force. The specimens are representative of typical design practices in force in Italy before 1980s, therefore characterized by low percentage of longitudinal and transverse reinforcement, with inadequate details, and lack of appropriate confinement reinforcement. The main goals are: (i) at global level, the evaluation of the failure mode, the ultimate drift capacity and the energy dissipation capacity of piers with different aspect ratio; (ii) at local level, the analysis of deformability contributions (i.e. flexure, shear and fixed-end-rotation) to the top displacement. Global experimental results are compared with main shear strength models, developed for RC members with solid cross section, in order to assess their predictive capacity when applied to hollow bridge piers. For hollow rectangular specimens, monotonic numerical modelling is applied in order to reproduce the experimental deformability contributions. Starting from the experimental results and shear strength comparison, the assessment of shear capacity of hollow RC members is further investigated. To this aim, two experimental database of tests on hollow rectangular and hollow circular columns, respectively, subjected to shear failure (with and without flexural yielding) are collected and critically analyzed. The predictive capacity of the main shear capacity models available in literature are applied to the database columns, in order to identify critical aspects of the application of such models to hollow columns. For hollow rectangular columns, based on the identified critical aspects, improvements to shear strength assessment are proposed and discussed, and an ad-hoc shear drift-capacity model is developed and proposed. For hollow circular columns, a critical discussion about existing shear strength models is carried out, and a new ad-hoc model is developed and assessed.

1.2 Dissertation outline

The presented work, whose motivations and main goals are reported above, is divided in eight sections.

Firstly, experimental studies on RC bridge piers with hollow rectangular and hollow circular cross-section are reviewed and discussed. An overview on analytical modeling of lateral response of RC columns, considering flexural, shear, and bar slip deformations, and more in detail, on shear strength models, is provided in **Chapter 2**.

Chapter 3 describes the test program including the test specimen details, material properties, test specimen construction, test setup, instrumentation, and the loading procedure.

A detailed description of the experimental response of each hollow rectangular specimen is provided in **Chapter 4,** together with a comparison with main code-based models for shear strength assessment. Finally, a monotonic numerical assessment of the global response, aiming to reproduce the experimental deformability contributions is carried out and discussed.

Chapter 5 presents in details global and local experimental results for hollow circular test specimens. Also in this case, a comparison between global experimental response and shear strength envelope from main code-based models is provided.

Using an experimental database of hollow rectangular columns with relatively large aspect ratios, **Chapter 6** evaluates the effectiveness of various force-based and displacement-based shear capacity models. Firstly, the collected database is described and analyzed. Then, the predictive capacity of main shear strength models, developed for members with solid cross section, is examined in relation to the database results. Based on the comparison results, some improvements for shear strength assessment of hollow rectangular columns are proposed and discussed. Finally, the main models for the assessment of displacement-based shear capacity, again developed for members with solid cross section, are applied to the columns database. Starting from a critical analysis of the effects of several response parameters on the column shear response, a new model for the evaluation of the drift at shear failure, ad-hoc for hollow rectangular columns is discussed and proposed.

Chapter 7 deals with the shear strength assessment for hollow circular columns. An experimental database of RC columns with hollow circular

columns and a single external layer of steel reinforcement is described. Then, the effectiveness of main existing models in predicting shear strength is investigated for columns database. Finally, after a critical discussion about shear-resisting mechanisms of hollow circular columns, a new shear strength model is developed and discussed.

In **Chapter 8** a summary of the research work is provided, together with main conclusions and some recommendations for future research in this field.

References

Calvi G. M., Pavese A., Rasulo A., Bolognini D. (2005) Experimental and numerical studies on the seismic response of RC hollow bridge piers. Bulletin of Earthquake Engineering; 3(3): 267-297.

Delgado R., Delgado P., Vila Pouca N., Arêde A., Rocha P., Costa A. (2009). Shear effects on hollow section piers under seismic actions: experimental and numerical analysis. Bulletin of Earthquake Engineering, 7(2), 377-389.

FHWA-ATC (1983). Retrofitting guidelines for Highway Bridges. Report ATC-06-2, Applied Technology Council, Redwood City, California.

Kim IH, Sun CH, Shin M. (2012) Concrete contribution to initial shear strength of RC hollow bridge columns. Structural Engineering and Mechanics; 41(1): 43-65.

Paulay T., Priestley M. J. N. (1992) Seismic Design of Reinforced Concrete and Masonry Buildings. New York: John Wiley & Sons.

Pinto P. E., Franchin P. (2010). Issues in the upgrade of Italian highway structures. Journal of Earthquake Engineering, 14(8), 1221-1252.

Pinto P. E., Lupoi A., Franchin, P. (2009). Valutazione e consolidamento sismico dei ponti esistenti. IUSS Press.

Pinto P. E., Mancini G. (2005). Seismic assessment and retrofit of existing bridges. The state of earthquake engineering research in Italy: the ReLUIS-DPC, 2008, 111-140.

Priestley M. J. N., Park R. (1987) Strength and ductility of concrete bridge columns under seismic loading. ACI Structural Journal; 84(1): 61–76.

Priestley M. J. N., Seible F., Calvi G. M. (1996) Seismic design and retrofit of bridges. New York: John Wiley & Sons.

Priestley M. J. N., Seible F., Xiao Y. (1994) Steel jacket retrofitting of reinforced concrete bridge columns for enhanced shear strength--Part 2: Test results and comparison with theory. Structural Journal; 91(5): 537-551.

Turmo J, Ramos G, Aparicio AC. (2009) Shear truss analogy for concrete members of solid and hollow circular cross section. Engineering Structures, 31(2): 455-465.

Xiao Y, Ma R. (1997) Seismic retrofit of RC circular columns using prefabricated composite jacketing. Journal of structural engineering; 123(10): 1357-1364.

Chapter 2
STATE OF THE ART AND BACKGROUND

In this chapter, a theoretical and experimental state-of-the-art is carried out. The first two sections review past experimental and analytical research on seismic performance of hollow reinforced concrete bridge piers, with rectangular and circular corss-section, respectively. Test details and a discussion of the experimental results are briefly presented, for each of the considered studies. Based on the analyzed experimental studies, several issues are identified, which can be considered still open. They will be subject of the present study.

The second part of the chapter deal with the review of several analytical models. First, the "classification issue" for reinforced concrete (RC) members, namely the prediction of the failure mode characterizing a RC member known its plastic and shear strength values, is recalled and discussed. Later, several existing models for the assessment of the lateral response in term of deformation of RC column are reviewed and analyzed. Finally, main models for shear strength evaluation from literature and codes are described and discussed, focusing on their experimental nature and, in particular, highlighting differencies between them. For all this models, the corresponding formulations are summarized, in order to provide the required definitions and uniform symbology. They will be applied in next chapters in different approaches depending on the objective that it is intended to pursue, and with the addition of new proposals.

2.1 Experimental studies: hollow rectangular RC columns

The use of hollow cross-section for reinforced concrete (RC) columns is widespread for bridge structures. This solution is economically attractive and technically adequate, because of several reasons, such as among others the larger moment-of-inertia than solid sections with a similar area, reduced inertia masses, saving of materials and equipment during construction, reduced problems related to the hydration of massive concrete (Priestley et al. (1996)).

However, the most important recent earthquakes evidenced the vulnerability of this type of section, particularly when no adequate seismic provisions are applied. In fact, shear strength and ductility of hollow section columns deeply depends on seismic details, in particular shear and confinement steel reinforcement (Priestley and Park (1987)). Only quite recently attention has been paid to experimental cyclic response of hollow columns: relatively few experimental studies, especially if compared with columns with solid cross section, are available in literature. Some of these studies are related to large-scale tests, others to reduced-scale tests. Among the firsts, the experimental studies by Yeh et al., (2002) and Pinto et al. (2003), among the seconds, the studies carried out by Mo and Nien (2002), Mo et al. (2004), Calvi et al. (2005) and Delgado (2009). Each of these works will be briefly described, discussed and analyzed hereafter. For each of them, the attention will be focused on the specimens' properties, test setup and experimental results. This literature review will be the basis for the collection of the database reported in the section 6.1.

2.1.1. Yeh, Mo and Yang (2002)

Within the context of the design and construction of a new high-speed rail project in Taiwan, in this paper, experimental results for two prototype and four scaled model hollow bridge columns are reported. Primary experimental variables of this study were axial load, amount of lateral reinforcement, and height-to-depth ratio.

Tests were performed under constant axial load ratios, varying from 0.082 to 0.176, and cyclically reversed horizontal load.

The scale ratio of prototype to model was equal to three. Therefore, all specimen properties and test data for models reported in this paper were

converted to prototype using the theory of small scaled models (ACI 1970). The configuration of lateral reinforcement was typical of bridge design in Taiwan. The cross section of each of the prototypes and models were 1.5x1.5m and 0.5x0.5 m, respectively. The wall thickness of the prototypes and models were 300 and 120 mm, respectively. The moment arms (distance between the horizontal loading point and the top of the reinforced concrete foundation) for the two prototypes were 6.5 and 4.5 m. For all four model specimens the moment arm was 1.8 m. Each specimen was identified by a three characters' code: the first character P or M in the specimen designation stood for prototypes or models, respectively. Comparing with the requirement of the ACI code (ACI 318-95), the second character S or I represented sufficient or insufficient shear reinforcement, respectively. The last character 1 or 2 indicated the axial load ratio close to 0.1 or 0.2, respectively. The spacing of the transverse reinforcement in all the specimens satisfied both the design requirements of the ACI code (ACI 318-95), and the requirement suggested by Priestley et al. (1996), in which the spacing needs to be less than six times the diameter of longitudinal rebars. For specimens PS1, MS1, and MS2, the provided shear reinforcement is more than that required by the ACI code (ACI 318-95) to avoid shear failure. For specimens PI1, MI1, and MI2, the provided shear reinforcement is only approximately 50% of that required by the ACI code (ACI 318-95). Each specimen was instrumented with load cells, displacement transducers, and strain gauges to monitor displacement and corresponding load as well as strains and relative deformations. The specimens were tested under displacement control according to a predetermined drift percentage. The time histories of displacement for the specimens consisted of cycles increasing with column drifts up to 6.5%. In each case, the displacement cycle was repeated to measure the strength degradation. All specimens developed stable responses up to certain displacement ductility levels. Flexural cracks perpendicular to the column axis developed first in regions close to the bottom of the columns. The flexural cracks became inclined and extended into the neutral axis of the columns due to the influence of shear, typically at a stage exceeding the first yielding of longitudinal rebars. At later stages of loading, typically at displacement ductility levels of 2 and 3, independent shear cracks started to occur. Plastic hinges were fully formed at the bottom end of the columns, which contributed to the development of ductility. Although each specimen developed the estimated flexural strength, the

ultimate performance and ductility level was different for each column.

Two of the tests experimented shear failure after flexural yielding. Specimen MI1, subjected to a lower axial load ratio of 0.086 and characterized by shear reinforcement equal to only 40% of that required by the ACI code (ACI 318-95), failed in shear developing a displacement ductility factor of 4.33. Ultimate performance for this specimen was dominated by shear capacity due to concrete crushing at the bottom of the specimen. The rupture of a few tensile longitudinal rebars occurred immediately before shear failure of the specimen, due to the low-cycle fatigue phenomenon. Specimen MI2 with insufficient shear reinforcement was subjected to a higher axial load ratio of 0.185. It was subjected to shear failure after flexural yielding. Some longitudinal rebars buckled in the loading stage close to the failure, but no rupture of tensile longitudinal rebars happened in this case. Figure 2.1 shows test specimens details and lateral load response for test models. In Figure 2.2, final state damages for specimens failing in shear are reported.

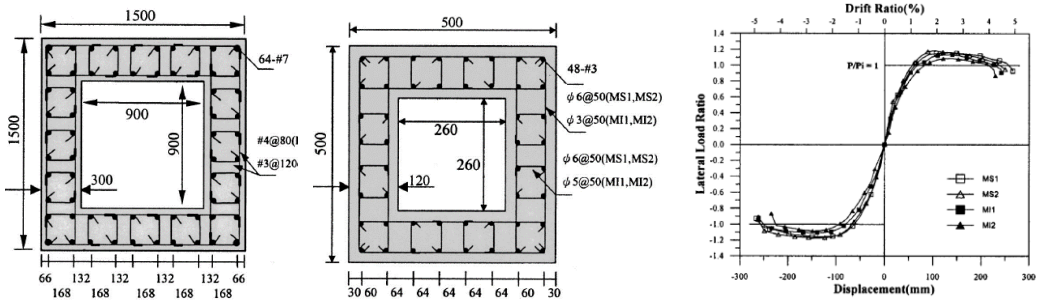

Figure 2.1 Details of test specimens and load-displacement response, Yeh et al. (2002)

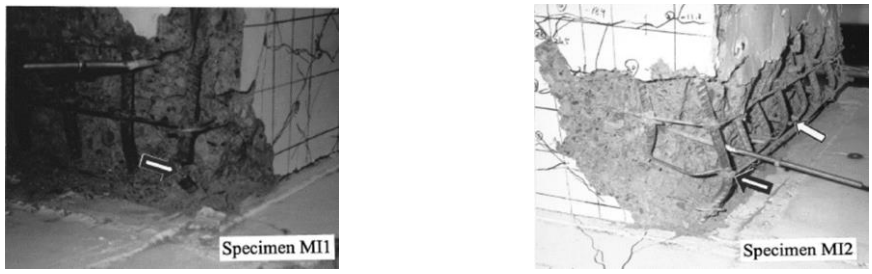

Figure 2.2. Final damage states for FS tests, Yeh et al. (2002)

Based on this study, Authors concluded that specimens with sufficient transverse reinforcement experimented flexure failure mode due to rupture of

longitudinal rebars, while specimens with insufficient transverse reinforcement failed in shear with lower displacement ductility capacity. Moreover, specimens with grater axial force had less ductility.

2.1.2. Mo and Nien (2002)

Within the same context of the previous study, Mo and Nien (2002) reported the experimental results of six hollow high-strength concrete columns. The concrete compressive strength fell in the range from 50 to 70 MPa. Primary experimental variables of this study included axial load, amount of lateral steel, and height-to-depth ratio. In particular, columns with height-to-depth ratio of 3.6 to 3.0 were designed to study their lateral response.

Tests were performed under constant axial load ratio, varying from 0.054 to 0.132, and cyclically reversed horizontal load.

The cross section of all specimens was 0.5x0.5 m and the wall 120 mm. The moment arms were 1.5 m or 1.8 m. As usual, each specimen was identified by a code in which the first character, ''H'', indicated high-strength concrete. The second character, ''S'' or ''I'', designated specimens with sufficient shear reinforcement or insufficient shear reinforcement, respectively, when compared with the ACI code (ACI 318-95). The third character, ''0'', ''1'', or ''2'', identified the varied axial load. If the last character in the specimen designation was ''b'', the moment arm of this specimen was 1.5 m. The moment arm of all the remaining specimens is 1.8 m. The spacing of the confining reinforcement in all specimens satisfies both the design requirements of the ACI code (ACI 318-95) and the requirements suggested by Priestley et al. (1996). For specimens HS-1 and HS-2, the provided shear reinforcement is more than that required by the ACI code (ACI 318-95) in order to avoid shear failure. For the remaining specimens the provided shear reinforcement ranges between 50 and 66% of that required.

The specimens were tested under displacement control following a predetermined displacement history defined in terms of column drift percentage. The displacement routines for the specimens consist of cycles with column drifts of up to 6.0%. The displacement cycles were repeated to measure the strength degradation.

All specimens developed stable responses up to certain displacement ductility levels. Flexural cracks perpendicular to each column's axis developed first in regions close to the bottom end of the columns. The flexural cracks

became inclined and extended into the web zone of the columns because of the influence of shear typically at a stage exceeding the first yield of longitudinal rebars. At later stages of loading, typically at displacement ductility levels of 2 and 3, independent shear cracks started to occur. Plastic hinges were fully formed at the bottom ends of the columns, which contributed to the development of ductility. Although all specimens exhibited the estimated flexural strength, their ultimate performance and the ductility levels achieved were different.

Three of the tests experimented shear failure after flexural yielding.

Specimen HI-0-b with smaller moment arm, lower axial force, and shear reinforcements of only 50% of the amounts required by the ACI code (ACI 318-95), developed a displacement ductility of 4.7. The ultimate performance for the specimen was first dominated by load-carrying capacity due to the rupture of tensile longitudinal rebars at the bottom end of the columns. Afterward, shear failure occurred. The same failure mode interested specimen HI-2-a.

Specimen HI-1-b was characterized by the same reinforcements and moment arm of the previous specimens, but it was subjected to a higher axial force. Also in this case, flexure-shear failure occurred. Although some longitudinal rebars buckled in the loading stage close to the failure, no rupture of tensile longitudinal rebars occurred.

Figure 2.3 shows test specimens details and lateral load response for test models.

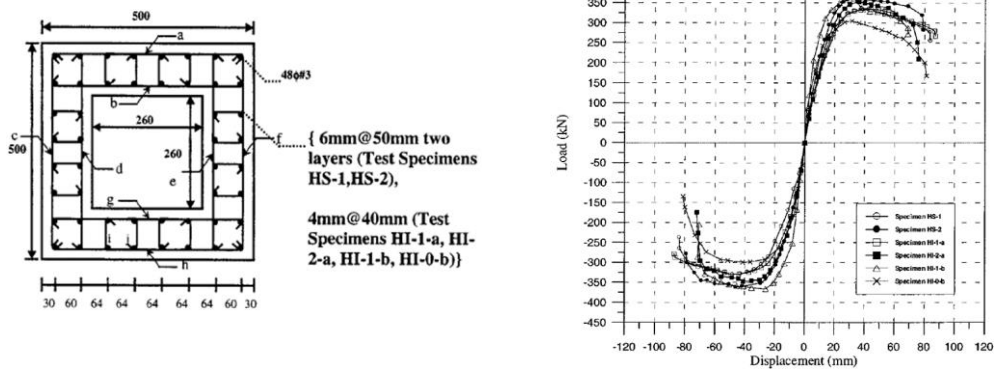

Figure 2.3. Final damage states for FS tests, Mo and Nien (2002)

Based on this study, Authors concluded that specimens with sufficient transverse reinforcement experimented flexure failure mode due to rupture of longitudinal rebars, while specimens with insufficient transverse reinforcement failed in shear with lower displacement ductility capacity. Moreover, specimens with grater axial force had less ductility.

Authors carried out also comparisons between experimental results and main shear strength models from literature and American codes. They noted that the experimental curves were lower than the shear capacity predictions. The reason of this was that all models were developed for normal-strength concrete.

2.1.3. Yeh et al., (2002)

Yeh et al., (2002) carried out an experimental investigation on three full-scale prototypes of hollow bridge piers for the design and construction of a new high-speed rail in Taiwan. Primary experimental variables of this study were amount of lateral reinforcement and height-to-depth ratio.

The prototypes were tested under a constant axial load ratio of approximately 0.08, and a cyclically reversed horizontal load. Piers had height-to-depth ratios of 4.3, 3.0 and 2.3. The cross section of each prototype was 1.5 m x 1.5 m. The wall thickness of the specimens was 300 mm. The moment arms were 3.5 m, 4.5 m and 6.5 m. In the specimen identification code, the first character, P, stands for prototypes, while the second character, such as S or I, represents sufficient or insufficient shear reinforcement, respectively, when compared to the requirements of the ACI code (ACI 318-95). The third character of 1 or 2 means the smaller or larger spacing of lateral reinforcement, respectively. The spacing of the confining reinforcement in specimens PS1 and PI1 satisfies both the design requirements of the ACI code (ACI 318-95), and the requirements suggested by Priestley et al. (1996), in which the spacing needs to be less than six times the diameter of longitudinal rebars. For specimen PSI, the provided shear reinforcement is more than that required by the ACI code (ACI 318-95) to avoid shear failure. For specimens PI1 and PI2, the provided shear reinforcement is only approximately 50 percent and 20 percent of that required by the ACI code (ACI 318-95), respectively (see Figure 2.4)

The specimens were tested under displacement control, following a predetermined displacement history defined in terms of pier drift percentage.

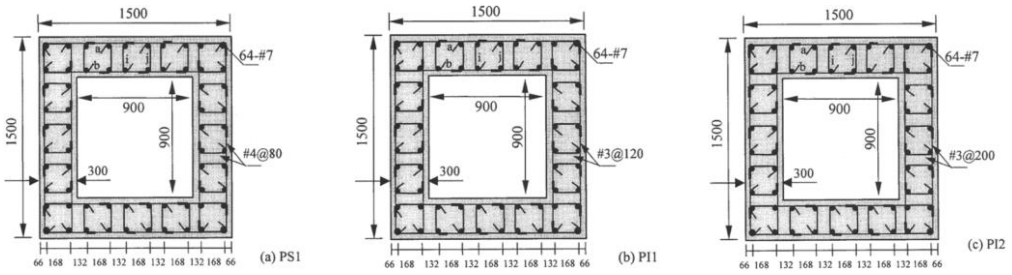

Figure 2.4. Details of the cross section, Yeh et al. (2002)

The displacement routines for all the three specimens consist of cycles with pier drifts up to 6.5 percent. The displacement cycles were repeated to measure the strength degradation. All specimens developed stable responses up to certain displacement ductility levels. Flexural cracks perpendicular to the pier axis developed first in regions close to the bottom of the piers. The flexural cracks became inclined and extended into the web zone of the piers due to the influence of shear, typically at a stage exceeding the first yield of longitudinal rebars. At later stages of loading, typically at displacement ductility levels of 2 and 3, independent shear cracks started to occur. Although all three specimens developed the estimated flexural strength, their ultimate performances and ductility levels achieved were different. In particular, specimen PI2 (with extremely insufficient shear reinforcement) was subjected to shear failure at displacement ductility of 4.1. Although some longitudinal rebars buckled in the loading stage close to the failure, no rupture of tensile longitudinal rebars happened (see Figure 2.5).

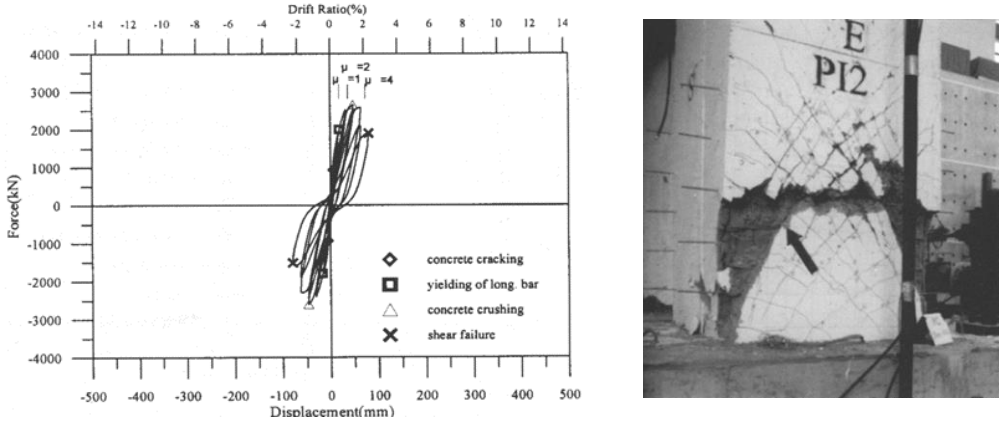

Figure 2.5. Hysteretic loops and damage state for Test PI2, Yeh et al. (2002)

Authors performed a comparison of the experimental results with some shear strength models [(ACI 318-95), Priestley et al., (1994), Ascheeim et al., (1992)]. The model by Priestley et al. (1994) gave a prediction close to experimental strength, while the others were conservative. Moreover, Authors concluded that prediction accuracy in terms of displacement for the specimen with shear failure needed to be further improved.

2.1.4. Pinto et al., (2003)

Pinto et al. (2003) presented cyclic tests on two large-scale (1:2.5) models of existing bridge piers with rectangular hollow cross-section performed in the ELSA laboratory. Test specimens were prototype of the piers of an existing reinforced concrete highway bridge constructed in Austria in 1975. Therefore, they presented several seismic deficiencies, such as lap splices within the potential plastic hinge region, bar cut-off at a not easily accessible height without adequate development length for the terminated rebars, low percentage of longitudinal and transverse reinforcement, short overlapping length, inadequate detailing of horizontal reinforcement and lack of appropriate confinement reinforcement. The two test specimens were different for height-to-length ratios (low and high).

The objectives of the test campaign were to investigate the performance of as-built rectangular hollow bridge piers without seismic detailing, to identify and confirm the deficiencies, and to assist in the design of the retrofitting solutions to be applied in a second stage of the research programme.

The scaled specimens had a rectangular hollow cross-section with external dimensions 2.74×1.02 m. The widths of the flange and the web were 0.21 m and 0.17 m, respectively. The height of the short pier was 6:5 m (height-to-length ratio L/D = 2.4) and the height of the tall pier was 14.0 m (L/D = 5.1). The concrete cover was chosen to be 0.015 m for ease of construction. For the short pier, the volumetric ratios were 0.4% and 0.09% for longitudinal and transverse reinforcement, respectively. The starter bars were terminated above the base block and the vertical rebars were spliced just above the base cross-section and within the potential plastic hinge region. No stirrups or closed hoops were placed, according to the original design of the piers. For the tall pier, the volumetric ratios were 0.7% and 0.09%. Longitudinal steel bars were characterized by inadequate overlapping length and reduction of almost 50% of the total amount at the height of 3.5 m. Figure 2.6 presents the reinforcement

details of the piers. As regards material properties, concrete C35/45 (characteristic cylinder strength f_{ck} = 35 MPa) and steel S500 (characteristic yield strength $f_{0:2k}$ = 500 MPa), as defined in Eurocode 2 (EC2), were used in accordance with the materials specified for the prototype pier.

Tests were performed under a constant axial load ratio of about 0.10, and cyclically reversed horizontal displacements with increasing amplitudes.

The experimental results from the tests on the short pier, with lap splices just above the block foundation, indicated that most of the non-linear deformation concentrated in a narrow slice at the base, leading to an equivalent plastic hinge much lower than the empirical values (38% of the empirical value). This resulted in a small drift capacity of 1.5% (see Figure 2.7).

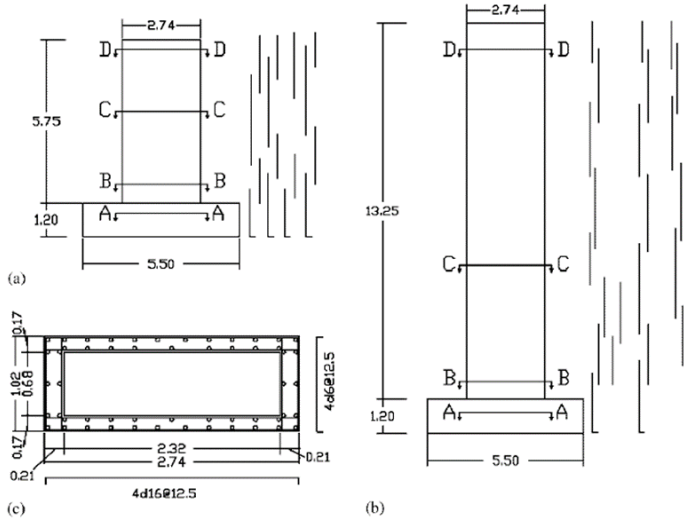

Figure 2.6. Geometry and reinforcement details, Pinto et al., (2003)

For a tall pier with bar cut-off, limited ductility was also observed (drift capacity of 1.6%). Failure occurred above the bar cut-off at 1/4 of the height (see Figure 2.8).

Numerical results from a fiber model were in good agreement with the experimental results, for the short pier with flexure-dominated behavior. For the tall pier, the fiber model was unable to simulate the tension shift due to the shear cracking in the lower part of the pier.

The test campaign confirmed that existing RC bridge piers with rectangular hollow cross section, designed without seismic requirements, are

expected to have poor hysteretic behaviour and low deformation capacity during a significant earthquake event.

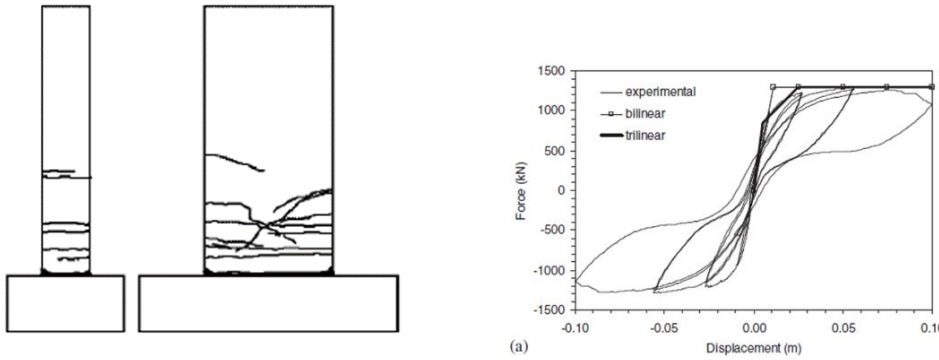

Figure 2.7. Final damage state and hysteretic loops for short test, Pinto et al. (2003)

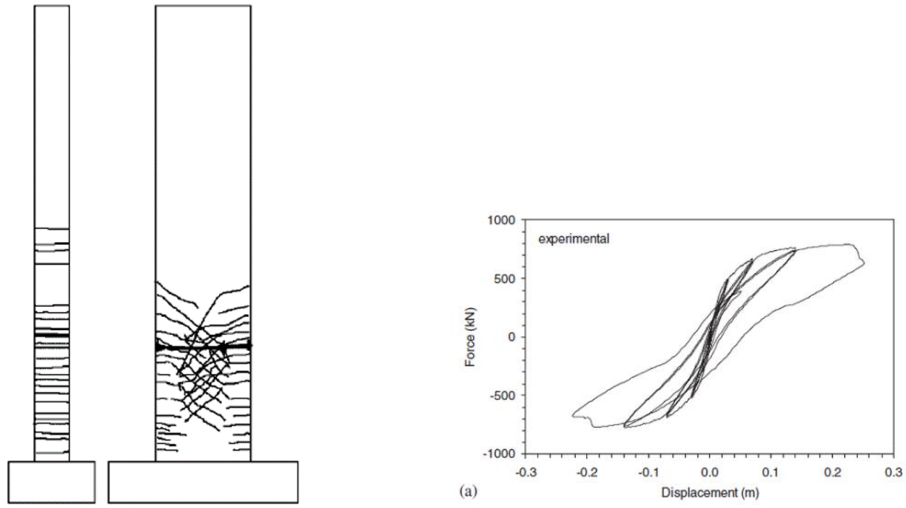

Figure 2.8. Final damage state and hysteretic loops for tall test, Pinto et al. (2003)

2.1.5. Mo et al., (2004)

The primary objective of the experimental study by Mo et al. (2004) was to present the results of an investigation on hollow rectangular columns retrofitted with carbon FRP (CFRP) composite straps.

Eight reinforced concrete hollow columns were tested under a constant axial load ratio varying from 0.080 to 0.136, and a cyclically reversed horizontal

load. Primary test parameters include transverse reinforcement, shear span, axial force level, and FRP retrofit.

The cross section of all specimens was 500x500 mm; the wall thickness of the hollow column was 120 mm. In this paper the spacing of the confining reinforcement satisfies both the design requirements of ACI code (ACI 318-95), and the requirements to prevent buckling suggested by Priestley et al. (1996), in which the spacing needs to be less than six times the diameter of the longitudinal rebars. However, the provided shear reinforcement of the specimens with an expected shear failure is much less than that required by the ACI code (ACI 318-95). In the group without FRP retrofit, there are two specimens, namely, NS1 and NI1-b. In specimen NS1, sufficient shear reinforcement was provided when compared to the ACI requirements. In specimen NI1-b, insufficient shear reinforcement was provided that was only about 35% of the ACI requirements. These two specimens served mainly as control specimens (see Figure 2.9).

The horizontal load was applied at a quasi-static rate in displacement-controlled cycles to displacements 5 mm, 10 mm, etc., for specimens NI1-b, and 10 mm, 20 mm, etc., for specimens NS1, until failure of the specimen occurred.

All hollow columns developed stable responses up to certain displacement ductility levels. Flexural cracks perpendicular to column's axis developed first in regions close to the bottom end of the columns. For the specimens without FRP sheets the flexural cracks became inclined and extended into the web zone of the columns due to the influence of shear, typically at a stage exceeding the first yield of longitudinal rebars. At later stages of loading, typically at displacement ductility levels of 2 and 3, independent shear cracks started to occur. In particular, for the as-built specimen NI1-b (with shear reinforcement of only 35% of the ACI requirement) shear failure occurred. Right before shear failure, this specimen had similar performance to retrofitted specimen. At the ultimate state, this specimen failed due to a very clear shear crack through the plastic hinge region.

Authors performed a comparison of the experimental results with some shear strength models [(ACI 318-95), Priestley et al., (1994), Ascheeim et al., (1992), Caltrans (1995)]. They concluded that for the specimen without FRP retrofit, the approach proposed by Priestley et al., (1994) to estimate the shear capacity gave the best prediction (see Figure 2.10)

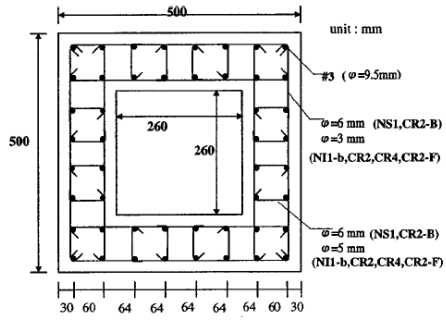

Fig. 1. Specimen sections

Figure 2.9. Comparison between experimental envelope and shear strength curves, Mo et al. (2002)

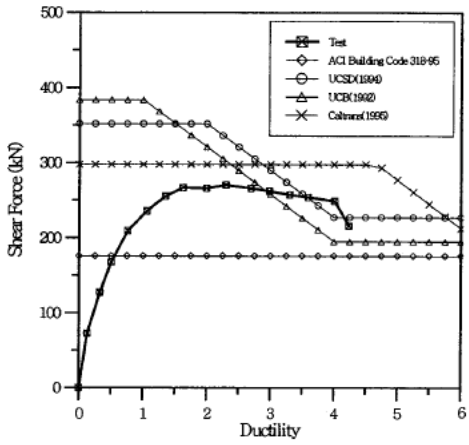

Figure 2.10. Comparison between experimental envelope and shear strength curves, Mo et al. (2002)

2.1.6. Calvi et al., (2005)

Calvi et al (2005) performed an experimental program on reduced-scale RC bridge piers with square hollow cross-section. The main objectives of the study were, among others, the evaluation of seismic response for different aspect ratios, and the assessment of the capacity of main shear strength models from codes and literature in prediction of collapse modes, strength and displacement capacity. Primary experimental variables of this study were aspect ratio, axial load and transverse reinforcement, for seven of the ten test specimens (hereinafter identified as "ordinary"). The remaining three

specimens were designed to investigate the effect of shift in critical section (interrupted longitudinal bars) and insufficient lap splice length.

All test specimens were designed in order to be representative of typical existing Italian hollow bridge piers. Among the ordinary specimens, two groups were defined, T-series and S-series, characterized by different aspect ratio (2 and 3, respectively). A hollow square cross section with side of 450 mm and thickness of 75 mm characterized all specimens. Short test units were characterized by lower reinforcement ratio, while tall specimens presented higher reinforcement ratios. For each series, three value of the axial load were defined and applied, in order to study the influence of this parameter on the lateral response. The properties of test specimens are reported in Figure 2.11. Tests were performed under constant axial load ratios, varying from 0.06 to 0.21, and cyclically reversed horizontal displacements, increasing with a sequence of drift ratios of 0.4%, 1.2%, 2.4%, 3.6%, and so on until failure occurred. A post-tensioned high strength Ø32 steel bar was used to give the initial axial load. The adopted test setup is reported in Figure 2.12.

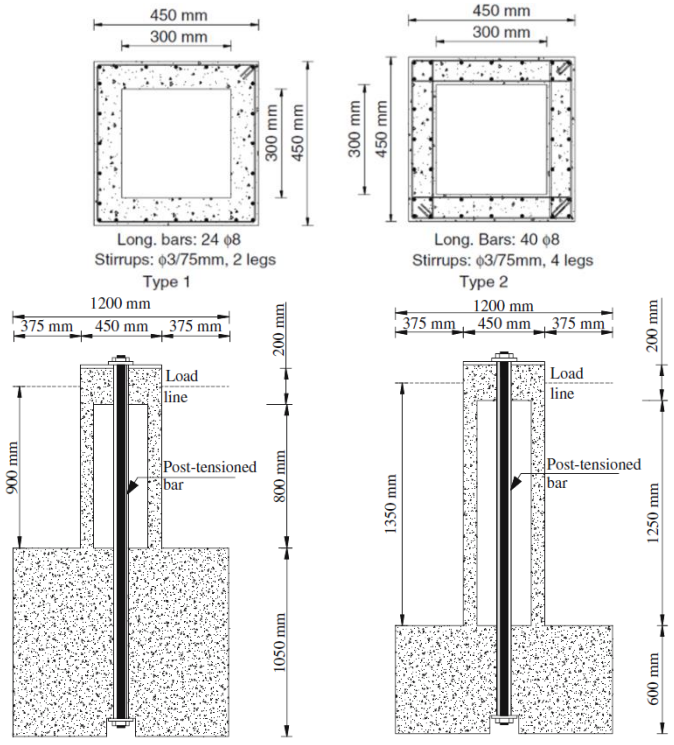

Figure 2.11. Properties of test specimens, Calvi et al. (2005)

As concerns materials, concrete compressive strength was of 30 MPa on average, while relatively high strength steel was used, with yield strength at approximately 550MPa and ultimate strength at approximately 670MPa.

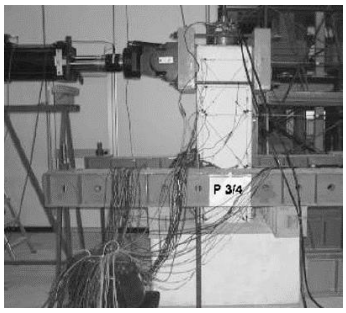

Figure 2.12. Test setup, Calvi et al. (2005)

The experimental results confirm that the collapse of the three S-specimens was essentially controlled by insufficient shear strength, with wide inclined cracks even from the beginning of the test and failure of the stirrups in the ultimate phase.

The taller pier tests were characterized by a mixed flexural–shear failure. They showed an increased capability of deformation with respect to the S-series but still insufficient. The yielding in longitudinal bars was reached, but the overall dissipation was reduced, deep inclined openings appeared on sidewalls, bars buckling in the critical section at the base of the column and finally failure of the transversal reinforcement. Shear cracks inclination varied between 25° and 29° for FS specimens (for which Flexure-Shear failure occurred), and between 29° and 35° for S specimens. Experimental results in terms of lateral force and drift are illustrated in Figure 2.13. Typical final damage states for S-specimens and T-specimens are depicted in Figure 2.14.

Authors compared prediction of few recent shear strength models with the experimental results. They concluded that the models proposed by Kowalsky and Priestley (2000) and Ashheim and Moehle (1992) were able to predict shear strength with sufficient accuracy. Less accurate was the maximum displacement estimation (ductility), obtained by intersecting the shear domains and the corresponding flexural response curves.

Authors observed that this was essentially due to the fact that the intersecting curves were almost flat in the intersection zone and a vertical

shifting due to the inherent uncertainty of the model resulted in a very large shifting in the horizontal direction of the intersection and finally in the displacement collapse estimation. Moreover, the issue of the lateral response assessment was considered not fully solved for hollow piers characterized by flexure-shear interaction, since fiber models, quite good in capturing flexural response, needed corrections in order to include some stiffness reduction due to shear cracking.

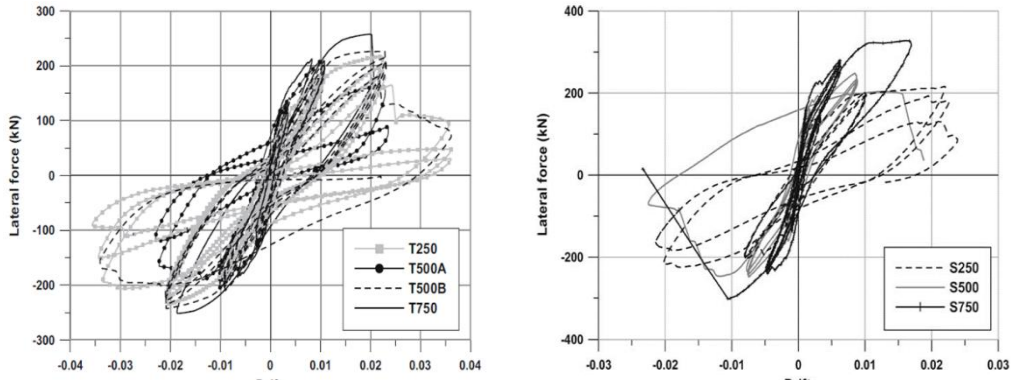

(a) (b)

Figure 2.13. Experimental response for T-specimens (a) and S-specimens, Calvi et al. (2002)

(a) (b)

Figure 2.14. Typical final crack patterns for S-specimens (a) and T-specimens, Calvi et al. (2002)

2.1.7. Delgado, (2009)

The study presented by Delgado (2009) is an extension of the previous

work (Calvi et al., 2005). The main objectives of the study were: the evaluation of seismic response of existing hollow section piers (typically those built until the seventies, thus not seismically detailed); the assessment of recent Eurocode 8 (EC8) provisions concerning stirrup ratio and detailing; the definition and testing of shear/confinement retrofit strategies for hollow section piers. Primary experimental variable of this study was transverse reinforcement ratio. Other secondary variables were the strength of concrete and reinforcement steel. Experimental tests were performed on twelve as-built reduced-scale RC bridge piers, six with hollow square cross section (identified as "PO1", identical to that considered in Calvi et al., 2005) and six with hollow rectangular cross section (identified as "PO2"). After the as-built tests were carried-out, all specimens were strengthened and re-tested. These last tests are not considered herein. The hollow square cross section had side of 450 mm, while the hollow rectangular cross section was 450 mm x 900 mm. Thickness was equal to 75 mm in both cases. The hollow rectangular specimens were tested along the shorter side, so no difference in the aspect ratio was considered. Longitudinal reinforcement consisted of 40 bars for PO1-specimens and 64 bars for PO2-specimens. All deformed steel bars with diameter of 8 mm were used. The test specimens were divided into three groups, different in material strength and transverse reinforcement details. First group (composed of Test PO1-N1 and PO2-N1) and second group (composed of Tests PO1-N2, PO1-N3, PO2-N2 and PO2-N3) were different in materials strength and transverse steel diameter, but both of them were characterized by the same reinforcement details. In particular, a single stirrup was present in each pier wall, typical of old bridge design and construction. Within the third group, different from the previous ones in terms of materials strength, three transverse reinforcement arrangements were considered: no seismic details for PO1-N4 and PO2-N4 (identical to first and second group); confinement reinforcement according to EC8 for PO1-N5 and PO2-N5; double amount of shear reinforcement for PO1-N6 and PO2-N6. Main specimens' properties are illustrated in Figure 2.15, Figure 2.16 and Figure 2.17.

Tests were performed under constant axial load of 250 kN, and cyclically reversed horizontal load. The horizontal load pattern is reported in Figure 2.18. These target displacements referred to measurements taken from the internal transducer of the hydraulic actuator that was affected by spurious deformations due to the reaction system and to the rotation of the foundation.

Since the actual specimen displacements do not match exactly those values, the correct values were obtained from an external transducer positioned at the level of the horizontal actuator axis, discounting the deflection due to foundation rotation that was also measured. For this reason, from the obtained force-displacement diagrams five deformation control stages were selected for the analysis of results. These stages were labelled from D1 to D5 and differed between piers.

Designação	Geometria	Betão	Arm. Long.		Arm. Transv.		
			área	aço	ϕ (mm)	f_{sy} (MPa)	tipo
PO1-N1	Quadrado	C20/25	40ϕ8	A500	3.8	390	2 ramos
PO2-N1	Rectangular	C20/25	64ϕ8	A500	3.8	390	2 ramos
PO1-N2	Quadrado	C25/30	40ϕ8	A400	2.6	437	2 ramos
PO1-N3	Quadrado	C25/30	40ϕ8	A400	2.6	437	2 ramos
PO2-N2	Rectangular	C25/30	64ϕ8	A400	2.6	437	2 ramos
PO2-N3	Rectangular	C25/30	64ϕ8	A400	2.6	437	2 ramos
PO1-N4	Quadrado	C25/30	40ϕ8	A500	2.6	443	2 ramos
PO1-N5	Quadrado	C25/30	40ϕ8	A500	2.6	443	2 ramos (EC8)
PO1-N6	Quadrado	C25/30	40ϕ8	A500	2.6	443	4 ramos (EC8)
PO2-N4	Rectangular	C25/30	64ϕ8	A500	2.6	443	2 ramos
PO2-N5	Rectangular	C25/30	64ϕ8	A500	2.6	443	2 ramos (EC8)
PO2-N6	Rectangular	C25/30	64ϕ8	A500	2.6	443	4 ramos (EC8)

Figure 2.15. Summary of specimens' properties, Delgado (2009)

Since important shear deformations were expected in these tests, an appropriate instrumentation configuration was adopted along the pier height using the LVDT layout shown in Figure 2.19, able to measure independently both the shear and flexural components of the specimen deformation. Actually, the two deformation components were not directly measured. In fact, resorting to instrumentation readings concerning horizontal displacements at several elevation levels as well as the top and base section rotations, it was possible to estimate the flexural component of the deformation. All specimens were characterized by shear failure. Damage state evolution was very similar for test specimens without seismic details, with both square and rectangular cross section. The early test stages D1 were largely characterized by cracking near the pier base (approximately in the lower third of the height of the specimen), inclined in the webs and horizontal in the flanges. At stage D2, cracking

developed along pier height, inclined at approximately 45◦ in the webs. At following stages, diagonal cracks along webs increased their width, while flexural cracks on the flanges were characterized by lower width. Therefore, lateral response was dominated by shear. In fact, after peak load was reached, a softening regime without any visible plastic plateau started. No plastic hinges developed at the bottom end of the specimens. It was noted that, for hollow rectangular test units, on the flanges in the upper part of the specimens, flexural cracks were no more exclusively horizontal, as usual for T- or I-shaped sections, due to the so-called "shear lag effect" that occurs for the ratio flange-width/section-height of about 2:1 or above.

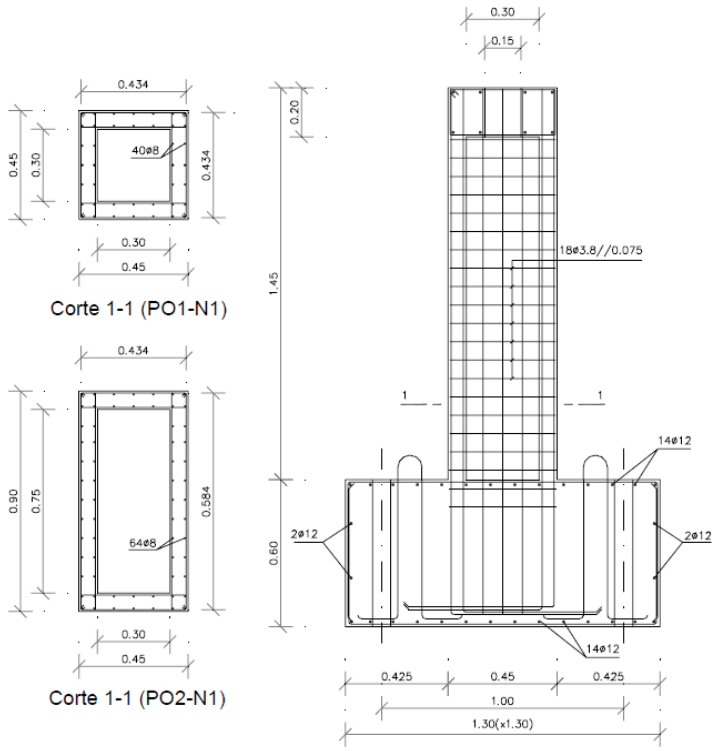

Figure 2.16. Specimens with no seismic details, Delgado (2009)

As regards test specimens with seismic details, damage state evolution was almost similar at initial stages, but diagonal cracks width was limited and delayed by the presence of additional transverse reinforcement. (see Figure 2.20). Comparing experimental response of specimens without seismic details with that of specimens with confinement reinforcement according to EC8,

Author noted no substantial differences, since they were interested by shear failure (see Figure 2.21). By observing the comparison between responses of specimens without seismic details and that of detailed specimens with double amount of shear reinforcement, Author noted an improvement in strength (of about 25%) and ductility (of about 45%), even if also in this case shear failure wasn't prevented (see Figure 2.22).

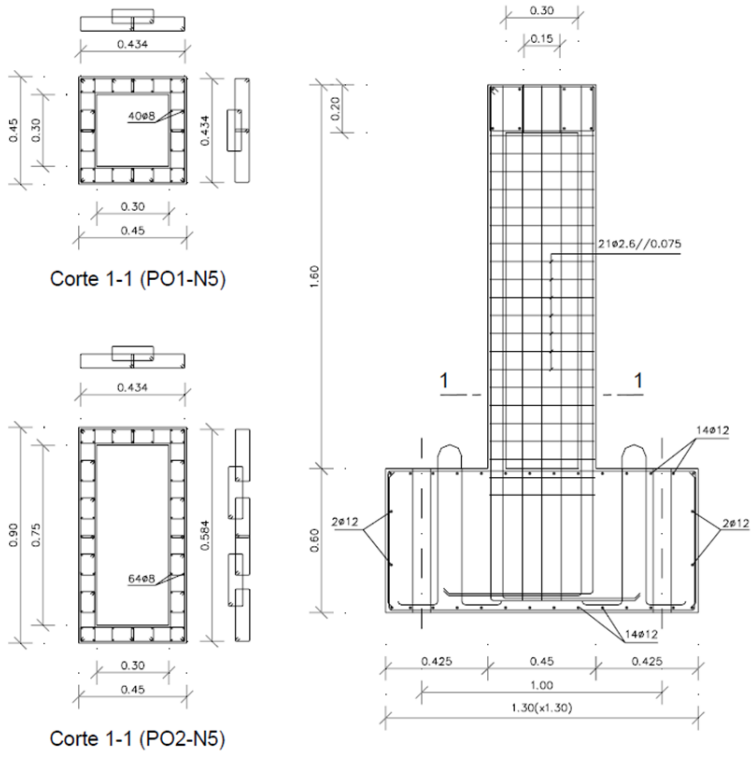

Figure 2.17. Specimens with seismic details, Delgado (2009)

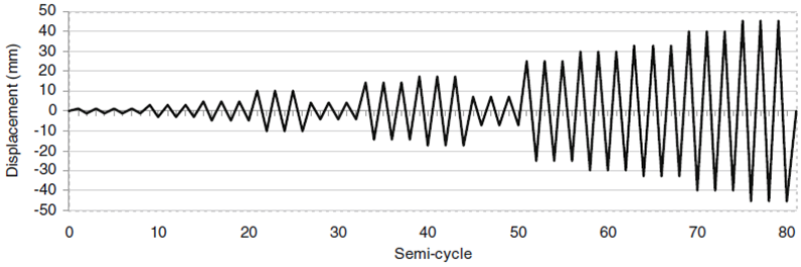

Figure 2.18. Lateral loading protocol, Delgado (2009)

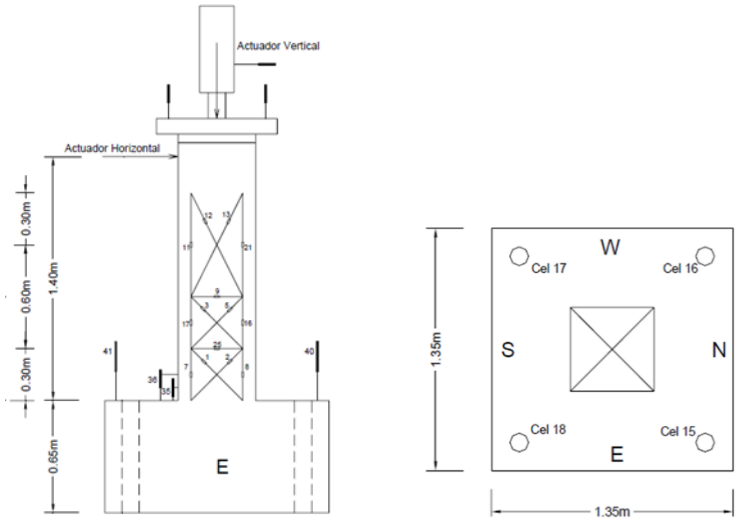

Figure 2.19. Lateral LVDT layout, Delgado (2009)

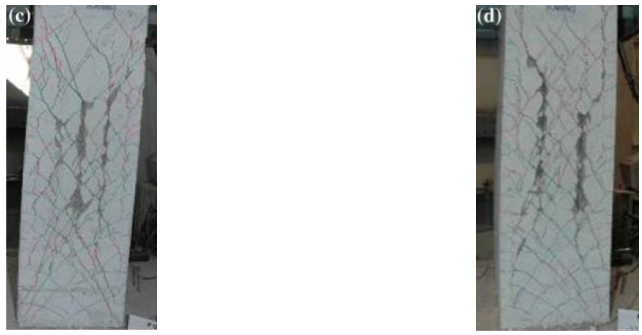

Figure 2.20. Crack patterns for Test PO2-N4 (2.14% drift – a) and PO2-N6 (3.14% drift – b), Delgado (2009)

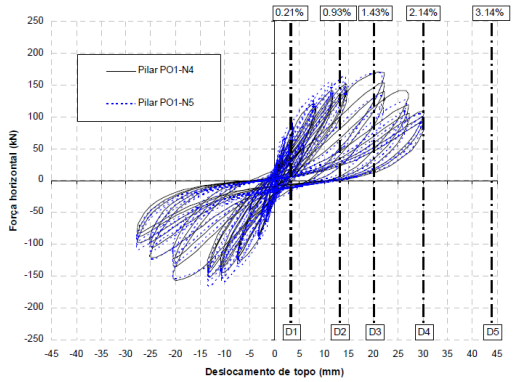

Figure 2.21. Experimental response comparison between Test PO1-N4 and Test PO1-N5, Delgado (2009)

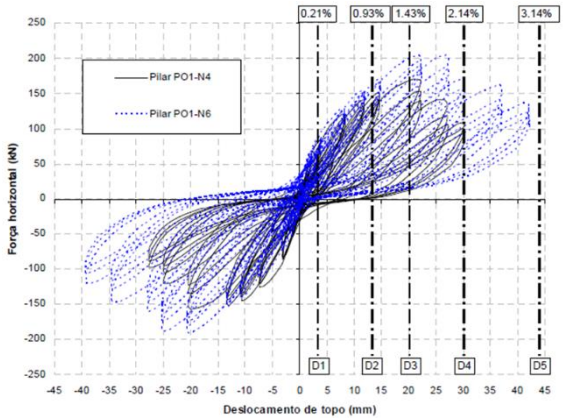

Figure 2.22. Experimental response comparison between Test PO1-N4 and Test PO1-N6, Delgado (2009)

Finally, as concerns deformation components, seismic details caused a significant reduction of shear deformation, which reached about 60% of total lateral displacement at shear failure stage, while it was of about 80% for specimens without seismic details (see Figure 2.23).

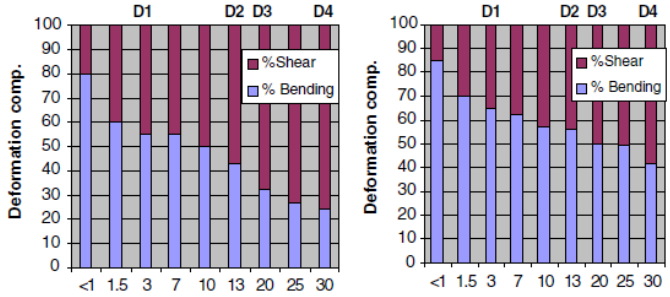

Figure 2.23. Shear and bending deformation components Test PO1-N4 and Test PO1-N6, Delgado (2009)

2.2 Experimental studies: hollow circular RC columns

Hollow section piers are a very popular structural solution for reinforced concrete (RC) bridge structures, due to, on one side, the economical convenience (saving of materials afforded by reduced section area), and on the other side, the higher efficiency with respect to solid sections from a structural point of view (larger moment-of-inertia than solid sections with a similar area, reduced inertia masses, limited cracking due to non-uniform development of

heat of hydration). In particular, circular shape of the RC hollow section piers is very used for highway bridges, because its lateral response under wind and seismic loads is similar in any direction. Despite their widespread use, relatively few experimental studies have been performed on RC hollow circular section members. Some experimental campaigns on RC piers with hollow-core circular cross section and double reinforcement layer are present in literature, since 80's. A first experimental study was focused on seismic response of RC hollow circular concrete scaled members of offshore concrete platform, characterized by two layers of longitudinal and well-detailed transversal reinforcement (presence of cross ties through the wall thickness). Such study proved that this kind of members were able to display a similar ductile load-deformation behavior to that available from well-detailed solid members (Whittaker et al., 1987). Similar results were obtained by the study conducted by Tokyu Construction Company on the behavior of slender and squat hollow circular members with rather thick wall (20% of the external diameter). Then, cyclic tests on three different bridge piers with hollow circular cross section and different layout of transversal reinforcement were performed in Yeh et al. (2001), in order to study the flexure-shear interaction. Results showed that the lack of the internal confinement reinforcement between the two longitudinal steel layers might involve failure in tension of some longitudinal steel bars at the bottom of the column after concrete crushing and buckling during previous compression cycles, and flexure-shear failure if external transverse reinforcement was not sufficient. Then, since their diffusion for bridge piers, the experimental attention was shifted on hollow circular sections with a single layer of longitudinal and transverse reinforcement, but very few experimental studies are available in literature focusing on this topic. Initially, the aim of the experimental studies was to study the change in flexural response due to the absence of the internal reinforcement layer (Zahn et al. (1990), Hoshikuma and Priestley (2000)). Once the flexural response was almost clear, the target of the experimental study was to improve the prediction capacity of shear strength for hollow circular columns (Ranzo and Priestley (2001)). Each of these works will be briefly described, discussed and analyzed hereafter. In particular, the attention will be focused on the specimens' properties, test setup and experimental results. This literature review will be the basis for the collection of the database reported in the section 7.1.

2.2.1. *Zahn et al. (1990)*

For column members of smaller cross-sectional size, it may be convenient to place the longitudinal and transverse reinforcement in one layer, only near the outside face of the cross section and not to tie the concrete through the wall thickness. This leads to a simpler arrangement of reinforcement, but then the concrete near the inside face of the hollow section is unconfined and the flexural failure may be brittle. Based on this observation, Zahn et al. (1990) carried out an experimental study on six columns with hollow circular reinforced concrete columns and a single layer of steel reinforcement near the outside face. The objectives of the study were to establish the parameters that control the available flexural strength and ductility for these elements. The experimental variables were the ratio of the inside to outside diameter of the column section (D/D_i), and the axial load ratio. In particular, three pairs of columns were designed with D/D_i ratios of 0.53, 0.63 and 0.73, corresponding to thickness of 90, 75 and 55 mm. All columns had an outside diameter of 400 mm. Figure 2.24 shows the principal dimensions and loading arrangements of the columns. It can be noted that each test unit is composed of two test units and a central stub to which horizontal load is applied.

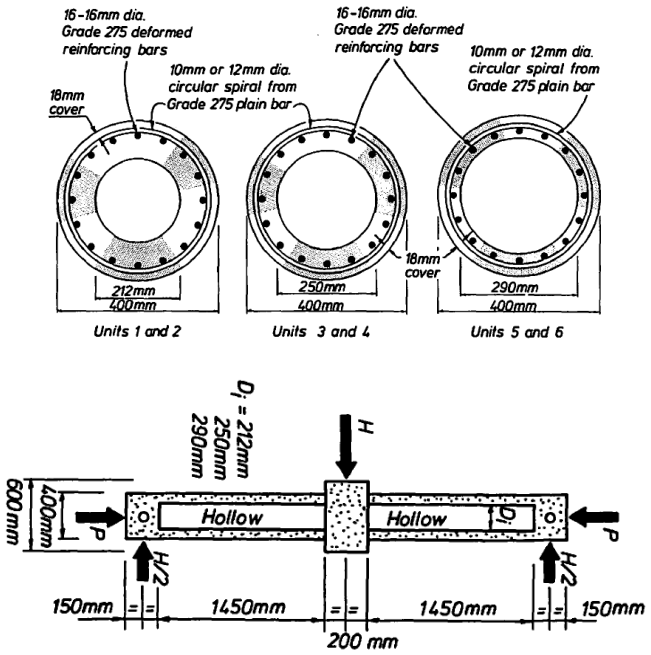

Figure 2.24. Geometry and reinforcement details, Zahn et al. (1990)

All tests were performed under constant axial load ratio, varying from 0.10 to 0.40, and increasing displacement cycles until failure occurred. Test units failed by the more or less rapid collapse of the concrete wall in the compression zone. No signs of shear failure were observed in any of the tests. Authors observed that the position of the neutral axis at the flexural strength had a significant influence on the available curvature ductility of the columns. If the neutral axis is close to the unconfined inside face of the tube, resulting in small longitudinal strain in the unconfined region of the concrete compression zone, ductile behavior can be expected. If, on the other hand, the neutral axis is some distance away from the inside face (toward the centroid of the section), the resulting high longitudinal compressive strain on the inside face causes early vertical splitting and crushing of the concrete and consequent low ductility, as a result of rapid deterioration of the flexural strength.

The main factors that control the neutral axis position at the flexural strength, are the axial load ratio, the inside to outside diameter ratio, the longitudinal steel ratio, and the material strengths. Appreciable ductility can only be achieved with low axial load, small longitudinal steel ratio, and a wall thickness of not less than 15% of the overall section diameter.

The amount of spiral steel placed near the outside face of the tube wall plays a relatively minor role in the available ductility of circular hollow column sections when the longitudinal strains on the inside face of the tube wall are relatively high. The radial confining stress exerted by spiral reinforcement puts the compressed portion of the curved wall into circumferential compression and thus helps to delay vertical cracking. However, because of the absence of any confinement in the radial direction on the inside face of the wall, annular cracks extending in the direction of the column axis start to form once a critical value of the longitudinal compressive concrete strain is exceeded there.

The tests conducted indicated that a value of 0.008 for the longitudinal compression concrete strain at the inside face of the tube wall at crushing there may be safely used as a limit state to determine the ultimate curvature for design purposes.

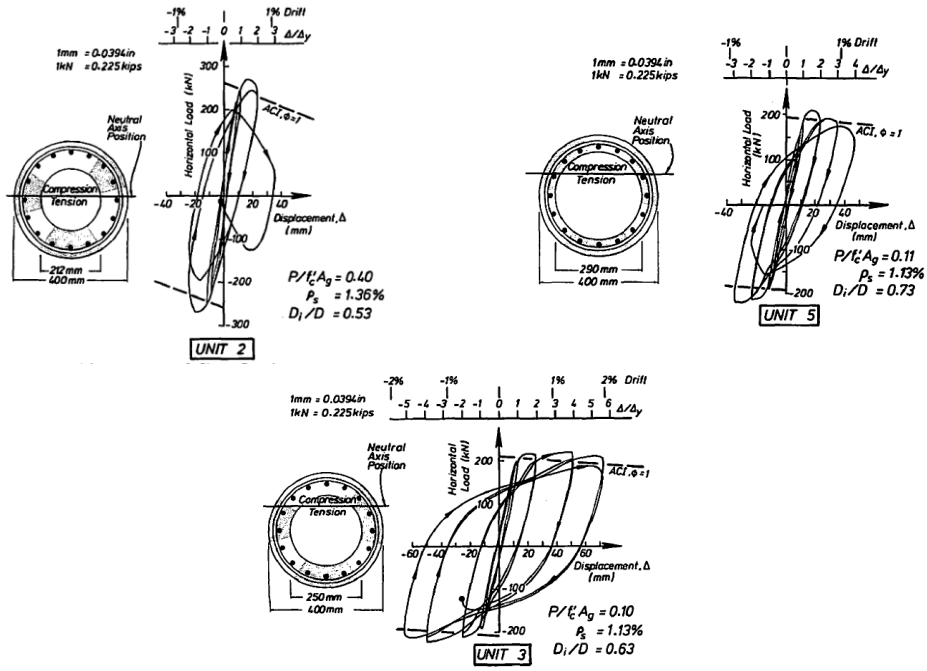

Figure 2.25. Horizontal load-displacement hysteresis loops, Zahn et al. (1990)

2.2.2. *Hoshikuma and Priestley (2000)*

Hoshikuma and Priestley (2000) presented an experimental report in which two reduced-scale hollow circular columns with different longitudinal reinforcement ratio were tested under constant axial load and cyclic lateral load. Scale factor of 1:4 was adopted, for which the scale effects would be minimal.

The outer diameter of the hollow section was 1524 mm and the inner diameter 1244mm, resulting in 140mm wall thickness or the wall thickness ratio of 0.092. The test unit below mid-height section was constructed by reinforced concrete with hollow section and a loading steel tube was connected to the column top for the extension of the height, to make on-site construction be speedy and efficient. The height of the hollow reinforced concrete section was 3480 mm, sufficient to observe the flexural performance at the plastic hinge region. A total column height from the base to loading point is 6528 mm, tested in single bending to give the aspect ratio of 4.28. Specimens were identified as HF1 and HF2, characterized by 1.45% and 3.18% longitudinal

reinforcement ratios respectively. Transverse reinforcement ratio was high in order to prevent shear failure. Figure 2.25 shows geometry and reinforcement details of test specimens. As regards material properties, concrete cylindrical compressive strength was of about 38 MPa, yield strength was equal to 430-440MPa and 625 MPa for longitudinal and transverse steel reinforcement, respectively. The applied axial load ratio was of about 0.13 for both test units.

Figure 2.27 shows the force-displacement response for both specimens. Damage state evolution for Test HF1 (with lower longitudinal reinforcement ratio) was characterized by first horizontal cracks for lateral force value of about 3/4 of the yielding force. After yielding, new horizontal cracks formed up to the whole height of the specimen, and existing cracks increased their width. After peak load was reached, some shear crack appeared, while no longitudinal reinforcement buckling was observed. Failure was reached, in fact, when the inside face concrete (monitored by video camera located in the void section) was crushed. This resulted into a sudden and severe drop of the lateral strength on the force-displacement response, which limited the ultimate ductility capacity.

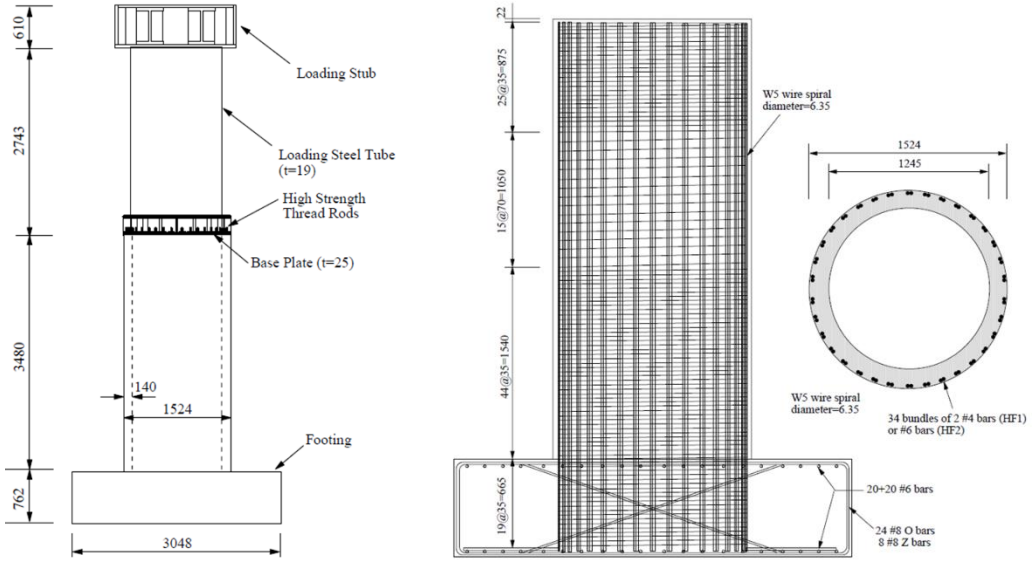

Figure 2.26. Geometry and reinforcement details of the test units, Hoshikuma and Priestley (2000)

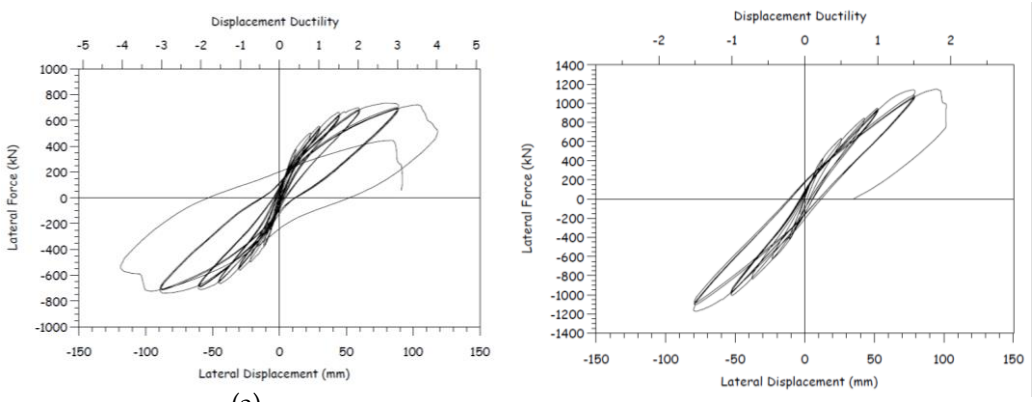

Figure 2.27. Lateral force-displacement hysteretic response for Test HF1 and Test HF2, Hoshikuma and Priestley (2000)

For Test HF1 (with higher longitudinal reinforcement ratio), first horizontal cracks formed for lateral force value of about 1/2 of the yielding force. After yielding, new horizontal cracks formed up to the whole height of the specimen, existing cracks increased their width and some shear cracks appeared. After peak load was reached, the onset of crushing of cover concrete was noted at the column base. No buckling of longitudinal bars was observed. Failure was reached, when the inside face concrete was crushed. This resulted into a sudden and severe drop of the lateral strength on the force-displacement response, which limited the ultimate ductility capacity.

By analyzing the experimental results, Authors concluded that the inside face concrete compression strain is one of the most important parameters to control the ductility capacity of the hollow columns. High axial load, a thin wall or a high longitudinal steel ratio causes the neutral axis pass through the void section with a deep clearance from the inside face, resulting in high longitudinal compression strain at the inside face. These observations were in accordance with the results by Zahn et al. (1990), presented in the previous section. Nevertheless, Authors suggested a different limit for concrete compression strain at the inside face corresponding to flexure brittle failure. The suggested limit was equal to 0.005, even though a sufficient amount of transverse steel was placed near outside face. In fact, the concrete wall in the circular hollow section is effectively subjected to biaxial compression, which causes the significant reduction in confinement effectiveness and then the

premature crushing of inside face concrete. A confinement strain of 0.001 was proposed for the maximum useful transverse steel confinement induced strain in the critical hollow section based on the test results. Under these assumptions, the flexural strength and the ductility capacity of the hollow columns may be evaluated with the use of the conventional moment-curvature analysis for the equivalent solid circular section with the same confinement effectiveness.

2.2.3. *Ranzo and Priestley (2001)*

The purpose of the experimental study by Ranzo and Priestley (2001) is to investigate the shear strength of thin-wall circular hollow columns, with a single layer of steel reinforcement. To this aim, cyclic tests with constant axial load were carried out on three specimens characterized by the same amount of transverse reinforcement, while the longitudinal reinforcement and the axial load were taken as experimental variables. For all test units, the ratio of the shear span to the section diameter was selected to be 2.5, and the same amount of the transverse reinforcement corresponding to 0.35% volumetric ratio was also provided. Figure 2.28 shows the main properties of test specimens.

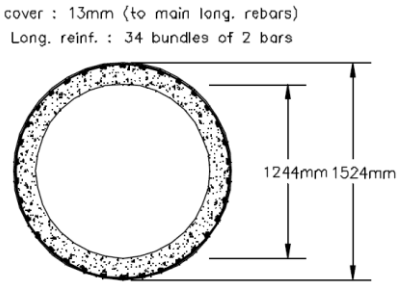

Specimen	M/VD	D (mm)	t (mm)	$P/f_c'A_n$ (%)	Long. Rebars (mm)	Trans. Reinf. (mm)	f_c' (MPa)
HS1	2.5	1560	152	5	68 D13	D6 @ 70	40
HS2	2.5	1524	139	5	68 D16	D6 @ 70	40
HS3	2.5	1524	139	15	68 D16	D6 @ 70	35

Figure 2.28. Properties of test specimens, Ranzo and Priestley (2001)

The longitudinal reinforcement ratios, referred to the section net area were 1.4% for unit HS1 and 2.3% for units HS2 and HS3. The section geometry with the arrangement of longitudinal and transverse reinforcement is shown in Figure 2.28. The first unit (HS1), characterized by low levels of longitudinal

reinforcement and axial load of 0.05, was designed to fail in flexure. The second (HS2), characterized by a higher level of longitudinal reinforcement and the same axial load, was instead designed to fail in shear. The third (HS3), with the same longitudinal reinforcement as HS2 and a higher axial load ratio of 0.15 was designed to induce a brittle flexural-shear failure. The transverse reinforcement consisted of a continuous spiral. Test specimens were deeply instrumented with strain gauges, curvature cells, and deformation panels, in order to monitor the main local deformability during the tests. In Figure 2.29 the adopted monitoring system is depicted.

Figure 2.29. Monitoring system, Ranzo and Priestley (2000)

The experimental response of test specimens are reported in Figure 2.30.

Specimen HS1 exhibited a ductile response. Flexure failure of the test unit was observed at ductility 6.0 due to implosion of concrete in the inside face of the column wall. Buckling of longitudinal rebars occurred in the compression region at column base, involving 4 layers of spiral reinforcement. Before failure, limited strength degradation occurred during repeated cycles.

The response of unit HS2 was characterized by little strength degradation occurred before ductility 3.0, when concrete spalling in the inside face occurred. This caused a sudden loss in strength of approximately 25%. The unit subsequently failed in a brittle flexure-shear mode at displacement ductility of 3.5. The transverse steel fractured along the crack in several layers (see Figure 2.31). The behavior of unit HS3 was greatly influenced by the higher level of axial load. The force-displacement cycles, showed a more evident pinched shape near the origin, due to the effect of the axial load.

Concrete spalling in the inside face occurred at ductility 2.0 in the push direction, and subsequently the unit failed in shear in the first cycle in the pull direction. The deformation capacity was 43% less than that observed in the unit HS2. The top displacement contributed by the shear deformation was measured to be 20%, 30%, and 40% for the unit HS1, HS2, and HS3, respectively.

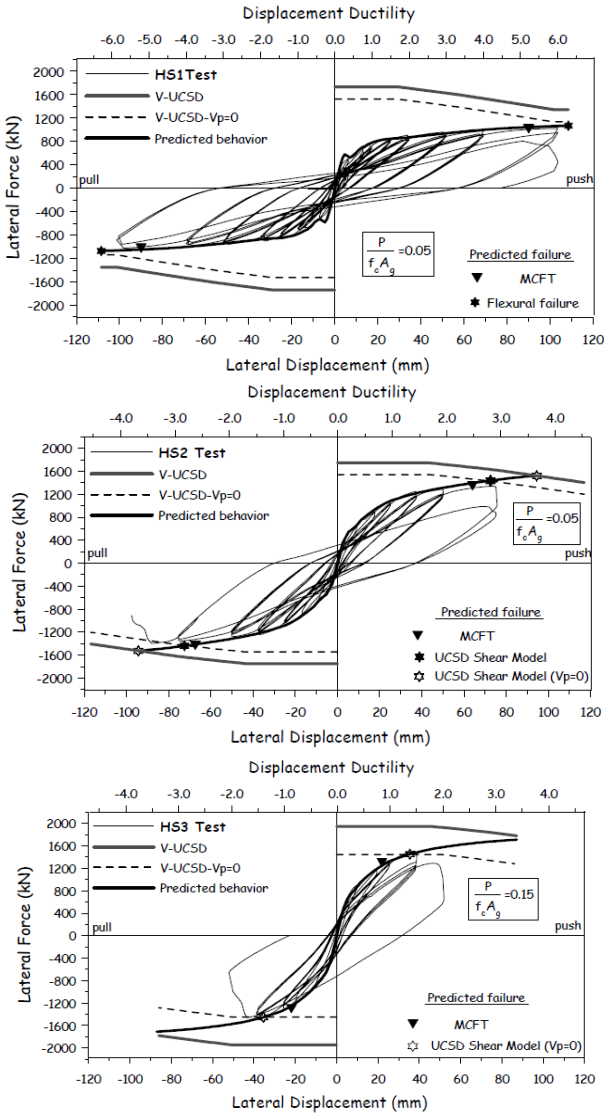

Figure 2.30. Force-displacement response of units HS1, HS2 and HS3, Ranzo and Priestley (2000)

Figure 2.31. Unit HS2 at failure, Ranzo and Priestley (2001)

Based on the experimental results, Authors proposed some modifications to shear strength model by Kowalsky and Priestley (2000), accounting for the shape of the cross section (different effective shear area) and the effect of the axial load. The same model can be used successfully to predict the load-deformation behavior with simple sectional analysis. This model gave good prediction of the experimental shear strength, slightly overestimating, while also more recent and sophisticated models such as MCFT model (Collins and Vecchio, (1988)), deeply underestimated both strength and ductility for shear-dominated specimens.

2.3 Modeling of existing RC columns

2.3.1. Classification issue

Nonlinear behavior of RC elements strictly depends on their failure typology. Flexural response of a RC element can be "limited" because of the onset of a premature shear failure and, in reverse, shear capacity can decrease because of the cyclic degradation of shear resistance contributions due to the increase in ductility demand after yielding. Three different failure modes can be identified for a RC column, as a result of the adoption of a degrading shear capacity model (Figure 2.32).

When the initial non degraded shear strength is lower than plastic shear capacity (Figure 2.32a), shear failure occurs limiting flexural response, namely deformation capacity or energy dissipation capacity, and causing a significant sudden strength reduction.

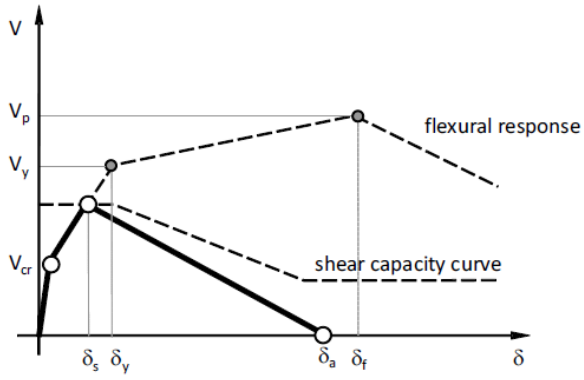

(a)

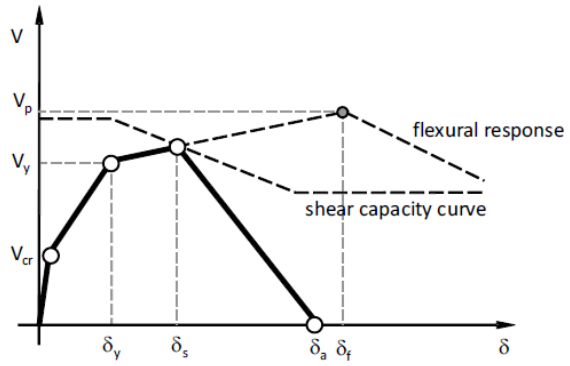

(b)

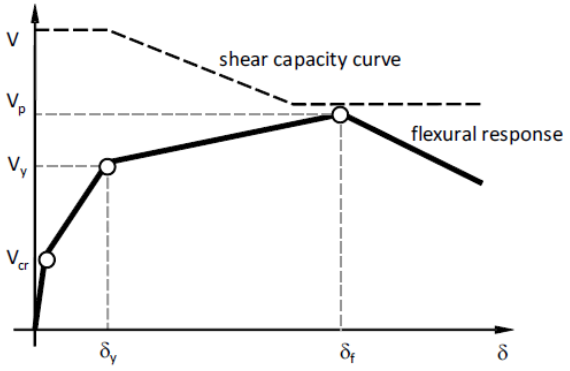

(c)

Figure 2.32. Classification: shear (a), flexure-shear (b), and flexural behaviour, De Luca and Verderame (2015)

When the degraded shear strength is higher than the plastic shear (Figure 2.32c), the flexural response can completely develop, without interaction with shear, exhibiting high ductility capacity up to the onset of degrading

phenomena as bar buckling or concrete crushing and cover spalling.

In all the other cases, the element can reach yielding, but the inelastic flexural response is modified by the onset of a post-yielding shear failure (Figure 2.32b). Anyway, after shear failure, the behavior of the element becomes strongly degrading up to the loss of axial load carrying capacity.

Thus, the behavior of a RC element can be classified on the basis of the ratio between plastic shear capacity and degrading shear strength. Several models have been developed to represent the degradation of shear strength with increasing inelastic ductility demand (Priestley et al. 1994, Biskinis et al., 2004; Sezen and Moehle, 2004, among other). Nevertheless, further literature researches (Zhu et al., 2007, Elwood et al., 2007, among other) proved that the failure mode classification cannot be adequately carried out on the basis only on the shear strength capacity and introduced a classification based also on other key parameters, e.g. transverse reinforcement ratio or stirrups-spacing-to-section-depth ratio.

2.3.2. Models for lateral response

The prediction of the deformation for a RC column subjected lateral load is a crucial issue of the displacement-based assessment of existing RC structure. Referring to a cantilever column, its lateral response is completely defined depending on total top displacement. The top displacement can be interpreted as the results of three coexisting response mechanisms: flexure deformation, shear deformation, and fixed-end-rotation due to longitudinal bar slip at column base. In the following, different modelling strategies aimed at reproducing each of the above-mentioned mechanisms, are briefly described and discussed.

2.3.2.1 Flexural behavior

Inelastic structural component models can be differentiated depending on how plasticity is distributed along the member length and through the member cross section. The most complex models discretize the element along its length and through the cross sections into micro- finite elements (Figure 2.33a) with nonlinear hysteretic constitutive properties that can have many input parameters, thus offering a great versatility, but also requiring a great effort in terms of model parameter calibration and computational resources. Reducing the complexity level, the fiber formulation models distribute

plasticity by numerical integrations through the member cross sections and along the member length (Figure 2.33b). Uniaxial material models are adopted to define the nonlinear hysteretic axial stress-strain behavior in the cross sections. The Bernoulli hypothesis on plane section is assumed, and uniaxial material "fibers" are numerically integrated over the cross section to obtain stress resultants (axial force and moments) and incremental moment-curvature and axial force-strain relations. The cross section parameters are then integrated numerically at discrete sections along the member length, using displacement or force interpolation functions (Kunnath et al. 1990, Spacone et al. 1996). Distributed fiber formulations provide strains in the steel and concrete cross section fibers, instead than plastic hinge rotations, and the calculated strain demands can be quite sensitive to element length, integration method, and strain hardening parameters. A further step to reduce complexity and computational efforts is represented by the "finite length hinge model" (Figure 2.33c). This modeling approach is an efficient distributed plasticity formulation where hinge zones at the member ends are pre-defined. Cross sections in the inelastic hinge zones are characterized through either nonlinear moment-curvature relationships or explicit fiber-section integrations assuming Bernoulli hypothesis on plane section. If hinge length is well designed, integration of deformations along the hinge length captures the spread of yielding more realistically than the concentrated hinges, and the finite hinge length facilitates calculation of hinge rotations.

The simplest models concentrate the inelastic deformations at the ends of the element, such as through a rigid-plastic hinge or an inelastic spring with hysteretic properties (Figure 2.33d and Figure 2.33e). These elements have numerically efficient formulations thanks to the concentration of the plasticity in zero-length hinges with moment-rotation model parameters.

Fiber and finite element models capture the axial force-moment (P-M) interaction directly, while concentrated and finite length hinge models may consider the P-M response through yield surfaces. On the other hand, the detailed fiber and finite element models are not necessarily capable of modeling effects such as degradation due to reinforcing bar buckling and fracture that can be captured by simpler phenomenological models. In fact, distributed plasticity formulations are able to model stress and strain variations through the section and along the member accurately, but important local phenomena, such as strength degradation due to local buckling of

reinforcing bars, or the nonlinear interaction of flexural and shear, are difficult to capture without sophisticated and numerically intensive models.

Vice-versa, models based on empirically-defined concentrated hinge may be more suitable to capture the nonlinear degrading response of members through the calibration of phenomenological moment-rotation relationships and hysteresis rules, using member test data, with the same or lower approximation of more sophisticated formulations.

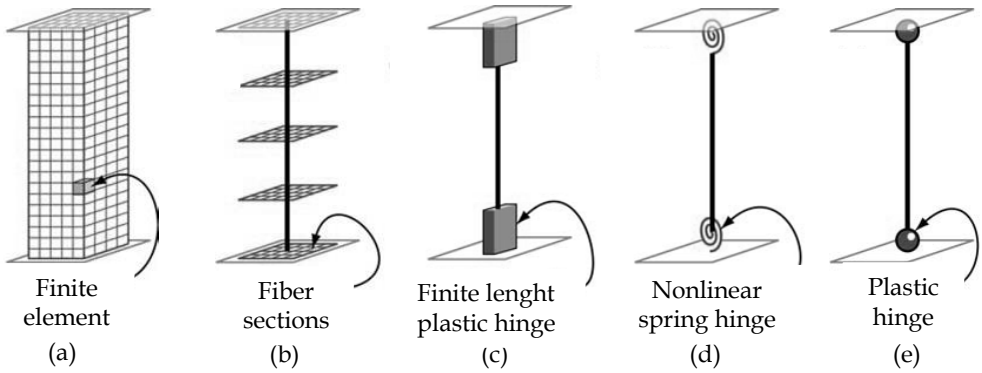

Figure 2.33. Flexural modelling - adapted from Dierlein (2010)

Concentrated hinge models obviously require a pre-determination of backbone relationships between characteristic forces and deformations of structural components, together with the associated hysteresis rules, to define component behavior, demand parameters, and acceptance criteria.

In the adoption of such pre-defined backbones, when a nonlinear analysis has to be performed, it is important to distinguish between "monotonic" and "cyclic envelope" curves. The former represents the response that would be observed for a component tested under monotonic loading, the latter represents the forces-displacements behavior under cyclic loading, depending on the applied cyclic loading history.

When the cyclic effects of earthquake loading are not modeled directly in the analysis, e.g. in nonlinear static analyses, the nonlinear component models should be defined based on the degraded cyclic envelope. For nonlinear dynamic analysis, the choice of components curves depends on how cyclic degradation is modeled. Direct modeling of cyclic degradation begins with a monotonic backbone curve and degrades this relationship as the analysis proceeds (Ibarra et al. 2005, Haselton et al. 2007). In indirect modeling

approach, the component backbone curve does not degrade and it is defined as the cyclic envelope, already including cyclic strength degradation.

Additional springs can be added to the flexural model in order to take into account also shear behavior, as explained in next section, or bond-slip of longitudinal reinforcing bars.

2.3.2.2 Shear behavior

The assessment of the shear behavior for RC members is a crucial issue, as recently highlighted by many studies, both at service and ultimate conditions. Models for response of columns with details satisfying current code requirements may reasonably ignore shear deformations, or model them using simplified procedures, because shear deformations are relatively small, and a ductile response dominated by flexure can be considered assured. Vice versa, the amount of shear deformations in existing (generally, shear-critical) columns, especially after the development of shear cracks, can be significant and needs to be modeled in order to represent total deformations in these members (Sezen, 2002). Moreover, for RC members characterized by lower aspect ratio (short and deep columns) the deformations caused by shear may become significant, while for relatively slender members (aspect ratio greater than 3) shear deformations can be ignored (Priestley et al., 2007). Regarding ultimate state condition, as explained in Section 2.3.1, to develop flexural behavior, the member shear strength must be larger than the flexural strength, which is the condition typically required in capacity design provisions for seismic design. Where the shear strength is not sufficient to preclude shear failure (such as in most of the existing structures), shear effects must be considered in the analysis model in addition to flexural and axial load effects. Once this shear failure is triggered before or after flexural yielding, shear and deformation capacities are progressively lost.

Only approximate methods for predicting shear deformations of concrete members during service condition are available, though the modified compression field theory (MCFT) (Vecchio and Collins, 1986) provides a means for predicting total deformation, including shear components, for monotonic response. It must be said that the latter approach appears very computationally demanding.

Priestley et al. (2007) proposed a simplified approach to compute shear deformations. The original procedure to calculate shear deformations was

presented by Park and Paulay (1975). Miranda et al. (2005) provided further development and study on reinforced concrete columns. Finally, Priestley et al. (2007) updated the procedure. According to this approach, the shear force-displacement response is assumed as multilinear curve, identified through four characteristic points: flexural cracking, shear cracking, yielding, and peak load. Four different shear stiffness values are defined, based on mechanics' theory.

Simpler attempts to capture the shear failure in columns were based on a post-processing of analyses results in which only flexural behavior is explicitly modeled (Otani and Sozen, 1972, Spacone et al., 1996, Liel et al. 2010). This approach is able to detect shear failure in a force-approach, but it does not properly estimate inelastic shear deformations and degrading behavior after shear failure.

A fairly straightforward approach to model shear effects is represented by the introduction of a nonlinear shear spring in series with the axial-flexural model (Pincheira et al. 1999, Lee and Elnashai 2001, Sezen and Chowdhury 2009, Jeon et al 2015). The definition of the backbone curve characterizing this shear spring can be based on the modified compression field theory (MCFT) (Vecchio and Collins, 1986) or on drift capacity at shear failure.

Pincheira et al. (1999) added a zero length shear spring that can account for the strength and stiffness degradation with increasing deformation demand (Figure 2.34a). The model is able to represent flexure or shear failure under monotonically increasing or reversed cyclic loading and stiffness degradation with cyclic loading can also be represented. Although the procedure they suggested to solve the convergence issue, it can be very computationally demanding.

Lee and Elnashai (2001) also utilized the MCFT to define the backbone curve of the shear spring and developed hysteretic rules including the variation of column axial loads (Figure 2.34b).

Sezen and Chowdhury (2009) developed the hysteretic model including the flexure-shear-axial interaction based on the backbone curve obtained from the MCFT, and also employed the bond-slip model developed by Sezen and Moehle (2003).

Jeon et al. (2015) simulated shear response by means of a zero-length shear spring located at one end of the column (Figure 2.34c). Shear failure begins once the column shear demand exceeds the column shear not-degraded

capacity. The adopted shear strength prediction derives from the ASCE 41-06 shear strength model but it does not take into account the possible degradation of shear strength capacity with increased ductility demand.

Some shear strength models (Kowalsky and Priestley 2000, Sezen and Moehle 2004, Biskinis et al.2004) calibrated on empirical data are useful for estimating the column shear strength as a function of inelastic ductility demand. However, they do not provide a reliable estimate of the drift capacity at shear failure (Elwood and Moehle 2005). Nevertheless, models that predict drift capacity for columns experiencing shear failure prior to or after than flexural yielding can be found in literature (Pujol et al. 1999, Elwood and Moehle 2005).

Pujol et al. (1999) proposed a drift capacity model for shear-critical columns by means of a statistical evaluation of an experimental database of 92 columns, also including columns with quite high transverse reinforcement ratios (higher than 0.01), thus not suitable for non-ductile columns.

Elwood and Moehle (2005) proposed an empirical drift capacity model, more inherent to non-ductile elements, by using a database of 50 flexure-shear-critical RC columns with configurations representative of those used in pre-1970s American buildings.

Later, on the basis of this drift capacity model, Elwood (2004) developed a drift-based shear failure model (the so-called "limit state material") that can identify a shear failure associated with column shear and column's total deformation by means of a shear spring in series with a nonlinear beam-column element (Figure 2.34d). The limit state material has a predefined tri-linear backbone curve and five parameters to define pinching and stiffness degradation; the limit state material changes the backbone of the material model to include strength degradation once the response of the beam-column element exceeds a predefined limit curve. However, a limited number of comparison studies with experimental results make it difficult to accurately validate the limit curve (Jeon 2013).

LeBorgne (2012) extended the model of Elwood (2004) to estimate the lateral strength degrading behavior of RC columns prone to shear failure through a rotation-based shear failure model that triggers shear failure once either a shear capacity or a plastic hinge rotation capacity is reached. When shear failure is detected, a zero-length shear spring with a tri-linear backbone curve linked in series with the beam-column element modifies its constitutive

properties to consider pinching and strength and stiffness degradation determined through linear regressions from experimental data.

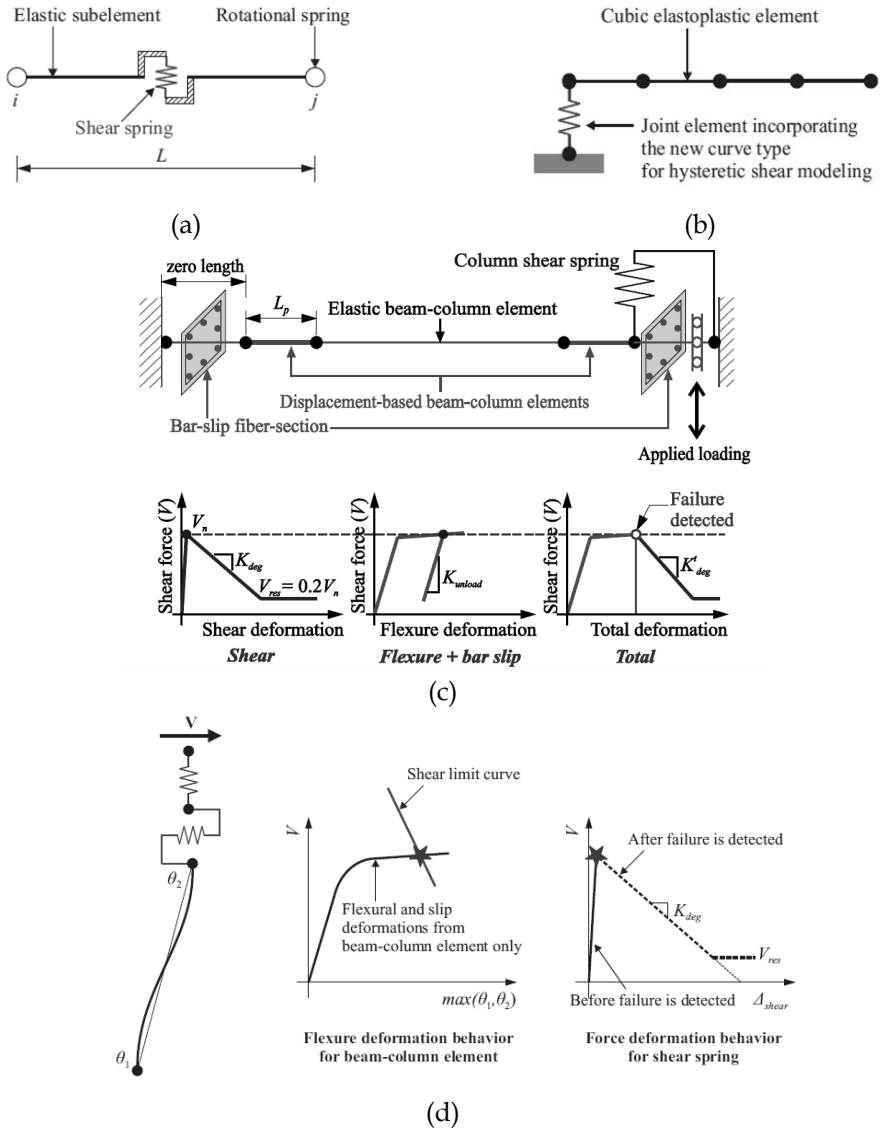

Figure 2.34. Examples of modeling of columns shear behavior – Pincheira et al. (1999) (a), Lee and Elnashai (2000) (b), Jeon et al. (2015) (c), Elwood (2004) (d)

Although the shear model offers very accurate results, the direct use of this shear model in the current software is not implemented making its

applicability still too much complex. A review of previous researches on the shear behavior of existing columns indicates that a reliable model to predict shear behavior both for service and failure conditions should be accurate, computationally efficient and compatible with existing software programs in order to practically conduct complex analyses. However, it is quite difficult that column shear models reviewed above satisfies all these requirements. The problem is still an open and important issue, and in the present work, some attention will be directly focused on this topic.

2.3.2.3 Bar slip

It is well known that, a reinforcing bar embedded in concrete subjected to tensile force will accumulate strain over the embedment length of the bar. This strain causes the reinforcing bar to extend, or slip, relative to the concrete in which it is embedded.

The longitudinal reinforcement in a reinforced concrete column with fixed ends subjected to bending may be in tension at the footing-column interface. Slip of the reinforcing bars outside the flexure length and in the anchoring concrete (that is, in the footing region) will cause rigid-body rotation of the column, as shown in Figure 2.35. This rotation is additive to the rotation calculated from flexural analysis of the column (described in Section 2.3.2.1). This increased rotation causes greater drift of columns and walls under lateral loads; therefore, it is important to account for reinforcement slip when determining the response of a reinforced concrete structure subjected to lateral loading. In fact, sometimes, reinforcement slip in footings regions can make a significant contribution to the total lateral displacement of a reinforced concrete member. Some experimental results indicated that the deformations due to reinforcement slip might be as large as column flexural deformations, and up to 40% of the total lateral displacement (Sezen, 2002). Thus, if deformations resulting from reinforcement slip are ignored in the member analysis, the predicted lateral deformations may be significantly underestimated or the predicted lateral stiffness may be overestimated.

Numerous researchers have investigated the anchorage behavior of reinforcing bars experimentally, and a number of analytical bond-slip models have been developed over the years. The various models fall into two broad categories. Macro models deal with the average slip behavior and often assume a uniform or stepped bond stress over the development length of the

reinforcing bar. They are very efficient from a computational standpoint. Micro models attempt to model the steel-concrete interface on a local level, and often use a varying bond stress-local slip relationship within a numerical model. These models tend to agree well with experimental data, but they are computationally intense.

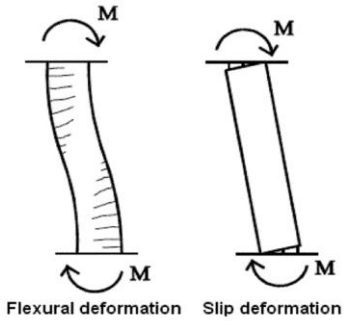

Figure 2.35. Flexural and slip deformations in reinforced concrete column - adapted from Sezen and Setzler (2008)

In literature, different examples of micro models are present. The model by Hawkins et al. (1982) uses a trilinear curve to relate the bond stress to the local slip at each location along the embedded length of the bar (Figure 2.36a).

The widely used bond stress-slip relationships by Eligehausen et al. (1983) were based on an experimental program of pullout tests at the University of California, Berkeley. They proposed a more complex and refined multilinear bond stress-slip relation (Figure 2.36b).

An analytical procedure was proposed by Alsiwat and Saatcioglu (1992) to predict the monotonic force-deformation relationship of a reinforcing bar embedded in concrete using a stepped bond stress distribution (Figure 2.36c). According to this model, four regions are developed along a reinforcing bar in tension, namely, an elastic region, a yield plateau region, a strain-hardening region, and a pullout-cone region. For each of these regions, a bond stress value is adopted, then the slip is calculated by integrating the strains over the development length.

The first example of macro model for the reinforcing slip evaluation was proposed by Otani and Sozen (1972). This model assumed that the stress in the bar decreases linearly with the distance and becomes zero at the distance of the development length. Using a uniform bond stress of $0.54\sqrt{f_c}$ (where f_c is

concrete compressive strength) along the development length, they computed the slip rotation as a function of the moment. Such a model was based on the hypothesis that the strain in the longitudinal reinforcement at column interface was at most equal to yield strain.

Lehman and Moehle (2000) demonstrated that at the beam-column interface, the strain in the reinforcing bar could be much larger than yield strain, causing columns to experience significant fixed-end rotations due to bar slip. Therefore, they proposed a bi-uniform bond stress-slip model according to which, for slip values lower than the slip corresponding to the yield strain in the bar, the uniform bond stress is taken as $1.0\sqrt{f_c}$, while for slip values exceeding the slip at yield, the bond stress is $0.5\sqrt{f_c}$.

Sezen and Setzler (2008) improved the original bar slip model developed by Sezen and Moehle (2003). This model assumes a stepped function for bond stress between the concrete and reinforcing steel over the embedment length of the bar. Based on experimental observations (Sezen 2002), the bond stress is taken as $1.0\sqrt{f_c}$ for elastic steel strains and $0.5\sqrt{f_c}$ for inelastic steel strains (Figure 2.36a). Under these assumptions, Authors computes the slip rotation as a function of the slip (extension of the outermost tension bar from the column end). The column lateral displacement due to reinforcement slip is equal to the product of the slip rotation and the column length.

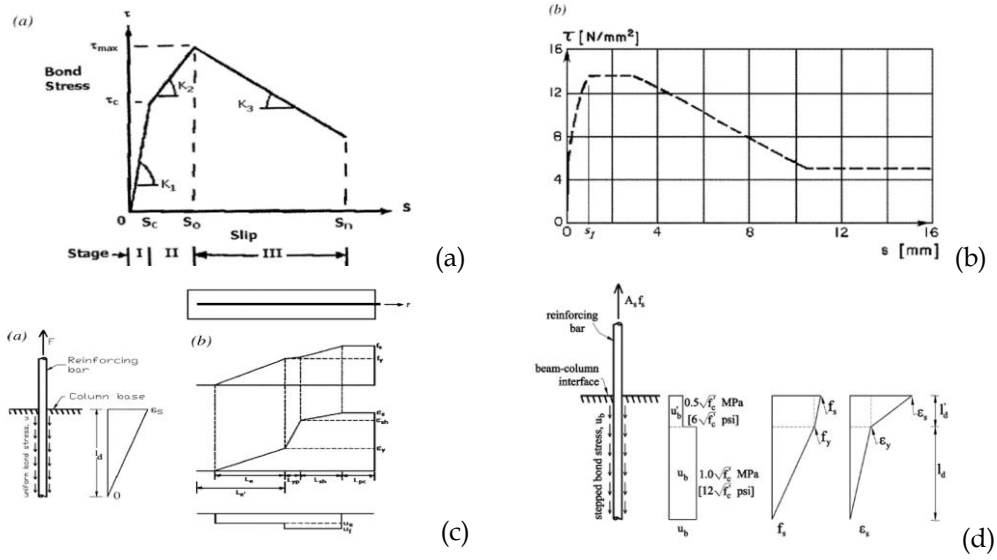

Figure 2.36. Reinforcement slip models - Hawkins et al. (1982) (a), Eligehausen et al. (1983) (b), Alsiwat and Saatcioglu (1992) (c), Sezen and Setzler (2008) (d)

2.3.3. Models for shear strength

When the assessment of the seismic capacity of existing RC columns is approached, it is crucial the classification issue, namely the capacity to predict the failure mode for that element. As discussed in detail in section 2.3.1, three different failure modes can be identified for a RC column, as a result of the adoption of a degrading shear capacity model. In fact, experimental evidence produced in the last years has made clear that traditional code formulations to predict shear strength tend to be overly conservative at low levels of ductility and increasingly non-conservative at high displacement ductility. In order to improve the uniformity of the level of conservatism, several phenomenological formulations have been proposed aiming to capture the shear strength degradation with ductility.

During the last few decades, several shear strength models have been proposed and used for the design and assessment of reinforced concrete columns. Examination of these models shows differences in the approaches used to develop the equations, and in terms of parameters used in the models. Anyway, according to most models, the shear strength can be computed as the sum of the strength contributions from concrete and transverse reinforcement. However, effects of various parameters such as axial load, displacement ductility, and aspect ratio are taken into account differently.

In the following, main shear strength capacity models from code and literature are described and discussed. All the considered shear models are based on the results of experimental tests on columns with solid cross sections. The studies reviewed in this paper include Aschheim and Moehle (1992), Prestley et al. (1994), Kowalsky and Priestley (2000), Sezen and Moehle (2004), Biskinis et al. (2004). The most relevant codes for assessment of existing RC structures, such as, FEMA 273 (1997), EC8/3 (2005), ASCE/SEI 41-06 (2006), FHWA (2006), and C617 (2009), essentially adopted the previously mentioned methods.

2.3.3.1 Aschheim and Moehle (1992)

The study by Aschheim and Moehle (1992) used laboratory data from cantilever bridge column tests. Columns had solid sections of different shapes, circular, rectangular and square, in particular. The original experimental database was composed of 71 units, characterized by different failure modes.

By analyzing the experimental response, Authors identified 49 specimens whose failure was influenced significantly by shear. Experimental data corresponding to these test were reviewed and analyzed. From the analysis, Authors observed that the column shear strength is a function of displacement ductility demand, μ, the quantity of transverse reinforcement, and axial load.

The shear strength is calculated as the summation of strength contributions from transverse reinforcement, V_w, and concrete, V_c (Equation 2.1).

$$V_R = V_c + V_w \tag{2.1}$$

The shear strength degradation influences only the concrete contribution, V_c, defined as:

$$V_c = 0.3\left(k + \frac{P}{13.8A_g}\right)\sqrt{f_c}(0.8A_g) \tag{2.2}$$

Here, k is the degradation factor decreasing with increasing displacement ductility (μ):

$$k = \frac{4-\mu}{3}; 0 \le k \le 1 \tag{2.3}$$

The contribution of transverse reinforcement, V_w, is computed according to the truss analogy for shear strength of reinforced concrete members, assuming an inclination of the compression struts with respect to the column longitudinal axis of 30°, based on studies of experimental collected data.

$$V_w = \frac{A_{sw} f_{yw} d}{s \tan(30°)} \tag{2.4}$$

In the above reported equations, P is the axial load, which is positive for compression, A_g is the cross-sectional area, f_c is the cylindrical concrete compressive strength, A_{sw} is the area of transverse reinforcement active along shear force direction, f_{yw} is the yielding strength of transverse reinforcement, d is the effective depth (taken as 0.8 times the cross-sectional height), s is the spacing of transverse reinforcement, μ is the ductility demand, i.e. the ratio

between the displacement demand and the displacement at yielding, Δ_y.

This model was intended to evaluate the shear strength at plastic hinge zones, and was later adopted in FEMA 273 (1997).

2.3.3.2 *Priestley et al. (1994)*

According to the model proposed by Priestley et al. (1994), also identified as "Original UCSD model", the shear strength of columns under cyclic lateral loads is calculated as the summation of contributions from concrete, V_c, transverse reinforcement, V_w, and arch mechanism associated with axial load, V_p. Based on experimental data available in literature, related to cantilever RC columns with circular and rectangular cross section, Authors proposed the following equations for shear strength evaluation.

$$V_R = V_c + V_w + V_P \tag{2.5}$$

The concrete component is given by:

$$V_c = k\sqrt{f_c}(0.8A_g) \tag{2.6}$$

where the degradation factor, k, is taken as 0.29 when the displacement ductility (μ) is less than 2 and 0.10 when μ is more than 4 (as shown in Figure 2.37). It linearly decreases between μ equal to two and four. Authors noted that the strength degradation is primarily because aggregate interlocking reduces as cracks become wider. The contribution of transverse reinforcement to shear strength is based on a truss mechanism using a 30-degree angle between the diagonal compression struts and the column longitudinal axis.

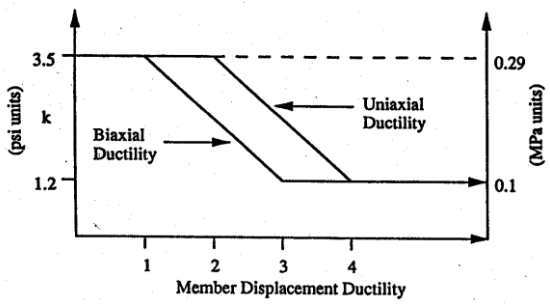

Figure 2.37. Concrete shear strength degradation with displacement ductility, Priestley et al. (1994)

For rectangular cross-section columns, the truss-mechanism component, V_w, is given by:

$$V_w = \frac{A_{sw} f_{yw} D'}{s} \cot(30°) \tag{2.7}$$

in which, D' is the distance measured parallel to the applies shear between centers of peripheral hoop.

The arch mechanism contribution, V_P, is given by:

$$V_P = P \tan(\alpha) = \frac{D - c}{2a} P \tag{2.8}$$

where a is the inclination of diagonal compression strut (see Figure 2.38), c is the neutral axis depth, D is the overall depth of the section, a is the shear span of the column. It should be noted that the neutral axis depth varies with the curvature at the critical section and, hence, with the displacement ductility. As the aspect ratio increases, the axial load contribution decreases.

The Italian technical code (C617, 2009), adopts a slightly modified version of the Original UCSD model for the evaluation of the shear strength of bridge piers. In fact, a 45° instead of a 30° angle truss mechanism is assumed in the calculation of V_w, and the coefficient k is assumed to vary between 0.29 and 0.10 for μ between 1 and 4.

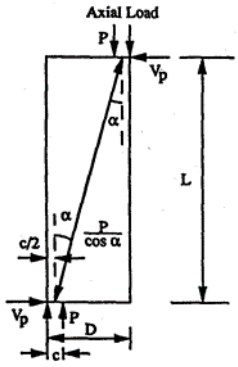

Figure 2.38. Axial load contribution to shear strength, Priestley et al. (1994)

2.3.3.3 Kowalsky and Priestley (2000)

Kowalsky and Priestley (2000) proposed three revisions to the Original UCSD shear model of Priestley et al. (1994). The revisions account for: the effect of column aspect ratio and longitudinal steel ratio on the concrete shear-resisting mechanism, different strength degradation development (much lower at larger displacement ductilities) and height of the truss mechanism. These revisions were validated on experimental results of 47 columns with solid circular cross-section, failing in shear and flexure.

The shear strength is still computed according to Equation (2.5), but in this case, the concrete contribution and the transverse reinforcement are evaluated as reported in the following equations.

The concrete contribution is given by:

$$V_c = \alpha\beta k\sqrt{f_c}(0.8A_g) \tag{2.9}$$

where *a* accounts the effect of aspect ratio and β includes the effect of the longitudinal steel ratio that would affect aggregate interlocking mechanism across concrete shear cracks. These coefficients can be computed as:

$$1 \le \alpha = 3 - \frac{M}{VD} \le 1.5 \tag{2.10}$$

$$\beta = 0.5 + 20\rho_l \le 1 \tag{2.11}$$

In the previous equations, *M* and *V* are moment and shear at critical section, ρ_l is longitudinal steel ratio. The variable *M/VD* is equivalent to the aspect ratio *L/D* where *L* is the distance from critical section to the point of contra-flexure.

The coefficient *k*, which represents the reduction in strength of the concrete shear resisting mechanism with increasing ductility is taken as 0.29 when the displacement ductility (μ) is less than 2 and 0.05 when μ is more than 8 (as shown in Figure 2.39).

The transverse reinforcement contribution is given by:

$$V_w = \frac{A_{sw} f_{yw} (D' - c)}{s} \cot(30°) \tag{2.12}$$

In the previous definition of the truss mechanism equation, it was assumed that a diagonal crack is able to mobilize transverse reinforcement along a crack length extending the full width of the confined core of the concrete. Authors observed that in the compression zone of the column (defined by the neutral axis depth *c*) however, any cracks are, by definition, closed. Therefore, if the crack is closed, shear cannot be transferred across it by tension strain in the transverse reinforcement. So they defined a reduced column width of *(D'-c)* more appropriate for calculating the number of spirals or hoops mobilized by the cracks between the compression struts (see Figure 2.40).

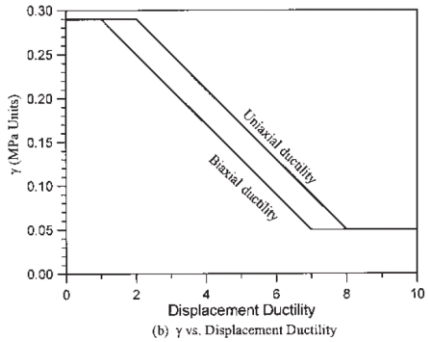

Figure 2.39. k-factor, Kowalsky and Priestley (2000)

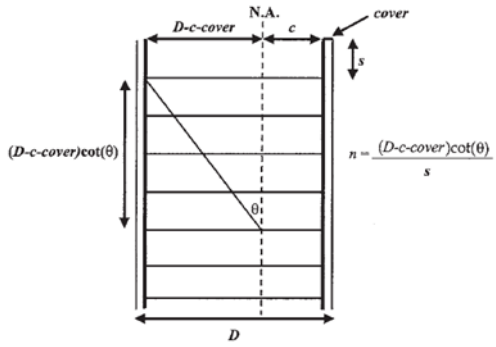

Figure 2.40. Effect of concrete compression zone on truss mechanism, Kowalsky and Priestley (2000)

The shear model by Kowalsky and Priestley (2000) was adopted by the

U.S. Federal Highway Administration (FHWA, 2006) provisions document for seismic retrofitting of bridges.

2.3.3.4 Sezen and Moehle (2004)

Sezen and Moehle (2004) developed a comprehensive shear model for older columns having less transverse reinforcement, compared with columns designed following current codes. In this model, the concrete contribution is affected by column aspect ratio, displacement ductility, and axial load. The proposed model was developed starting from experimental data of 51 test columns failing in shear after flexural yielding. All tested columns presented rectangular solid cross sections and inadequate and poorly detailed transverse reinforcement. Shear strength is computed as the summation of strength contributions from transverse reinforcement, V_w, and concrete, V_c (Equation 2.1). The concrete contribution is given by:

$$V_c = k\left(\frac{0.5\sqrt{f_c}}{a/d}\sqrt{1+\frac{P}{0.5\sqrt{f_c}A_g}}\right)0.8A_g \tag{2.13}$$

where d is the effective depth (distance from extreme compression fiber to centroid of longitudinal tension reinforcement).

The transverse reinforcement contribution is given by:

$$V_s = k\frac{A_{sw}f_{yw}d}{s} \tag{2.14}$$

Unlike in any of the above-mentioned models, the k factor multiplies both transverse reinforcement and concrete contributions to the shear strength of RC columns, since, in the Authors opinion, concrete damage likely leads to loss of anchorage of longitudinal and transverse reinforcement to degrade the truss mechanism. This factor decreases linearly from 1 to 0.7 for μ varying between 2 and 6, as depicted in Figure 2.41.

The shear model by Sezen and Moehle (2004) was adopted in ASCE/SEI 41-06 (2006), the most recent report on "seismic rehabilitation of existing buildings", which succeeded the previous editions on the same subject, FEMA 273 (1997) and FEMA 356 (2000).

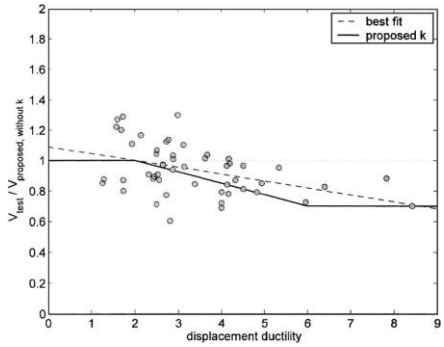

Figure 2.41. Shear strength degradation with displacement ductility, Sezen and Moehle (2004)

2.3.3.5 Biskinis et al. (2004)

Biskinis and colleagues (2004) created a regression model for the assessment of shear strength of existing RC columns, which employed a database of 239 elements. Columns of the collected database presented different cross-section shapes, such as hollow rectangular, in addition to the more traditional solid rectangular and circular shapes.

The analytical formulation changes in the case of shear failure is controlled by diagonal compression or by diagonal tension. Both the empirical formulas account for shear strength degradation through the plastic ductility factor $\mu_{\Delta pl}$, equal to the chord rotation demand over the yielding chord rotation minus 1, $(\vartheta/\vartheta_y\text{-}1)$. The shear strength degradation because of cyclic loads varies linearly between $\mu_{\Delta pl}$ equal to 0 and 5. $\mu_{\Delta pl}$ equal to 5 is the value at which the maximum degradation is attained. The regression model by Biskinis and colleagues is employed in Eurocode 8 part 3 (EC8/3, 2005) for existing buildings. According to this model, in the case of elements characterized by aspect ratio lower or equal to 2, shear failure is controlled by diagonal compression. On the contrary, in the case of aspect ratio higher than 2, shear failure is controlled by diagonal tension. Two different formulations are defined for these two different cases.

However, in most practical cases, the shear failure is controlled by diagonal tension. For this reason, in the following, the only regression model for elements that fail in diagonal tension, is considered, given its more relevant practical interest for typical RC columns.

The regression model in equations (2.15) to (2.18) accounts for three

contributions: the classical 45- degrees truss model (V_w), the concrete contribution (V_c), and the axial load contribution (V_P).

$$V_R = V_P + k(V_c + V_w) \tag{2.15}$$

$$V_c = 0.16\max(0.5;100\rho_l)\left(1-0.16\min\left(5;\frac{a}{d}\right)\right)\sqrt{f_c}A_c \tag{2.16}$$

$$V_w = \frac{A_{sw}}{s}(d-d')f_{yw} \tag{2.17}$$

$$V_P = \frac{(D-x)}{2a}\min(N;0.55A_c f_c) \tag{2.18}$$

where, d' is the depth of the compression reinforcement layer and x the neutral axis depth. For hollow rectangular piers, the concrete cross-sectional area is assumed as $b_w d$ (where b_w is the width of the web and d the effective depth). Also for this shear model, the coefficient k accounting for shear strength degradation due to ductility demand μ multiplies both the concrete and the transverse steel contributions. It varies linearly between 1.00 (non-degraded shear strength) and 0.75 for μ between 1 and 6.

2.4 Summary

In this chapter, a review of the state of the art and of the theoretical background, essential for the comprehension and development of this work, has been performed. First of all, the review process has focused on the past experimental and analytical research on seismic performance of hollow reinforced concrete bridge piers. In the section 2.1, literature review considering past experimental tests on RC columns with hollow rectangular cross section has been presented. In the section 2.2, similarly, the attention has been moved on the experimental tests available in literature on RC columns with hollow circular section and a single steel reinforcement layer. It is noteworthy that very few experimental studies are available on the latter topic. This part of the literature review will be the basis for the collection of the database reported in sections 6.1 and 7.1.

Several analytical models have been reviewed, too. First, some of the existing models for the evaluation of lateral response of RC column have been briefly discussed. The models have been divided into three main topics: flexural behavior, shear behavior and bar slip. Later, main models for shear strength evaluation from literature and codes are described and discussed.

Some of the reviewed models will be applied in next chapters in different approaches, depending on the objective that it is intended to pursue, and with the addition of new proposals.

References

American Concrete Institute (ACI). Models for concrete structures. Special Publication, SP-24, Detroit, 1970.

American Concrete Institute, Committee 318. Building code requirements for reinforced concrete (ACI 318-95) and Commentary (ACI 318R-95). Detroit, 1995.

Aschheim M. and Moehle J. P. (1992) Shear strength and deformability of RC bridge columns subjected to inelastic cyclic displacements. Rep. No. UCB/EERC-92/04, Earthquake Engineering Research Centre, University of California at Berkeley, Berkeley, CA, 100 pp.

Biskinis D.E., Roupakias G.K., Fardis M.N. (2004). Degradation of shear strength of reinforced concrete members with inelastic cyclic displacement. ACI Structural Journal, 101(6):773–83.

Buckle I., Friedland I., Mander J.., Martin G, Nutt R.; Power M. (2006). Seismic retrofitting manual for highway structures: Part 1 – bridges. Report No. FHWA-HRT-06-032, Federal Highway Administration, McLean, Virginia.

Caltrans. (1995). Memo to designers change letter 02, California Department of Transportation, Sacramento, California.

Calvi G. M., Pavese A., Rasulo A., Bolognini D. (2005) Experimental and numerical studies on the seismic response of RC hollow bridge piers. Bulletin of Earthquake Engineering; 3(3): 267-297.

CEN (2005) European standard EN1998-3. Eurocode 8: design provisions for earthquake resistance of structures – Part 3: assessment and retrofitting of buildings. European Committee for Standardisation, Brussels

CEN. Eurocode 2: Design of Concrete Structures – Part 1: General Rules and Rules for Buildings. Comité Européen de Normalisation: Brussels, 2000.

CEN. European Standard ENV 1998-1-1/2/3. Eurocode 8: Design provisions for earthquake resistance of structures – Part I: General rules. Technical Committee 250/SC8, Comité Européen de Normalisation, Brussels, 2004.

Circolare 617. Circolare del Ministero dei Lavori Pubblici n. 617 del 2/2/2009. Istruzioni per l'applicazione delle "Nuove norme tecniche per le costruzioni" di cui al D.M. 14 gennaio 2008. G.U. n. 47 del 26/2/2009, 2009. (in Italian)

Collins M.P., Vecchio F.J. (1988) Predicting the Response of Reinforced Concrete Beams Subjected to Shear using Modified Compression Field Theory. ACI Structural Journal.

Delgado, P. (2009). Avaliação da Segurança Sísmica de Pontes (Doctoral dissertation, Ph. D., FEUP, 2009 (in Portuguese) (http://ncrep. fe. up. pt/web/artigos/PDelgado_PhD_Thesis. pdf)).

Elwood K.J. and Moehle J.P. (2005). Drift capacity of reinforced concrete columns with light transverse reinforcement, Earthquake Spectra, Vol. 12, No. 1, pp. 71–89.

Elwood K.J. Modelling failures in existing reinforced concrete columns. Canadian Journal of Civil Engineering 31.5 (2004): 846-859.

Elwood K.J., Matamoros A.B., Wallace J.W., Lehman D.E., Heintz J.A., Mitchell A.D., Moore M.A., Valley M.T., Lowes L.N., Comartin C.D., and Moehle J.P. (2007). Update to ASCE/SEI 41 Concrete Provisions. Earthquake Spectra: August 2007, Vol. 23, No. 3, pp. 493-523.

Fardis M. N. (2007). LESSLOSS–Risk mitigation for earthquakes and landslides. Guidelines for displacement-based design of buildings and bridges. Report n 5/2007." (2007).

Fardis, M. N. (2009). Seismic design, assessment and retrofitting of concrete buildings: based on EN-Eurocode 8 (Vol. 8). Springer Science & Business Media.

Federal Emergency Management Agency (1997). NEHRP Guidelines for the Seismic Rehabilitation of Buildings. FEMA 273, Washington, D.C.

Federal Emergency Management Agency (2000). Prestandard and Commentary for the Seismic Rehabilitation of Buildings. FEMA 356, Washington, D.C.

Haselton C.B. and Deierlein G.G. (2007). Assessing seismic collapse safety of modern reinforced concrete moment frame buildings, Blume Earthquake Engineering Center TR 156, Stanford University, Stanford, CA.

Hoshikuma J. I., Priestley M. J. N. Flexural behaviour of circular hollow columns with a single layer of reinforcement under seismic loading. SSRP 2000; 13. University of California, San Diego.

Ibarra L., Medina R., and Krawinkler H. (2005). Hysteretic models that incorporate strength and stiffness deterioration, Earthquake Engineering and Structural Dynamics, 34 (12), p. 1489-1511.

Jeon J.S., Lowes L.N., DesRoches R.., and Brilakis I. (2015). Fragility curves for non-ductile reinforced concrete frames that exhibit different component response mechanisms." Engineering Structures 85 (2015): 127-143

Jeon Jong-Su (2013). Aftershock vulnerability assessment of damaged reinforced concrete buildings in California.

Kowalsky M. J. and Priestley M. J. N. (2000) Improved analytical model for shear strength of circular reinforced concrete columns in seismic regions. ACI Structural Journal. 97(3), 388–396.

Kowalsky M.J. and Priestley M.J.N. (2000) Improved analytical model for shear strength of circular reinforced concrete columns in seismic regions. ACI Structural Journal. 97(3), 388–396.

Kunnath S. K., Reinhorn A. M. and Park Y. J. (1990). Analytical modeling of inelastic seismic response of R/C structures, Journal of Structural Engineering, American Society of Civil Engineers, 116 (4), p. 996-1017.

LeBorgne M.R. (2012). Modeling the post shear failure behavior of reinforced concrete columns, Ph.D. Thesis, The University of Texas at Austin, Austin, TX.

Lee D.H. and Elnashai A.S. (2001). Seismic analysis of RC bridge columns with flexure-shear interaction, ASCE Journal of Structural Engineering, Vol. 127, No. 5, pp. 546–553.

Liel A.B., Haselton C.B., and Deierlein G.G. (2010). Seismic collapse safety of reinforced concrete buildings. II: Comparative assessment of nonductile and ductile moment frames. Journal of Structural Engineering 137.4: 492-502.

Miranda P. H., Calvi G. M., Pinho R., and Priestley M. J. N. (2005). Displacement-based assessment of RC columns with limited shear resistance. ROSE Research Report No. 2005/04, IUSS Press, Pavia, Italy.

Mo Y. L. and Nien I. C. (2002). Seismic performance of hollow high-strength concrete bridge columns. Journal of Bridge Engineering, 7(6), 338-349.

MoY. L., Yeh Y. K., Hsieh D. M. (2004). Seismic retrofit of hollow rectangular bridge columns. Journal of Composites for Construction, 8(1), 43-51.

Otani S. and Sozen M.A. (1972). Behavior of multistory reinforced concrete frames

Otani S. and Sozen M.A. (1972). Behavior of multistory reinforced concrete frames during earthquakes, Structural Research Series No. 392, University of Illinois at Urbana-Champaign, IL.

Park R. and Paulay T. (1975) Reinforced Concrete Structures. JohnWiley and Sons, Inc., New York.

Pincheira J.A., Dotwiala F.S., and D'Souza J.T. (1999). Seismic analysis of older reinforced concrete columns, Earthquake Spectra, Vol. 15, No. 2, pp. 245–272.

Pinto A. V., Molina J. e Tsionis G. (2003). Cyclic tests on large-scale models of existing bridge piers with rectangular hollow cross-section. Earthquake Engineering and Structural Dynamics, 32 (13): 1995-2012.

Priestley M. J. N., Seible F., and Calvi G. M. (1996). Seismic design and retrofit of bridges. Wiley, New York.

Priestley M. J. N., Verma R. and Xiao Y. (1994). Seismic shear strength of reinforced concrete columns. ASCEJ. Struct. Engrg, 120 (8) 2310-2329.

Priestley, M. J. N., Calvi G. M., and Kowalsky M. J. (2007) Displacement Based Seismic Design of Structures. IUSS Press, Pavia, Italy.

Pujol S., Ramirez J.A., and Sozen M.A. (1999). Drift capacity of reinforced concrete columns subjected to cyclic shear reversals, Seismic Response of Concrete Bridges, SP-187, American Concrete Institute, Farmington Hills, MI, pp. 255–274.

Ranzo G., Priestley M. J. N. Seismic performance of circular hollow columns subjected to high shear. SSRP 2001; 1. University of California, San Diego.

Sezen H. (2002). Seismic behavior and modeling of reinforced concrete building columns, Ph.D. Thesis, Department of Civil and Environmental Engineering, University of California at Berkeley, CA.

Sezen H. and Chowdhury T. (2009). Hysteretic model for the lateral behavior of reinforced concrete columns including shear deformation, ASCE Journal of Structural Engineering, Vol. 135, No. 2, pp. 139–146.

Sezen H. and Mohele J.P. (2004). Shear Strength Model for Lightly Reinforced Concrete Columns. ASCE Journal of Structural Engineering, 130(11), 1692-1703.

Spacone E., Filippou F. C., and Taucer F. F. (1996). "Fiber beam-column model for nonlinear analysis of R/C frames. 1: formulation," Earthquake Engineering and Structural Dynamics, 25 (7), p. 711-725.

Spacone E., Filippou F.C., and Taucer F.F. (1996) Fibre beam-column model for nonlinear analysis of R/C frames: Part I Formulation, Earthquake Engineering and Structural Dynamics, Vol. 25, No. 7, pp. 711–725.

Tokyu Construction Company. Test Notes on Hollow Bridge Columns. Unpublished report (1998), Tokyo, Japan.

Vecchio F.J. and Collins M.P. (1986). The modified compression field theory for reinforced concrete elements subjected to shear, ACI Structural Journal, Vol. 83, No. 2, pp. 219–231.

Whittaker D., Park R., Carr A. J. (1987). Experimental tests on hollow circular concrete columns for use in offshore concrete platforms. Proc. Of the Third Pacific Conference on Earthquake Engineering, New Zeland, Vol. 1.

Yeh Y. K., Mo Y. L., Yang C. Y. (2001) Seismic performance of hollow circular bridge piers. ACI Structural Journal; 98(6): 862-871.

Yeh Y. K., Mo Y. L., Yang C. Y. (2002). Full-scale tests on rectangular hollow bridge piers. Materials and Structures, 35(2), 117-125.

Yeh, Y. K., Mo, Y. L., & Yang, C. Y. (2002). Seismic performance of rectangular hollow bridge columns. Journal of Structural Engineering, 128(1), 60-68.

Zahn FA, Park R, Priestley MJN, Flexural Strength and Ductility of Circular Hollow Reinforced Concrete column without Confinement on Inside Face. ACI Structural Journal 1990; 87(2): 156-166.

Zhu L., Elwood K. and Haukaas T., (2007). Classification and seismic safety evaluation of existing reinforced concrete columns. Journal of Structural Engineering, (September), 1316–1330.

Chapter 3
EXPERIMENTAL PROGRAM

Experimental simulation is generally paramount for understanding fundamental characteristics of the behavior of structural components and systems. However, simulation of the effects of real events on actual structures usually requires idealization and simplification for most problems of interest.

This chapter provides details of the experimental investigation carried out at the Laboratory of the Department of Structures for Engineering and Architecture, University of Naples "Federico II" to address the seismic performance of existing reinforced concrete (RC) bridge piers with hollow cross-sections. The experimental program, carried out under the financial support of STRESS S.c.a.r.l. STRIT Project "PON Ricerca e Competitività 2007-2013", comprised testing six reduced-scale reinforced concrete (RC) bridge piers with hollow cross-section (four rectangular shaped and two with circular shaped), until failure occurring.

Test units have to be seen as isolated from a typical existing Italian bridge, subjected to gravity and earthquake loads, reproduced as a constant axial load and a cyclic increasing displacement pattern.

The design procedure of test specimens is discussed. The construction of specimens, crucial for the success of experimental tests, is described. Finally, test setup, loading protocol and monitoring system are illustrated and analyzed.

3.1 Test specimen design

The design of test specimens is discussed in this section, focusing on the representativeness issue with respect to the existing Italian transport

infrastructures stock.

3.1.1. Design philosophy

The main goal of the design procedure is to obtain specimens representative in all aspects, such as materials, geometry and reinforcement details, of the existing bridge columns typical of the Italian transport infrastructures realized before 1980.

To this aim, the results of a broad investigation on a sample of about 400 existing Italian RC beam bridges placed along main national roads are considered (STRIT RT D.1.2, 2015), intersected with general indications available in literature (FIB 39, 2007). Among others, the parameters taken into account in this preliminary study are:

- seismic resisting sub-system typology
- cross-section shape
- slenderness (or aspect ratio)
- axial load ratio
- geometrical longitudinal reinforcement ratio
- geometrical transverse reinforcement ratios
- mean values of materials strength

The following figures show the distribution of the above-mentioned properties characterizing the considered sample of existing Italian RC beam bridges. Figure 3.1 shows the distribution of the different typologies of vertical structural sub-system resisting to lateral actions. Walls and single piers represent the most used, together with frame systems. Seismic performance of RC walls and frames are well known, since there are common solutions for buildings, while as regards piers, especially if characterized by no ordinary cross-section, few experimental studies are available in literature. By observing Figure 3.2, it is possible to note that hollow cross-section is the most used solution for RC bridge piers. Other widespread solutions are solid circular and rectangular piers. In Figure 3.3 and Figure 3.4, the slenderness (or aspect ratio) distribution is reported for both principal bridge directions (longitudinal and transverse). Slenderness of piers is defined as the height to cross-section depth ratio. The most of piers are characterized by an aspect ratio lower than 5.0, and a great part presents slenderness values smaller than 2.5.

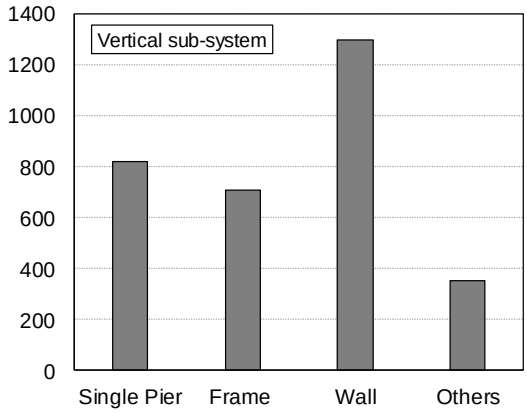

Figure 3.1. Distribution of the seismic resisting sub-system typology (STRIT RT D.1.2, 2015)

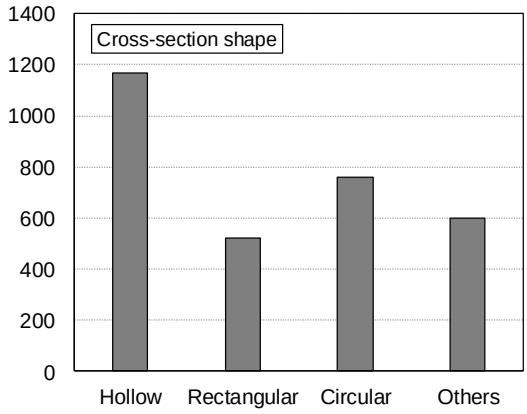

Figure 3.2. Distribution of piers cross-section shape (STRIT RT D.1.2, 2015)

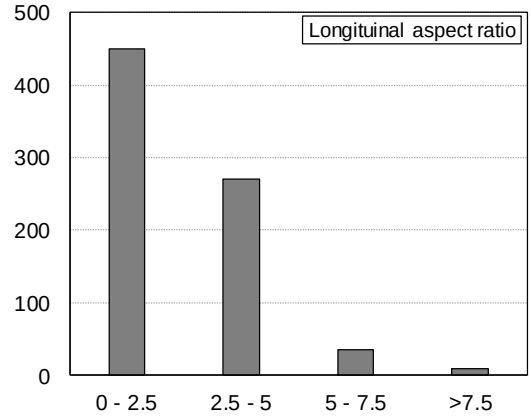

Figure 3.3. Distribution of piers slenderness along bridge longitudinal direction (STRIT RT D.1.2, 2015)

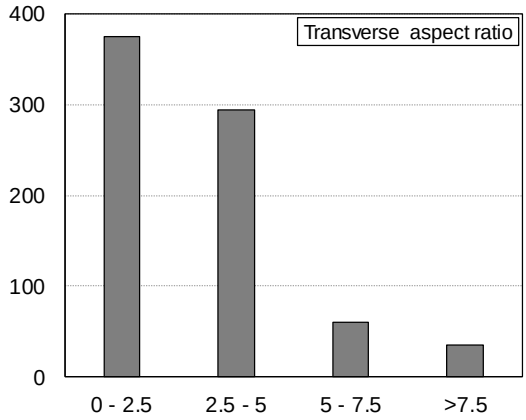

Figure 3.4. Distribution of piers slenderness along bridge transverse direction (STRIT RT D.1.2, 2015)

Typical serviceability values of axial load ratio (ν) are included between 1% and 5% (Figure 3.5). As already discussed in the Chapter 1, most of existing Italian bridges have been constructed prior to 1980, before the advancement in earthquake engineering principles and seismic design codes. For this reason, bridge piers are generally poorly detailed, as it may be observed in Figure 3.6 and Figure 3.7, in which geometrical longitudinal and transverse reinforcement ratios are reported, respectively. Common values for longitudinal reinforcement are lower than 1%, while for transverse steel typical values are included between 0.04% and 0.12%.

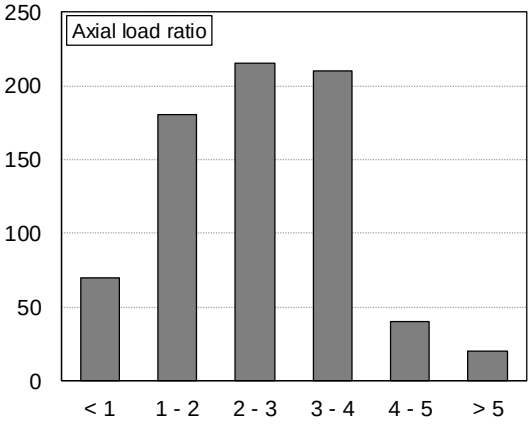

Figure 3.5. Distribution of axial load ratio on bridge piers (STRIT RT D.1.2, 2015)

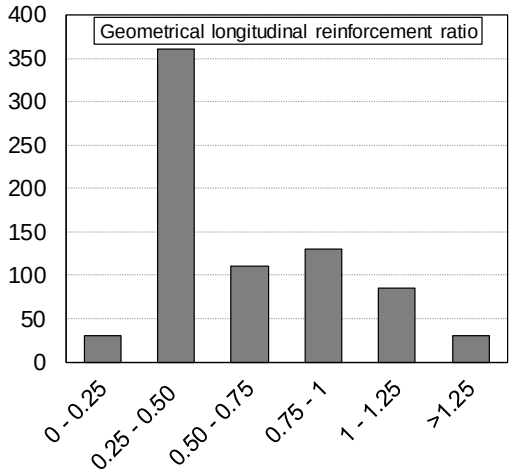

Figure 3.6. Distribution of the geometrical longitudinal reinforcement ratio (STRIT RT D.1.2, 2015)

Figure 3.7. Distribution of the geometrical transverse reinforcement ratio (STRIT RT D.1.2, 2015)

Finally, as regards material properties typical of Italian bridge piers, clear sketches are reported in Figure 3.8 and Figure 3.9, for concrete and steel respectively. Typical mean values of concrete cylindrical compressive strength (f_c) are between 10 MPa and 30 MPa; mean values of yielding strength (f_y) for steel range between 400 MPa and 550 MPa. Therefore, typical Italian bridge piers are generally characterized by poor concrete and relatively high strength steel.

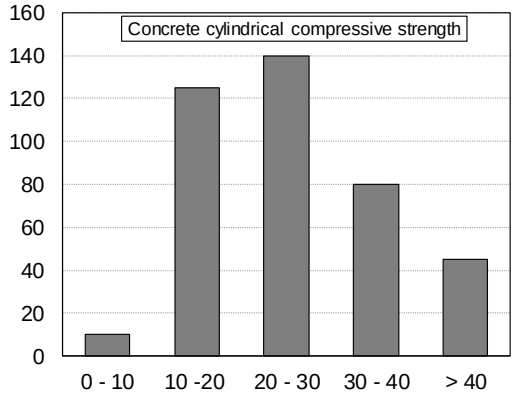

Figure 3.8. Distribution of mean values of concrete cylindrical compressive strength (STRIT RT D.1.2, 2015)

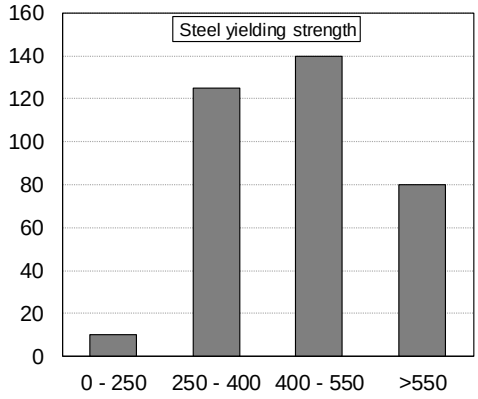

Figure 3.9. Distribution of mean values of steel yielding strength (STRIT RT D.1.2, 2015)

3.1.2. Test specimen description: hollow rectangular piers

Four specimens representing cantilever bridge piers with hollow rectangular cross section are considered in this experimental study. The main goal of the design procedure is to obtain specimens representative in all aspects, such as materials, geometry and reinforcement details, of the existing bridge columns typical of the Italian transport infrastructures realized before 1980. Starting from the results highlighted in the section 3.1.1, a typical bridge pier cross-section was designed, as regards both geometry and reinforcement details, according with common non-seismic design practice. In order to allow for testing within the capacity of the laboratory, a scaling factor equal to 1:4

was introduced. Schematic plain and elevation views of all hollow rectangular test specimens are illustrated in Figure 3.10.

All the specimens were characterized by the same cross section and reinforcement details. Exterior dimensions of the rectangular hollow section were 600×400mm and thickness (t_w) was 100mm. The geometrical longitudinal reinforcement percentage (ρ_l) was equal to 0.88%, given by 28 steel bars with a diameter (d_b) equal to 8mm, arranged in two layers of 18 and 10 bars, along the external and internal edges respectively. The transverse reinforcement ratio (ρ_w) was equal to 0.12%, with stirrups of diameter (d_b) 3 mm, spaced at a distance of 120 mm and 90-degree end hooks. The tested piers had different aspect ratio (L_V/H), in which L_V is the shear span (height from the base to the loading point) and H is the section depth (dimension of the cross-section in the loading direction). Two piers had a height of 900mm and two of 1500mm. Each one was tested along one of the principal directions, so that four different values of the aspect ratio were considered, labelled as P1, P2, P3, and P4. All scaled piers reproduced non-seismic design, typical of the considered period, thus resulting in poorly detailed reinforcement (no tie between opposite longitudinal bars and 90° hooks, leading to lack of confinement). For the tested specimens, cyclic response and collapse mode were very sensitive to flexure-shear interaction, due to low transverse reinforcement ratio as well as the shape of the cross-section. Main geometric properties of specimens are identified in Table 3.1 together with reinforcement details. Terms B and H in Table 3.1 represent the dimensions perpendicular and parallel to imposed displacement direction, respectively. A rigid cap was realized on the top of the piers in order to distribute axial and lateral loads on section flanges, and to represent typical piers cap. Footings were designed to prevent any local damage. Applied axial load level was 5% of the compressive axial capacity, within the range typical of service conditions of Italian bridge piers.

Test ID	L_V (mm)	B (mm)	H (mm)	Aspect Ratio (L_V/H)	t_w (mm)	ρ_l	ρ_w
P1	1500	400	600	2.50	100	0.88%	0.12%
P2		600	400	3.75			
P3	900	400	600	1.50			
P4		600	400	2.25			

Table 3.1. Hollow rectangular specimens' properties

3.1.3. *Test specimen description: hollow circular piers*

Also for hollow circular specimens, the design procedure has as main goal to obtain specimens representative in all aspects of the existing typical bridge columns of the Italian transport infrastructures realized before 1980.

Starting from the results highlighted in the section 3.1.1, a typical bridge pier cross-section was designed, as regards both geometry and reinforcement details, according with common non-seismic design practice. In order to allow for testing within the capacity of the laboratory, a scaling factor equal to 1:4 was introduced. Schematic plain and elevation views of all hollow rectangular test specimens are illustrated in Figure 3.11. The experimental program was performed on two specimens, identified hereinafter as P5 and P6, representing cantilever bridge piers characterized by the same hollow circular cross section and reinforcement details. The external diameter D was equal to 55 cm and the thickness (t_w) was 10 cm. The geometrical longitudinal reinforcement percentage (ρ_l) was 0.85%, given by a single layer of bars with a diameter (d_b) of 8 mm, placed along the external edge, characterized by a cover equal to 17 mm. The transverse reinforcement ratio (ρ_w) was equal to 0.06%, with circular ties of diameter (d_b) 3 mm, spaced at a distance of 120 mm and 90-degree end hooks. The taller specimen P5 had a height of 165 cm, while the shorter one P6 of 110 cm. Consequently, the tested piers had different aspect ratio (L_V/D), in which L_V is the shear span (height from the base to the loading point) and D is the external diameter. Main geometric properties of specimens are identified in Table 3.2 together with reinforcement details. Terms B and H in Table 3.2 are dimensions perpendicular and parallel to imposed displacement direction, respectively. A rigid cap was realized on the top of the piers in order to distribute axial and lateral loads on section flanges, and to represent typical piers cap. Footings were designed to prevent any local damage.

Test ID	D (mm)	L_V (mm)	Aspect Ratio (L_V/H)	t_w (mm)	ρ_l (-)	ρ_w (-)
P5	550	1650	3.00	100	0.85%	0.06%
P6		1100	2.00			

Table 3.2. Hollow circular specimens' properties

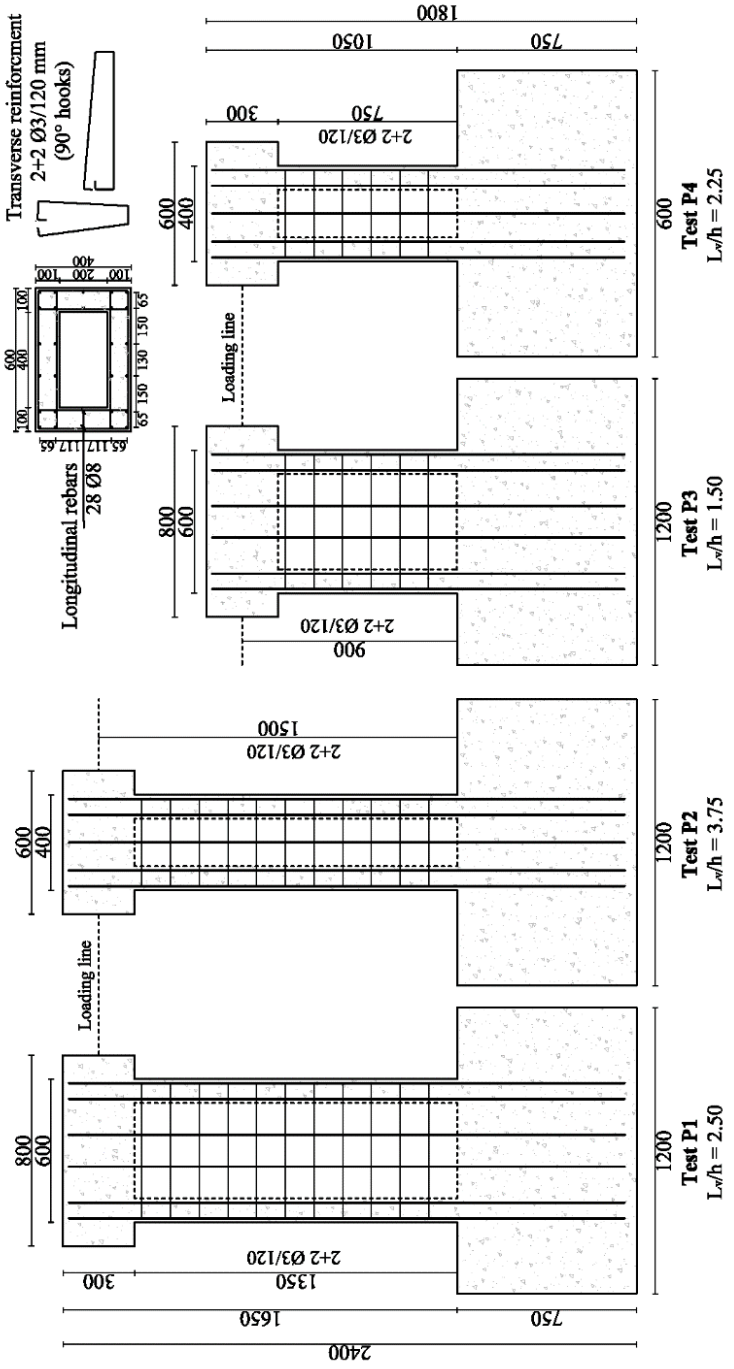

Figure 3.10. Geometry and reinforcement details (hollow rectangular specimens)

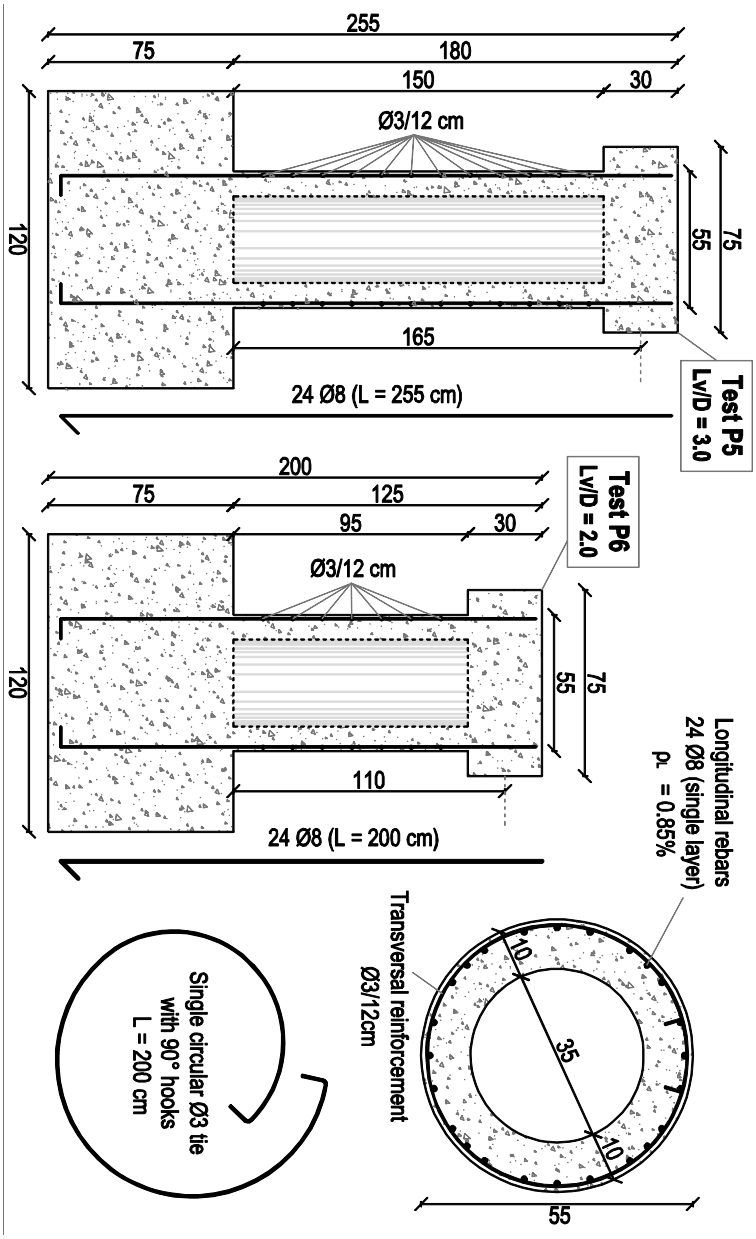

Figure 3.11. Geometry and reinforcement details (hollow circular specimens)

3.1.4. Material properties

The test specimens were constructed using normal weight conventional concrete supplied by a local contractor. The target compressive strength was 20.0 MPa to simulate the typical strength in old Italian bridge. The used materials included crushed gravel aggregates with a nominal size of 10 mm, natural river sand and ordinary cement. The water to cement ratio (w/c) for each specimen was about 0.8. Aggregates dimensions were defined in order to be representative of real-scale concrete, on one side, and compatible with the tight concrete cover (10mm) due to the small scale of the specimens, on the other. Table 3.3 displays the mix design used for the test specimens, while in Figure 3.12 granulometric curves for concrete aggregates are showed.

Cement	Water	Coarse aggregates	Fine aggregates	Plasticizer
460	380	992	2972	2.76

Table 3.3. Concrete mix design (kg/m^3)

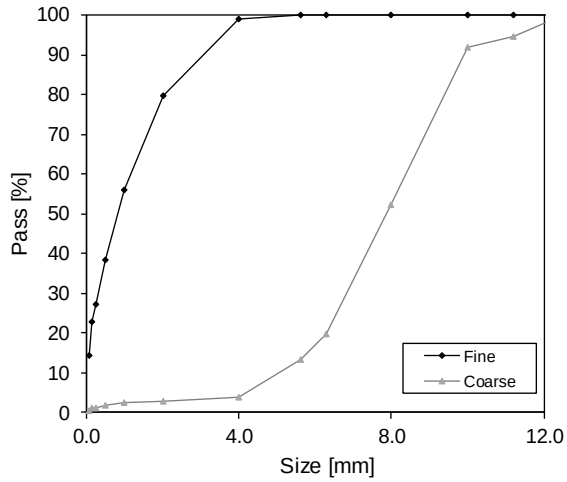

Figure 3.12. Concrete aggregates granulometry

For each test specimen, three 150×150×150 mm cubic samples were casted and exposed to the same environmental condition of the corresponding specimen. They were tested to determine the compressive strengths on the same day of specimen testing. Table 3.4 and Table 3.5 give the concrete

strength of the corresponding specimens, for hollow rectangular and circular specimens respectively. The variation in concrete strength was mainly due to the variation in age on the day of testing and to the difference in sampling stages. In the following of this study, mean values of cylindrical compressive strength equal to 17 MPa and 13.3 MPa are considered for hollow rectangular and circular specimens, respectively. These values were evaluated by applying the widely assumed relationship for which compressive cylinder strength may be assumed as 80% of compressive cube strength (Neville and Brooks, 1987).

Sample ID	Mass (kg)	Compressive cube strength (MPa)
P1a	7.63	18.4
P1b	7.50	18.8
P1c	7.58	18.2
P2a	7.59	20.8
P2b	7.56	20.9
P2c	7.52	20.5
P3a	7.67	22.2
P3b	7.56	20.5
P3c	7.55	22.1
P4a	7.64	22.0
P4b	7.53	22.6
P4c	7.56	18.2

Table 3.4. Concrete compressive cube strength for hollow rectangular specimens

Sample ID	Mass (kg)	Compressive cube strength (MPa)
P5a	7.63	14.7
P5b	7.50	16.4
P5c	7.58	18.2
P6a	7.59	14.8
P6b	7.56	16.2
P6c	7.52	18.1

Table 3.5. Concrete compressive cube strength for hollow circular specimens

Commercial typology of reinforcing steel, adopted for longitudinal deformed bars with a diameter of 8 mm, is B450C (NTC 2008), i.e., class C reinforcement with f_{yk} = 450 MPa according to Annex C provisions of

Eurocode 2 (EN 1992-1-1:2004 Annex C). High strength plain commercial steel was used for transverse reinforcement with a diameter of 3 mm. Steel with yielding strength of 540 MPa and ultimate strength at approximately 620 MPa was used for longitudinal bars. Yielding strength of transverse reinforcement steel was equal to 655 MPa, and ultimate strength equal to 690 MPa. Tensile tests were carried out on three samples for each bar diameter. In Figure 3.13 and Figure 3.14, steel stress-strain behavior are reported for all samples, corresponding to longitudinal and transverse reinforcement respectively.

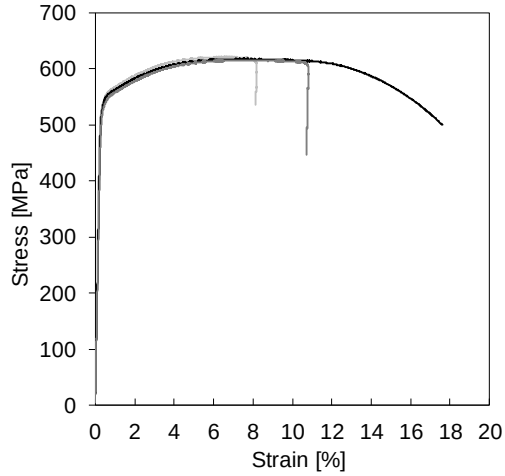

Figure 3.13. Steel tensile test stress-strain relation (longitudinal reinforcement)

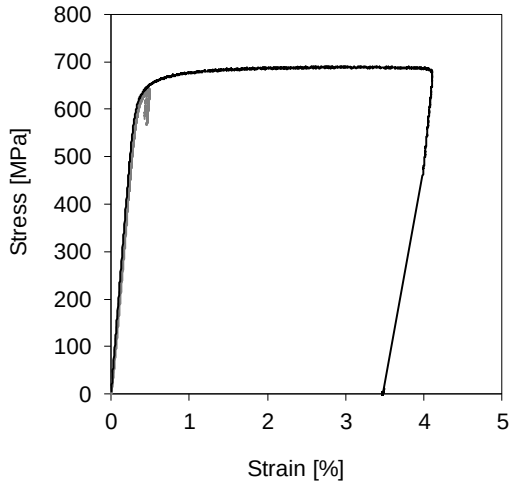

Figure 3.14. Steel tensile test stress-strain relation (transverse reinforcement)

Table 3.6 reports mean values of their mechanical properties, namely yield strength (f_y), ultimate strength (f_t) and hardening ratio (f_t/f_y).

d_b (mm)	f_y (MPa)	f_t (MPa)	f_t/f_y (-)
8	540	620	1.15
3	655	690	1.05

Table 3.6. Properties of steel

3.2 Construction of the specimens

The construction of two groups of specimens (namely, hollow rectangular and hollow circular) was carried-out at two different stages at the same construction site of a local contractor. First specimens with hollow rectangular section were realized, later the hollow circular series. Construction steps were the same for both specimens, therefore they are described below.

The construction site was prepared by cleaning and leveling the ground, and building the wooden forms for the specimens' foundations. Special care was given to leveling the formwork during construction to minimize the effects of accidental eccentricities.

The foundation reinforcement cages were assembled outside the forms, in order to ensure its crucial symmetry and the right location of PVC tubes, placed to create the dedicated holes for laboratory restrain system (Figure 3.15). Then, after a careful check on steel reinforcement spacing and alignment, the steel cages were placed into the wooden forms (Figure 3.16). After the foundation reinforcement cages were fixed in the right position using appropriate spacers, pier reinforcement cages were partially assembled.

The planned longitudinal and transverse steel bars (see section 3.4) were removed to be subject to a strain gauging process at a different venue. A meticulous labeling method was applied to the strain gauges installed onto the steel reinforcement that enabled identification of their locations by quick inspection of the label (Figure 3.17). Throughout the construction process, functionality of strain gauges was checked to identify, fix, or replace any malfunctioning gauge. At the end of the strain gauging process, the gauged steel bars were put back in the cage. It is worthy to mention that installing the longitudinal reinforcement with strain gauges was a quite challenging job, due

to the intersection with the foundation reinforcement (Figure 3.18).

Before completing pier reinforcement cages, for each specimen, 3 post-tensioned high strength (d_b = 15.7 mm) steel strands were positioned, fixed by means of anchorages on the bottom side of the foundation. The steel strands passed through a special system designed ad hoc to avoid local rupture at steel/concrete interface, and crossed the void in the piers.

The system, illustrated in Figure 3.19, was fixed to the top steel bars of the foundation. At this point, the foundations of the specimens were cast. In order to avoid any cracking problem, a high strength concrete was used. Since the engorgement of steel bars, especially within the overlap between pier and foundation, shoot and shovel were used to place the concrete in the bottom of the form. Concrete was vibrated using high-frequency vibrator to reduce the presence of voids or honeycombs. After casting, the top concrete surface of the foundations was finished (Figure 3.20). Piers cages were completed and a careful check on steel reinforcement spacing and alignment was performed. Polystyrene profiles were inserted to create the void. Wooden forms for piers were assembled and closed (Figure 3.21).

After the construction of the dedicated forms, the pier cap cages were assembled in place, being careful to the overlap with the pier longitudinal bars (Figure 3.22). Pier shafts and pier caps were cast together. Concrete was supplied by a local contactor. The mix design required at least 160-210 mm of slump to facilitate casting in the congested areas of specimens and along the thin walls. Concrete was thoroughly compacted using electrical rod type vibrators that were applied internally within the fresh concrete body and externally on the column and joint wooden form surfaces. After casting, the top concrete surface of the caps was finished. Each test unit was allowed to cure for at least seven days before they were removed from the forms. The completed specimens are shown in Figure 3.23.

All specimens were placed at the construction site during the hardening process of concrete, under shelter from the weather. The test specimens were moved into the laboratory two months after the columns were cast.

Figure 3.15. Foundation steel cage construction

Figure 3.16. Foundation steel cage in the formwork

Figure 3.17. Strain gauges labelling

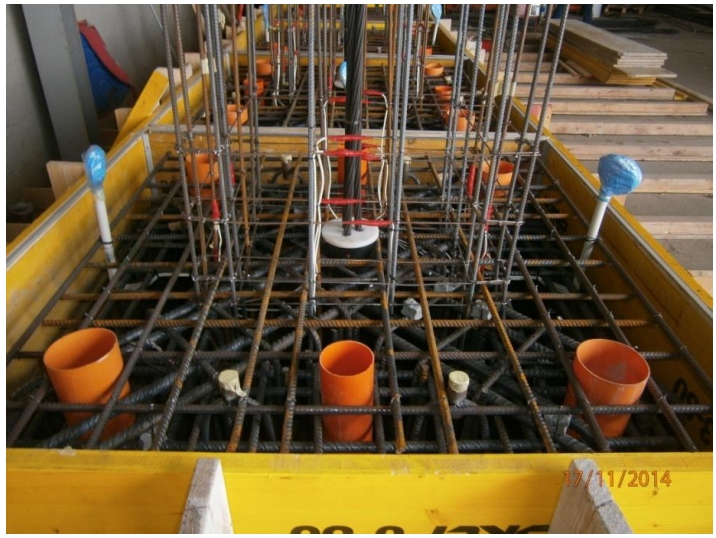

Figure 3.18. Strain gauges installation

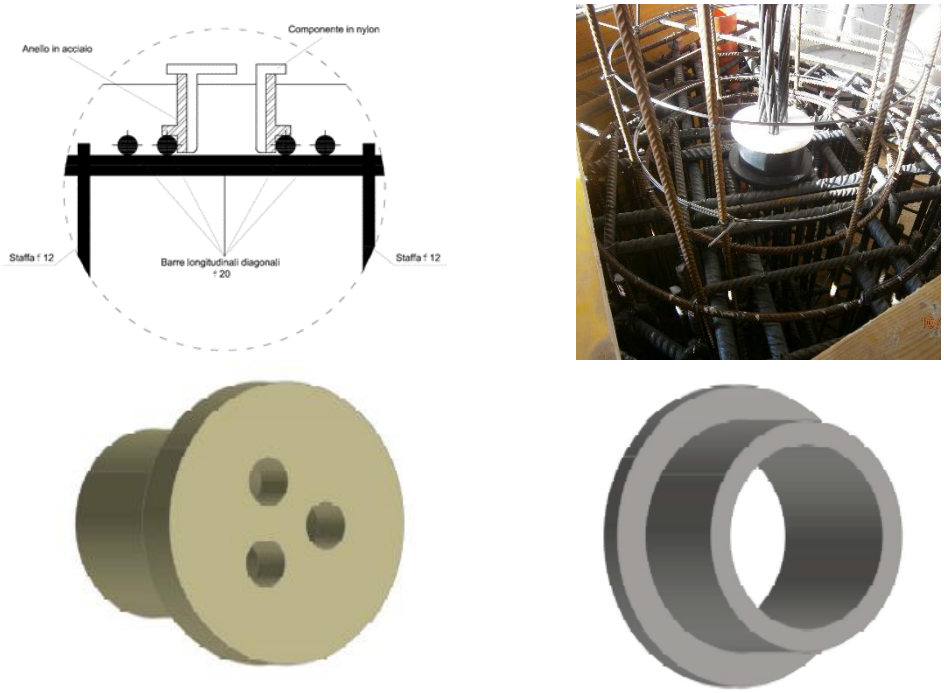

Figure 3.19. System for centering of steel strands

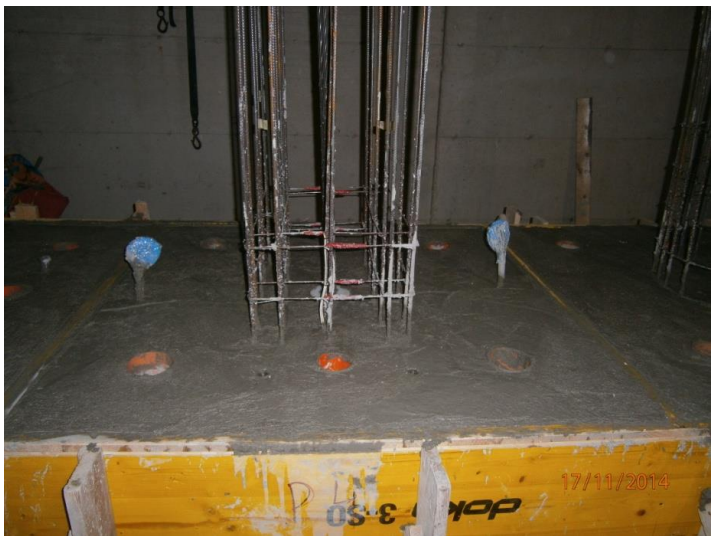

Figure 3.20. Foundation after concrete casting

Figure 3.21. Pier steel cage in the formwork

Figure 3.22. Pier cap steel cage construction

Figure 3.23. Completed test specimens after removing wood forms

3.3 Test setup and loading protocol

The experimental tests were carried out at the Laboratory of the Department of Structures for Engineering and Architecture, University of Naples "Federico II". The overall test setup is depicted in Figure 3.26. All tests were performed in quasi-static way by applying increasing horizontal displacement cycles with constant axial load. In this Section, the test setups for gravity and lateral load simulation are described separately, together with the corresponding loading protocol.

3.3.1. Axial loading setup

The objective of the axial loading setup was to simulate service gravity load on the specimens. As already discussed in Section 3.1.1, the designed gravity load ratio was of about 5%, typical value for existing Italian bridges. This load was monotonically applied to each specimen by means of an appropriate closed system. The system consisted of 3 post-tensioned high strength $d_b = 15.7$ mm steel strands, fixed on the bottom side by means of anchorages embedded in the foundation. A full height hole is realized in the

cap in order to allow strands crossing the specimen. On the top, between the anchor plate of the strands and the cap top surface, a hydraulic jack was interposed, acting in load control. Between the anchor plate and the hydraulic jack, a load cell was installed to monitor the axial load value during the test. This closed system was designed in order to clear the view for taking pictures of the damage states and to avoid P-Δ effects, since axial load direction was always identical to specimens' axis. The footing was restrained to the laboratory strong floor by four post-tensioned tempered steel bars avoiding any rotation or movement during the test. A global graphic scheme of the axial loading setup is illustrated in Figure 3.27.

3.3.2. Lateral loading setup

The lateral earthquake load was simulated as a symmetric, quasi-static, cyclic, increasing displacement pattern. The lateral loading protocol was applied to the centerline of the pile cap by a single horizontal 500 kN capacity hydraulic actuator under displacement control. The actuator-to-specimen connection was schematized as a hinge constraint that does not restrain the rotation of the top during the test. The horizontal actuator was attached to a steel reaction wall.

For tests on hollow rectangular specimens, the horizontal loading sequence consisted of three cycles alternatively in push and pull direction at displacements of $1/3\Delta_y$, $2/3\Delta_y$, Δ_y, $2\Delta_y$, $4\Delta_y$, $6\Delta_y$, $8\Delta_y$, $10\Delta_y$, $12\Delta_y$, where Δ_y is the theoretical yielding displacement estimated according to Biskinis and Fardis (2010), unless failure occurred earlier (Figure 3.24).

For tests on hollow circular specimens, the horizontal loading sequence, consisted of three cycles at displacements corresponding to peak drifts (i.e. top displacement-to-shear span ratio) values: 0.25%, 0.50%, 0.75%, 1.00%, 2.00%, 3.00%, 4.00%, 5.00%, unless failure occurred earlier. (Figure 3.25).

It is worth noting that such displacement protocol corresponded to that measured from the internal transducer of the hydraulic actuator. Since the reaction system was affected by small spurious deformations (due mainly to backlashes and deformations of contrast system), actual specimen displacements do not match exactly those values, especially for lower levels of drift. Anyway, all experimental considerations are based on the exact values obtained from the external potentiometer positioned at the level of the horizontal actuator axis. The loading rate was 0.5 mm/sec for elastic cycles and

1.0 mm/sec for the inelastic cycles. In order to better understand the experimental results reported in the following sections, an orientation system is provided herein: specimens were tested along East–West direction.

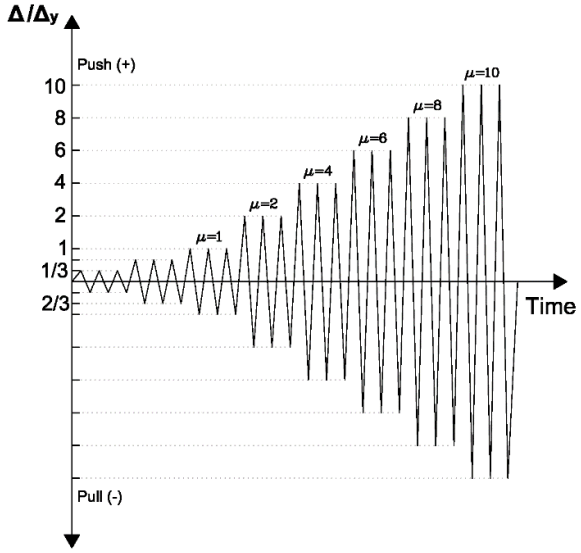

Figure 3.24. Lateral loading history for hollow rectangular specimens

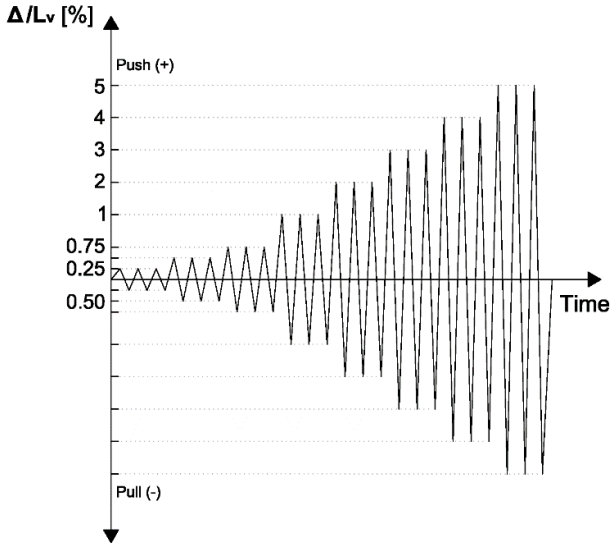

Figure 3.25. Lateral loading history for hollow circular specimens

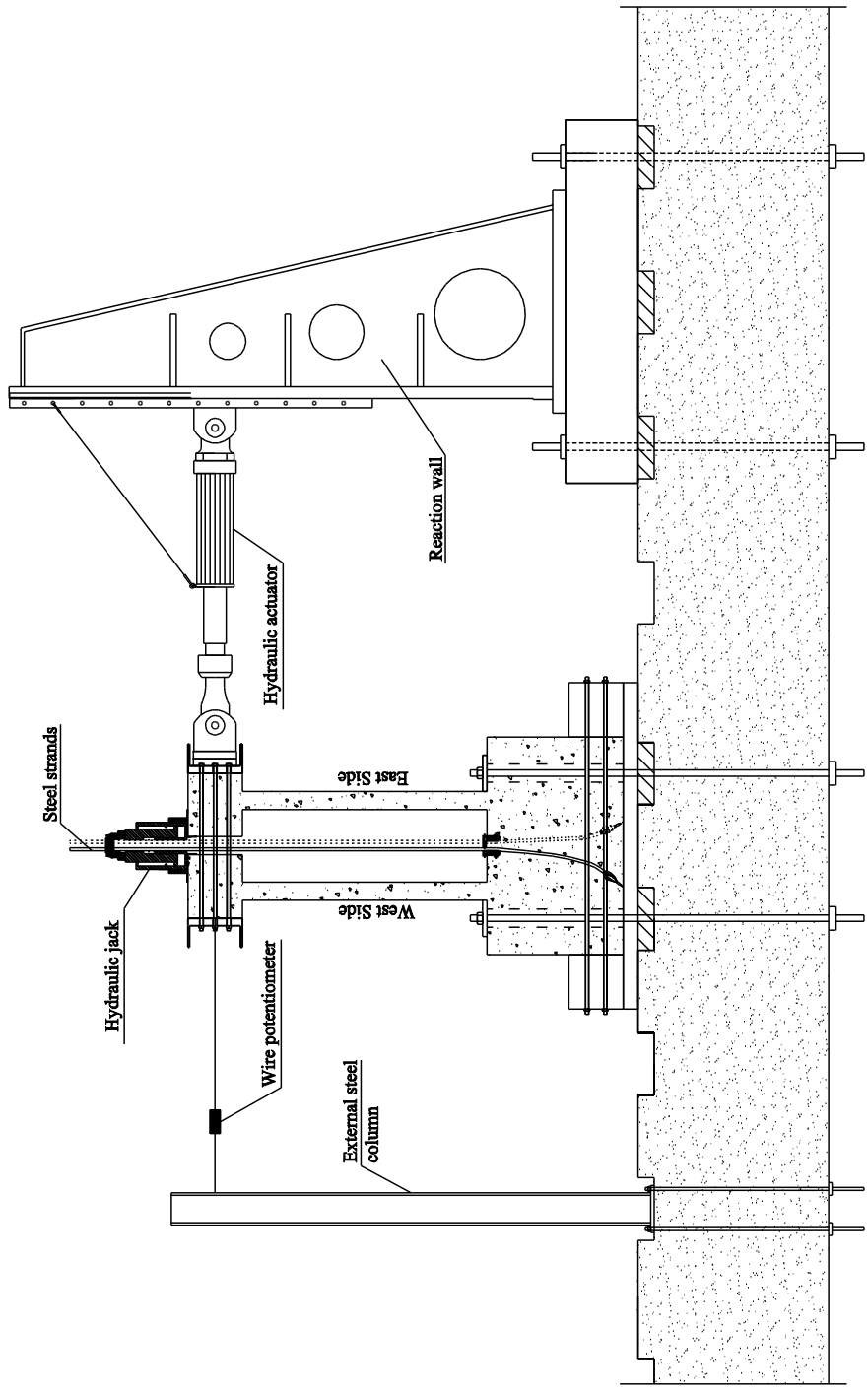

Figure 3.26. Schematic view of the test setup

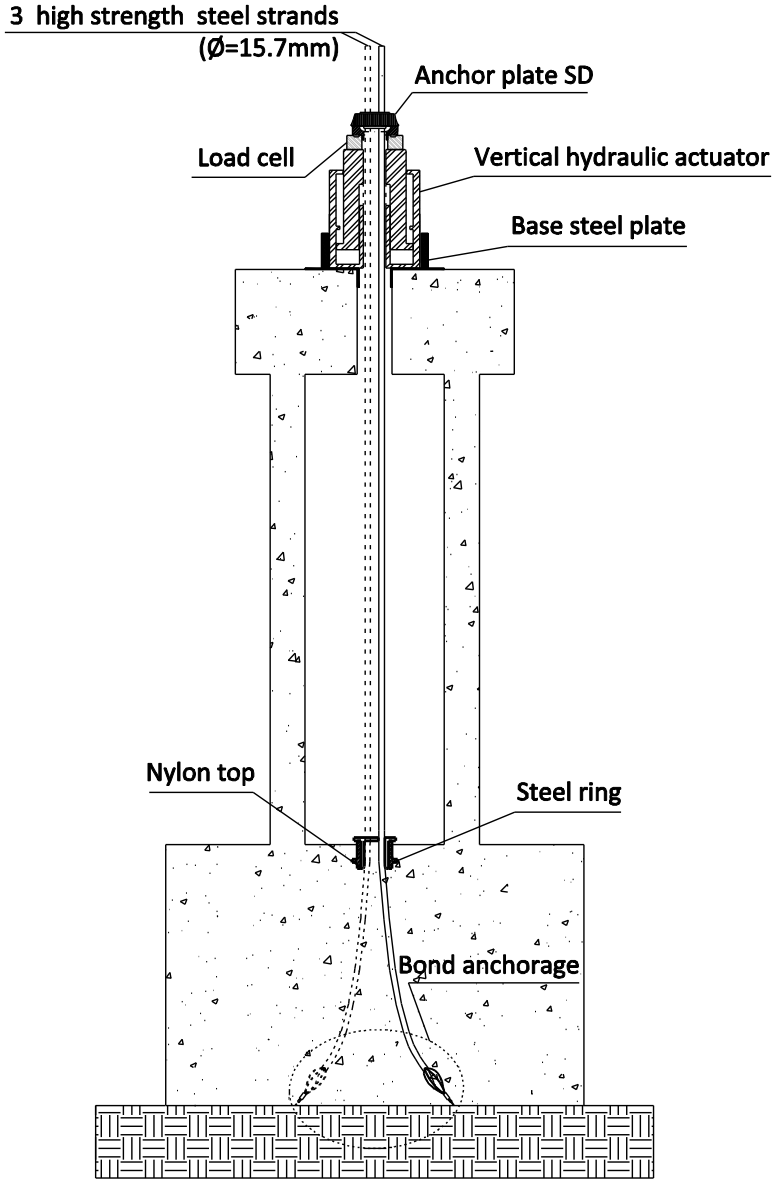

Figure 3.27. Schematic view of the axial loading setup

3.4 Monitoring system

Monitoring system was composed of two sub-systems, the former used for global measures, defining structural response of the specimen (forces and displacement), and the latter for local measures, related to local deformation components associated with different response mechanisms. Global system consisted of two load cells, for horizontal and vertical forces respectively, and a wire potentiometer fixed to an external steel column and connected to centroid of the pier cap (see Figure 3.26).

In order to investigate deeply about local deformation components coexisting in the specimens (flexure contribution, shear contribution and fixed end rotation at cantilever base), an appropriate instrumentation was installed along the pier height by using an arrangement of Linear Potentiometers (LPs), located along the horizontal loading direction. The installation of the LPs system was different for the two series of specimens (namely, hollow rectangular and hollow circular). A schematic view of the LPs frame installed on hollow rectangular specimens is reported in Figure 3.28. In order to preserve the reliability of the local measures, no drillings in the thin flanges were performed, which might have affected cracks opening. Therefore, wood pieces were screwed and glued on both sides of the pier surface perpendicular to the loading direction. Then, aluminum tubes were mounted on the wood pieces on both sides, connected each other by two springs, aimed at holding the instrumentation frame together. Both vertical and diagonal LPs (identified as "LPv" and "LPd" respectively in Figure 3.28a) were connected to the ends of these aluminum tubes. To prevent the buckling of the diagonal LPs under compression deformations, the LPs section was increased by appropriate aluminum rigid boxes. Figure 3.29 shows a schematic view of the LPs arrangement for hollow circular specimens. Due to the circular cross-section shape, the aluminum tubes were fixed to the pier external edge by means of two bolts embedded in specific holes realized in the wall thickness along the loading direction. Then, aluminum tubes were connected by two springs aimed at holding the instrumentation frame together and to give more stiffness to the instrumentation system. The diagonal LPs (identified as "LPd" in Figure 3.29a), were connected to the ends of the aluminum tubes, while the vertical LPs (identified as "LPv" in Figure 3.29a) to the central bolts. Also in this case, to prevent the buckling of the diagonal and horizontal LPs under compression

deformations, the LPs section was increased by appropriate aluminum rigid boxes. Each LP measured diagonal/vertical displacement between two opposite points. In this way, two curvature cells and two shear deformation panels were realized.

A couple of vertical Linear Variable Displacement Transducers (LVDTs) monitored flexural deformations and fixed-end-rotation at cantilever base. They were fixed to the center of the flanges and connected to the foundation upper surface (see Figure 3.28.b), for hollow rectangular specimens.

For hollow circular specimens, they were placed diametrically opposed along the loading direction, fixed to the external edge of the base cross-section and connected to the foundation upper surface (identified as "LVDTb" in Figure 3.29a, where "b" indicates base deformation). Four additional LVDTs are installed as shown in Figure 3.29b only for squat specimen P6, in order to monitor the width of shear cracks during the test.

In order to monitor longitudinal strain in steel reinforcement, strain gauges (SGs) were installed on longitudinal and transverse reinforcement. Figure 3.28 shows the SGs arrangement for hollow rectangular specimens. Of the sixteen SGs, eight were placed on the corner longitudinal bars, above the column base end and inside the footing, to control the development of plastic deformations. The remaining SGs were placed on the first two stirrups, along all four braces in the direction parallel to the lateral loading direction. Eigth SGs were installed on the outermost couple of longitudinal bars (along the loading direction) and on a couple of longitudinal bars identified by a 45° inclined direction respect to the loading direction (see Figure 3.29c). Also these strain gauges were installed above the column base end and inside the footing, in order to control the development of plastic deformations. Finally, four cameras were installed along the four cardinal directions, on the opposite sides and at same distance from the specimen; a couple on the loading direction (i.e. East, West) and the other on the orthogonal one (i.e. North, South), in order to monitor cracking development. For hollow circular specimens, since the three-dimensional cracking development, a reference grid with square mesh was plotted on the external surface of the specimen, so that locations and directions of cracks could be uniquely determined.

Figure 3.30 and Figure 3.31 show a view of the applied system for hollow rectangular and hollow circular specimens, respectively.

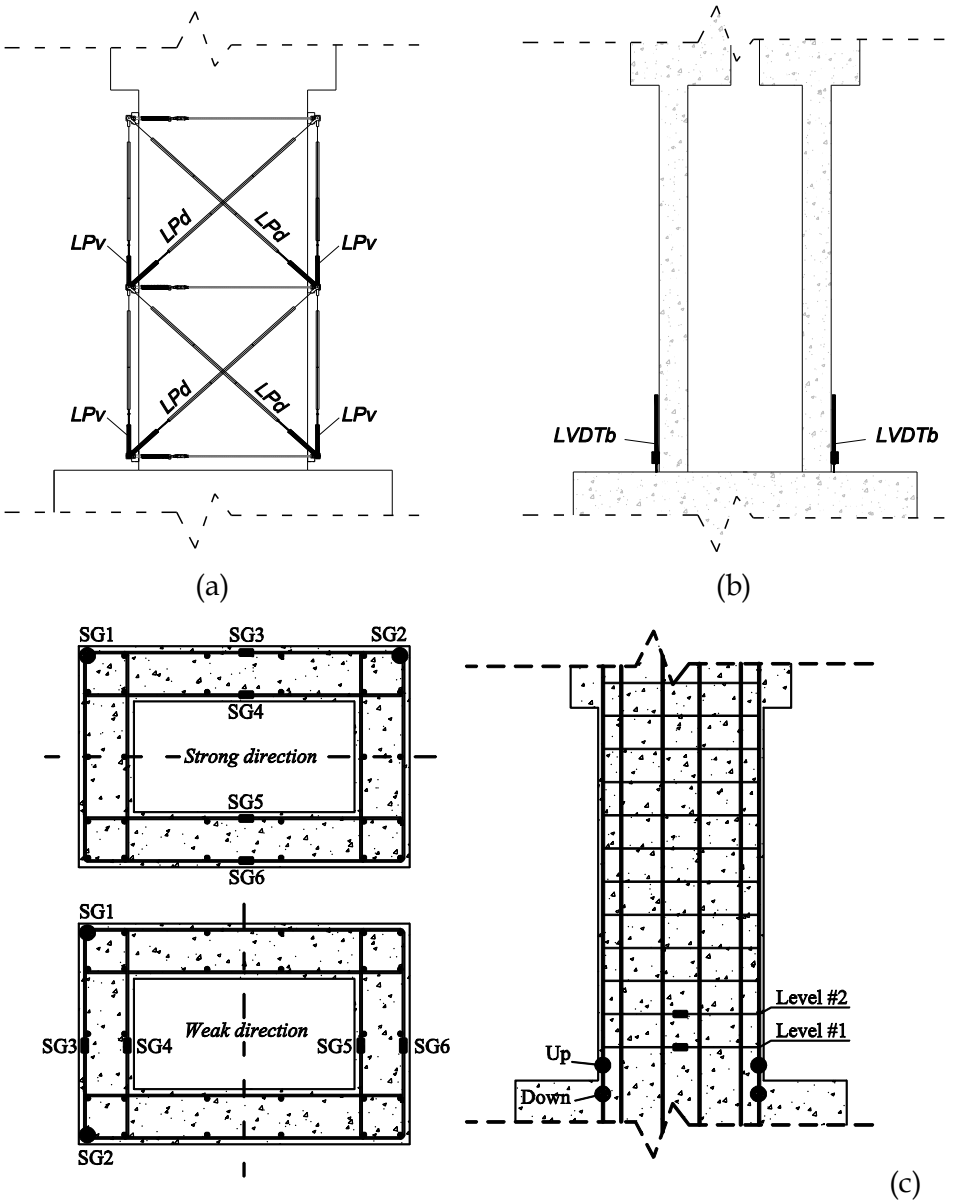

Figure 3.28. Instrumentation scheme: LPs (a), Base LVDTs (b) and Strain Gauges (SGs) (c) – Hollow rectangular specimens

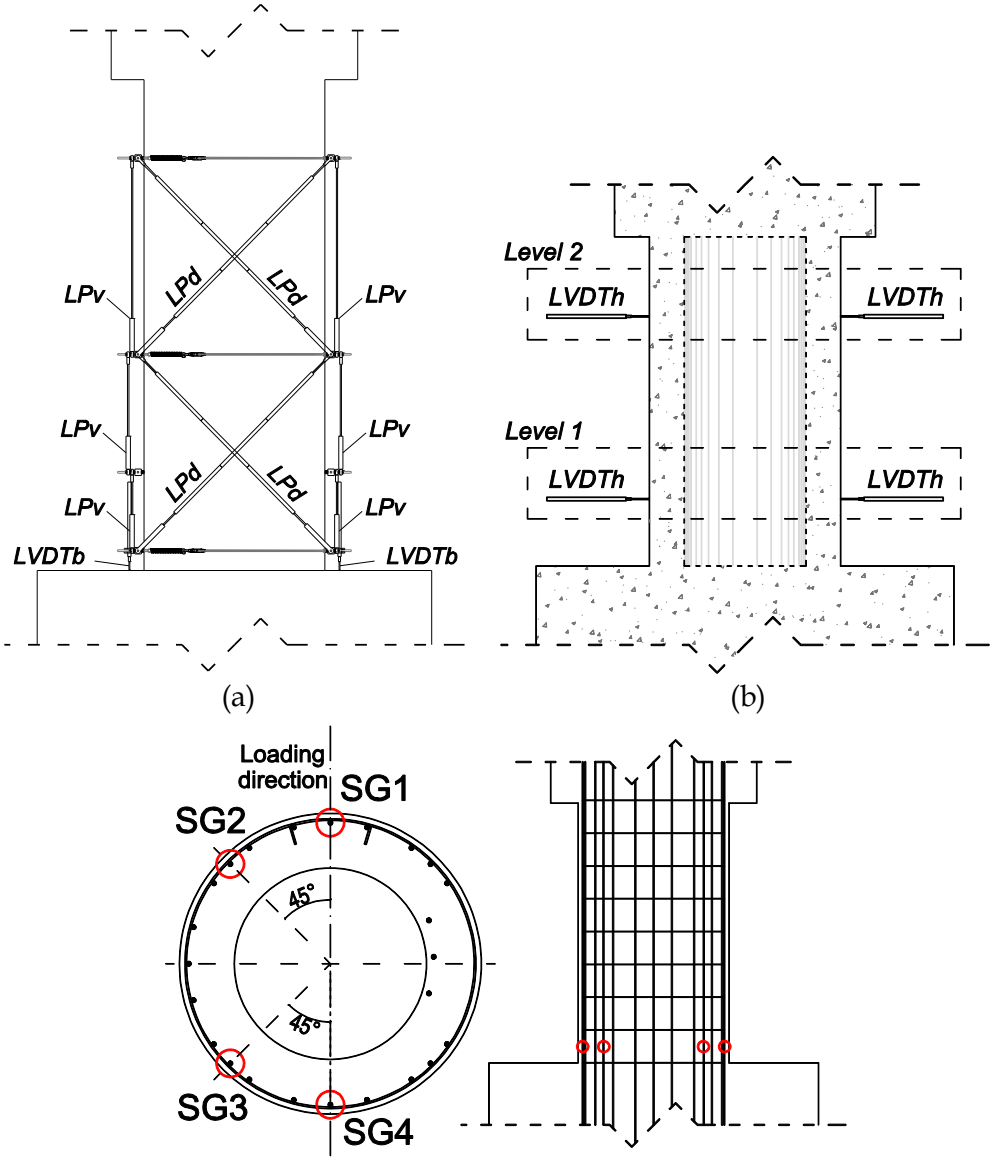

Figure 3.29. Instrumentation scheme: LPs and Base LVDTs (a), Horizontal LVDT for Test P6 (b) and Strain Gauges (SGs) (c) – Hollow circular specimens

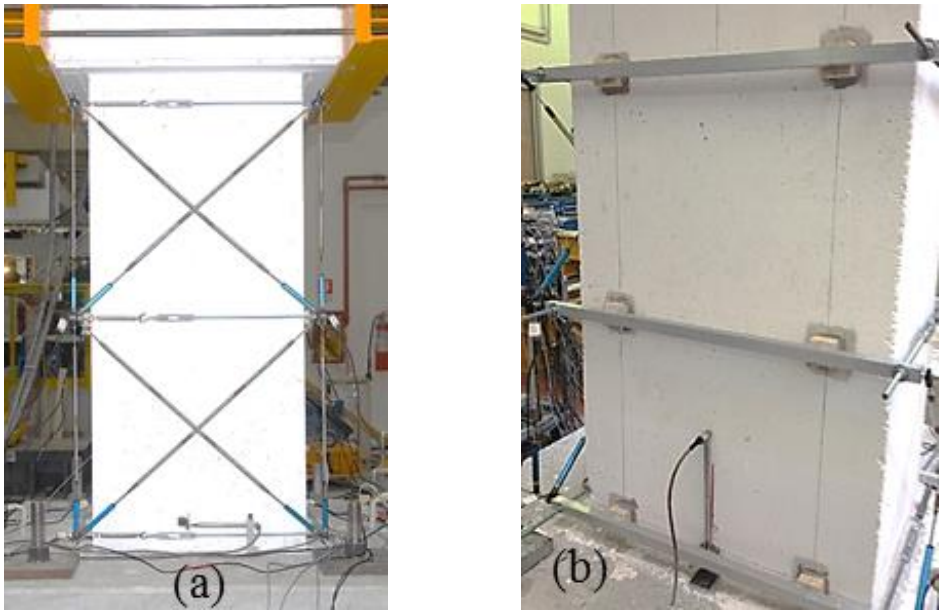

Figure 3.30. View of the applied monitoring system (hollow rectangular)

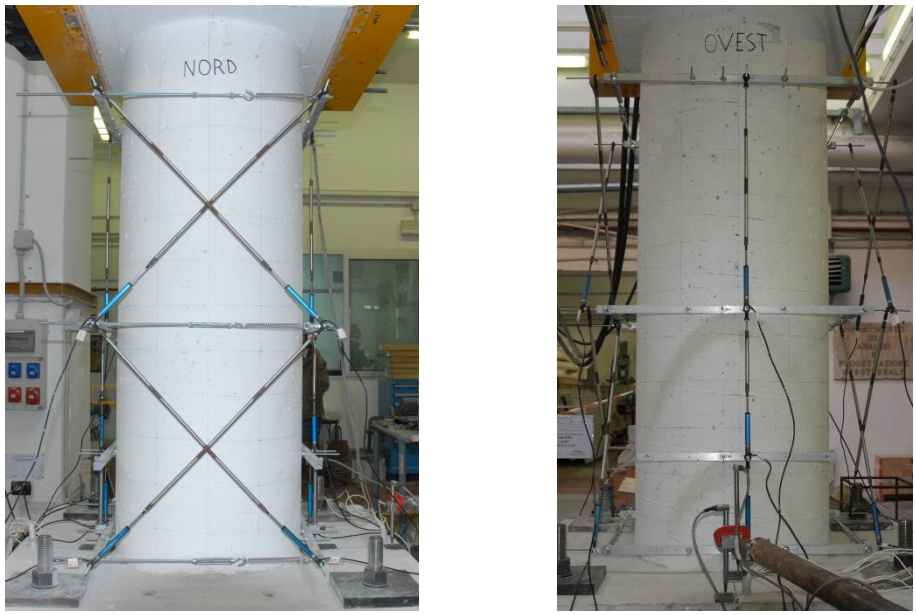

Figure 3.31. View of the applied monitoring system (hollow circular)

3.5 Summary

In this Chapter, the main issues about the experimental campaign have been approached.

The main goal of the design procedure is to obtain specimens representative of the existing bridge columns typical of the Italian transport infrastructures realized before 1980. To this aim, the results of an important investigation on a sample of about 400 existing Italian RC beam bridges are considered (STRIT RT D.1.2, 2015), taking into account key parameters, such as cross-section shape, slenderness, axial load ratio, geometrical reinforcement ratio, materials strength, among others. Starting from those results, two typical bridge pier cross-section are designed (hollow rectangular and hollow circular), as regards both geometry and reinforcement details, according with common non-seismic design practice. In order to allow for testing within the capacity of the laboratory, a scaling factor equal to 1:4 is introduced. Therefore, six reduced-scale reinforced concrete (RC) bridge piers with hollow cross-section (four rectangular shaped and two with circular shape) are defined. Fixed the cross-section, test specimens differ for aspect ratio (height to depth ratio). Medium-low aspect ratios are considered (between 1.5 and 3.75), since the main goal of the experimental program is to investigate deeply about flexure-shear interaction and failure mode prediction. The representativeness issue is considered also for the material properties definition, resulting into a poor concrete and relatively high strength steel.

The construction process, crucial for the success of experimental tests, has been described, focusing on some critical aspects of the construction procedure.

All tests are performed in quasi-static way by applying increasing horizontal displacement cycles with constant axial load of about 5%, typical value for existing Italian bridges service load. The gravity load is applied by means of a closed system able to avoid P-Δ effects, since axial load direction was always identical to specimens' axis. The lateral loading protocol was applied to the centerline of the pile cap by a single horizontal hydraulic actuator under displacement control.

In order to investigate deeply about local deformation components coexisting in the specimens (flexure contribution, shear contribution and fixed end rotation at cantilever base), an appropriate instrumentation is installed. In

particular, it is composed of an arrangement of Linear Potentiometers (LPs) and Linear Variable Displacement Transducers (LVDTs), monitoring flexural and shear deformation, and strain gauges (SGs), monitoring axial steel strain of both longitudinal and transverse reinforcement.

References

Biskinis D.E., Fardis M.N. (2010). Flexure-controlled ultimate deformations of members with continuous or lap-spliced bars. Structural Concrete, 11(2), 93-108.

Biskinis D, Fardis MN. Deformations at flexural yielding of members with continuous or lap-spliced bars. Structural concrete 2010; 11(3): 127-138.

CEN, 2004. European standard EN1992-1-1. Eurocode 2: Design of concrete structures - Part 1-1: General rules and rules for buildings. Comité Européen de Normalisation, Brussels.

Decreto Ministeriale del 14/1/2008. Approvazione delle nuove norme tecniche per le costruzioni. G.U. n. 29 del 4/2/2008, 2008. (in Italian)

Federation Internationale du Beton. Seismic bridge design and retrofit – structural solutions. FIB Bulletin 39, 2007.

Neville, A. M., & Brooks, J. J. (1987). Concrete technology.

STRIT RT D.1.2 – part 1. Inventory e sviluppo database per la caratterizzazione della vulnerabilità delle infrastrutture viarie. STRIT Project "PON Ricerca e Competitività 2007-2013", 2015.

Chapter 4

EXPERIMENTAL RESULTS: HOLLOW RECTANGULAR RC PIERS

This chapter provides a summary of the test results for specimens characterized by hollow rectangular cross-section, including damage description and test data measured during each test.

Based on visual observations and recorded test data, the performance of each test specimen is analyzed and discussed. For each specimen, the measured lateral load-displacement relations and plots of other important test parameters are presented. The damage description of specimens and their implications are discussed, and the measured response are compared.

The following sections discuss, first, the global response of each specimen, and then the evolution of damage observed during the tests. Later, experimental local behavior, in particular referred to the main deformability contributions due to different deformation mechanisms, is analyzed and discussed. Finally, the hysteretic energy dissipation and the related equivalent damping are investigated. Discussions about experimental results are presented, by making in each section a comparison between the four tests.

4.1 Analysis of global response

In this Section, the lateral load-displacement response of tested specimens is analyzed. Response curves, in terms of lateral load versus drift (i.e. top displacement-to-shear span ratio) are shown and commented. The results are reported for each specimen, separately.

4.1.1. Test P1 – Aspect ratio equal to 2.5

The loading history actually applied consists of eight complete cycles of three push/pull sub-cycles. The results in terms of lateral load versus drift response for Test P1 are shown in Figure 4.1.

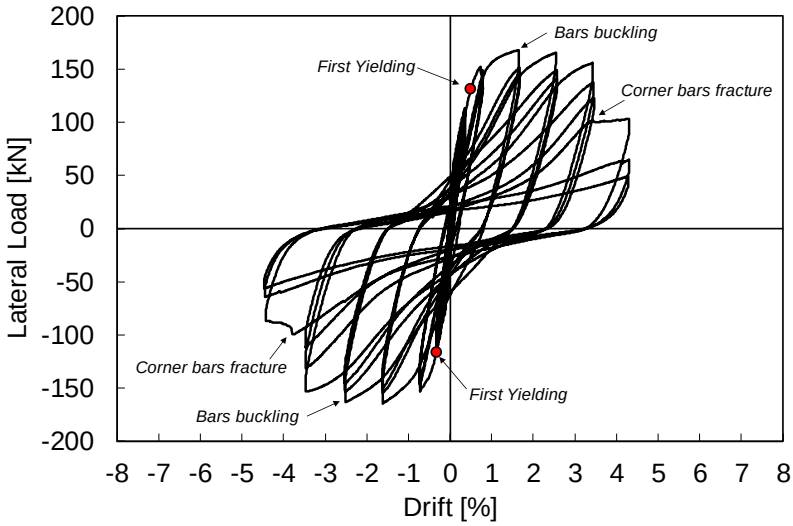

Figure 4.1. Lateral load versus cyclic response (Test P1)

Experimental response appears quite symmetric during the push-pull cycles. A first reduction of the initial stiffness was already observed during the first cycle, for a drift equal to 0.08%, due to first flexural hairline cracks on the flanges. Second loading step (drift = 0.21%) was characterized by a further stiffness decrease corresponding to the development of horizontal flexural cracks towards webs. Stiffness decreased gradually for a drift range between 0.21% and 0.34%, during the third cycle, when existing cracks increased their width and new others formed up. A considerable stiffness reduction was observed during the fourth set of sub-cycles, for a drift value of 0.76% and a force equal to about 153 kN Specimen reached yielding condition, as

confirmed by longitudinal bars strain measures provided by strain gauges located at the base of the test unit. It is interesting to highlight the pinching effect characterizing the hysteretic loops starting from this cycles set, exalted by the sudden increase in width of diagonal cracks. Peak load was reached for a drift equal to +1.68% for positive loading direction (push) and -1.63% for negative loading direction (pull). The corresponding peak values of top lateral load were +164 kN and -168 kN, respectively. The post-peak response was governed by flexure. Indeed, it was characterized by a gradual degradation due to concrete spalling and buckling of longitudinal bars, with a softening stiffness (calculated on the envelope of first sub-cycles) equal to -7.3% and -6.7% of the initial stiffness, in positive and negative loading direction respectively.

Experimental response was symmetric also in inelastic cycles. The intra-cycle strength drop developed from 10% to 27% from fourth to seventh loading step. In particular, during the seventh cycle (drift = 3.47%) a maximum load value of about 155 kN was reached (-7% respect to peak load). This because of a significant concrete spalling together with significant buckling of longitudinal bars. During the last cycle (drift = 4.37%) a sudden intra-cycle strength drop/stiffness decrease in negative/positive direction was observed due to failure in tension due to oligo-cyclic fatigue caused by buckling/tension cycles. The drops in shear strength were of -52% and -43% in push and pull directions, respectively. Test P1 was characterized by flexural failure.

4.1.2. Test P2 – Aspect ratio equal to 3.75

The loading history actually applied consisted of seven complete sets of three push/pull sub-cycles. The results in terms of lateral load versus drift response for Test P2 are shown in Figure 4.2.

Experimental response appeared quite symmetric during the push-pull cycles only up to peak load, while post-peak phase was characterized by different evolutions in positive and negative load direction. Also for Test unit P2, a first reduction of the initial stiffness was observed during the first cycle (drift = 0.23%), for a lateral load value of about +48 kN (push) and -42 kN (pull). Such a stiffness reduction was a consequence of first hairline cracks. Stiffness decreased gradually for a drift range between 0.23% and 0.79%, that is during second and third loading cycles, when gradual development of cracking was observed along the specimen. Longitudinal bars reached yielding

strain value during the third loading step (drift = 0.79%), as confirmed by the strain gauges located at the base of the test unit. In fact, a substantial stiffness reduction was observed during the fourth cycle (drift = 1.69%). Also for Test unit P2, a clear pinching effect characterized the hysteresis loops starting from this cycle.

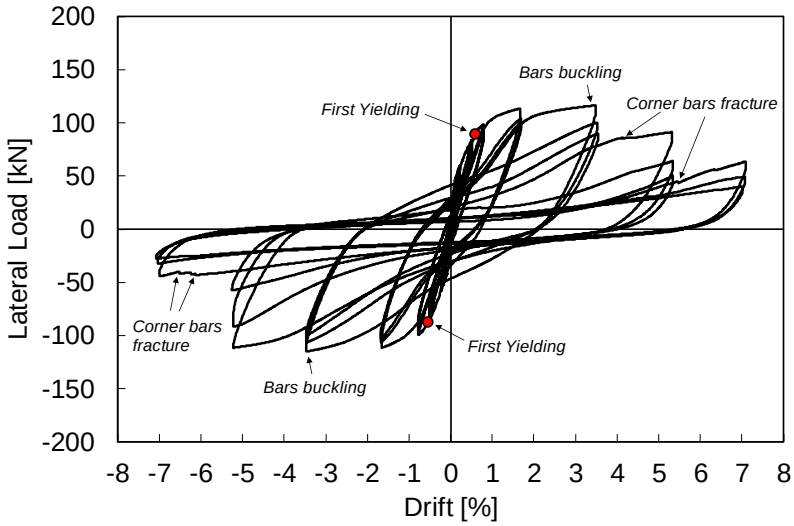

Figure 4.2. Lateral load versus cyclic response (Test P2)

Peak load was reached for a drift equal to 3.50% for both positive and negative loading direction, with a corresponding strength peak of 116 kN This loading step was characterized by an intra-cycle drop in strength equal to -22.7% (push) and -13.1% (pull).

The post-peak response was asymmetric and governed by flexure. In fact, during sixth cycle (drift = 5.25%) different load values were reached in positive and negative direction, equal to +91 kN and -111 kN respectively. Such an asymmetry was due to first longitudinal corner rebar failure in tension (because of oligo-cyclic fatigue) during pushing phase. Softening stiffness values (calculated on the envelope of first sub-cycles) were equal to -6% and -3% of the initial stiffness in positive and negative loading direction, respectively. During the last cycles, for a drift of 7.08%, a sudden intra-cycle strength drop/stiffness decrease in negative/positive direction was observed due to failure in tension due to oligo-cyclic fatigue caused by buckling/tension cycles. In fact, remaining longitudinal corner bars failed in tension and this

phenomenon implicated a drop in strength (45% in push direction and 60% in pull respect to peak lateral load). Corresponding hysteresis loops were very narrow. Test P2 was characterized by flexural failure.

4.1.3. Test P3 – Aspect ratio equal to 1.50

The loading history actually applied consisted of four complete cycles of three push/pull cycles and a last single push/pull sub-cycle corresponding to shear failure. The results in terms of lateral load versus drift response for Test P3 are shown in Figure 4.3. Experimental response appeared slightly non-symmetric during the push-pull cycles. This effect, more evident with increasing drift, is associated with the shear cracking extension and reversal process. Once a set of cracks is open for a given loading direction, the reversal into the opposite direction is partially characterized by closing of the previously opened shear cracks. Therefore, for a given imposed horizontal displacement, a stiffness decrease is observed.

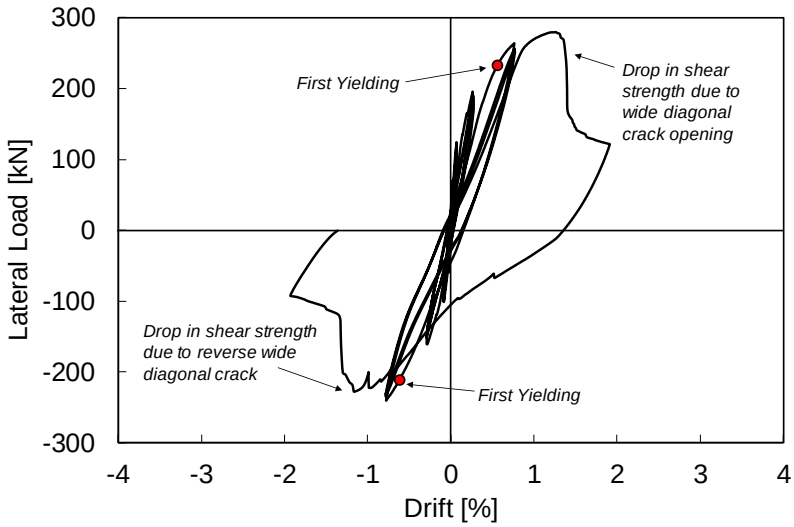

Figure 4.3. Lateral load versus cyclic response (Test P3)

A first reduction of the initial stiffness was observed during the first cycle (drift = 0.02%), for load values of about 69 kN and 58 kN in positive and negative direction respectively. Stiffness decreased gradually during second and third loading step, for a drifts range between 0.08% and 0.28%, when flexural and shear cracks developed along webs surfaces. A substantial

stiffness reduction was observed during the fourth cycle at a drift of 0.78%, corresponding to a lateral load of +264 kN in pushing phase and -240 kN in pulling phase.

Longitudinal bars reached yielding strain value, as confirmed by the strain gages located at the base of the test unit. Fifth cycles set (drift = 1.92%) was characterized by a single push/pull cycle. During pushing phase, for a drift value of +1.26%, drop in strength equal to 58% was observed, from +278 kN to +118 kN, at a drift value of +1.92%. For this drift value, a relevant diagonal crack suddenly opened. Pull phase was characterized by a lower stiffness. For a drift equal to -1.16% another drop in strength was observed (from -228 kN to -92 kN), corresponding to the opening of a reverse diagonal crack. Test P3 failed in shear after flexural yielding.

4.1.4. *Test P4 – Aspect ratio equal to 2.25*

The loading history actually applied consisted of five complete cycles and a last single push/pull sub-cycle corresponding to shear failure. The results in terms of lateral load versus drift response for Test P4 are shown in Figure 4.4.

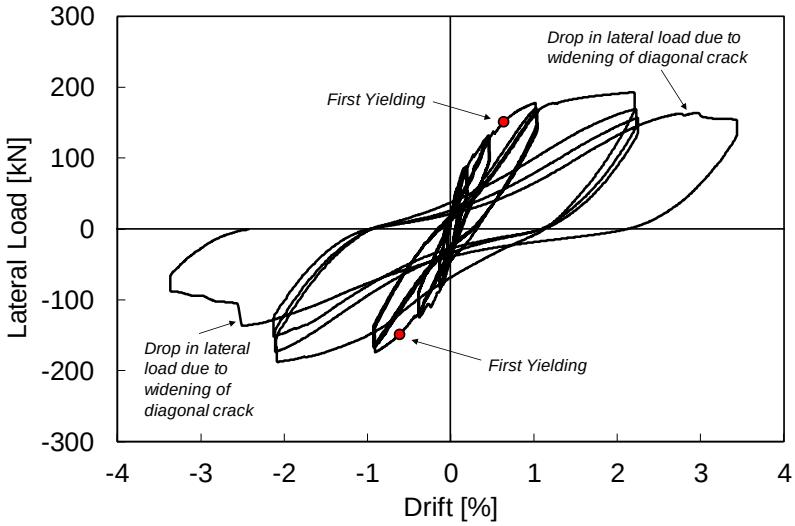

Figure 4.4. Lateral load versus cyclic response (Test P4)

Experimental response appeared quite symmetric during all the applied push-pull cycles. Also in Test unit P4, a first reduction of the initial stiffness was observed during the first three sub-cycles (drift = 0.06%), at which the

specimen reached lateral load values of +57 kN and -52 kN, in positive and negative directions. Stiffness decreased gradually during second and third cycles, for a drift range between 0.06% and 0.43%, when gradual development of cracking was observed along the specimen, first as flexural cracks, quickly evolving in diagonal cracks.

A substantial stiffness reduction was observed during the fourth cycle (drift = 0.99%). Longitudinal bars reached yielding strain value, as confirmed by the strain gages located at the base of the test unit.

Lateral load reached values of +178kN (push) and -174kN (pull). Peak load values were reached for a drift of 2.19%, +193kN and -188kN, in positive and negative loading direction respectively. The inter-cycle strength drop developed from 5% to 19% passing from fourth to fifth cycle. Sixth cycle (drift = 3.40%) was characterized by one push/pull sub-cycle. During pushing phase, for a drift value of +2.80%, response curve evolved along a horizontal slope, maintaining an about constant force value equal to +155 kN (equal to 80% of peak load) up to a drift of +3.40%. This was due to a sudden opening of main diagonal crack on the specimens' webs.

During the following pull phase, for a drift value of -2.49%, a sudden strength drop was observed (from -137 kN to -87 kN). The loss in strength respect to global peak load was equal to 54%. Corresponding to this drop, reverse main shear crack opened suddenly up to a width of about 10 mm. Test P4 failed in shear after flexural yielding.

4.1.5. Comparison of global response

Table 4.1 summarizes experimental first yielding values (V^{+}-, V^{-}_{y}, D^{+}_{y}, D^{-}_{y}), peak values (V^{+}_{max}, V^{-}_{max}, D^{+}_{max}, D^{-}_{max}) and "ultimate" drifts (D^{+}_{u}, D^{-}_{u}), of lateral force and drifts for both positive and negative loading directions. Ultimate drifts values were evaluated as those corresponding to a strength reduction equal to 20% with respect to the peak load on the experimental backbone. Observed failure modes are also reported (F: flexure mode; FS: shear failure after flexural yielding).

Lateral load-drift envelopes corresponding to the first sub-cycles for each loading step are shown in Figure 4.5 for all tests.

As expected, it can be observed that lateral strength increases as the aspect ratio decreases, fixed the loading direction. On the other hand, similarly, a reduction of ultimate deformation capacity with decreasing level of aspect

ratio can be noted.

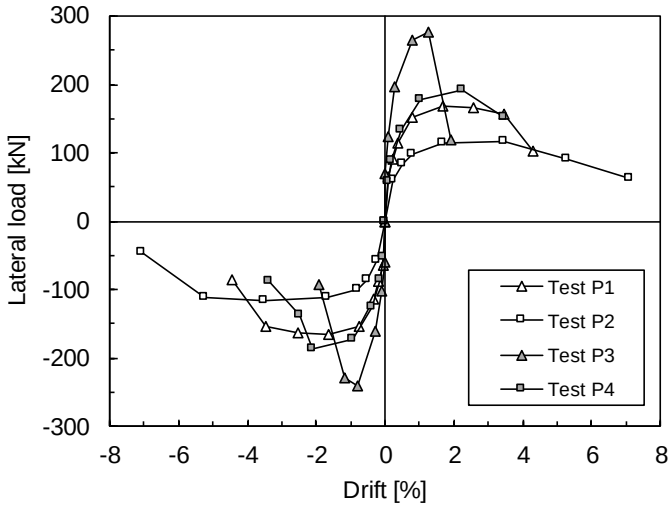

Figure 4.5. Envelopes of lateral load versus drift response

Lower values of ultimate drifts are related to shorter specimens, characterized by shear failure after flexural yielding.

Table 4.1. Yielding, peak and ultimate values of lateral force and drift together with observed failure modes

Test ID	Aspect Ratio	V^+_y	D^+_y	V^-_y	D^-_y	V^+_{max}	D^+_{max}	V^-_{max}	D^-_{max}	D^+_u	D^-_u	Failure Mode*
	(-)	(kN)	(%)	(kN)	(%)	(kN)	(%)	(kN)	(%)	(%)	(%)	(-)
P1	2.50	132.1	0.49	-116.4	-0.32	168.3	1.68	-164.4	-1.63	3.80	-3.79	F
P2	3.75	89.3	0.58	-87.3	-0.55	116.6	3.48	-115.2	-3.53	5.15	-5.25	F
P3	1.50	233.5	0.56	-211.4	-0.62	277.7	1.26	-240.6	-0.78	1.35	-1.27	FS
P4	2.25	152.3	0.65	-149.2	-0.62	193.0	2.24	-187.5	-2.13	3.40	-2.53	FS

$^{+(-)}$: push (pull) direction of the applied displacement.
V_y, D^+_y, are experimental first yielding values of lateral force and drifts, respectively.
V_{max}, D_{max}, are experimental peak values of lateral force and corresponding drifts.
D_u, is the ultimate drift corresponding to a strength reduction of 20% of the peak load on the experimental backbone.
* : experimental failure mode (F: flexure mode; FS: shear failure after flexural yielding).

4.2 Damage evolution and crack pattern

In this Section, the evolution of observed damage with increasing imposed displacement is described and related to the above-analyzed lateral load-drift response of tested specimens. Damage evolutions and final damage states are shown and damage descriptions are summarized in tabular form for each loading step. The results are reported for each specimen, separately.

4.2.1. Test P1 – Aspect ratio equal to 2.5

The evolution with the drift of the damage state and the final damage state are showed in Figure 4.6 and summarized in Table 4.2. During the first cycle, for a drift value of 0.08%, some horizontal hairline cracks formed up on the flanges, in the lower part of the specimen. The second loading step (drift = 0.21%) was characterized by the development of horizontal flexural cracks on the webs along the first three layers of transverse reinforcement (see Figure 4.6a). For a drift range between 0.21% and 0.34%, the flexural cracks located on the lower half of the element evolved along diagonal directions and slight cracks appeared on the central part (Figure 4.6b).

After the first yielding condition was reached, during the fourth cycle (drift = 0.76%), existing cracks increased their width and new flexural cracks formed up to a height of about 1 m from the column base. Further shear cracks formed as extensions of flexural cracks on the upper part of the specimen. It is noteworthy, the sudden increase in width of diagonal cracks causing a pronounced pinching effect in the hysteretic loops (Figure 4.6c). The cycle corresponding to peak load was characterized by the extension of existing cracks towards the compression zone and their considerable increase in width. In particular, the damage at the base of the column developed quickly: vertical cracks appeared in concrete cover corners due to longitudinal bars buckling (Figure 4.6d). The post-peak cycles were characterized by concrete spalling and buckling of longitudinal bars at the base of the column, and the gradual widening of the existing diagonal cracks, leading to a slight softening of the experimental response. In particular, during the sixth cycle, for a drift of 2.55%, flexural cracks at the column base considerably widened and concrete cover corners completely spalled off. The subsequent cycles set (drift = 3.47%) was characterized by a significant concrete spalling together with significant

buckling of longitudinal bars within the distance between the base and the first layer of transverse reinforcement (Figure 4.6e). During the last cycle (drift = 4.37%), concrete of the compressed flanges was completely crashed and spalled (Figure 4.6f). Longitudinal corner bars failed in tension due to oligo-cyclic fatigue caused by buckling/tension cycles (detail in Figure 4.6h). A picture of the final damage state is reported in Figure 4.6g.

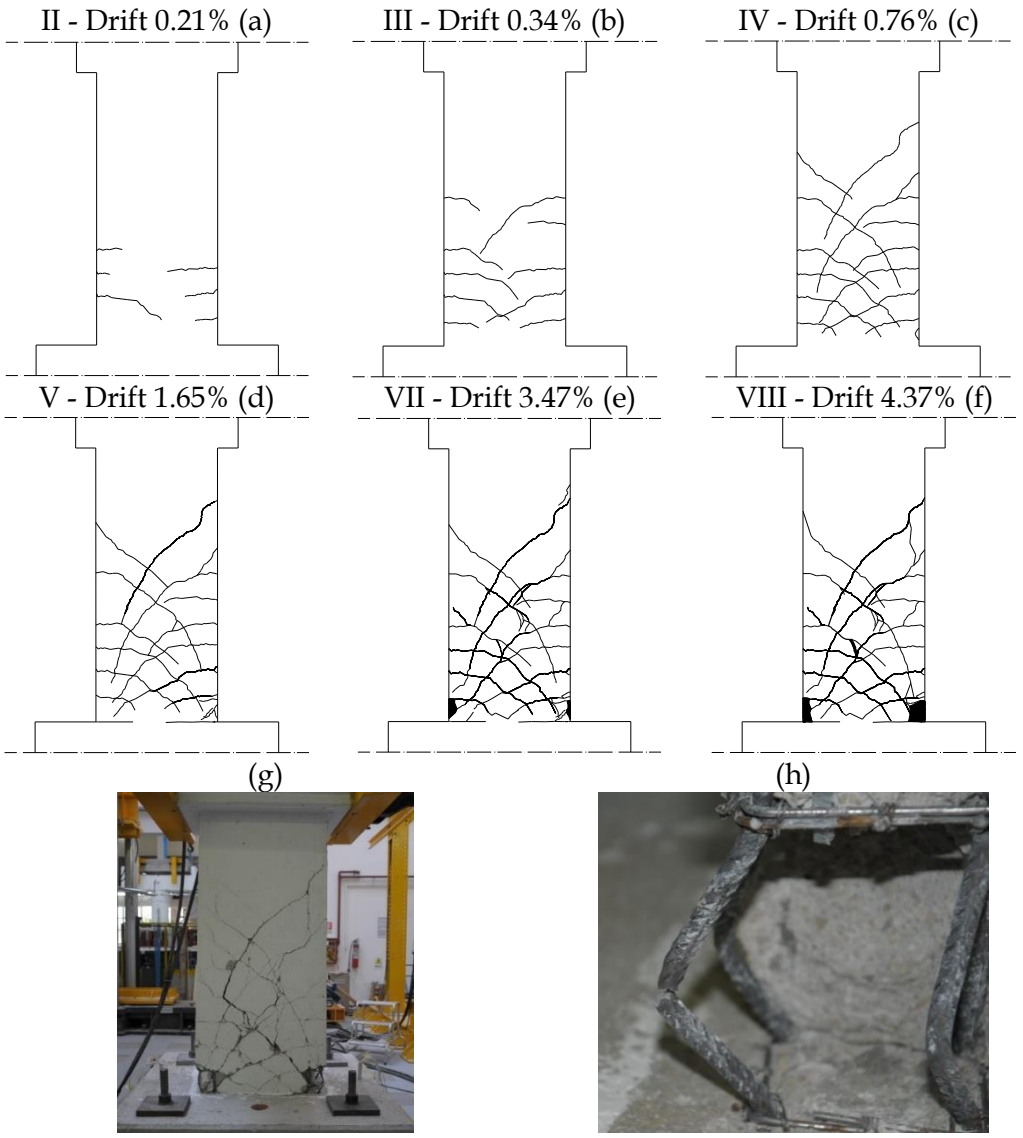

Figure 4.6. Test P1: evolution of damage (a) – (f), final damage state (g), corner bar fracture (h)

Cycle	Drift (%)	Damage description
1	0.08	Horizontal hairline cracks on flanges
2	0.21	Horizontal cracks on webs
3	0.34	Evolution of the flexural cracks along diagonal directions
4	0.76	Increase in width of existing cracks and new diagonal cracks
5	1.65	Vertical cracks in concrete cover corners due to longitudinal bars buckling
6	2.55	Wide crack at the pier/foundation interface and spalling of concrete cover corners
7	3.47	Complete concrete cover spalling and significant buckling of longitudinal bars
8	4.37	Failure in tension of longitudinal corner bars due to oligo-cyclic fatigue

Table 4.2. Overview of the evolution of damage during Test P1

4.2.2. Test P2 – Aspect ratio equal to 3.75

The evolution with the drift of the damage state and the final damage state are showed in Figure 4.7 and summarized in Table 4.3.

A first reduction of the initial stiffness was observed during the first cycle (drift = 0.23%), when hairline cracks were observed on the East and West surfaces, along the first three layers of transverse reinforcement (Figure 4.7a).

For a drift range between 0.23% and 0.79%, slight cracks appeared on the upper half of the element and the existing flexural cracks evolved along diagonal directions (Figure 4.7b). Specimen reached first yielding condition during the third loading step (drift = 0.79%), in fact a substantial aggravation of damage state was observed in the subsequent cycles. The fourth cycle (drift = 1.69%) was characterized by a sudden increase in width of the existing cracks, new flexural cracks formed and further shear cracks appeared as extensions of flexural cracks in the central zone (Figure 4.7c).

When peak load was reached, for a drift equal to 3.50%, diagonal cracks increased their width suddenly, intersecting with each other in correspondence of the central longitudinal bar, causing a concrete cover spalling along a vertical centerline. Damage at the base of the column developed quickly: vertical cracks appeared on cover corners due to longitudinal bars buckling and concrete spalled off (Figure 4.7d)., leading to a considerable strength drop.

The post-peak response was asymmetric, mainly due to first longitudinal

corner rebar failure in tension (because of oligo-cyclic fatigue) during the first pushing phase of sixth cycle (drift = 5.25%), when damage state developed further, as shown in Figure 4.7e. During the last cycle, for a drift of 7.08%, compressed concrete between the base and the first stirrups layer completely crushed and spalled off. Remaining longitudinal corner bars failed in tension and this phenomenon implicated a severe drop in strength (Figure 4.7f).

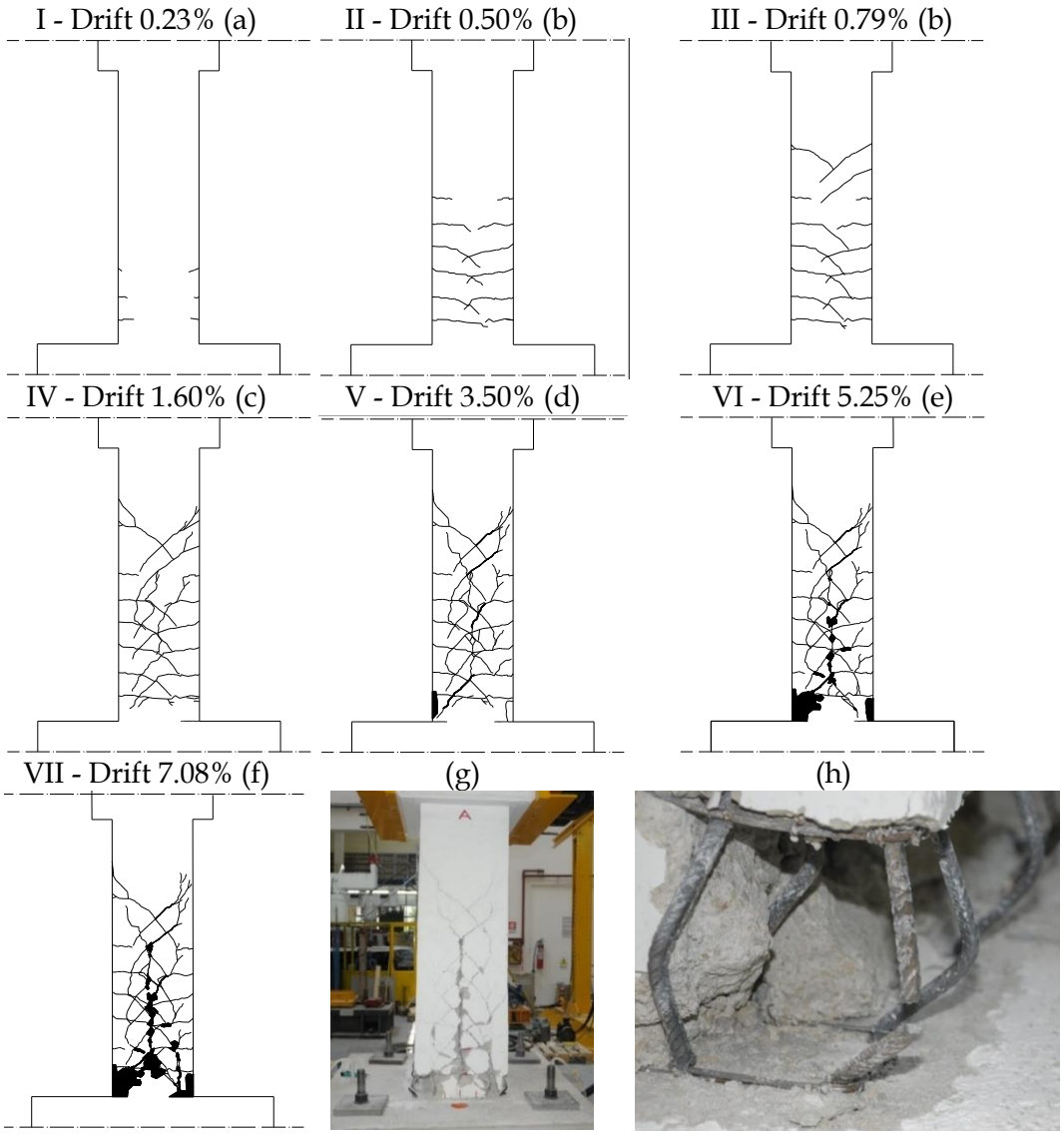

Figure 4.7. Test P2: evolution of damage (a) – (f), final damage state (g), corner bar fracture (h)

By inspecting the damage state at the end of the test (see Figure 4.7g – 4.6h), it is interesting to note that also internal layers of longitudinal steel bars are characterized by an intense buckling.

Cycle	Drift (%)	Damage description
1	0.23	Horizontal hairline cracks on flanges
2	0.50	Horizontal cracks along webs
3	0.79	Evolution of the flexural cracks along diagonal directions and new diagonal cracks
4	1.60	Increasing in width of existing cracks and new diagonal cracks
5	3.50	Spalling of concrete cover corners due to buckling of corner bars
6	5.25	Wide crack at the pier/foundation interface and first corner bar failure due to oligo-cyclic fatigue
7	7.08	Complete concrete crushing and failure of further longitudinal corner bars

Table 4.3. Overview of the evolution of damage during Test P2

4.2.3. Test P3 – Aspect ratio equal to 1.50

The evolution with the drift of the damage state and the final damage state are showed in Figure 4.8 and summarized in Table 4.4. No cracks were observed along the specimen surfaces during the first cycle (drift = 0.02%). Only at the base/foundation interface, at the extreme external fibers, slight cracks were observed.

For a drifts range between 0.02% and 0.28%, cracks appeared on the East surface along the first four layers of transverse reinforcement and on and West surface along first, second, third and fifth stirrups level. Flexural cracks evolved quickly along diagonal directions towards compressed zone, during the third step (drift = 0.28%). In particular, two diagonal cracks formed from top to down opposite corners with an inclination angle of about 45 degrees (Figure 4.8 a).

During the fourth cycle, at a drift of 0.78%, first yielding condition was reached and damage state developed quickly: existing shear cracks increased their width and length, particularly two principal ones, no flexural cracks formed and new slight shear cracks appeared as extensions of flexural ones in the central zone. It is noteworthy highlighting that, unlike Test P1 and Test P2, no considerable damage was observed on the base zone (Figure 4.8 b).

Fifth cycle (drift = 1.92%) was characterized by a single push/pull cycle. During pushing phase, for a drift value of +1.26%, the main existing shear crack opened suddenly up to a width of about 10 mm, along an ideal concrete strut with a medium inclination angle of about 42 degrees (Figure 4.8c). A sliding between the upper and the lower part of the specimen was observed, with buckling of longitudinal bars crossing the main diagonal crack (Figure 9d). Shear sliding also caused buckling of the longitudinal bars next to the base section with resulting concrete cover spalling (Figure 4.8e).

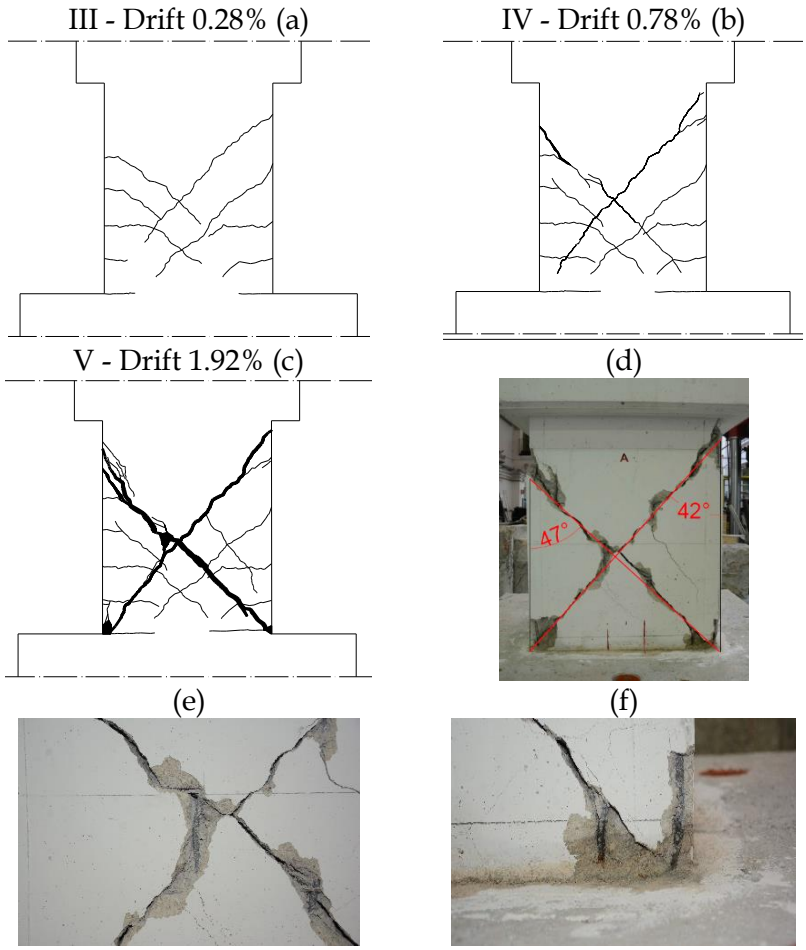

Figure 4.8. Test P3 evolution of damage (a) – (f), final damage state (g), corner bar fracture (h)

Pull phase was characterized by a lower stiffness. For a drift equal to -

1.16% another drop in strength was observed (from -228kN to -92kN). Shear crack with a medium inclination of about 47 degrees opened suddenly, causing buckling in longitudinal bars and concrete cover spalling (Figure 4.8f). Test P3 failed in shear after flexural yielding.

Cycle	Drift (%)	Damage description
1	0.02	Horizontal hairline cracks on flanges at the pier/foundation interface
2	0.08	Horizontal cracks along flanges
3	0.28	Evolution of the flexural cracks along diagonal directions and new diagonal cracks
4	0.78	Increasing in width of existing cracks and new diagonal cracks
5	1.92	Sudden widening of main diagonal cracks up to 10 mm

Table 4.4. Overview of the evolution of damage during Test P3

4.2.4. *Test P4 – Aspect ratio equal to 2.25*

The evolution with the drift of the damage state and the final damage state are showed in Figure 4.9 and summarized in Table 4.5. Also for Test unit P4, during the first cycle, no cracks were observed along the specimen surfaces, but only at the specimen/foundation interface. The second cycle (drift = 0.17%) was characterized by slight cracks on the East and West specimen surfaces, along second and third stirrups layers, evolving quickly along diagonal directions toward compressed zone. Existing cracks increased their width during the third loading step (drift = 0.43%), some flexural hairline cracks appeared next to the base and two wider diagonal cracks formed from top to down opposite corners with an inclination angle of about 38 degrees (Figure 4.9a). Specimen reached yielding condition for a drift = 0.99% and damage state developed quickly: existing shear cracks increased their width and length and new slight shear cracks appeared in the central zone, next to principal ones (Figure 4.9b).

Peak load values were reached for a drift of 2.19%, during the fifth cycle, both in positive and negative loading direction. Damage state evolved quickly causing a severe inter-cycle strength drop: new shear cracks formed in the upper part, existing main diagonal cracks increased their width and extended reaching the base corners, causing concrete cover cracking. A clear fixed-end

rotation was observed (Figure 4.9c).

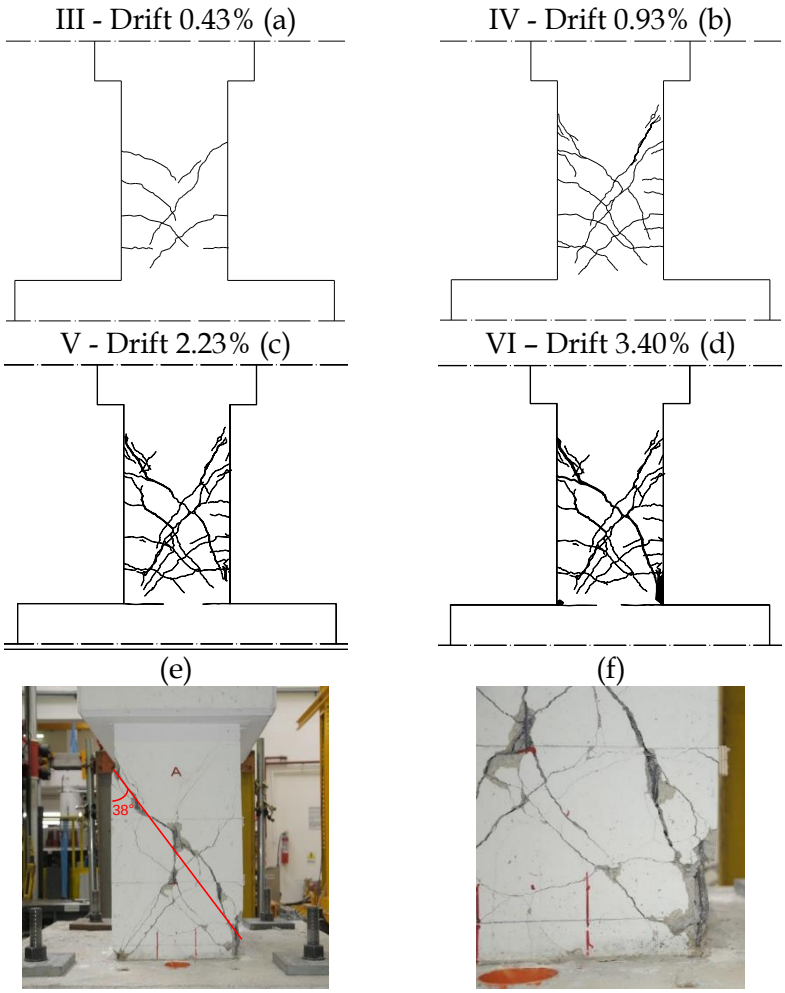

Figure 4.9. Test P4: evolution of damage (a) – (d), final damage state (e), corner bar buckling (f)

Sixth loading step (drift = 3.40%) was characterized by one push/pull cycle. During pushing phase, for a drift value of +2.80%, East-West main diagonal crack opened suddenly. During the following pull phase, for a drift value of -2.49%, a sudden widening of West-East main shear crack was observed, along an ideal concrete strut with a medium inclination of about 38 degrees (Figure 4.9d). A sliding between the upper and the lower part of the specimen was observed (Figure 4.9e), with buckling of longitudinal bars crossing the shear crack. Shear sliding caused buckling of the longitudinal bars

next the base section with resulting concrete cover spalling (Figure 4.9f).

Cycle	Drift (%)	Damage description
1	0.06	Horizontal hairline cracks on flanges at the pier/foundation interface
2	0.17	Horizontal cracks along flanges
3	0.43	Evolution of the flexural cracks along diagonal directions and new diagonal cracks
4	0.99	Increasing in width of existing cracks and new diagonal cracks
5	2.19	Lengthening of main diagonal crack and concrete cover cracking
6	3.40	Sudden widening of main diagonal cracks up to about 10 mm

Table 4.5. Overview of the evolution of damage during Test P4

4.3 Local behavior

In this Section, the most significant local measurement data are analyzed and discussed.

4.3.1. Strain of longitudinal and transverse reinforcement

During the experimental tests, strain of both longitudinal and transverse reinforcement was monitored by means of strain-gauges (SGs) installed according the scheme reported in Figure 3.28.

Figure 4.10 shows strain of longitudinal bars (ε_s) during the test for each specimen, until measures can be considered as reliable. Yielding strain ($\varepsilon_{s,y}$ = 2.7‰) is indicated through a dotted line in the diagrams, so it is possible to identify the cycle and the drift value at which first yielding was reached. In particular, Test P1 reached the first yielding condition between third and fourth loading step, for a drift of about 0.40%. In Test P2, first yielding occurred between second and third cycles set, for a drift of about 0.50%. Test P3 and P4 reached first yielding condition during fourth cycle, for drift range between 0.28% and 0.90%.

Experimental measures related to SGs installed on the longitudinal bars under the base section at a depth of 60mm (identified as SG-Down) are analyzed too, in order to investigate about strain penetration into the foundation block. As expected, these measures are smaller than the corresponding located above the base section. Also in this case, it is possible to

identify the cycle and the drift range at which yielding strain reached the above mentioned depth. For both taller specimens (namely P1 and P2), this condition was reached during the loading step following the one in which first yielding occurred. In particular, for Test P1 the condition was reached during fifth loading step, for a drift range between 0.76% and 1.65%, corresponding to peak load. For Test P2, yielding strain penetration was detected during fourth cycle, for a drift varying between 1.60% and 3.50%. For Test P3, it is interesting to note that the shear failure after flexural yielding limited strain penetration into the foundation, so yielding strain was not recorded. Finally, for Test P4, yielding strain penetration was recorded during pushing phase, while the drop in strength related to shear failure during pulling phase limited strain penetration.

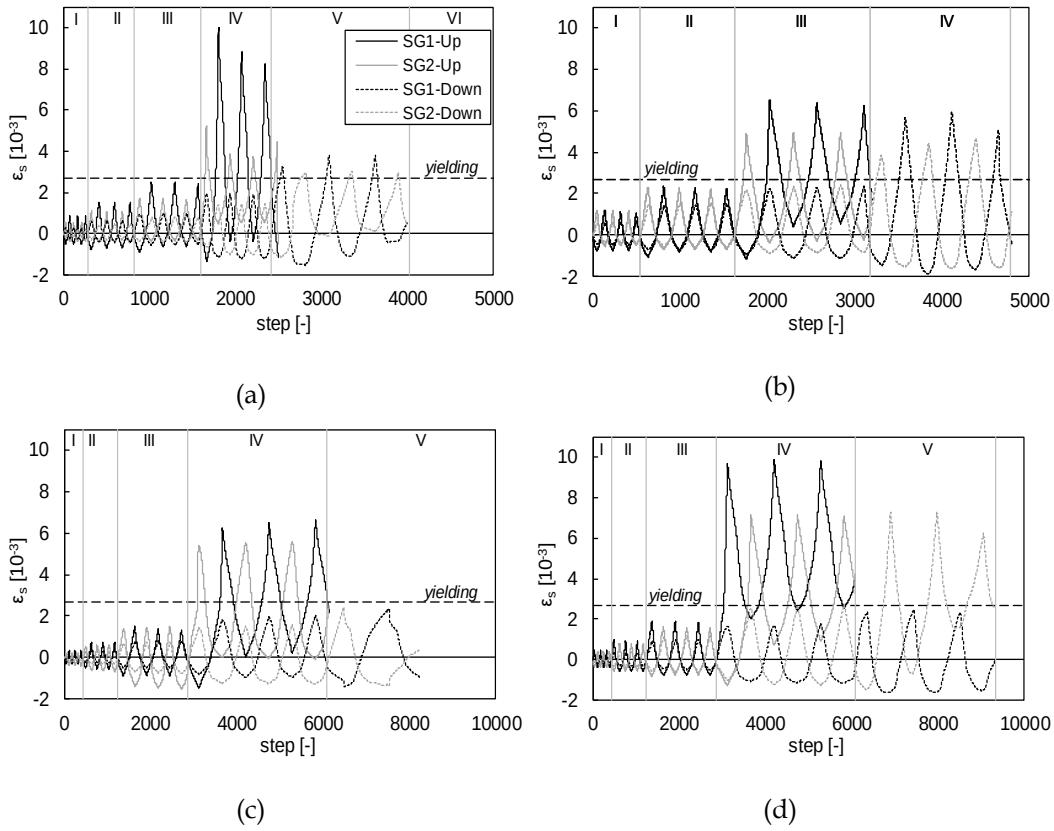

Figure 4.10. Strain of longitudinal bars for Tests P1(a), P2(b), P3(c), P4(d)

The strain in transverse reinforcement provided by strain gauges mounted

on both braces of the two stirrups at Level #1 and at Level #2 (see Figure 3.28) is reported in Figure 4.11.

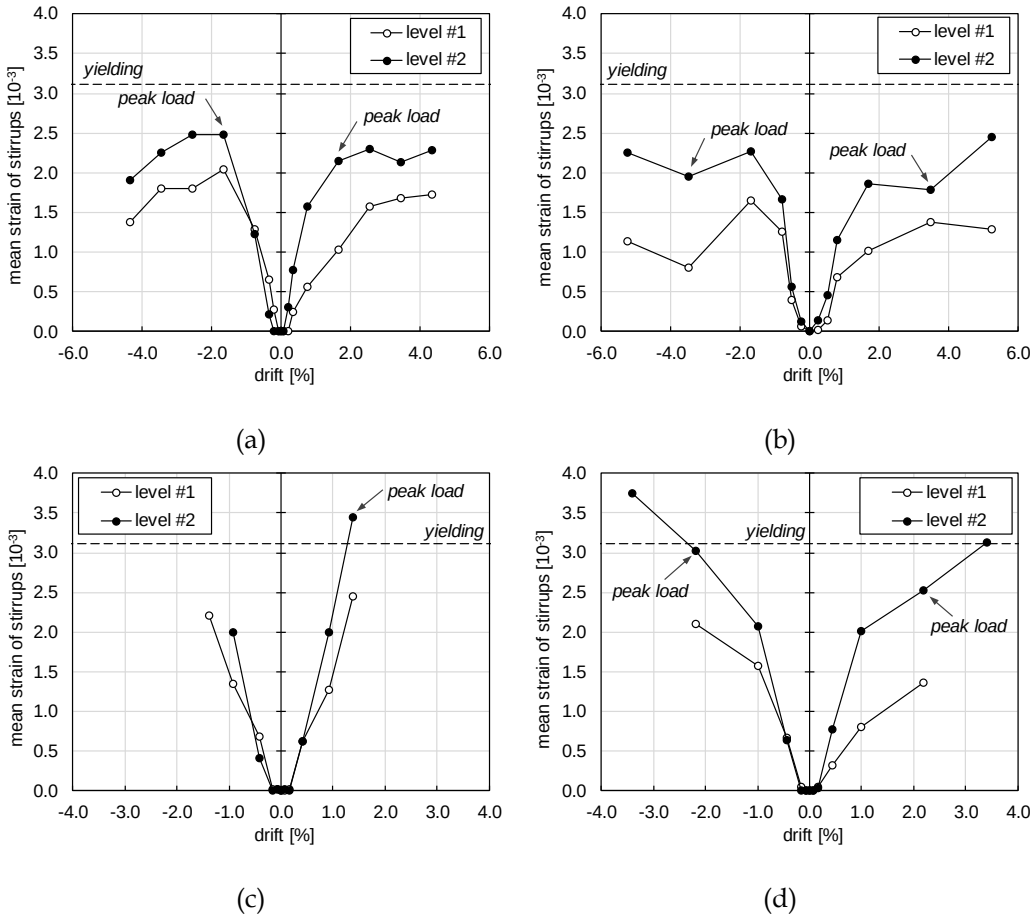

Figure 4.11. Envelope of mean strain of stirrups versus drift for Tests P1 (a), P2 (b), P3 (c), P4 (d)

The average strain at each level is evaluated, as measured at the first (positive and negative) sub-cycle, for each imposed drift, until the measures can be considered reliable. As observed, in all the tests the stirrup strain is nearly null during the very first cycles, before the development of first diagonal cracks (e.g., for the first two cycles, up to 0.17% drift, for Test P3). Moreover, the measured strain at Level #2 is systematically higher than at Level #1. This is consistent with the generally more severe observed diagonal cracking involving Level #2 stirrups compared with Level #1, given equal the

imposed drift. In Tests P1 and P2, which showed a failure mode controlled by flexure, the strain in stirrups does not reach the yielding value. In both of these specimens, both at Level #1 and #2, the peak value of strain in stirrups is attained in the cycle corresponding to maximum lateral load – as expected – or in the immediately previous or following cycle. Subsequently, softening in lateral response leads to a slightly decreasing or quasi-constant strain with increasing drift. In Tests P3 and P4, characterized by a shear failure after flexural yielding, a monotonic increase in stirrup strain is observed with imposed drifts. In both cases, yielding of stirrups is observed at Level #2, roughly in correspondence with the peak load.

4.3.2. Flexural and Shear Deformability Contributions

Seismic response of RC elements with hollow sections, typical of bridge piers, can be governed by a considerable flexure-shear interaction, depending on their aspect ratio. Such an interaction leads to typical cracks layout on web surfaces, similar to cantilever walls. Shear deformation mechanism may represent a considerable portion of the global deflections, limiting ductile energy dissipation. In order to investigate experimentally this issue, an appropriate monitoring system was installed (see Figure 3.28).

The top displacement of the specimens (Δ) can be interpreted as the results of three response mechanisms: flexure (Δ_f), shear deformation along webs (Δ_s) and fixed-end-rotation due to longitudinal bar slip at column base (Δ_θ) (see Figure 4.12 and Eq. (4.1)).

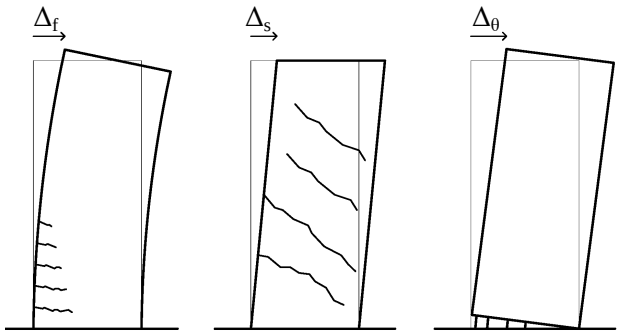

Figure 4.12. Deformability contributions to total displacement

Assuming a uniform curvature distribution along each of the two curvature cells, the flexural component Δ_f was calculated as the sum of the

rotations measured by vertical LPs multiplied by corresponding distances from the top of the column (Eq. (4.2)). Strictly speaking, the fixed-end-rotation contribution Δ_θ is due to the slip from the foundation and it cannot be directly evaluated; instead, the base rotation θ_b can be measured by the two LVDTs monitoring vertical deformation along the height $h_b = 50$ mm from the base section. θ_b is associated to the base crack width including slip from element and from foundation, and to flexural deformation along h_b. The corresponding displacement Δ_b was calculated according to Eq. (4.3), similar to Eq. (4.2).

Based on the hypothesis of small angles and uniform shear deformation over the measuring panel height, the shear component Δ_s was estimated using Eq. (4.4). In Eqs. (4.2) – (4.4), h_i, h_j, l, d, are respectively heights, width and diagonal of the measuring panels; h_b is the height of first curvature cell, next to base section; $\delta_{o,i}$ and $\delta_{e,i}$, δ_1 and δ_2 are average values between North and South specimen surfaces of vertical and diagonal experimental measurements.

$$\Delta=\Delta_f+\Delta_b+\Delta_s \tag{4.1}$$

$$\Delta_f=\sum_{i=1}^{2}\theta_i\left[L_v-\left(\sum_{j=1}^{i-1}h_j+h_i/2\right)-h_b\right];\ \theta_i=\frac{\delta_{o,i}-\delta_{e,i}}{l} \tag{4.2}$$

$$\Delta_b=\theta_b\left(L_V-h_b/2\right) \tag{4.3}$$

$$\Delta_s=\frac{d}{2l}\left(\delta_1-\delta_2\right) \tag{4.4}$$

Figure 4.13 and Figure 4.14 show deformability components as a function of the top displacement, for tall and short specimens respectively (until all measures can be considered reliable and for first cycle at each drift level, both in positive and negative directions). Global symmetry of the response in push/pull direction is confirmed also in terms of local deformations. For Tests P1 and P2, damage state evolution led to a loss of some instruments, so for these specimens, diagrams stop at peak load drift, while for Tests P3 and P4 measures are reliable up to failure drift. For all the tests, flexural deformability contribution (sum of Δ_b and Δ_f) was predominant with respect to shear one.

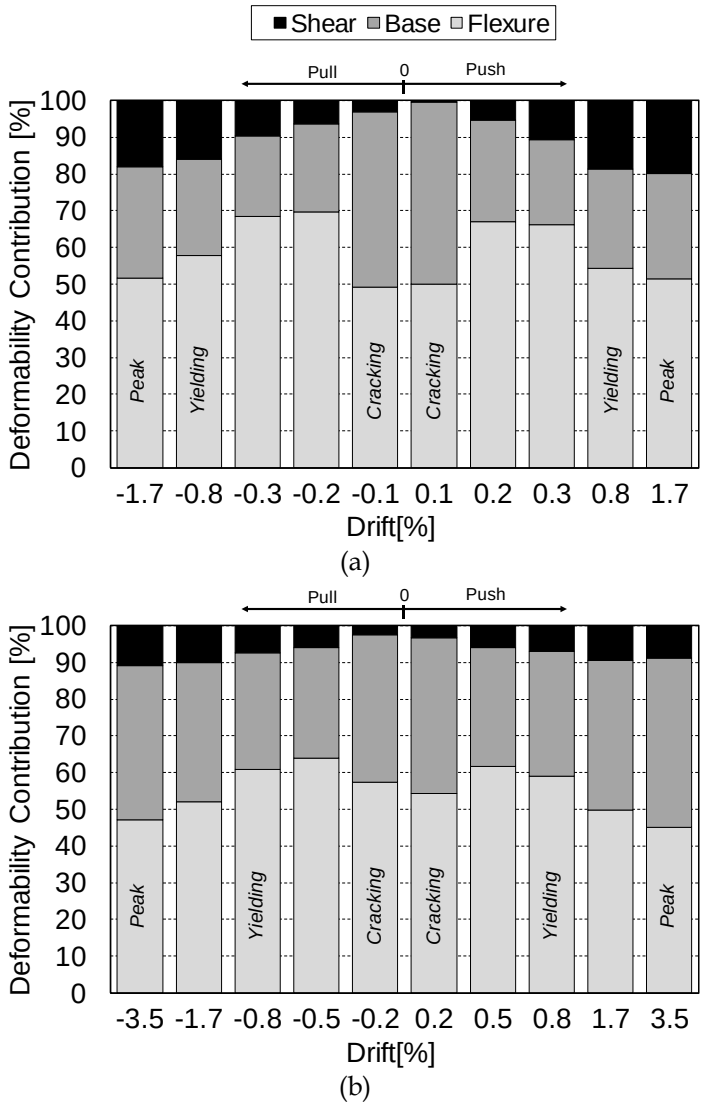

Figure 4.13. Experimental deformability contributions to total displacement ratio for tall specimens: Test P1 (a) and Test P2 (b)

It is interesting to note that for tall specimens (i.e. P1 and P2) flexural deformation was distributed over the height since from first cycle, with a cracking layout typical of slender elements (balanced dark and light grey in figure). For short columns (i.e. P3 and P4), flexural deformation was initially concentrated at the base, with hairline cracks formed only at column/foundation interface (dark grey predominance in Figure 4.13). It seems possible to identify a relation between shear contribution to top

displacement (Δ_s/Δ) and aspect ratio (L_V/H). In fact, for slenderest specimen (i.e. P2) maximum value of shear contribution is equal to 10.8%. For Test units P1 and P4, characterized by similar aspect ratios (equal to 2.50 and 2.25 respectively), for a drift value corresponding to peak load, shear contribution is about 20.0% of the top displacement.

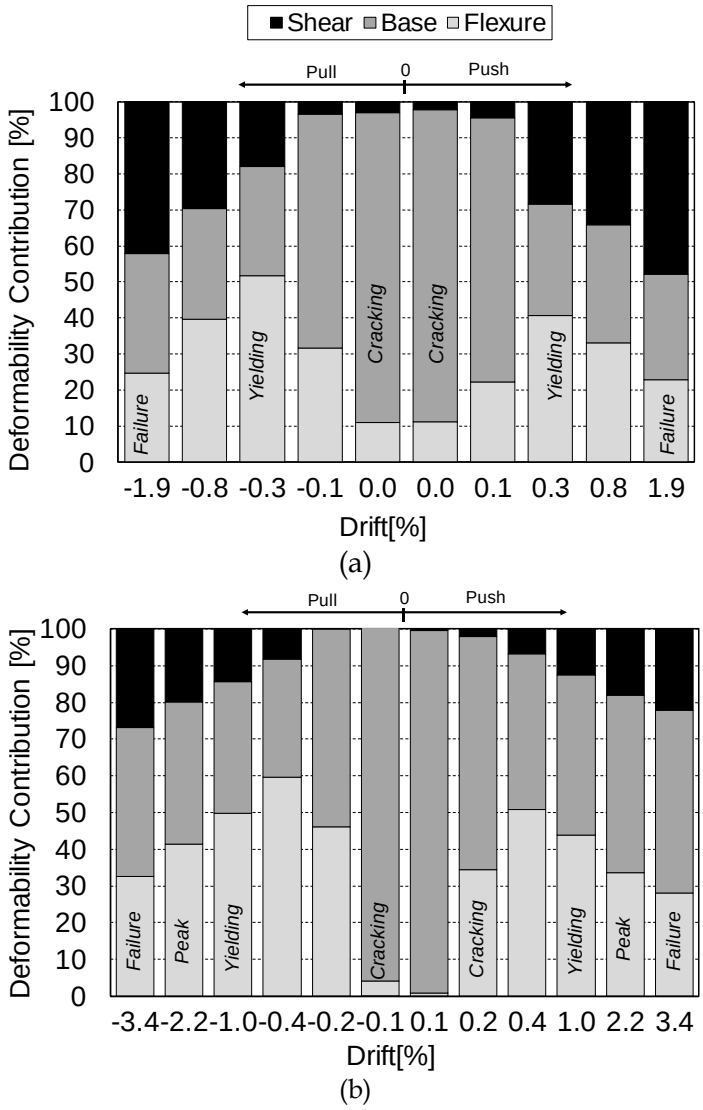

Figure 4.14. Experimental deformability contributions to total displacement ratio for short specimens: Test P3 (a) and Test P4 (b)

At shear failure, shear contribution to top displacement for Test P4 reaches

a value of 27%. The Test P3 is characterized by higher shear deformations since first cycles. In fact, Δ_s/Δ ratio reached an average value of 31.9% at yielding cycle and 44.9% at shear failure. Another interesting observation about deformability contributions is that for taller Tests P1 and P2, after flexural yielding, the base contribution Δ_b/Δ starts to grow (of about 10% respect to previous value), due ductile dissipative system concentrated at the base. For tests P3 and P4, Δ_b/Δ is about constant from yielding to shear failure.

It is noteworthy to underline that the subdivision of deformations of inelastic RC hollow piers into shear and flexural deformations can provide a useful link between the experiments and numerical models, particularly if beam models are used. Of particular interest is the assessment of the shear contribution to lateral displacement in the inelastic range, to better understand whether shear deformations are essential to consider in structural analysis. In this regard, Figure 4.15 shows the trend of shear contribution Δ_s/Δ with the drift for all tests (i.e. for different values of the aspect ratio L_v/H). As expected, shear deformation increases when aspect ratio decreases. Furthermore, by observing Tests P1 and P4 trends, it seems that shear contribution depends also by the web depth. In fact, even if Test P1 is characterized by a lower aspect ratio respect to Test P4, it is interested by higher shear deformations, especially for drift values lower than drift corresponding to load peak. Anyway, these specimens are characterized by similar aspect ratios and they present vary close values of shear deformations.

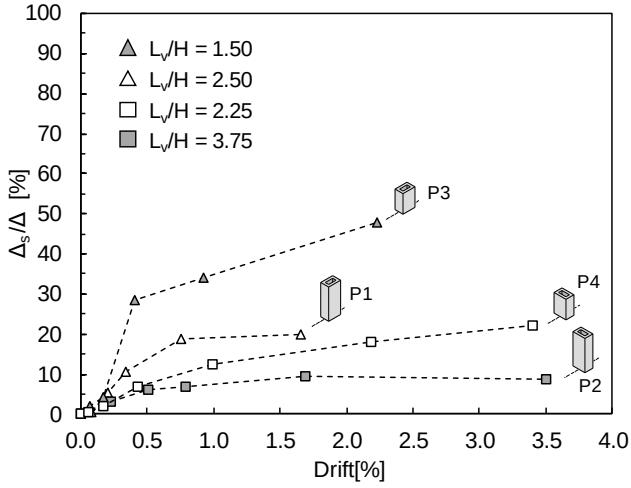

Figure 4.15. Shear deformability contributions for all Tests

Finally, it is very interesting to observe the averaged experimental deformability contribution to total displacement ratios between push and pull direction (Figure 4.16), in order to draw up some conclusions about their trends. It is possible to note an almost constant trend of shear contribution (Δ_s/Δ) after yielding, characterizing both ductile specimens; for the specimens interested by a shear failure, a clear linear increasing trend with the drift demand is otherwise observable.

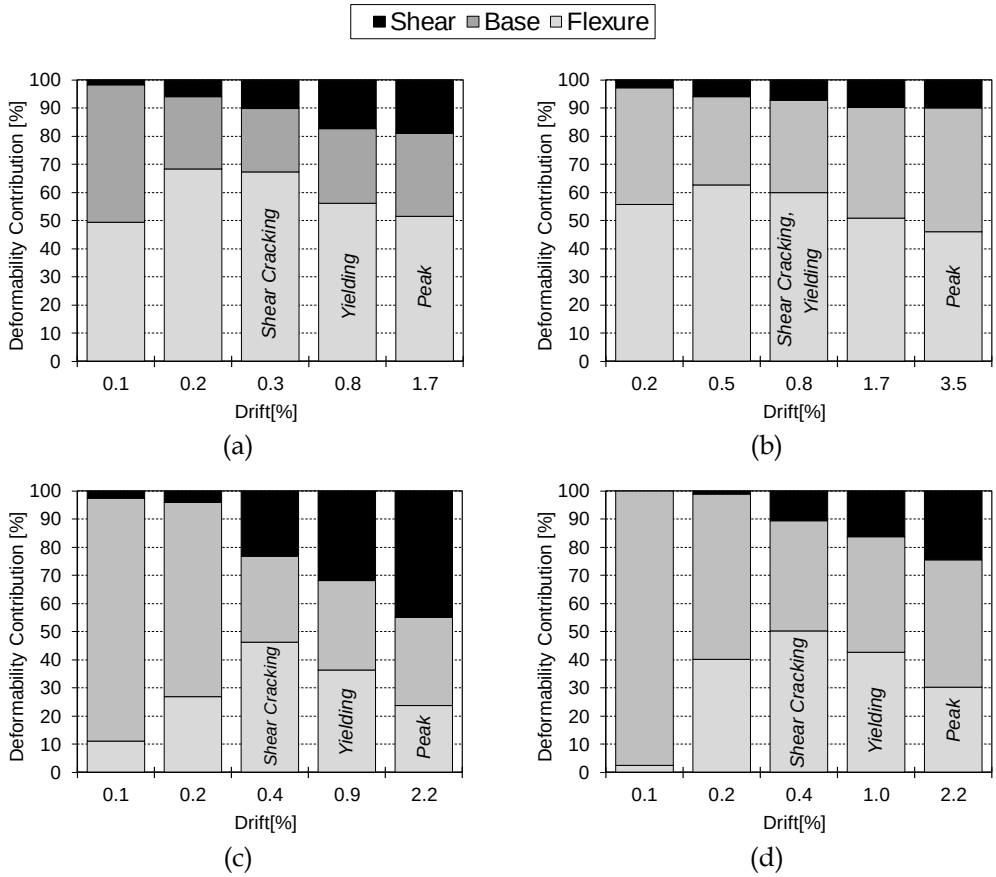

Figure 4.16. Averaged deformability contributions for Tests P1(a), P2(b), P3(c), P4(d)

4.4 Dissipated energy and equivalent viscous damping

The hysteretic energy dissipated by the presented tests is shown and analyzed, and equivalent viscous damping is estimated. First, the dissipated energy, calculated as the area underneath the experimental lateral force-

displacement curve, is shown in Figure 4.17 for all the tests, with increasing drift. In particular, Figure 4.17a reports the cumulative dissipated energy, whereas Figure 4.17b shows the energy dissipated in each cycle.

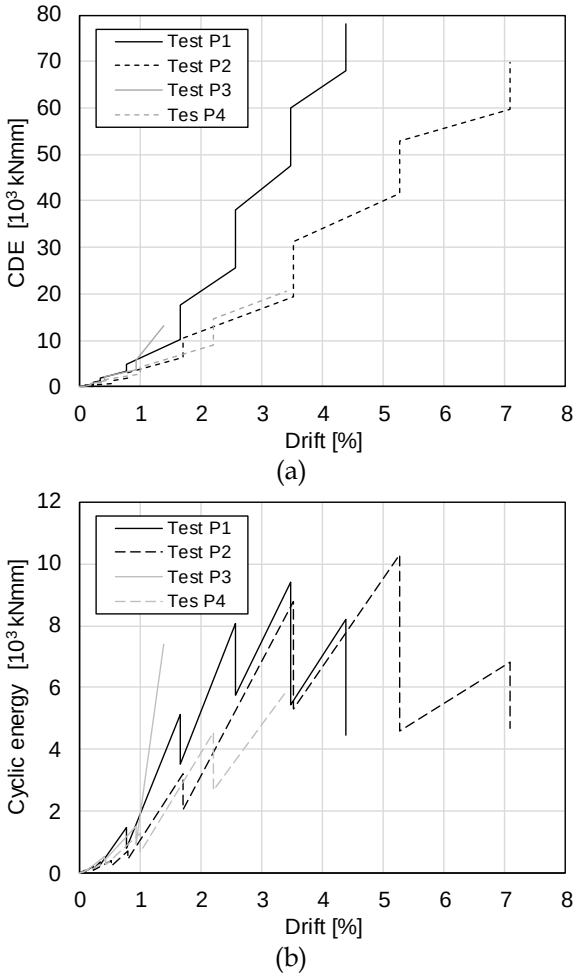

Figure 4.17. Hysteretic energy dissipation: cumulative dissipated energy (a), energy dissipated in each cycle (b)

It can be noted that total cumulative dissipated energy (CDE) evolution is very different between specimens. Of course, the considerations reported below are influenced by the different strength of the specimens. The specific energy dissipation capacity will be evaluated later, through the equivalent damping ratios. As expected, ductile Tests P1 and P2 are characterized by a higher hysteretic energy dissipation capacity respect to Tests P3 and P4,

interested by a shear failure after yielding. In particular, assuming a loading direction, for Test P1 total CDE is about six times that related to Test P3, while Test P2 shows a total CDE equal to 3.5 times that of Test P4. In a comparison between shorter specimens, Test P4 shows a higher CDE, of about 60%, respect to Test P3, since shear failure occurred for a larger drift value, after that peak value of lateral force was reached. With regard to cumulative dissipated energy evolutions, it is possible to note that CDEs are very similar in the specimens, for drift values lower than 0.8%. Starting from this drift value, CDE of Test P1 is higher respect to others specimens. In fact, given equal drift, Test P2 shows a cumulative dissipated energy varying between 35% and 60% compared to Test P1. This because, on one side the former was tested along the minimum stiffness direction, so lower values of horizontal reaction (up to 35%) during pre-peak phase, on the other side, during post-peak phase it was characterized by a larger strength and stiffness degradation. Similar consideration for tests P3 an P4, with the former that shows higher values of CDE (given equal drift, between 20% and 31%).

Another interesting way to deal with the experimental dissipated energy is through the evaluation of the equivalent damping ratio ξ_{eq}, often adopted in literature to normalize the dissipated energy (Priestley et al., 2007). The equivalent viscous damping accounts for both elastic damping and energy dissipation due to hysteresis in nonlinear response caused by the inelastic deformations of the structure. This coefficient is widely used in displacement-based seismic design or assessment (as in our case, for existing structures, e.g. Cardone (2014)), together with a stiffness secant to the performance point of interest (Priestley et al., 2007). Basically, the value of the equivalent viscous damping ratio can be defined as the sum of elastic and hysteretic damping, according to Eq. (4.5).

$$\xi_{eq} = \xi_{el} + \xi_{hyst} \tag{4.5}$$

The hysteretic damping ξ_{hyst} can be obtained equating the energy dissipated by a linear viscous damper with the energy dissipated from nonlinear behavior. According to this definition, the equivalent viscous damping is evaluated herein for each test. First of all, each cycle *i* can be identified through a maximum value and a minimum value of lateral load (V_i^+ and V_i^-, respectively), and a maximum value and a minimum value of top

displacement (Δ_i^+ and Δ_i^-, respectively). The lateral load $\bar{V}_i$ is defined as the mean between V_i^+ and V_i^-, and the displacement $\bar{\Delta}_i$ is defined as the mean between Δ_i^+ and Δ_i^-. Then, the equivalent damping at each cycle $\xi_{eq,i}$ is calculated as function of the energy dissipated in each cycle $E_{h,i}$ (area within one complete cycle of stabilized force-displacement response), according to Eq. (4.6):

$$\xi_{eq,i} = \frac{1}{2\pi} \cdot \frac{E_{h,i}}{\bar{V}_i \cdot \bar{\Delta}_i} \tag{4.6}$$

In literature, several expressions have been developed to provide such a coefficient as a function of the displacement ductility (μ), based on different hysteretic models. Generally, ignoring the period dependency, the equations have a common functional form (Blandon and Priestley, 2005), reported in Eq. (4.7):

$$\xi_{eq} = \xi_0 + a \cdot \left(1 - \frac{1}{\mu^{\beta}}\right) \tag{4.7}$$

where ξ_0 is the initial viscous damping (usually equal to 0.05 for RC structures), μ is the ductility, a and β are coefficient based on the hysteretic model adopted. For RC bridge piers, as indicated by Blandon and Priestley (2005) and Kowalsky et al., (1995), the evaluation of the equivalent viscous damping ξ_{eq} has to be computed by assuming a modified "thin" Takeda hysteresis model (with "narrow" loops) in which the unloading coefficient is taken equal to 0.5 and the post-yield stiffness ratio is assumed to be 5%. Under these assumptions, coefficients a and β in Eq. (4.7) are equal respectively to 95/π and 0.5, as reported in Priestley (2003), leading to Eq. (4.8):

$$\xi_{eq} = 5 + \frac{95}{\pi} \cdot \left(1 - \frac{1}{\mu^{0.5}}\right) \tag{4.8}$$

In order to perform a comparison between experimental and predicted viscous damping ratios, herein, for each specimen, the equivalent damping is computed as a function of the displacement ductility (μ). μ is defined as the

ratio between the maximum imposed displacement in each cycle and the yielding displacement (Δ_y). The latter is obtained through a bi-linearization of the experimental envelope according to EC8-1 (Annex B.3), by imposing the equal-area rule until the lateral peak load is reached. Then, a non-linear least square regression is performed to obtain the best-fit to the experimental results for the parameters a and β, assuming the functional form reported in Eq. (4.7) with initial damping $\xi_0 = 5\%$. The resulting expression (Eq. (4.9)) is depicted in Figure 4.18 together with Eq. (4.8).

$$\xi_{eq} = 5 + \frac{50}{\pi} \cdot \left(1 - \frac{1}{\mu^{2.9}}\right) \tag{4.9}$$

On average, quite similar values are observed, but the experimental fitting is characterized by a steeper increasing trend of the equivalent viscous damping for lower ductility values (namely, for μ up to about 4), and a quasi-constant trend for higher ductility levels. The obtained results seem to highlight a lower energy dissipation capacity with respect to the "thin" Takeda model hypothesis in large inelastic field. Finally, note that the equivalent damping–displacement ductility relationship is strongly influenced by the yielding displacement, and, therefore, by the approach followed in its calculation.

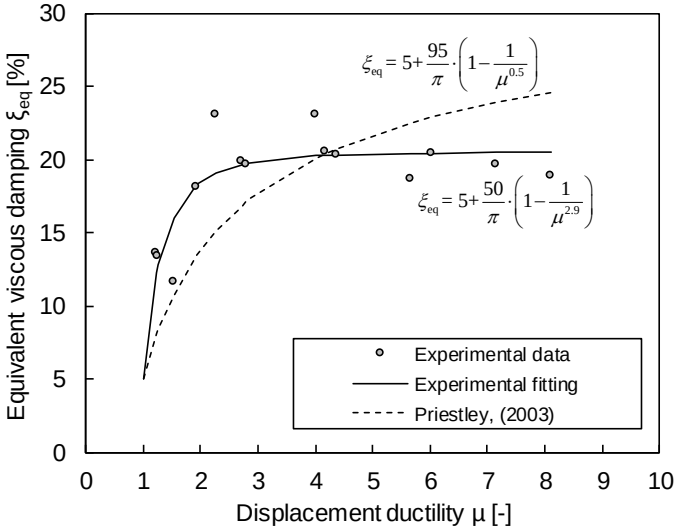

Figure 4.18. Equivalent damping-displacement ductility relationship

4.5 Comparison between experimental results and code-based capacity models

In this section, the experimental responses of the tests P1, P2, P3, and P4, are compared with code-based capacity models. In particular, the aim of such a comparison is to evaluate the capability of relevant code-based shear strength models in prediction the experimental failure modes and the shear capacity (for specimens failing in shear). As deeply discussed in section 2.3, for an adequate assessment of existing RC members, it is crucial the classification, i.e. the prediction of the failure mode, in order to plan, eventually, suitable retrofitting systems. As described in section 4.1, based on experimental evidence and observed damage, two tests (P1 and P2) were characterized by a flexure-controlled failure mode (F-mode), and the remaining two (P3 and P4) by a shear failure following flexural yielding (FS-mode), hence due to shear strength degradation in post-elastic field. In the following, the capability of main shear strength capacity models from code and literature in predicting such failure modes will be evaluated. The considered models have been described in detail in section 2.3.3. Therefore, they're briefly recalled below:

- FHWA: the model adopted by the U.S. Federal Highway Administration provisions document for seismic retrofitting of bridges (FHWA, 2006) corresponds to the model proposed by Kowalsky and Priestley, (2000)
- EC8/3: the model adopted by the Eurocode 8 – part 3 (EC8/3, 2005) corresponds to the model proposed by Biskinis et al., (2004)
- C617: the model suggested by the Italian Code (Circolare 617, 2009) for the assessment of shear capacity of bridge columns is a slightly modified version of the Original UCSD model (Priestley et al., 1994). A 45° instead of a 30° angle truss mechanism is assumed, and the degradation coefficient is assumed to vary between 0.29 and 0.10 for displacement ductility between 1 and 4

Note that the degrading shear strength models considered herein require the estimation of the expected displacement at yielding, in order to evaluate the displacement ductility, which should be evaluated consistent with the procedures proposed or adopted by the respective Authors. Hence, when applying the C617 and the FHWA models, the expected displacement at yielding is estimated as reported in Priestley et al. (1996):

$$\Delta_y = \frac{\phi_y^*}{3}\left(L_V + 0.022 f_y d_b\right)^2 \tag{4.10}$$

where ϕ_y^* is the curvature at the corner of a bilinear envelope of the moment-curvature relationship (Priestley et al., 1996), L_V is the shear span, f_y is the steel yielding strength and d_b is the diameter of the longitudinal bars. When applying the EC8/3 model, the expected displacement at yielding is estimated as reported in Biskinis and Fardis (2010):

$$\Delta_y = \left(\frac{\phi_y L_V}{3} + 0.0013 + \frac{\phi_y f_y d_b}{8\sqrt{f_c}}\right) L_V \tag{4.11}$$

where, ϕ_y is the curvature at first yielding and f_c is the concrete compressive strength. As discussed in section 2.3.1, the behavior of a RC element can be classified based on the ratio between plastic shear capacity and degrading shear strength. For this reason, it is necessary the evaluation of the plastic load for the specimens. The following Table 4.6 reports a comparison between observed and predicted lateral loads at first yielding (V_y) and at maximum (V_{max}), based on corresponding moments M_y and M_{max} evaluated on the basis of a section analysis, assuming the Mander et al. (1988) stress-strain model for concrete, and elastic-plastic with strain hardening stress-strain relationship for steel.

Test ID	*Experimental*				*Analytical*		*(Anal. - Exp.) / Exp.*	
	V^+_y (kN)	V^-_y (kN)	V^+_{max} (kN)	V^-_{max} (kN)	V_y (kN)	V_{max} (kN)	yielding (%)	peak (%)
P1	132.1	-116.4	168.3	-164.4	121.6	167.7	4.5	-0.4
P2	89.3	-87.3	116.6	-115.2	79.2	110.3	-9.3	-5.4
P3	255.9	-211.4	277.7	-240.6	202.7	279.4	-4.1	-
P4	152.3	-149.2	193.0	-187.5	132.0	183.9	-11.5	-

Table 4.6. Yielding and peak lateral load: experimental vs analytical comparison

A moderate underestimation, on average equal to 5%, is observed between the calculated V_y and the corresponding experimental value (minimum between positive and negative) assumed as corresponding to the attainment of

yielding strain in longitudinal reinforcement; a similar underestimation, on average equal to 3%, is observed for V_{max} (maximum between positive and negative). Note that such a comparison should be carried out mainly for P1 and P2 tests, since in tests P3 and P4 the development of flexural over-strength might have been at least partially prevented by the occurrence of shear failure.

On that note, the predicted failure mode can be derived by comparing the analytical value of the yielding (V_y) and peak lateral load (V_{max}) with the maximum (non-degraded) and minimum shear strength values, as reported in Table 4.7. The same procedure is depicted in Figure 4.19 and Figure 4.20 in terms of shear strength envelopes an experimental response.

Test ID	*Analytical*		*FHWA*			*C617*			*EC8/3*			*Exp*
	V_y (kN)	V_{max} (kN)	Max (kN)	Min (kN)	FM	Max (kN)	Min (kN)	FM	Max (kN)	Min (kN)	FM	FM
P1	122	168	260	174	F	266	166	FS	128	101	FS	F
P2	79	110	205	120	F	228	127	F	78	62	S	F
P3	203	279	327	199	FS	282	182	FS	150	121	S	FS
P4	132	183	216	130	FS	238	138	FS	96	77	S	FS

Table 4.7. Predicted and observed lateral loads corresponding to flexural strength at yielding and maximum and failure mode

As observed, the FHWA model (FHWA, 2006) shows a very good capacity of failure mode prediction; similarly, except for the Test P1, C617 model (Circolare 617, 2009) shows a good capacity of failure mode prediction, too; a lower predictive capacity is observed for EC8/3 model (EC8/3, 2005), due to the conservatism in model predictions. Note that this model was applied assuming the formulations providing shear strength in the case of diagonal tension failure, which generally controls the shear failure. Strictly speaking, the displacement ductility capacity of RC members failing in shear should not be evaluated from the inverse application of the shear strength model because this would not lead to a reliable evaluation of the drift at shear failure (Biskinis et al., 2004). Vice-versa, it is possible to evaluate the predicted degraded shear strength corresponding to the observed ductility at failure. Therefore, for Tests P3 and P4, showing a shear failure following flexural yielding, Table 4.8 reports the failure mode and the shear strength capacity predicted by the considered models (as described, the latter is evaluated corresponding to the

observed ductility at failure if a FS failure is predicted, otherwise as the non-degraded shear strength if a S failure is predicted).

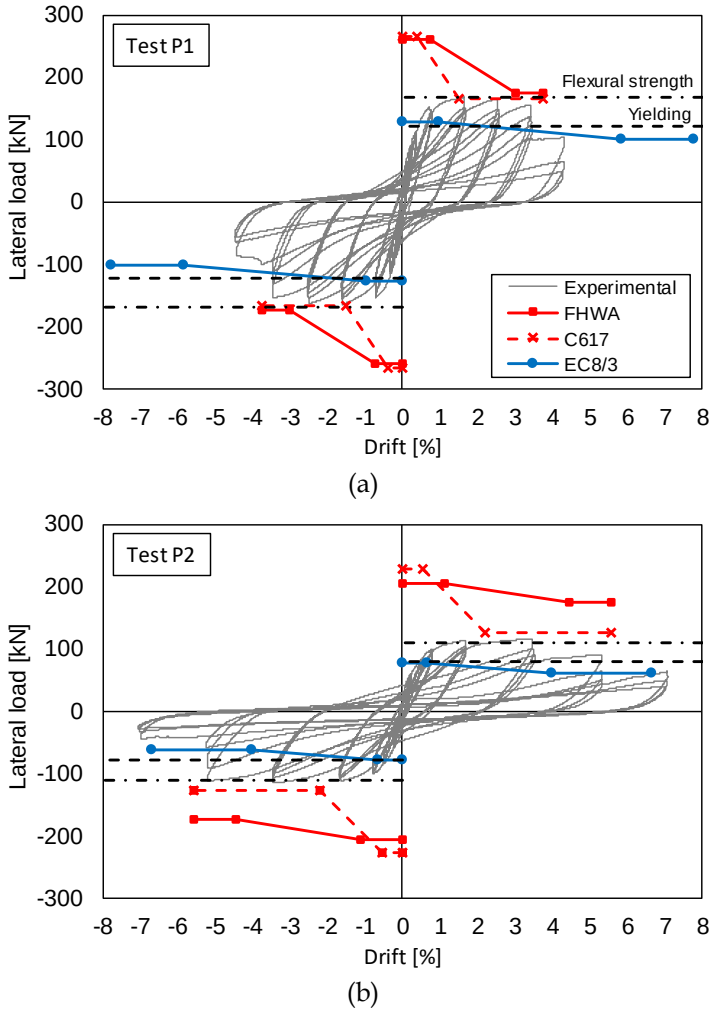

Figure 4.19. Experimental lateral load-drift responses and shear strength envelopes predicted according to the considered capacity models for tall specimens

The displacement at failure (see Table 4.1) is evaluated as the displacement corresponding to 20% strength decay on the envelope of the experimental lateral load-drift response, for the EC8/3 model, whereas, for the remaining models, it is assumed as that corresponding to the maximum load. The corresponding ductility values are calculated depending on the displacement at yielding evaluated consistent with each model.

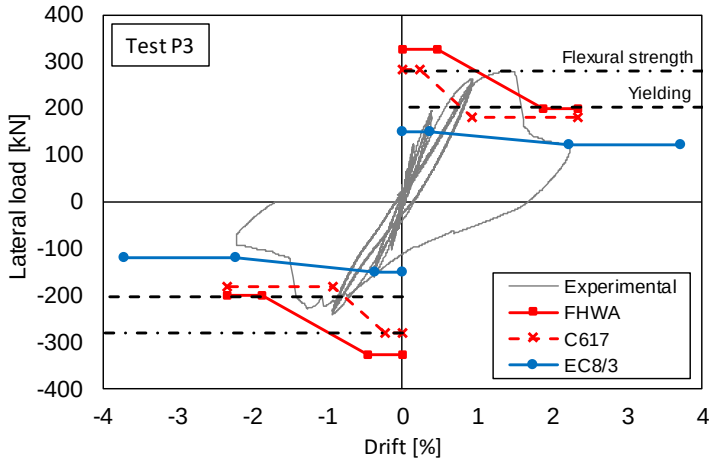

(a)

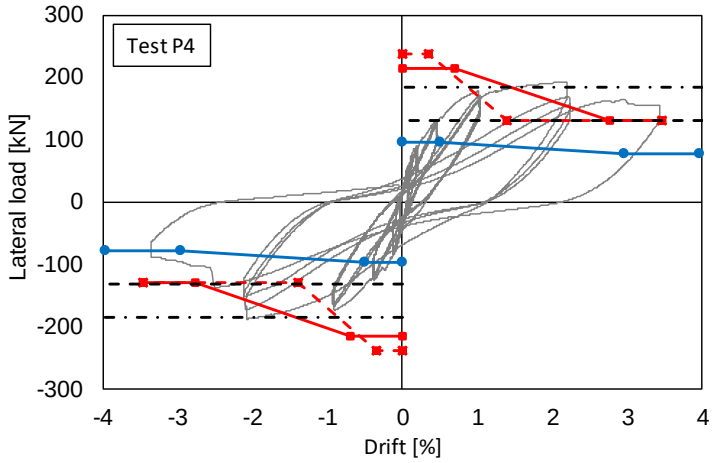

(b)

Figure 4.20. Experimental lateral load-drift responses and shear strength envelopes predicted according to the considered capacity models for short specimens

Test ID	Experimental			FHWA				C617				EC8/3	
	Failure Mode	V_{max} (kN)	D_u (%)	FM	D_y (%)	μ (-)	V_R (kN)	FM	D_y (%)	μ (-)	V_R (kN)	FM	V_R (kN)
P3	FS	279	1.50	FS	0.37	4.05	232	FS	0.37	4.05	182	S	150
P4	FS	183	2.53	FS	0.50	5.06	140	FS	0.50	5.06	138	S	96

Table 4.8. Predicted failure mode and shear strength for Tests P3 and P4

In terms of shear strength evaluation, the quite good predictive capacity of

FHWA and C617 models is not confirmed by the results reported in Table 4.8. In fact, a quite large shear strength underestimation of 20% is highlighted on average for the specimens; vice-versa, the EC8/3 model confirm the low predictive capacity, underestimating the experimental shear strength by about 50%.

4.6 Load-deformation numerical modelling

As outlined in section 2.3.2, several models are available in literature to simulate the actual behavior of structures. Generally, the response of RC columns subjected to lateral load can be interpreted as the results of three coexisting mechanisms: flexure deformation, shear deformation, and fixed-end-rotation due to longitudinal bar slip at column base. While for columns with height-to-depth ratio higher than 4 the shear flexibility can be neglected, the latter has to be computed for columns characterized by medium-low aspect ratio. This is confirmed also by the experimental measures presented in section 4.3.2, which highlight considerable shear deformations for all the tests.

In this section, a load-deformation numerical model is analyzed and applied, in order to reproduce the experimental response of the test specimens P1, P2, P3, and P4, described in the section 4.1. The main goal is the monotonic modelling of the experimental response, and, in particular, the assessment of the local deformability contributions reported in the section 4.3.2. To this aim, a three-component model is adopted, in which the three mechanisms characterizing the lateral response of RC columns are separately modelled.

4.6.1. Numerical model

In this section, the adopted three-component model is described and analyzed, focusing on details and formulations, in order to provide the background for the understanding of the analysis results.

Flexural deformation

The flexural response is modelled with a displacement-based (DB) nonlinear beam-column fiber element with distributed plasticity, available in OpenSees (McKenna et al., 2011), with five Gauss-Lobatto integration points. The cross section has been divided into 6400 concrete fibers. In addition, 28 steel fibers have been used to model the longitudinal reinforcement (see Figure

4.21). Two different stress-strain relationships have been used to describe the mechanical behavior of concrete and steel, and then assigned to the corresponding fibers of the column model. Since the specimens were characterized by the absence of reinforcement details (no tie between opposite longitudinal bars, 90° hooks, high spacing between stirrups), unconfined concrete is assumed for all concrete fibers. The mechanical behavior of unconfined concrete has been modelled with the law by Popovics (1973). The constitutive model by Giuffré-Menegotto-Pinto (1973) has been adopted for steel.

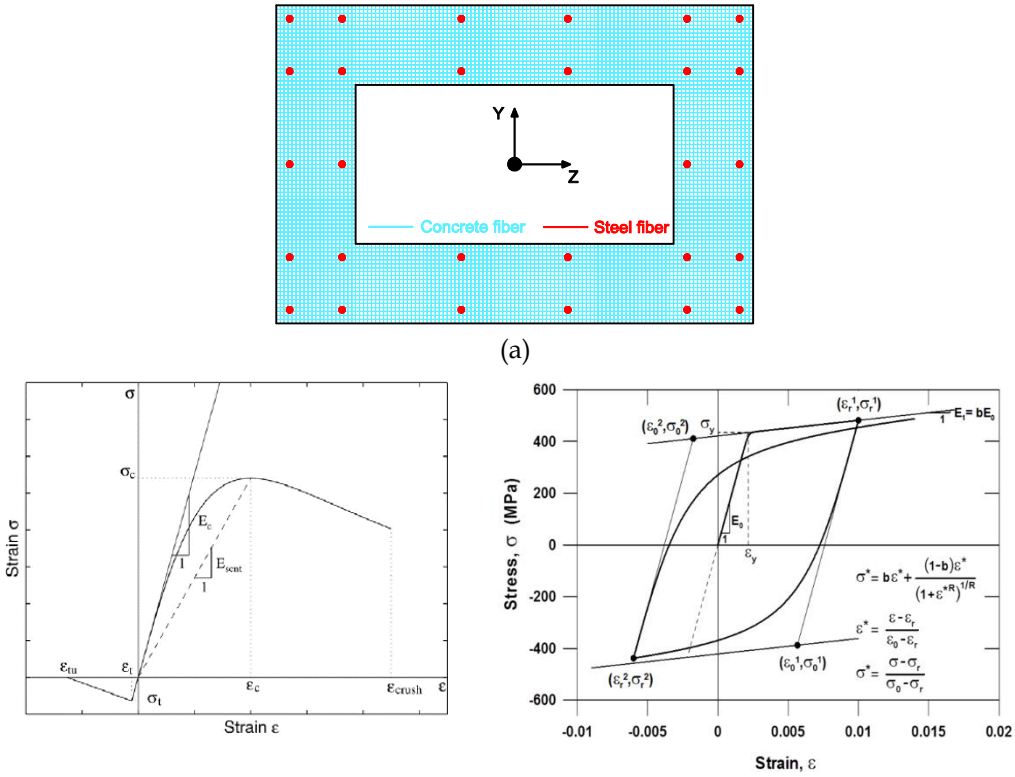

Figure 4.21. Fiber discretization of the transverse cross-section (a) and constitutive laws for concrete (b) and steel (c)

All the previously mentioned stress-strain relationships have been calibrated based on the experimental results of the characterization tests carried out on the specimens collected during the construction of the piers (see

the section 3.4). In Figure 4.22 the predicted moment-curvature relationships are reported for all the specimens, with the comparisons between experimental and predicted values of cracking, yielding and peak moment. The experimental yielding moments are well predicted by the fiber section analysis, with slight overestimation for tests P2 and P4. Slightly less rigorous are the predictions of the flexural cracking moment, with a mean error, evaluated as the predicted-to-experimental cracking moment ratio, equal to 85%.

The peak loads are well predicted for tests P1 and P2, subjected to flexural failure. For tests P3 and P4, the experimental peak values are lower than the predicted ones, since shear failure occurred before reaching of the flexural capacity.

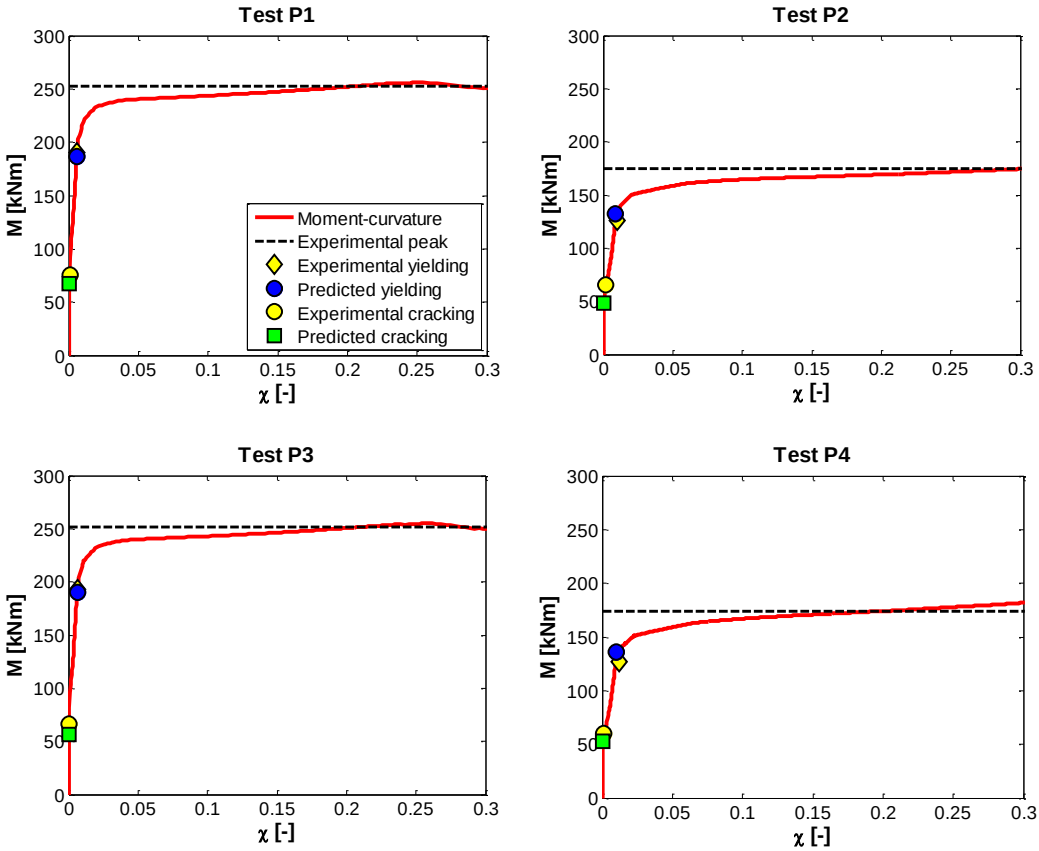

Figure 4.22. Moment-curvature predictions compared with experimental results

Shear deformation

The shear flexibility of the test specimens up to the peak force is accounted through the procedure proposed by Krolicki et al. (2011). This procedure was initially presented by Park and Paulay (1975). Later it was improved by Miranda et al. (2005), updated by Priestley et al. (2007), and, finally, revised by Krolicki et al. (2011). In particular, Krolicki et al. (2011) applied the procedure to obtain the lateral response of reinforced concrete walls. According to this approach, the calculation of shear deformation is carried out assuming a multilinear response. In particular, starting from the fiber moment-curvature (M,χ) relationship for the base critical section, four phases are identified, each one characterized by a different shear stiffness. They are listed below.

Shear response prior to flexural cracking ($M \le M_{f,cr}$)

Shear stiffness of uncracked column is assumed as that given by Park and Paulay (1975):

$$k_{se} = \frac{GA_v}{H};\ \ A_v = 2 \cdot t_w \cdot d \tag{4.12}$$

where, G is the shear elastic modulus, A_v is the effective shear area, t_w and d represent thickness and effective depth of the cross section, respectively, the latter assumed as 0.8 times cross-sectional height (H). The corresponding displacements are computed as:

$$\Delta_{se} = \frac{M_{f,cr}}{k_{se} L_V};\ \ 0 \le M \le M_{f,cr} \tag{4.13}$$

where, $M_{f,cr}$ is the moment at flexural cracking and L_V is shear span.

Shear response after flexural cracking ($M_{f,cr} \le M \le M_{s,cr}$)

Shear stiffness prior to shear cracking is approximately proportional to the reduction in flexural stiffness, taken as:

$$k_{sf} = \frac{GA_v}{H} \cdot \frac{EI_{eff}}{EI_g};\ \ EI_{eff} = \frac{M_y}{\chi_y} \tag{4.14}$$

where, E is concrete Young's modulus, I_g and I_{eff} are the inertia moment of uncracked and cracked section, respectively, M_y and χ_y are yielding moment and curvature, respectively. The corresponding displacements are computed as:

$$\Delta_{sf} = \frac{(M - M_{f,cr})}{k_{sf} L_V}; \quad M_{f,cr} \le M \le M_{s,cr} \tag{4.15}$$

in which $M_{s,cr}$ is the measured moment at shear cracking.

Shear response after shear cracking ($M_{s,cr} \le M \le M_y$)

Shear stiffness after onset of diagonal cracking is based on an equivalent strut-and-tie model, incorporating both the compression of the diagonal strut, and the extension of the tie representing the transverse reinforcement:

$$k_{s,sc} = \frac{\rho'' \sin^4(\theta) \cot^2(\theta)}{\sin^4(\theta) + 10\rho''} E_s \cdot 2t_w \cdot d \tag{4.16}$$

In equation (4.16), ρ'' is transverse reinforcement ratio, θ is the measured angle between diagonal cracks and member axis, E_s is steel Young's modulus, and d is the effective depth. The corresponding displacements are computed as reported in eq. (4.17)

$$\Delta_{sc} = \frac{(M - M_{s,cr})}{k_{s,sc} L_V}; \quad M_{s,cr} \le M \le M_y \tag{4.17}$$

Shear response after flexural first yield ($M_y \le M \le M_{max}$)

In the post-yield phase the concrete compression struts will continue to soften, and thus shear deformation will continue to increase. Therefore, after flexural first yield the shear deformation increases proportional to the flexural deformation:

$$\Delta_{sc} = \Delta_f \frac{\Delta_{s,sc}}{\Delta_{f,y}}; \quad M_y \le M \le M_{max} \tag{4.18}$$

where $\Delta_{f,y}$ is the top flexural lateral displacement corresponding to first yielding moment, $\Delta_{s,sc}$ is top shear displacement corresponding to first yielding moment (computed according to eq. 4.17), Δ_f is top flexural displacement. A scheme of the adopted shear response is depicted in Figure 4.23.

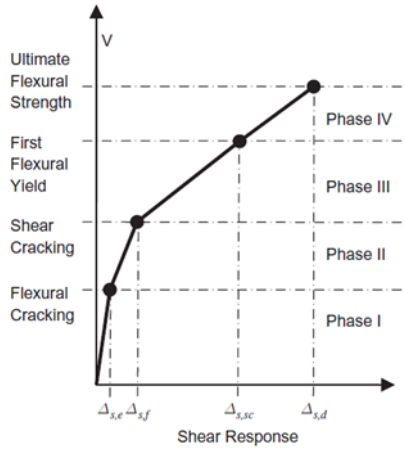

Figure 4.23. Lateral load-shear displacement response – adapted from Krolicki et al., (2011)

In Figure 4.24 the predicted relationships between lateral-load and shear-displacement are reported for all the specimens, together with the characteristic point of the lateral response, namely, flexural cracking, shear cracking, flexural yielding and peak load. All the plots are reported with the same axis limits, in order to carry out a comparison of the results between specimens. The predicted response is assessed starting from the moment-curvature analysis: for each of the four above-described phases, the moment values are placed in equations (4.13 – 4-15 – 4.17 – 4.18), and the corresponding displacement is computed.

As expected, the shear deformability is very low for the slenderest specimen P2, while it is almost similar for the remaining specimens. For all the specimens, the shear stiffness is very high up to diagonal cracking onset, with a behavior almost rigid up to first flexural yielding. After first diagonal cracking, shear deformation increases with the drift demand as a function of the measured inclination of the compressive strut, since all the other parameters of equation (4.16) are constant for all the specimens. Note that the values of lateral load (V) corresponding to first shear cracking and yielding are

very similar for test P2. For this reason, the increase of shear deformation in this range of the lateral response is almost negligible. Once yielding condition is reached, shear deformation increase proportionally with flexural deformations.

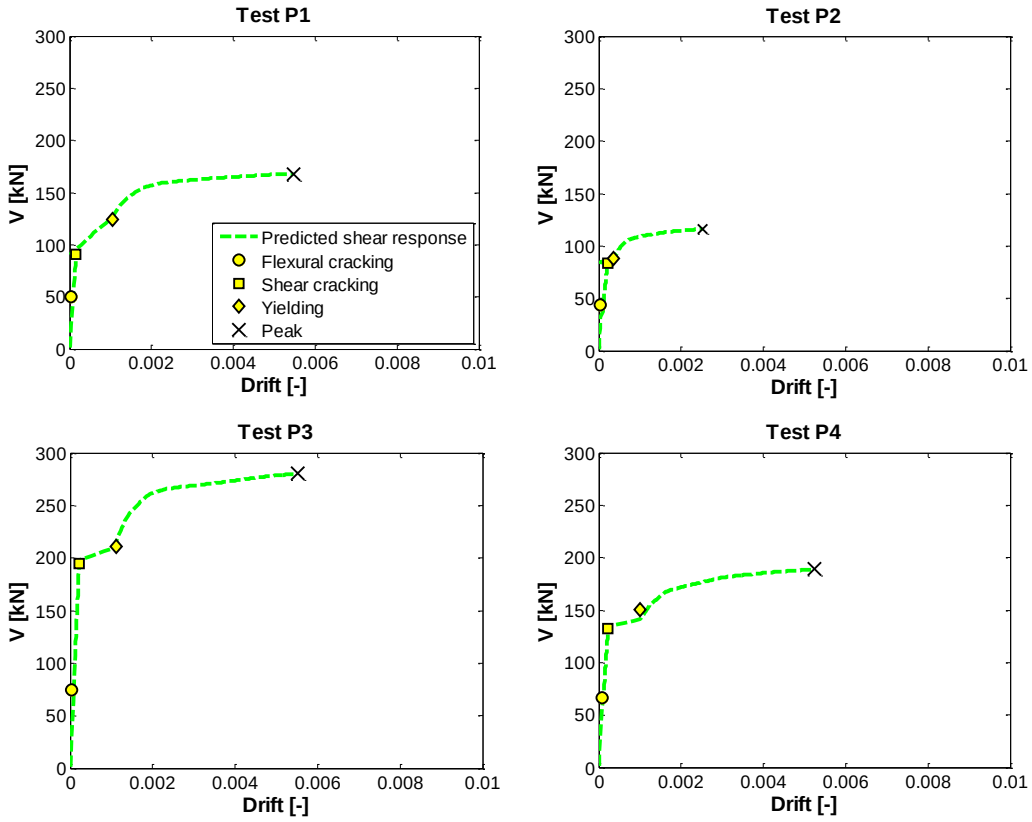

Figure 4.24. Predicted lateral load-shear displacement response

Bar slip

The longitudinal reinforcement in a reinforced concrete column with fixed ends subjected to bending may be in tension at the footing-column interface. Slip of the reinforcing bars outside the flexure length and in the anchoring concrete (that is, in the footing region) will cause rigid-body rotation of the column, additive to the rotation calculated from flexural. Sometimes, reinforcement slip in footings regions can make a significant contribution to the total lateral displacement of a reinforced concrete member; therefore,

deformations resulting from reinforcement slip have to be accounted in the member analysis.

As outlined in the section 2.3.2.3, several bar slip models are available in literature. In this study, a practice-oriented macro model is used, in lieu of complex and computationally micro models. In particular, the model by Sezen and Setzler (2008) is adopted. This model assumes a stepped function for bond stress (u_b) between the concrete and reinforcing steel over the embedment length of the bar within the foundation. Based on experimental observations (Sezen 2002), the bond stress is taken as $1.0\sqrt{f_c}$ for elastic steel strains and $0.5\sqrt{f_c}$ for inelastic steel strains for deformed bars. Under these assumptions, Authors computes the rotation due to reinforcement slip (θ_s) as reported in equation (4.19).

$$\theta_{slip} = \frac{\varepsilon_s f_s d_b}{8 u_b (d - d')} \text{ for } \varepsilon_s \le \varepsilon_y$$
$$\theta_{slip} = \frac{d_b}{8 u_b (d - d')} (\varepsilon_s f_y + 2(\varepsilon_s + \varepsilon_y)(f_s - f_y)) \text{ for } \varepsilon_s > \varepsilon_y \quad (4.19)$$

In equation (4.19): ε_s and f_s are respectively steel deformation and stress of the outermost bars layer at the column-foundation section, d_b is the longitudinal bars diameter, u_b is the assumed bond stress, ε_y and f_y are respectively steel yielding deformation and stress, d is the effective depth, and d' is the center of the compression reinforcement from the extreme compression fibers. The column lateral displacement due to reinforcement slip is equal to the product between the slip rotation and the column length L_V:

$$\Delta_{slip} = \theta_{slip} \cdot L_V \quad (4.20)$$

In Figure 4.25 the predicted relationships between moment and slip-rotation are reported for all the specimens, together with the yielding point. Also in this case, all the plots are reported with the same axis limits, in order to carry out a comparison of the results between specimens. The predicted response is assessed starting from the moment-curvature analysis: for each of the two above-described phases (namely before and after the yielding condition is reached from longitudinal bars at the base section), the moment

values are placed in equation (4.19), and the corresponding displacement is computed. The rotation due to reinforcement slip is higher for specimen P2, characterized by the higher value of aspect-ratio and whose response was dominated by flexural mechanisms. For the remaining specimens, the deformation due to slip is almoste comparable.

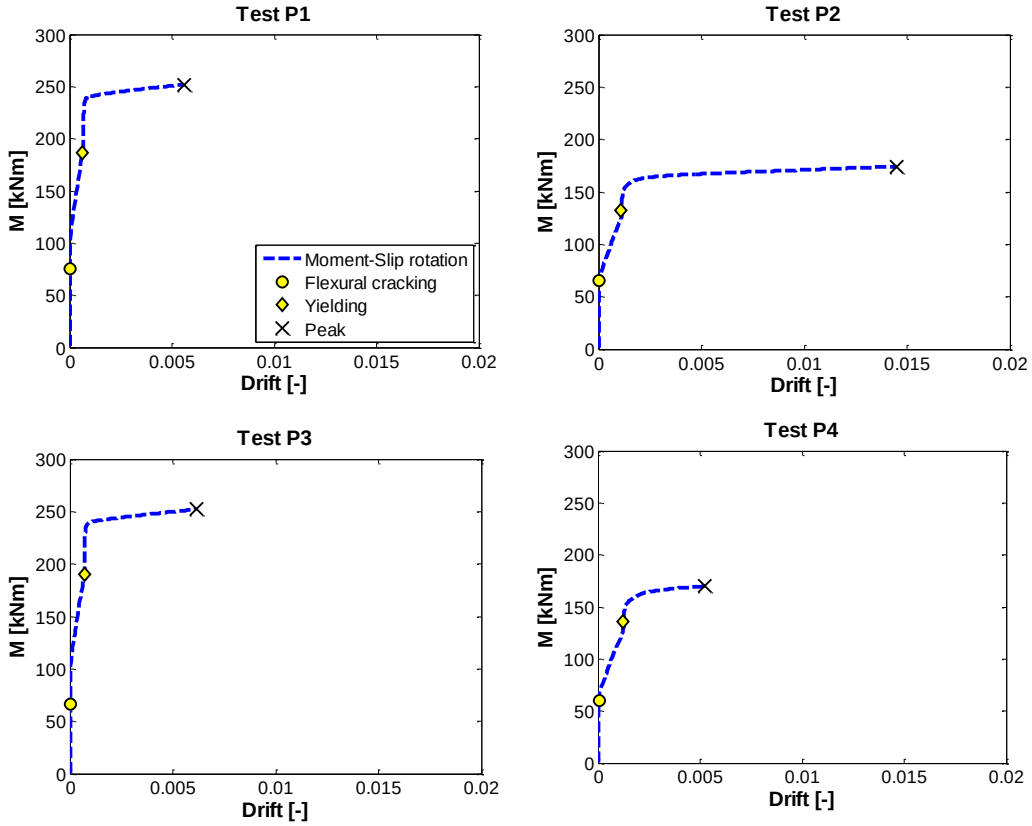

Figure 4.25. Predicted moment-slip rotation response

4.6.2. *Numerical response and comparison with experimental results*

The experimental deformability contributions can be assumed as reliable up to the peak load, due to the severe damage state characterizing the test specimens, which compromised the monitoring system (see section 4.3.2). Since, as above discussed, the main goal of the numerical analysis is to reproduce the experimental deformability contributions, the numerical lateral response is investigated up to the peak load condition, through the numerical

model defined in the previous section. A schematic view of the adopted numerical model is shown in Figure 4.26.

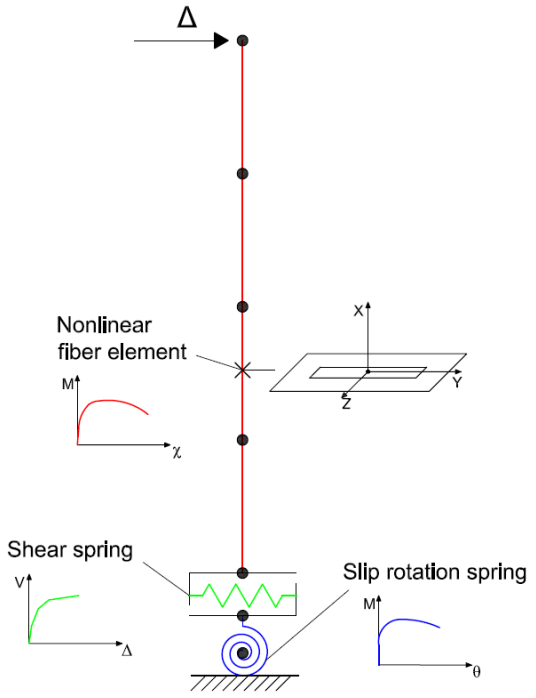

Figure 4.26. Scheme of the adopted three-component numerical model

In Figure 4.27 the monotonic predicted response is reported for each deformation component, namely flexure, shear and bar slip, together with the global response, defined as the sum of the three components. By observing Figure 4.27, the flexural component is predominant for all the specimens, particularly for test P2, with the higher aspect ratio. Regarding tests P1 and P4, characterized by similar aspect ratio, shear and bar slip contributions are close, even if, after yielding condition, the deformation due to shear damage became slightly higher. Finally, concerning test P3, on the shorter specimen, flexural and shear deformations became very similar after the shear-cracking onset.

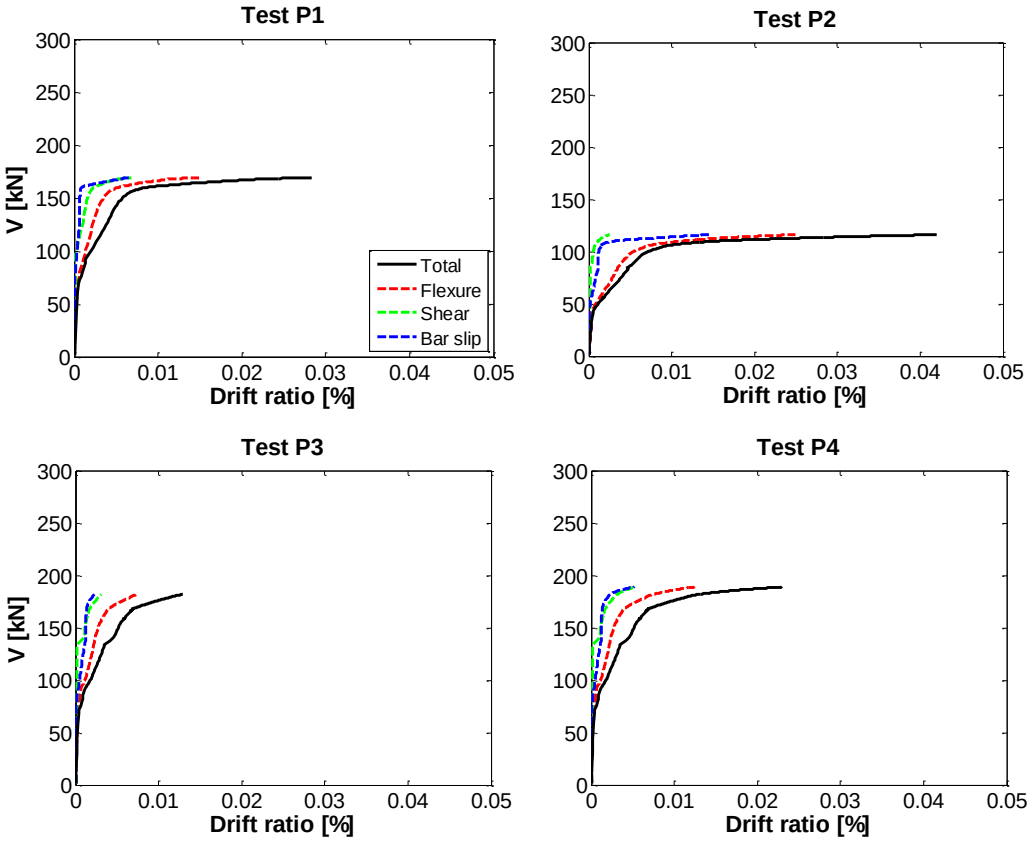

Figure 4.27. Predicted global response and flexure, shear and bar slip components

In Figure 4.28 and Figure 4.29, the monotonic numerical global response, obtained by applying the model described in section 4.6.1, is compared with cyclic experimental loops, for short and tall specimens, respectively.

The monotonic numerical model is able to well reproduce the envelope of the experimental global response up to peak condition for all the specimens. For the tests P3 and P4, subjected to flexure-shear failure, the numerical model slightly overestimates the negative peak load (namely, measured during pull phase). This is due to the experimental asymmetry caused by the shear damage state: once the peak load is reached during pushing phase, diagonal cracks formed cause degradation of strength in the reverse direction (i.e., pull direction).

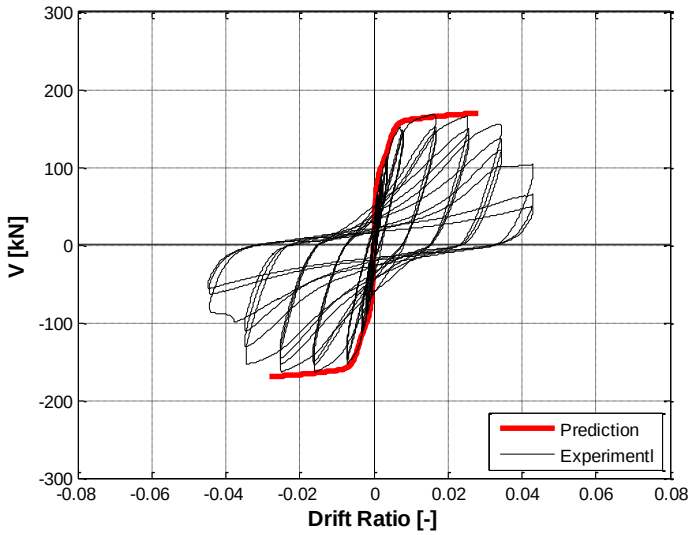

(a)

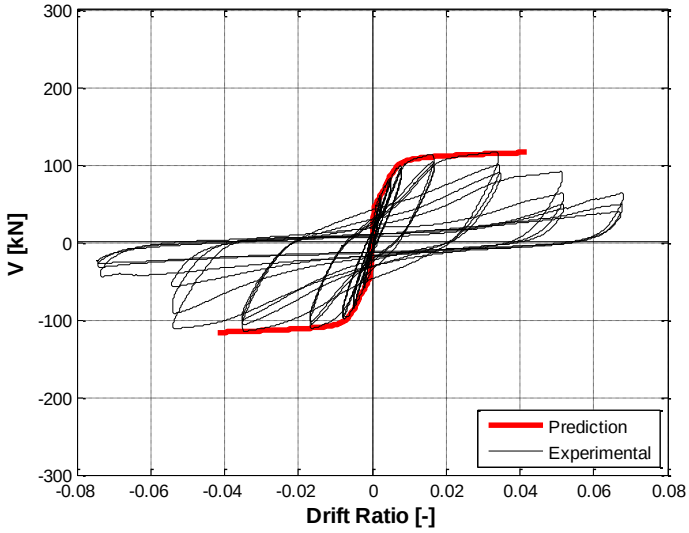

(b)

Figure 4.28. Numerical vs experimental global response for tests P1 (a) and P2 (b)

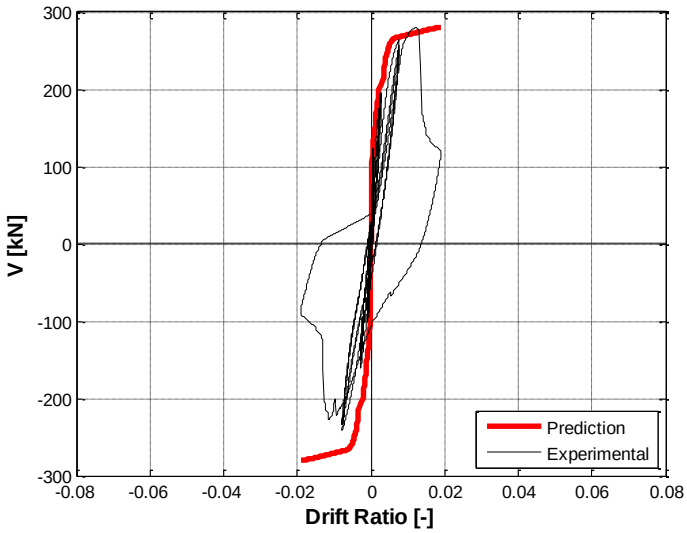

(a)

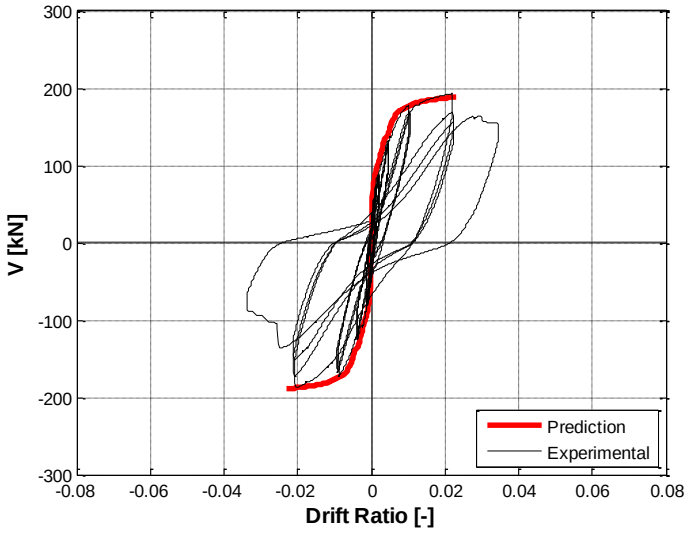

(b)

Figure 4.29. Numerical vs experimental global response for tests P3 (a) and P4 (b)

It is very interesting to compare the experimental deformability contributions with those numerically obtained. The comparison is depicted from Figure 4.30 to Figure 4.33 for all the specimens.

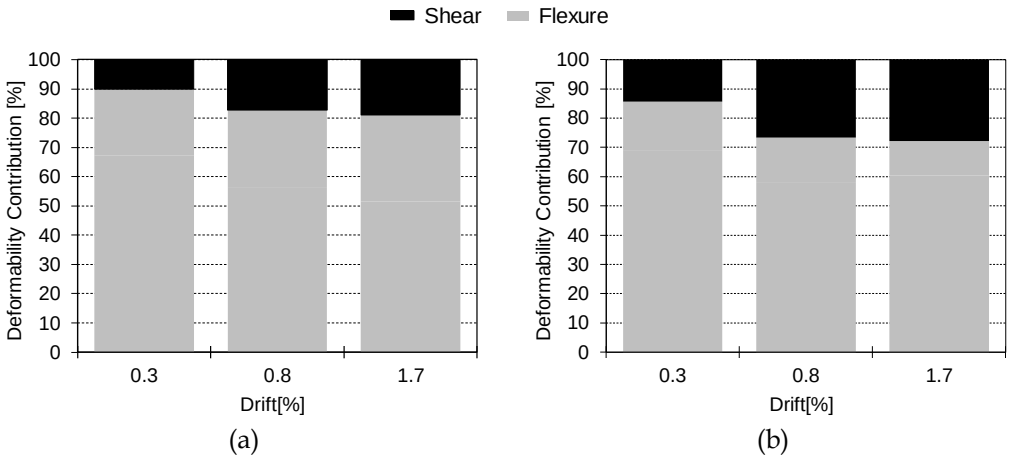

Figure 4.30. Comparison between averaged experimental (a) and numerical (b) deformability contributions Tests P1 (shear cracking, yielding, peak load)

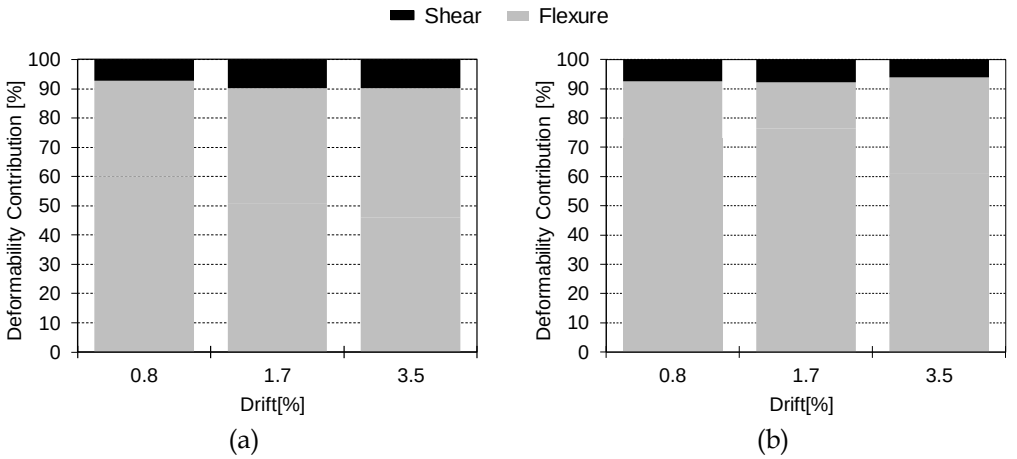

Figure 4.31. Comparison between averaged experimental (a) and numerical (b) deformability contributions for Tests P2 (shear cracking, yielding, peak load)

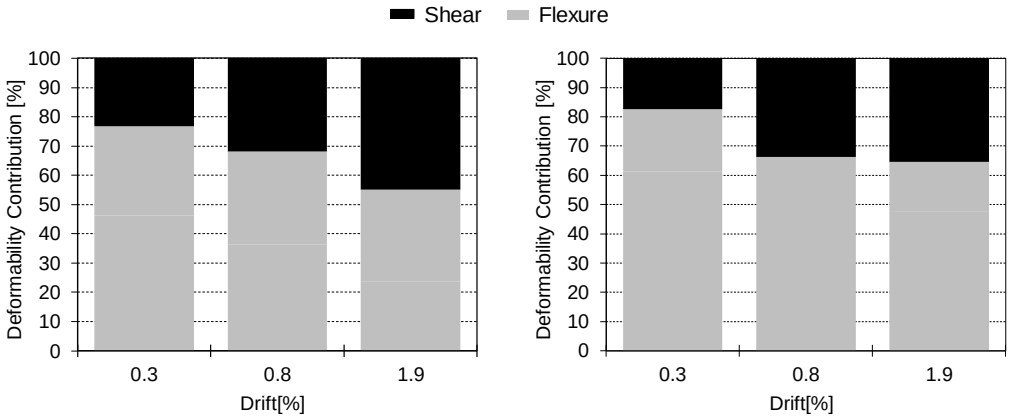

Figure 4.32. Comparison between averaged experimental (a) and numerical (b) deformability contributions for Tests P3 (shear cracking, yielding, peak load)

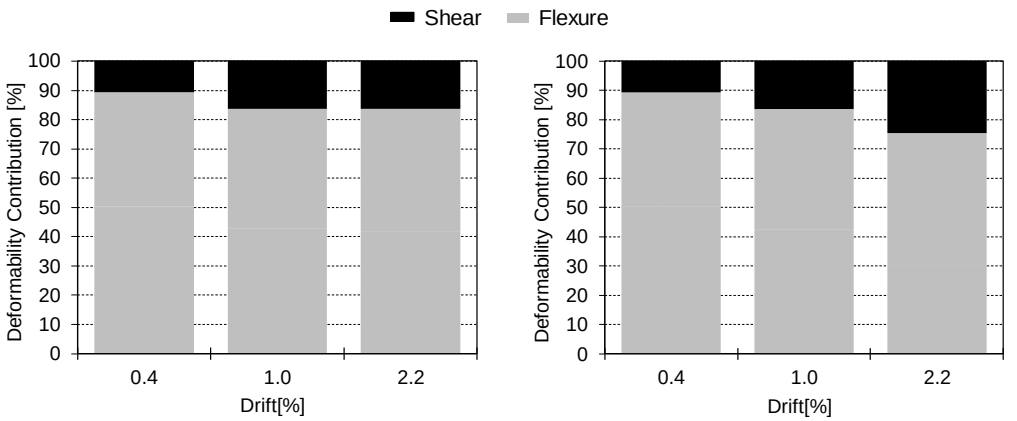

Figure 4.33. Comparison between averaged experimental (a) and numerical (b) deformability contributions for Tests P4 (shear cracking, yielding, peak load)

Note that the predicted flexural and bar slip contributions are added here into a single component. The averaged (between push and pull directions) deformability contributions are reported for the characteristic points of the experimental response: first shear cracking, yielding and peak load. The experimental mean trends of the deformability contributions to the overall imposed drift are well reproduced by the numerical model for all the specimens. In particular, the almost constant trend of the shear contribution for

the taller specimen P2 is captured by the numerical analysis. Similarly, the increasing trend of the shear contribution with the drift demand is well represented for all the other specimens.

The same comparison is depicted in Figure 4.34 in terms of experimental and predicted flexural contributions to the total lateral top displacement for all the specimens. In this case, the numerical flexural contribution accounts for both flexure and fixed-end rotation, in order to be directly compared with the corresponding experimental value. On the horizontal and vertical axis are reported the experimental and numerical flexural contribution, respectively.

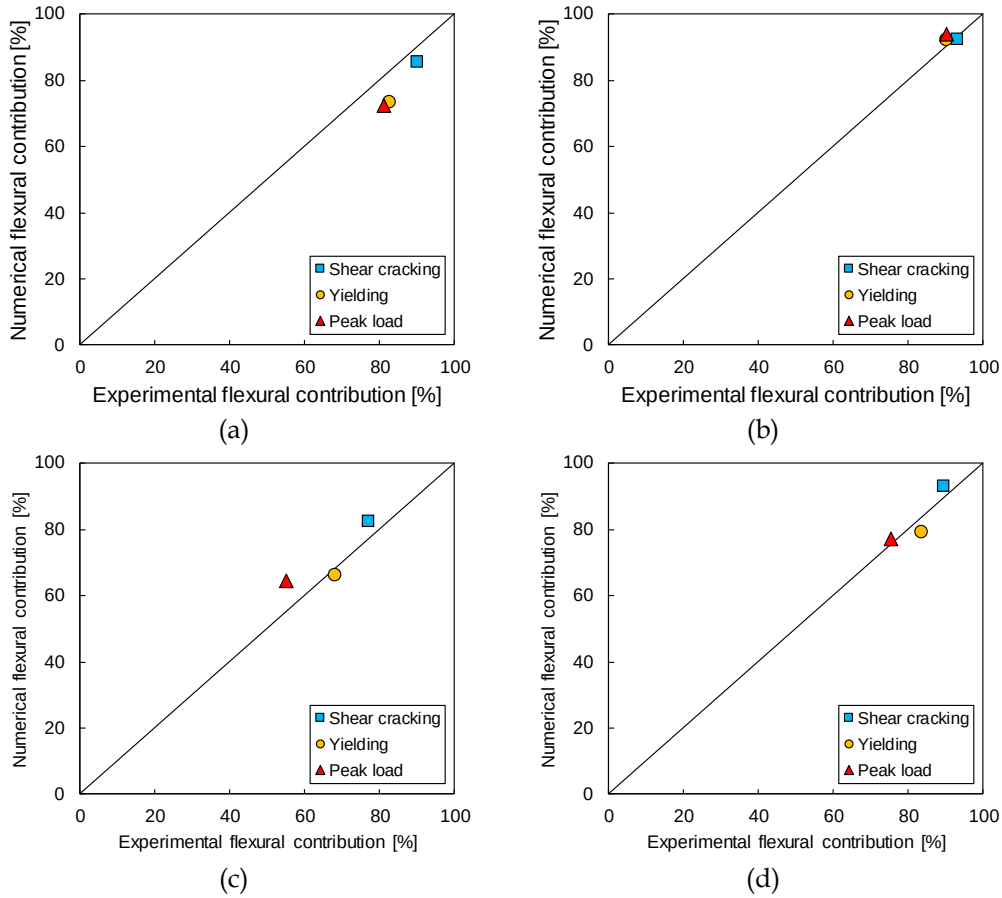

Figure 4.34. Comparison between averaged experimental (a) and numerical (b) flexural deformability contribution for Tests P1 (a), P2 (b), P3 (c), and P4 (d)

The plots of Figure 4.34 confirm the very good agreement between

experimental and numerical values: all the points are close to the bisector, highlighting an almost exact reproduction of the experimental deformability contributions. A similar comparison is depicted in Figure 4.35 in terms of shear contribution to total top displacement. Also in this case, the shear contibutions is well predicted.

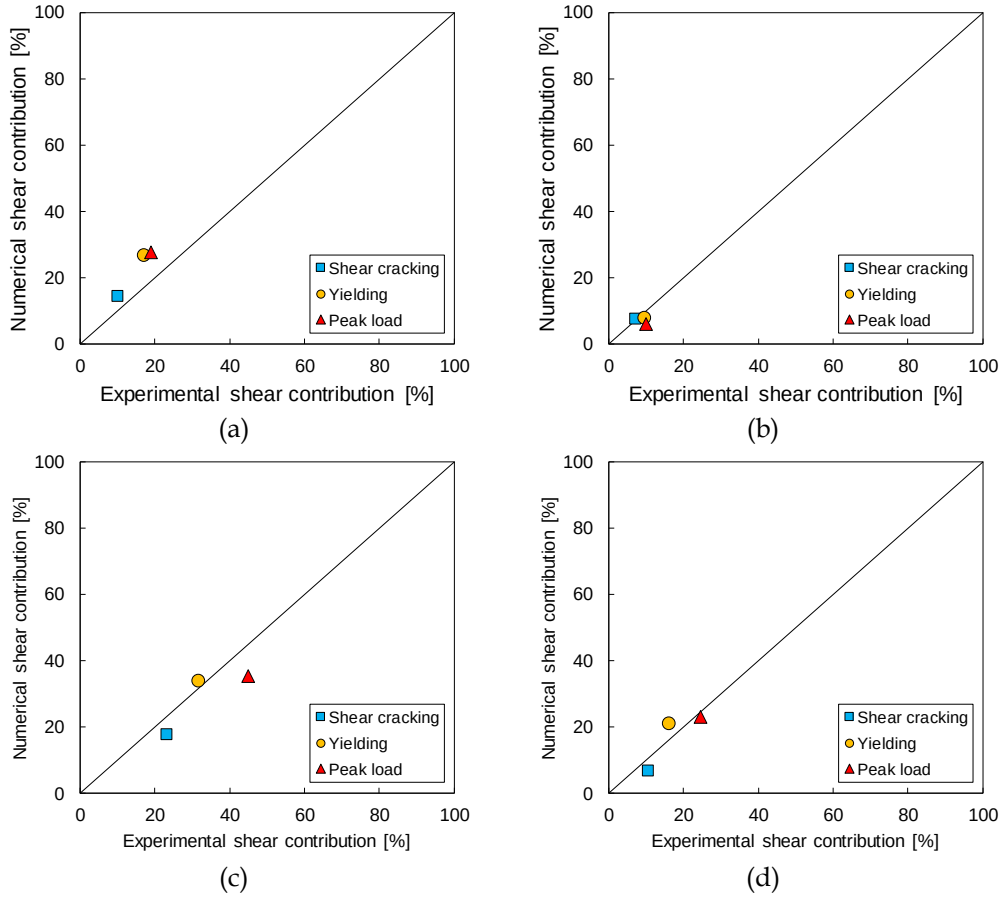

Figure 4.35. Comparison between averaged experimental (a) and numerical (b) shear deformability contribution for Tests P1 (a), P2 (b), P3 (c), and P4 (d)

4.7 Summary

In this chapter, experimental results of cyclic tests on reduced-scale RC bridge piers with rectangular hollow cross-section are shown and analyzed. Test units were representative of typical Italian bridge piers constructed prior to 1980s, and they were designed without earthquake provisions (low transverse reinforcement ratio and inadequate seismic details). Given the cross-section and the reinforcement details, different aspect ratios were considered depending on height of the specimens and loading direction.

Depending on the aspect ratio, different failure modes were expected, namely flexure failure for tall piers and shear failure after flexural yielding for short piers. Experimental results, in terms of lateral load versus drift and damage evolution showed that:

- Tests P1 and P2, characterized by a higher aspect ratio ($L_V/H \geq 2.5$), showed flexural failure modes, with an inelastic response controlled by ductile mechanisms. Damage evolution was typical of ductile members, with most of damage consisting of concrete crushing and longitudinal bars buckling.
- Test P3, characterized by an aspect ratio $L_V/H=1.5$, showed shear failure after flexural yielding. The cyclic response was typical of squat columns, governed by shear mechanisms. In fact, damage evolution was characterized by significant diagonal cracking since linear phase. Shear failure mode was characterized by a large drop in strength (of about 60% respect to maximum reached value) related to evident diagonal cracks opening, inclined of about 45 degrees.
- Test P4, characterized by an aspect ratio $L_V/H=2.25$, showed shear failure after flexural yielding. The cyclic response was characterized by flexure-shear interaction. In fact, during non-linear phase damage evolution was characterized initially by flexural cracks at the base, for drift values higher than Test P3, and later by significant diagonal cracks, up to shear failure.

An experimental analysis of deformability contributions to the top displacement was performed, mainly in order to better understand the relevance of taking into account shear deformations for bridge piers assessment. From experimental results, it seems possible to identify a relation between shear contribution to top displacement (Δ_s/Δ) and aspect ratio (L_V/H). In particular, (i) for slenderest specimen P2, maximum value of shear contribution was about equal to 11%; (ii) for Test units P1 and P4,

characterized by lower similar aspect ratios, about 20% of top displacement corresponding to peak load was due to shear deformations; (iii) for squat Test unit P3, shear deformability contribution to top displacement was about 32% and 45% respectively at yielding and peak load conditions.

The energy dissipation capacity was analyzed, evaluating the equivalent damping ratio and its evolution with ductility, which was compared with a common literature formulation usually used for RC bridge piers, highlighting a slightly lower energy dissipation capacity in large inelastic field for the tested specimens.

The reported comparison between the observed failure modes and shear strength values and the corresponding predictions based on capacity models from literature and/or codes provided a useful support to the evaluation of the reliability of these models when applied to existing hollow rectangular RC piers. From this comparison, it seems clear the need to improve the prediction capacity of shear strength models available in codes and literature. This issue will be addressed in the Chapter 6.

The global response is modelled through a three-component numerical model, in which flexure, shear and bar slip are considered separately. The numerical results show that the adopted model is able to reproduce the experimental global response and the deformability contributions, with adequate accuracy.

The tests presented herein can provide a useful contribution to enlarge the relatively limited experimental database on existing hollow rectangular RC piers. In particular, the experimental analysis of all the sources of deformability characterizing cyclic response can be a valid reference for the proposal/validation of nonlinear modeling approaches and capacity models for seismic assessment of existing bridge structures.

References

Biskinis D., Fardis M. N. (2010). Deformations at flexural yielding of members with continuous or lap-spliced bars. Structural concrete; 11(3): 127-138.

Biskinis D.E., Roupakias G.K., Fardis M.N. (2004). Degradation of shear strength of reinforced concrete members with inelastic cyclic displacement. ACI Structural Journal, 101(6):773–83.

Blandon CA, Priestley MJN. Equivalent viscous damping equations for direct displacement based design. Journal of earthquake Engineering 2005; 9(sup2): 257-278.

Cardone D. Displacement limits and performance displacement profiles in support of direct displacement-based seismic assessment of bridges. Earthquake Engineering & Structural Dynamics 2014; 43(8): 1239-1263.

CEN (2005) European standard EN1998-3. Eurocode 8: design provisions for earthquake resistance of structures – Part 3: assessment and retrofitting of buildings. European Committee for Standardisation, Brussels

CEN [2004a] European Standard ENV 1998-1-1/2/3. Eurocode 8: Design provisions for earthquake resistance of structures – Part I: General rules. Technical Committee 250/SC8, Comité Européen de Normalisation, Brussels, 2004.

Circolare 617. Circolare del Ministero dei Lavori Pubblici n. 617 del 2/2/2009. Istruzioni per l'applicazione delle "Nuove norme tecniche per le costruzioni" di cui al D.M. 14 gennaio 2008. G.U. n. 47 del 26/2/2009, 2009. (in Italian)

Federal Emergency Management Agency (1997). NEHRP Guidelines for the Seismic Rehabilitation of Buildings. FEMA 273, Washington, D.C.

Kowalsky M. J. and Priestley M. J. N. (2000) Improved analytical model for shear strength of circular reinforced concrete columns in seismic regions. ACI Structural Journal. 97(3), 388–396.

Kowalsky MJ, Priestley MJN, MacRae GA. Displacement-based design of RC bridge columns in seismic regions, Earthquake engineering & structural dynamics 1995; 24(12): 1623-1643.

Krolicki, J., Maffei, J., & Calvi, G. M. (2011). Shear strength of reinforced concrete walls subjected to cyclic loading. Journal of Earthquake Engineering, 15(S1), 30-71.

Mander JB, Priestley MJN, Park R. Theoretical stress-strain model for confined concrete. ASCE Journal of Structural Engineering 1988, 114(8): 1804-1826.

McKenna, F., Fenves, G.L. and Scott, M.H. (2000). Open system for earthquake engineering simulation, http://opensees.berkeley.edu.

Menegotto, M. and Pinto, P.E. (1973), "Method of analysis of cyclically loaded RC plane frames including changes in geometry and non-elastic behavior of elements un-der normal force and bending", Preliminary Report, IABSE, 13, 15–22.

Park, R. and Paulay, T. [1975] Reinforced Concrete Structures, JohnWiley and Sons, Inc., New York.

Popovics, S. (1973). A numerical approach to the complete stress strain curve for concrete. Cement and concrete research, 3(5), 583-599.

Priestley M. J. N., Seible F., and Calvi G. M. (1996). Seismic design and retrofit of bridges. Wiley, New York.

Priestley M. J. N., Verma R. and Xiao Y. (1994). Seismic shear strength of reinforced concrete columns. ASCEJ. Struct. Engrg, 120 (8) 2310-2329.

Priestley MJN, Calvi GM, Kowalsky MJ. Displacement-based seismic design of structures. Pavia, Italy: IUSS press, 2007.

Priestley MJN. Myths and fallacies in earthquake engineering. Revisited. Pavia, Italy: IUSS press, 2003.

Sezen, Halil, and Eric J. Setzler. "Reinforcement slip in reinforced concrete columns." ACI Structural Journal 105.3 (2008): 280.

Chapter 5

EXPERIMENTAL RESULTS: HOLLOW CIRCULAR RC PIERS

This chapter provides a summary of the experimental results of the hollow circular cross-section specimens, including damage description and test data measured during each test.

Based on visual observations and recorded test data, the performance of each test specimen is analyzed and discussed. For each specimen, the measured lateral load-displacement relations and plots of other important test parameters are presented. The damage description of specimens and their implications are discussed, and the measured response are compared.

The following sections discuss, first, the global response of each specimen, and then the evolution of damage observed during the tests. Experimental local behavior, in particular about the main deformability contributions due to different deformation mechanisms, later is analyzed and discussed. Finally, the hysteretic energy dissipation and the related equivalent damping are investigated. Analysis and discussion of the above mentioned experimental topics are presented, considering together the two tests in each section in order to develop some consideration through comparisons.

5.1 Analysis of global response

The most relevant global results obtained from the two tests are reported in this section. In particular, the lateral load-displacement response of tested specimens is analyzed. Response curves, in terms of lateral load versus drift (i.e. top displacement-to-shear span ratio) are shown and commented.

5.1.1. Test P5 – Aspect ratio equal to 3.0

The results in terms of lateral load versus drift response for Test P5 are shown in Figure 5.1. The loading history actually applied consisted of eight complete sets of three push/pull cycles. The experimental response appears quite symmetric during the push/pull cycles. Test P5 exhibited an initial uncracked stiffness equal to 67.7 kN/mm, a secant lateral stiffness to first cracking of 37.9 kN/mm, while the secant value at the first point of the experimental backbone was 17.3 kN/mm. A first reduction of the uncracked stiffness was observed for a lateral load of 29 kN, from which some horizontal flexural cracks formed up. Lateral stiffness decreased considerably for a drift range between 0.20% and 0.67%. In particular, during the third loading step (drift = 0.67%), for values equal to 86.7 kN and -86.4 kN of the horizontal force, respectively in push and pull directions, specimen reached first yielding condition. This was confirmed by longitudinal bars strain measures, provided by strain gauges located at the base of the test unit. Steel strain of longitudinal bars exceeded yielding strain ($\varepsilon_{s,y}$ = 2.7‰) both in push and pull directions, for drift values of +0.49% and - 0.44%, respectively. Beyond those values, SGs measures cannot be considered reliable. Peak load was reached for a drift equal to 1.91% for positive (push) loading direction and and -1.87% for negative (pull) loading direction. The corresponding peak values of lateral load were +108.2 kN and -102.4 kN, respectively. The post-peak response was governed by flexure. In fact, it was characterized by a gradual degradation due to concrete spalling and buckling of longitudinal bars next to the base section. The post-peak backbone evolved along an almost linear branch with a softening stiffness (calculated on the envelope of first cycles of V, VI and VII loading steps) equal to -10% and -5% of the uncracked stiffness, in positive and negative loading direction respectively. Experimental response appeared quite symmetric also in inelastic cycles. The intra-cycle strength drop developed from 15% to 23% from fifth to seventh loading step. During the last cycles set

(drift = 4.90%), a series of sudden intra-cycle strength drops/stiffness decreases was observed both in negative/positive direction. Such drops corresponded to the failure of outer longitudinal bars in tension due to oligo-cyclic fatigue caused by buckling/tension cycles. This phenomenon occurred when the imposed drift overcame the maximum drift attained during the previous cycles set. When the test was interrupted (at the end of the eighth loading step at 4.90% drift), the strength reduction respect to peak load (evaluated on the backbone of the response) was equal to 40%, both in positive and negative directions. Test P5 was characterized by flexural failure.

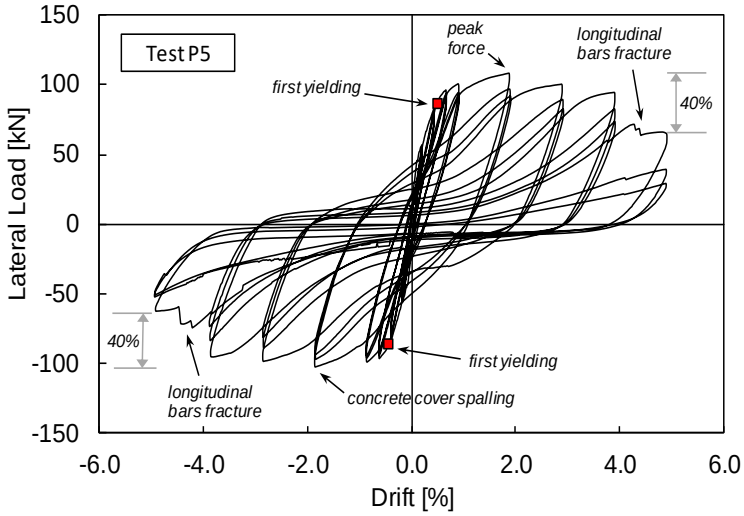

Figure 5.1. Lateral load versus cyclic response (Test P5)

5.1.2. Test P6 – Aspect ratio equal to 2.0

The results in terms of lateral load versus drift response for Test P6 are shown in Figure 5.2. The loading history actually applied consisted of five complete sets of three push/pull cycles and a last single push/pull cycle corresponding to shear failure. As opposed to previous case, the experimental response is characterized by a slight asymmetry during the push/pull cycles. This effect, more evident with increasing drift, is associated with the shear cracking extension and reversal process. Once a set of cracks is open for a given loading direction, the reversal into the opposite direction is partially characterized by closing of the previously opened shear cracks. Therefore, for a

given imposed horizontal displacement, a stiffness decrease is observed.

Test P6 exhibited an initial uncracked stiffness equal to 206.8 kN/mm, a secant lateral stiffness at first cracking of 133.8 kN/mm, while the secant value at the first point of the experimental backbone was 46.8 kN/mm. A first reduction of the uncracked stiffness was observed for a lateral load of 45 kN, from which some flexural cracks started to occur. A more significant reduction was observed for a drift range between 0.16% and 0.60%. In particular, during the third loading step (drift = 0.60%), for horizontal force values equal to 138.0 kN and -133.6 kN, respectively in push and pull directions, specimen reached first yielding condition. Longitudinal bars strain measures provided by strain gauges located at the base of the test unit confirmed this aspect. Steel strain of longitudinal bars exceeded yielding strain ($\varepsilon_{s,y}$ = 2.7‰) both in push and pull directions, for drift values of 0.49% and - 0.52% respectively. SGs measures are reported up to values considered to be reliable.

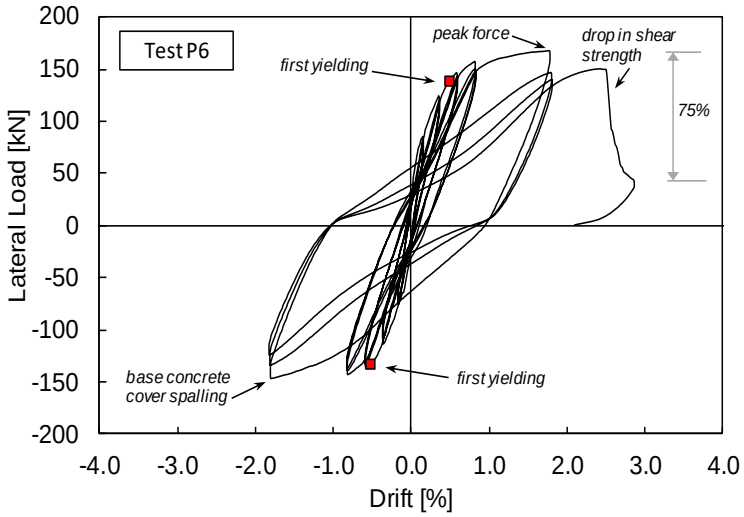

Figure 5.2. Lateral load versus cyclic response (Test P6)

Peak load was reached for a drift equal to +1.78% for positive loading direction (push) and -1.80% for negative loading direction (pull). The corresponding peak values of lateral load were +170 kN and -147 kN, respectively. The intra-cycle strength drop developed reached 15%. Test P6 was interrupted at the end of the push phase of the first cycle at 2.87% drift. In fact, during pushing phase, for a drift value of +2.49%, a drop in strength equal

to 72% was observed, from +149 kN to +42 kN at a drift value of +2.87%. The sudden and deep widening of the main shear crack caused such a drop. The strength reduction with respect to peak load (evaluated on the backbone of the response) was equal to 75%. Test P6 was interested by a shear failure after flexural yielding.

5.1.3. Comparison of global response

Table 5.1 summarizes experimental first yielding values (V^{+}_{y}, V^{-}_{y}, D^{+}_{y}, D^{-}_{y}), peak values (V^{+}_{max}, V^{-}_{max}, D^{+}_{max}, D^{-}_{max}) and "ultimate" drifts (D^{+}_{u}, D^{-}_{u}), of lateral force and drifts for both positive and negative loading directions. Ultimate drifts values were evaluated as those corresponding to a strength reduction equal to 20% with respect to the peak load on the experimental backbone. Observed failure modes are also reported (F: flexure mode; FS: shear failure after flexural yielding). Lateral load-drift envelopes corresponding to the first sub-cycles for each loading step are shown in Figure 5.3 for all tests.

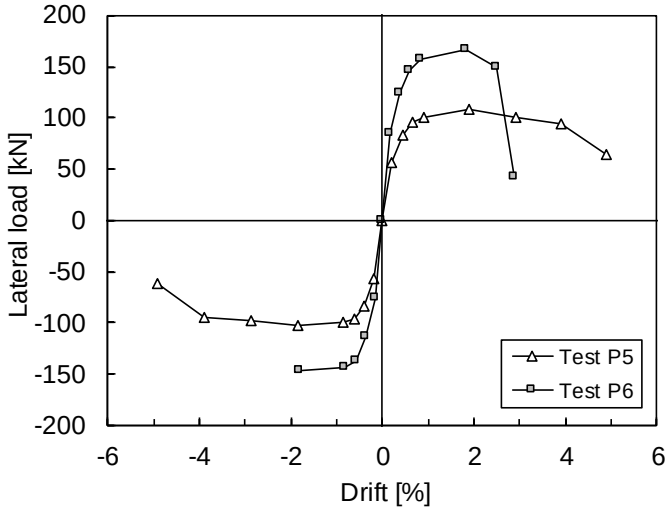

Figure 5.3. Envelopes of lateral load versus drift response

As expected, it can be observed that lateral strength increases as the aspect ratio decreases, fixed the loading direction. Similarly, a reduction of ultimate deformation capacity with decreasing level of aspect ratio can be noted. Specimen P6, characterized by flexure_shear failure, presents a lower value of ultimate drift.

Table 5.1. Yielding, peak and ultimate values of lateral force and drift together with observed failure modes

Test ID	Aspect Ratio	V^+_y	D^+_y	V^-_y	D^-_y	V^+_{max}	D^+_{max}	V^-_{max}	D^-_{max}	D^+_u	D^-_u	Failure Mode*
	(-)	(kN)	(%)	(kN)	(%)	(kN)	(%)	(kN)	(%)	(%)	(%)	(-)
P5	3.0	86.7	+0.49	-86.4	-0.44	108.2	1.91	-102.4	-1.87	4.18	-4.30	F
P6	2.0	138.0	0.49	-133.6	-0.52	166.9	1.78	-147.1	-1.80	2.55		FS

$^{+(-)}$: push (pull) direction of the applied displacement.

V_y, D^+_y, are experimental first yielding values of lateral force and drifts, respectively.

V_{max}, D_{max}, are experimental peak values of lateral force and corresponding drifts.

D_u, is the ultimate drift corresponding to a strength reduction of 20% of the peak load on the experimental backbone.

* experimental failure mode (F: flexure mode; FS: shear failure after flexural yielding).

5.2 Damage evolution and crack pattern

In this section, the evolution of observed damage with increasing imposed displacement is described and related to the above-analyzed lateral load-drift response of tested specimens. Damage evolutions and final damage states are shown and damage descriptions are summarized in tabular form for each loading step. The results are reported for each specimen, separately.

5.2.1. Test P5 – Aspect ratio equal to 3.0

The evolution with the drift of the damage state is showed in Figure 5.4, for the pre-yielding phase, and in Figure 5.5, for the post-yielding phase. Due to three-dimensionality of the crack patterns, each damage state is represented by four points of view, identified with the cardinal points. Finally, Table 5.2 presents a summary of damage states. Horizontal hairline cracks, orthogonal to loading direction, formed up on the west and wast faces along the first three layers of transverse reinforcement during first loading stages, namely at 0.20% drift (see Figure 5.4a).

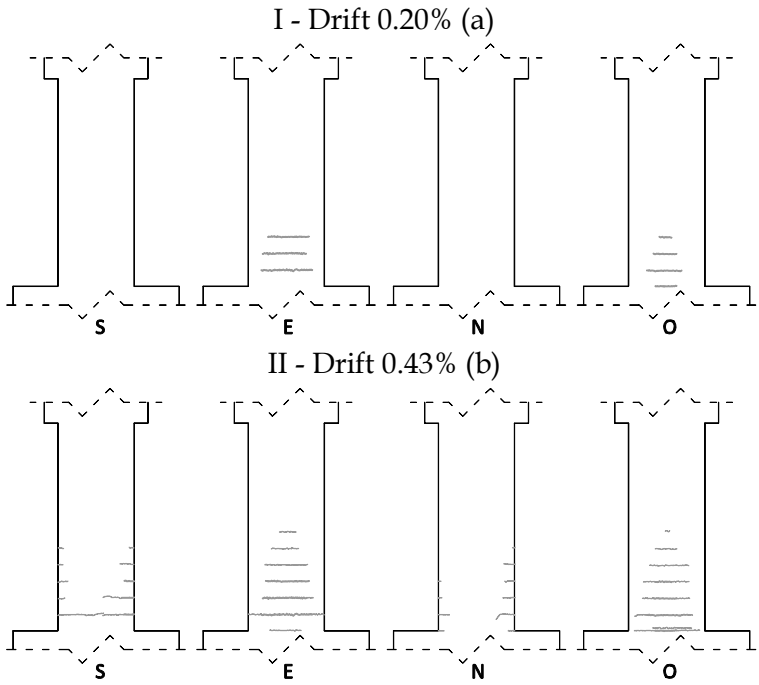

Figure 5.4. Test P5: evolution of damage (a, b) during pre-yielding phase

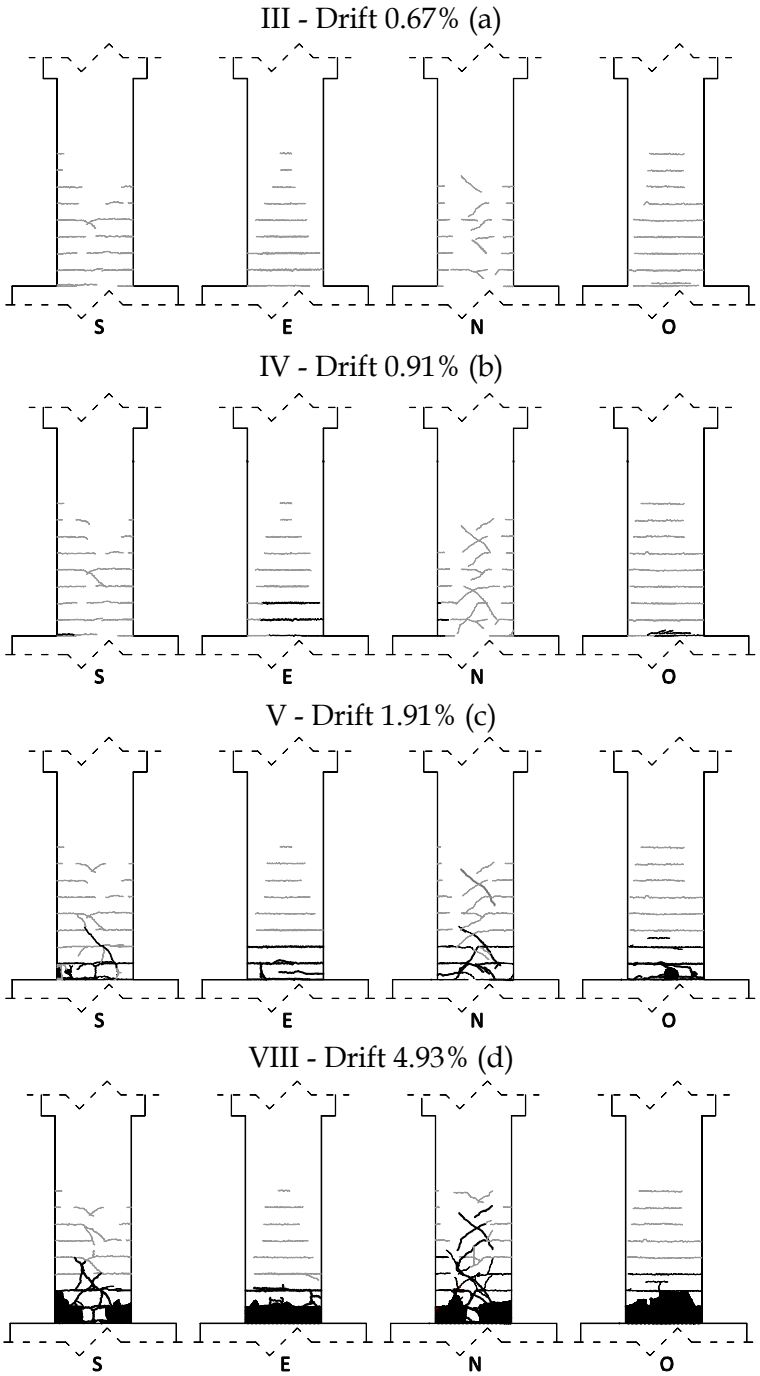

Figure 5.5. Test P5: evolution of damage (a, d) during post-yielding phase

The second loading step (drift = 0.43%) was characterized by a spreading of flexural cracks along the specimen's height, as reported in Figure 5.4b.
First slight diagonal cracks appeared on the north and south faces as extension of the flexural cracks for a drift of 0.67% (see Figure 5.5a), at 96.2 kN in positive direction and -96.4 kN in negative direction. For a drift value of 0.91%, the existing cracks increased their width and further shear cracks formed as extensions of flexural cracks. It is interesting to highlight the pinching effect characterizing the hysteretic loops starting from this cycles set, exalted by the sudden increase in width of diagonal cracks (see Figure 5.5b). When a drift equal to 1.91% was reached, corresponding to peak load, damage at the base of the column developed quickly: vertical cracks appeared in concrete cover due to longitudinal bars buckling and concrete spalling was observed near to base section on west face (negative loading direction), as showed in Figure 5.5c.

A significant concrete spalling related to intense buckling of longitudinal bars within the distance between the base and the first layer of transverse reinforcement was observed at 2.92% drift. The concrete cover spalling resulted into a strength reduction with respect to the peak load (evaluated on the backbone of the response) of about 7% and 3% for positive and negative loading respectively.

Cycle	Drift (%)	Damage description
1	0.20	Horizontal hairline cracks on the West and East faces
2	0.43	Spread of horizontal cracks along specimen's height
3	0.67	First slight diagonal cracks
4	0.91	Increase in width of existing cracks and new diagonal cracks
5	1.91	Longitudinal bars buckling and concrete cover spalling near to base section on West face
6	2.92	Intense buckling of longitudinal bars and significant concrete spalling
7	3.91	Complete concrete cover spalling, intense buckling of longitudinal bars and wide diagonal cracks
8	4.93	Failure in tension of the outer longitudinal bars due to oligo-cyclic fatigue

Table 5.2. Overview of the evolution of damage during Test P5

During seventh cycles set, for a drift of 3.91%, diagonal cracks considerably widened and concrete cover within the distance between the base and the first layer of transverse reinforcement completely spalled off, except

for a small central portion. This phenomenon is associated to an intra-cycle strength degradation equal to about 23% for both loading directions.

During the last cycles set (drift = 4.93%), concrete of the compressed flanges was completely crashed and concrete cover spalling spread at second level of transverse reinforcement (see Figure 5.5d). Test P5 failed in flexure.

A picture of the final damage state at the base of the column is reported in Figure 5.6.

Figure 5.6. Test P5: final damage state at the base of the column

5.2.2. *Test P6 – Aspect ratio equal to 2.0*

The evolution with the drift of the damage state is showed in Figure 5.7, for the pre-yielding phase, and in Figure 5.8, for the post-yielding phase. Due to three-dimensionality of the crack patterns, each damage state is represented by four points of view, identified with the cardinal points. Table 5.3 presents a summary of damage states.

First hairline cracks appeared on the west and wast faces along the first three layers of transverse reinforcement during first loading stages, namely at 0.16% drift (see Figure 5.7a). The second loading step (drift = 0.37%) was characterized by a spreading of flexural cracks and the appearance of first diagonal cracks as extension of the flexural ones toward compressed zone (see Figure 5.7b). More evident diagonal cracks appeared on the north and south faces for a drift of 0.60%, at 146 kN in positive direction and -137 kN in negative direction. In particular, two diagonal cracks formed from top to down opposite corners with an inclination angle of about 42 degrees (see Figure 5.8a).

For a drift value of 0.83%, existing shear cracks increased their width, particularly two principal ones, and further shear cracks formed in the central part of the specimen. It is noteworthy highlighting that, unlike Test P5, no

considerable damage was observed on the base zone at this drift level (see Figure 5.8b). When a drift equal to 1.82% was reached, corresponding to peak load, damage at the base of the column developed quickly: vertical cracks appeared in concrete cover due to longitudinal bars buckling and concrete spalling was observed in a small portion near to base section along the east/west direction, as showed in Figure 5.8c.

During the subsequent pushing phase, for a drift value of +2.49%, the main shear crack opened suddenly up to a width of about 13 mm, along an ideal concrete strut with a medium inclination angle of about 42 degrees (see Figure 5.8d). Shear sliding between the upper and the lower part of the specimen was observed, which caused the failure in tension of the circular ties along the main diagonal crack and the flexural deformation of the dowel bars involved.

Test P6 failed in shear after flexural yielding.

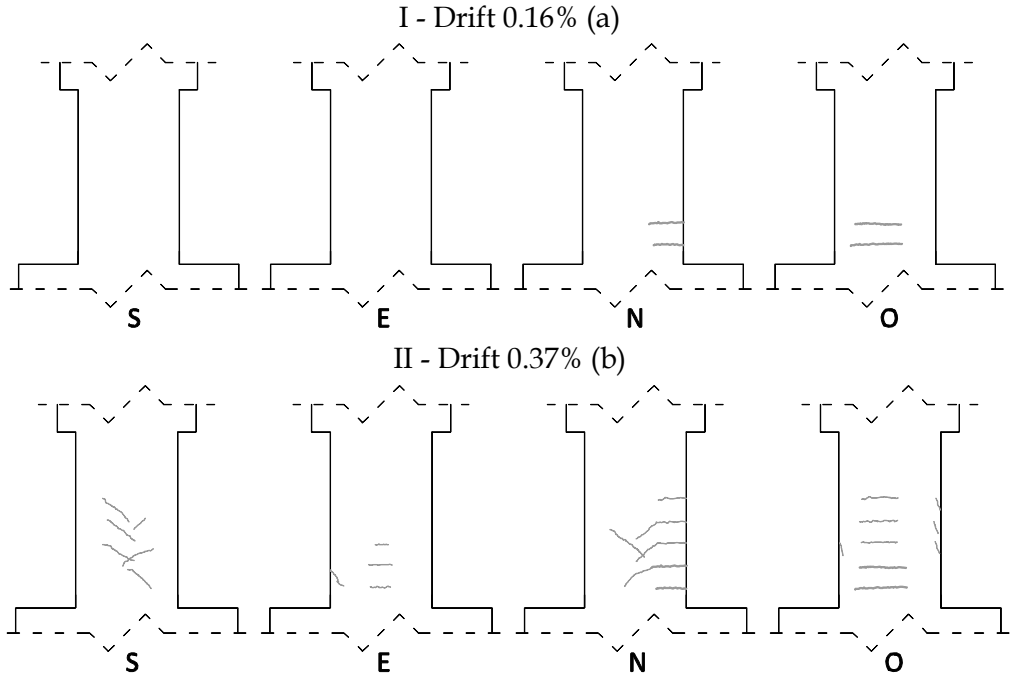

Figure 5.7. Test P6: evolution of damage (a, b) during pre-yielding phase

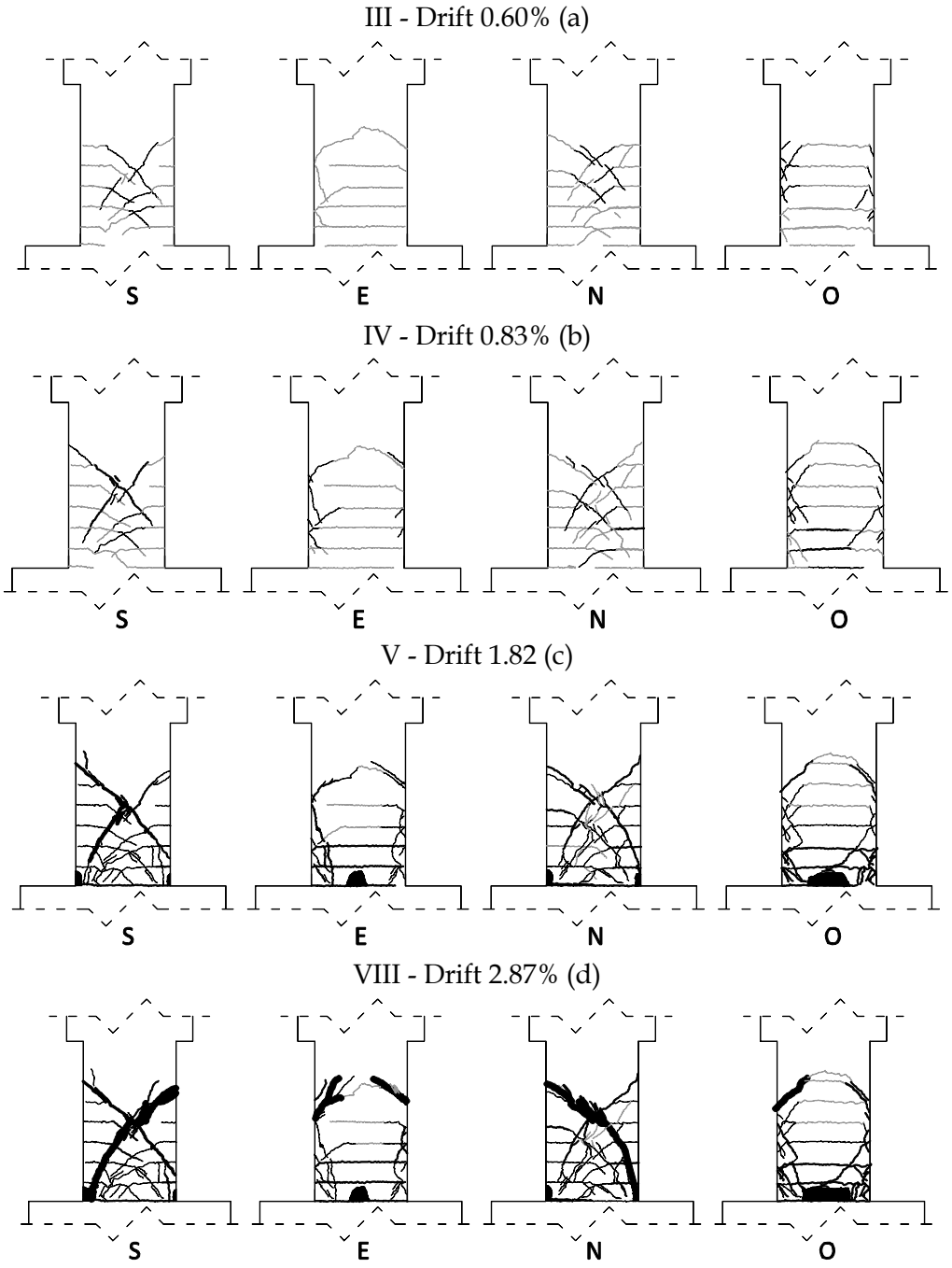

Figure 5.8. Test P6: evolution of damage (a, d) during post-yielding phase

Cycle	Drift (%)	Damage description
1	0.16	Horizontal hairline cracks on the West and East faces
2	0.37	First slight diagonal cracks on the Nord and South faces
3	0.60	Increasing in width of existing cracks and new diagonal cracks
4	0.83	Widening of existing main shear cracks
5	1.82	Concrete cover spalling in a small portion near to base section along the East/West direction
6	2.87	Sudden widening of main diagonal crack up to 13 mm

Table 5.3. Overview of the evolution of damage during Test P6

Figure 5.9 shows a picture of the final damage state, together with a detail of a circular tie failed in tension and the flexural deformation of a dowel bar involved along the main diagonal crack and.

(a) (b)

Figure 5.9. Test P5: final damage state (a) and failure in tension of circular ties involved in the main diagonal crack (b)

5.3 Local behavior

In this Section, the most significant local measurement data are analyzed and discussed.

5.3.1. Strain of longitudinal reinforcement

During the experimental tests, strain of both longitudinal and transverse reinforcement was monitored by means of strain-gauges (SGs) installed according the scheme reported in Figure 3.29. Figure 4.10 shows strain of longitudinal bars (ε_s) during the test for each specimen, until measures can be

considered as reliable. Yielding strain ($\varepsilon_{s,\ y}$= 2.7‰) is indicated through a dotted line in the diagrams, so it is possible to identify the cycle and the drift value at which first yielding was reached. Test P5 reached the first yielding condition between second and third loading step, for drift values of +0.49% and - 0.44% respectively in push and pull directions, when steel strain of longitudinal bars exceeded yielding strain ($\varepsilon_{s,y}$ = 2.7‰). Beyond those values, SGs measures cannot be considered reliable. Test P6 reached the first yielding condition during the third loading step, for a drift equal to 0.60%. Longitudinal bars strain measures provided by strain gauges located at the base of the test unit confirmed that steel strain exceeded yielding strain for drift values of 0.49% and - 0.52% respectively in push and pull directions. Experimental measures related to SGs installed on the longitudinal bars under the base section at a depth of 60mm (identified as SG-Down) are analyzed, too, in order to investigate about strain penetration into the foundation block.

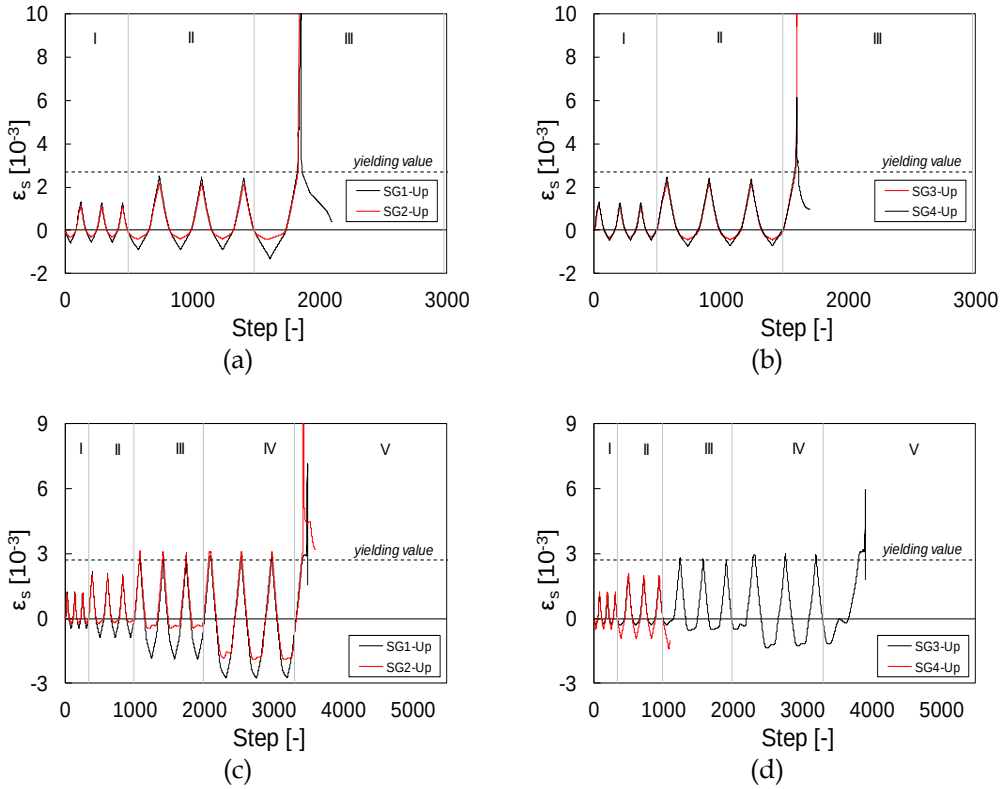

Figure 5.10. Strain of longitudinal bars for Tests P5 (a, b) and P6(c, d)

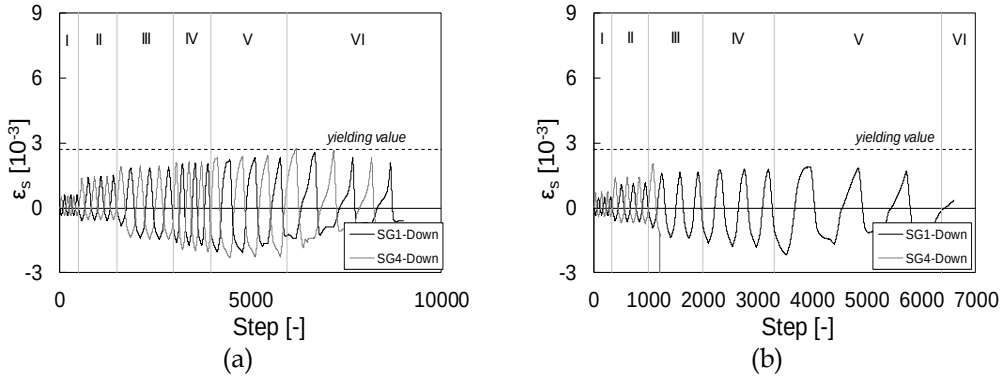

Figure 5.11. Strain of longitudinal bars in the footing for Tests P5 (a) and P6(b)

As expected, these measures are smaller than the corresponding located above the base section. Also in this case, it is possible to identify the cycle and the drift range at which yielding strain is eventually reached. For Test P5, this condition was reached during the sixth loading step, corresponding to the first cycle after the load peak. For Test P6, it is interesting to note that the shear failure after flexural yielding limited strain penetration into the foundation, so yielding strain was not recorded.

5.3.2. *Shear cracks monitoring – Test P6*

Focusing on Test P6, as well described in the section 5.2.2, during the pushing phase of the last cycle, the main diagonal crack suddenly increased in width, causing an irreversible drop in shear strength. Such a phenomenon was directly controlled by dedicate monitoring system described in Figure 2.34. Figure 5.12 reports the difference between data recorded by two diametrically opposed horizontal LVDTs for each horizontal level.

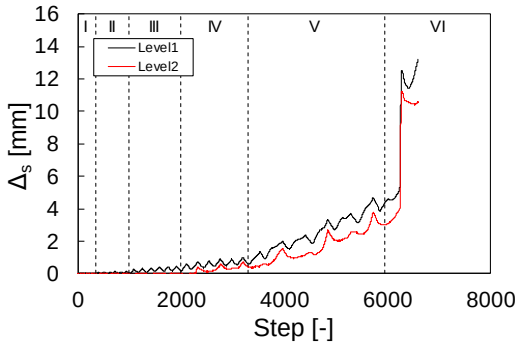

Figure 5.12. Shear cracks width – Test P6

It can be noted that up to third loading step (drift = 0.60%), the width of diagonal cracks is almost negligible and only some diagonal cracks near to base section are present. The fifth loading step (drift = 1.82%) is characterized by an almost linear increase of the shear cracks width with repetition of the three push/pull cycles. During first push phase at +2.87%, for a drift of +2.49% a sudden increase in width is observable, corresponding to the widening of main shear crack. Maximum width measured is about 13 mm. It is noteworthy to underline that the main shear crack is larger in the upper part with respect to lower one. So, it seems that the failure mechanism has been characterized by a slight rotation as well as a horizontal sliding.

5.3.3. Flexural and Shear Deformability Contributions

As already discussed in Section 4.3.2, seismic response of RC elements with hollow sections, typical of bridge piers, can be characterized by a considerable flexure-shear interaction. Shear deformations may represent a considerable portion of the global deflections, limiting ductile energy dissipation.

In order to investigate experimentally this issue, an appropriate monitoring system was installed.

The top displacement of the specimens (Δ) can be interpreted as the results of three response mechanisms: flexure (Δ_f), shear deformation along webs (Δ_s) and fixed-end-rotation due to longitudinal bar slip at column base (Δ_θ) (see Figure 5.13 and Eq. (5.1)).

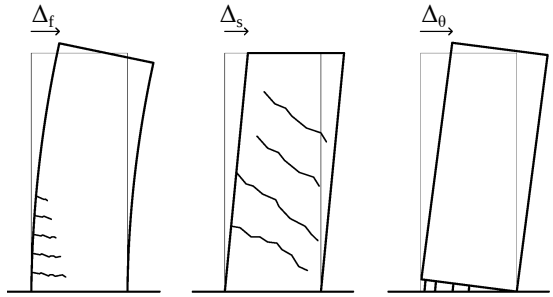

Figure 5.13. Deformability contributions to total displacement

Assuming a uniform curvature distribution along each of the two curvature cells, the flexural component Δ_f was calculated as the sum of the

rotations measured by vertical LPs multiplied by corresponding distances from the top of the column (Eq. (5.2)).

Strictly speaking, the fixed-end-rotation contribution Δ_θ is due to the slip from the foundation and it cannot be directly evaluated; instead, the base rotation θ_b can be measured by the two LVDTs monitoring vertical deformation along the height h_b=50 mm from the base section. θ_b is associated to the base crack width including slip from element and from foundation, and to flexural deformation along h_b. The corresponding displacement Δ_b was calculated according to Eq. (5.3), similar to Eq. (5.2).

Based on the hypothesis of small angles and uniform shear deformation over the measuring panel height, the shear component Δ_s was estimated using Eq. (5.4).

In Eqs. (5.2) – (5.4), h_i, h_j, l, d, are respectively heights, width and diagonal of the measuring panels; h_b is the height of first curvature cell, next to base section; $\delta_{o,i}$ and $\delta_{e,i}$, δ_1 and δ_2 are average values between north and south specimen surfaces of vertical and diagonal experimental measurements.

$$\Delta=\Delta_f+\Delta_b+\Delta_s \tag{5.1}$$

$$\Delta_f=\sum_{i=1}^{2}\theta_i\left[L_v-\left(\sum_{j=1}^{i-1}h_j+h_i/2\right)-h_b\right];\ \theta_i=\frac{\delta_{o,i}-\delta_{e,i}}{l} \tag{5.2}$$

$$\Delta_b=\theta_b\left(L_V-h_b/2\right) \tag{5.3}$$

$$\Delta_s=\frac{d}{2l}\left(\delta_1-\delta_2\right) \tag{5.4}$$

Figure 5.14 shows the deformability components as a function of the top displacement for both Tests P5 and P6 (until all measures can be considered as reliable and for first cycle at each drift level, both in positive and negative directions). For Tests P5, damage state evolution led to a loss of some instruments, so for these specimens, diagrams stop at peak load drift, while for Tests P6 measures are reliable up to failure drift. Global symmetry of the response in push/pull direction is almost confirmed also in terms of local

deformations.

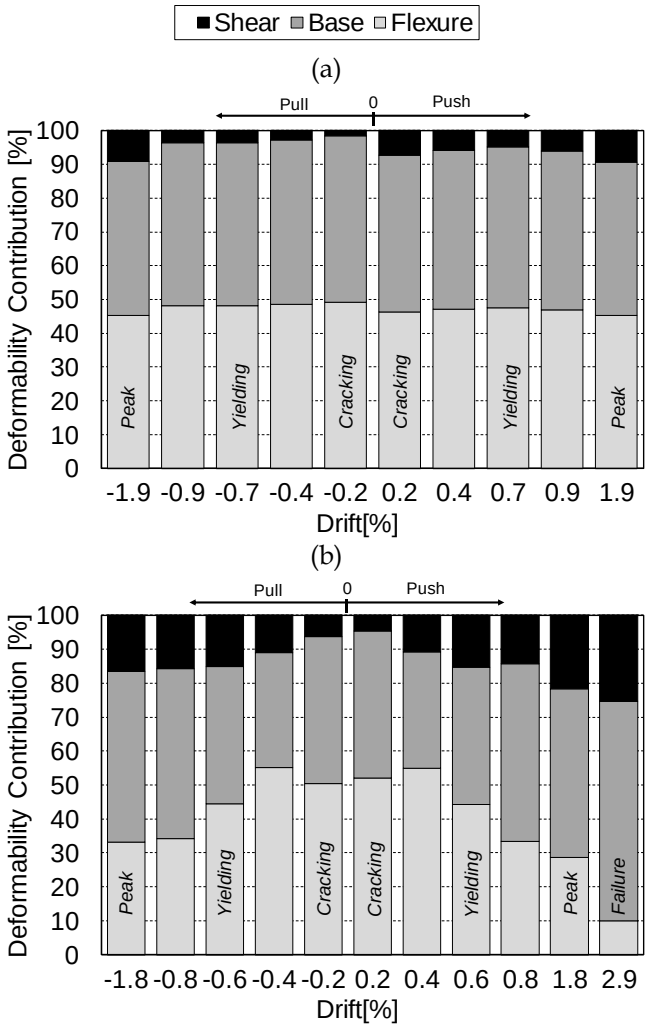

Figure 5.14. Experimental deformability contributions to total displacement ratio for Test P5 (a) and Test P6 (b)

A slight dissymmetry can be noted as regards shear deformability contribution, during the first two cycles of Test P5. This is probably due to a slight dissymmetry of crack patterns, which are more developed on the east side, i.e. the push direction. For all the tests, flexural deformability contribution (sum of Δ_b and Δ_f) was predominant respect to shear one. It is interesting to note that flexural deformation was distributed over the height since from first

cycle (balanced dark and light grey in figure). It seems possible to identify a relation between shear contribution to top displacement (Δ_s/Δ) and aspect ratio (L_V/H). In fact, for slenderest specimen (i.e. P5), shear contribution is almost constant and very low (namely, $\Delta_s/\Delta = 4.5\%$) up to 0.91% drift. Corresponding to peak (drift = 1.91%), the increase in width of existing diagonal cracks lead to a shear contribution on peak top displacement equal to 9.4%, which is the maximum value measured during Test P5. Test P6 is characterized by shear contribution higher than 10% since second cycle (drift = 0.37%), when Δ_s/Δ already reaches a value of 11.0%. Unlike Test P5, Test P6 is characterized by an almost linear growing trend. In fact, Δ_s/Δ ratio reaches an average value of 15.3% at yielding cycle and 25.4% at shear failure.

Another interesting observation about deformability contributions is that for Test P6, after flexural yielding, the base contribution Δ_b/Δ starts to grow (of about 10% respect to previous value) together with shear contribution Δ_s/Δ. This is mainly because significant cracks on the specimen were diagonal, while flexural dissipative damages were concentrated at the base. On the other side, for test P5, Δ_b/Δ is about constant, probably because flexural cracks were distributed along the specimen.

It is noteworthy to underline that the subdivision of deformations of inelastic RC hollow piers into shear and flexural deformations can provide a useful link between the experiments and numerical models, particularly if beam models are used.

Of particular interest is the assessment of the shear contribution to lateral displacement in the inelastic range, to understand when it is essential to consider shear deformations in structural analysis. In this regard, Figure 5.15 shows the trend of shear contribution Δ_s/Δ with the drift for all the tests (i.e. for different values of the aspect ratio L_v/H), while Figure 5.16 shows the averaged (between push and pull direction) experimental deformability contributions to total displacement ratios.

As expected, shear deformation increases when aspect ratio decreases. Furthermore, it is possible to observe an almost constant trend of shear contribution (Δ_s/Δ) characterizing ductile specimen P5, and a proportionally linear increasing trend for the specimens interested by a shear failure.

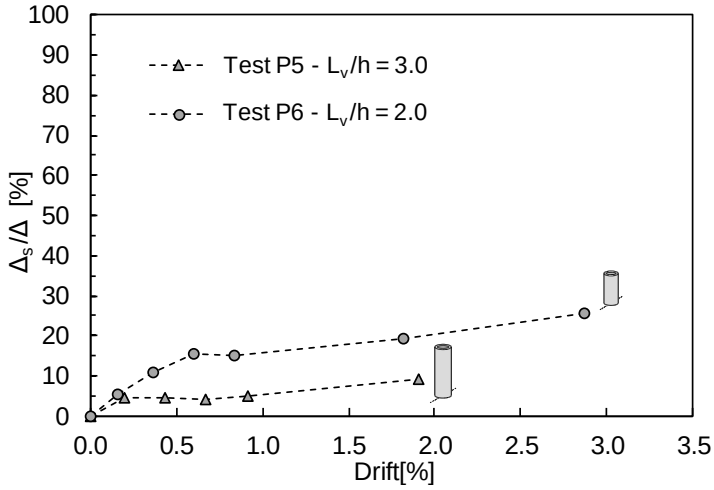

Figure 5.15. Shear deformability contributions for Tests P5 and P6

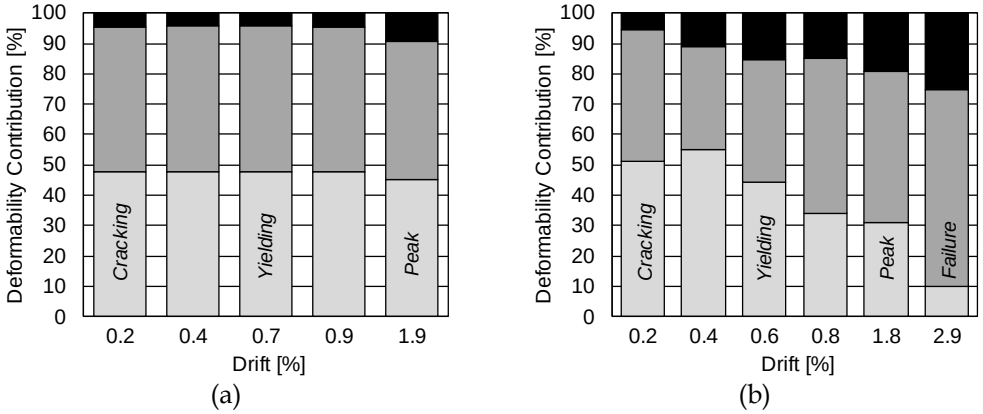

Figure 5.16. Averaged deformability contributions for Tests P5(a) and P6(b)

5.4 Dissipated energy and equivalent viscous damping

In this Section, the hysteretic energy dissipated in the presented tests is shown and analyzed and equivalent viscous damping is estimated.

The dissipated energy, calculated as the area underneath the experimental lateral force-displacement curve, is shown in Figure 5.17 for all the tests, with increasing drift. In particular, Figure 5.17a reports the cumulative dissipated energy, whereas Figure 5.17b shows the energy dissipated in each cycle.

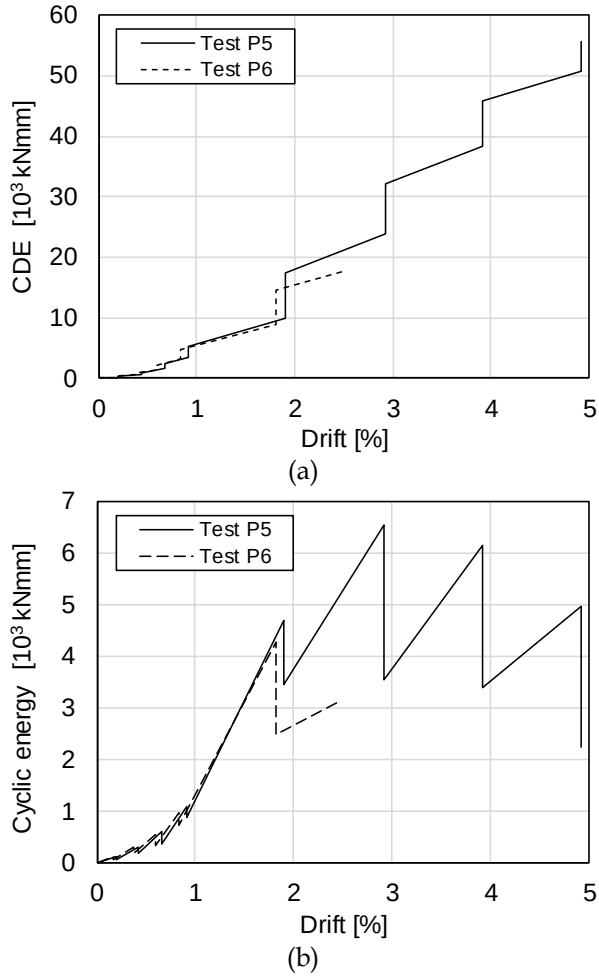

Figure 5.17. Hysteretic energy dissipation: cumulative dissipated energy (a), energy dissipated in each cycle (b)

Globally, as expected, ductile Tests P5 is characterized by a higher hysteretic energy dissipation capacity respect to Tests P6, interested by a shear failure after yielding. In particular, the total CDE showed by the squat specimen P6 is about 32% of that related to slender Test P3. It can be also noted that total cumulative dissipated energy (CDE) evolution is very similar between the two specimens. Of course, the considerations reported below are influenced by the different strength of the specimens. The specific energy dissipation capacity will be evaluated later, through the equivalent damping ratios. In a comparison between shorter specimens, Test P4 shows a higher CDE, of about 60%, respect to Test P3, since shear failure occurred for a larger

drift value, after that peak value of lateral force was reached. With regard to dissipated energy for each cycle, it is possible to note that Test P6 is characterized by a drop during the last cycle (drift = 2.87%) of about 48% respect to the previous. The reason of such a drop is probably due to the sudden development of shear cracks and the reduction of the other more dissipative mechanism (as shown in Figure 5.16). Finally, focusing on Test P5, dissipated cyclic energy is characterized by a significant increase since the fourth cycle (drift = 0.91%), from which the element is in non-linear field (yielding of longitudinal bars steel reached during the previous cycle).

Another interesting way to deal with the experimental dissipated energy is through the evaluation of the equivalent damping ratio ξ_{eq}, often adopted in literature to normalize the dissipated energy (Priestley et al., 2007).

The equivalent viscous damping accounts for both elastic damping and energy dissipation due to hysteresis in nonlinear response caused by the inelastic deformations of the structure. This coefficient is widely used in displacement-based seismic design or assessment (as in our case, for existing structures, e.g. Cardone (2014)), together with a stiffness secant to the performance point of interest (Priestley et al., 2007).

Basically, the value of the equivalent viscous damping ratio can be defined as the sum of elastic and hysteretic damping, according to Eq. (5.5).

$$\xi_{eq} = \xi_{el} + \xi_{hyst} \tag{5.5}$$

The hysteretic damping ξ_{hyst} can be obtained equating the energy dissipated by a linear viscous damper with the energy dissipated from nonlinear behavior. According to this definition, the equivalent viscous damping is evaluated herein for each Test. First of all, each cycle i can be identified through a maximum value and a minimum value of lateral load (V_i^+ and V_i^-, respectively), and a maximum value and a minimum value of top displacement (Δ_i^+ and Δ_i^-, respectively). The lateral load $\overline{V}_i$ is defined as the mean between V_i^+ and V_i^-, and the displacement $\overline{\Delta}_i$ is defined as the mean between Δ_i^+ and Δ_i^-. Then, the equivalent damping at each cycle $\xi_{eq,i}$ is calculated as function of the energy dissipated in each cycle $E_{h,i}$ (area within one complete cycle of stabilized force-displacement response), according to Eq. (5.6):

$$\xi_{eq,i} = \frac{1}{2\pi} \cdot \frac{E_{h,i}}{\bar{V}_i \cdot \bar{\Delta}_i} \tag{5.6}$$

In literature, several expressions have been developed to provide such a coefficient as a function of the displacement ductility (μ), based on different hysteretic models. Generally, ignoring the period dependency, the equations have a common functional form (Blandon and Priestley, 2005), reported in Eq. (5.7):

$$\xi_{eq} = \xi_0 + a \cdot \left(1 - \frac{1}{\mu^{\beta}}\right) \tag{5.7}$$

where ξ_0 is the initial viscous damping (usually equal to 0.05 for RC structures), μ is the ductility, a and β are coefficient based on the hysteretic model adopted.

For RC bridge piers, as indicated by Blandon and Priestley (2005) and Kowalsky et al., (1995), the evaluation of the equivalent viscous damping ξ_{eq} has to be computed by assuming a modified "thin" Takeda hysteresis model (with "narrow" loops) in which the unloading coefficient is taken equal to 0.5 and the post-yield stiffness ratio is assumed to be 5%. Under these assumptions, coefficients a and β in Eq. (5.7) are equal respectively to 95/π and 0.5, as reported in Priestley (2003), leading to Eq. (5.8):

$$\xi_{eq} = 5 + \frac{95}{\pi} \cdot \left(1 - \frac{1}{\mu^{0.5}}\right) \tag{5.8}$$

In order to perform a comparison between experimental and predicted viscous damping ratios, herein, for each specimen, the equivalent damping is computed as a function of the displacement ductility (μ). μ is defined as the ratio between the maximum imposed displacement in each cycle and the yield displacement (Δ_y). The latter is obtained through a bi-linearization of the experimental envelope according to EC8-1 (Annex B.3), by imposing the equal-area rule until the lateral peak load is reached. Then, a non-linear least square regression is performed to obtain the best-fit to the experimental results for the parameters a and β, assuming the functional form reported in Eq. (5.7) with

initial damping $\xi_0 = 5\%$.

The resulting expression (Eq. (5.9)) is depicted in Figure 5.18 together with Eq. (5.8).

$$\xi_{eq} = 5 + \frac{51}{\pi} \cdot \left(1 - \frac{1}{\mu^{2.2}}\right) \tag{5.9}$$

On average, quite similar values are observed, but the experimental fitting is characterized by a steeper increasing trend of the equivalent viscous damping for lower ductility values (namely, for μ up to about 4), and a quasi-constant trend for higher ductility levels. The obtained results seem to highlight a lower energy dissipation capacity with respect to the "thin" Takeda model hypothesis in large inelastic field. Finally, note that the equivalent damping–displacement ductility relationship is strongly influenced by the yielding displacement, and, therefore, by the approach followed in its calculation.

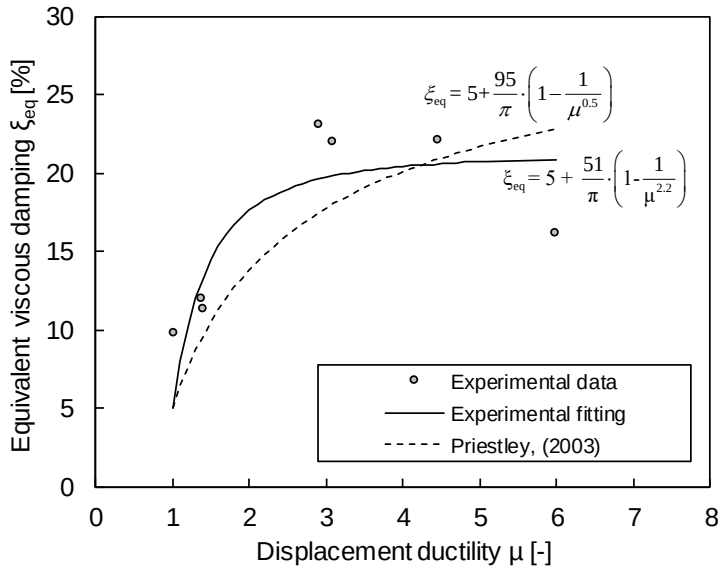

Figure 5.18. Equivalent damping-displacement ductility relationship

5.5 Comparison between experimental results and code-based capacity models

In this section, the experimental responses of the tests P5 and P6, are compared with code-based capacity models. In particular, the aim of such a comparison is to evaluate the capability of relevant code-based shear strength models in prediction the experimental failure modes, and the shear capacity (for specimens failing in shear). As discussed in detail in section 2.3, for an adequate assessment of existing RC members, it is crucial the classification, i.e. the prediction of the failure mode. It is noteworthy, despite their widespread use (bridge piers, piles, offshore platforms), none of the codes addresses specialized attention to shear strength of RC hollow core members, both for design and assessment (Turmo et al. 2009). As described in section 5.1, based on experimental evidence and observed damage, test P5 was characterized by a flexure-controlled failure mode (F-mode), and test P6 by a shear failure following flexural yielding (FS-mode), hence due to shear strength degradation in post-elastic field.

In the following, the capability of main shear strength capacity models from code and literature in predicting such failure modes will be evaluated. The considered models have been described in detail in section 2.3.3. Therefore, they're briefly recalled below:

- FHWA: the model adopted by the U.S. Federal Highway Administration provisions document for seismic retrofitting of bridges (FHWA, 2006) corresponds to the model proposed by Kowalsky and Priestley, (2000)
- EC8/3: the model adopted by the Eurocode 8 – part 3 (EC8/3, 2005) corresponds to the model proposed by Biskinis et al., (2004)
- C617: the model suggested by the Italian Code (Circolare 617, 2009) for the assessment of shear capacity of bridge columns is a slightly modified version of the Original UCSD model (Priestley et al., 1994). A 45° instead of a 30° angle truss mechanism is assumed, and the degradation coefficient is assumed to vary between 0.29 and 0.10 for displacement ductility between 1 and 4

The degrading shear strength models considered herein require the estimation of the expected displacement at yielding, in order to evaluate the

displacement ductility, which should be evaluated consistent with the procedures proposed or adopted by the respective Authors. Hence, when applying the C617 and the FHWA models, the expected displacement at yielding is estimated as reported in Priestley et al. (1996):

$$\Delta_y = \frac{\phi_y^*}{3}\left(L_V + 0.022 f_y d_b\right)^2 \tag{5.10}$$

where φ_y^* is the curvature at the corner of a bilinear envelope of the moment-curvature relationship (Priestley et al., 1996), L_V is the shear span, f_y is the steel yielding strength and d_b is the diameter of the longitudinal bars.

When applying the EC8/3 model, the expected displacement at yielding is estimated as reported in Fardis (2007):

$$\Delta_y = \left(\frac{\phi_y L_V}{3} + 0.0022 \cdot \max\left(0, \left(1 - \frac{L_v}{6D}\right)\right) + \frac{\phi_y f_y d_b}{8\sqrt{f_c}}\right) L_V \tag{5.11}$$

where, φ_y is the curvature at first yielding, f_c is the concrete compressive strength, and D is the external diameter of the cross section. As discussed in section 2.3.1, the behavior of a RC element can be classified based on the ratio between plastic shear capacity and degrading shear strength. For this reason, it is necessary the evaluation of the plastic load for the specimens. The following Table 5.4 reports a comparison between observed and predicted lateral loads at first yielding (V_y) and at maximum (V_{max}), based on corresponding moments M_y and M_{max} evaluated on the basis of a section analysis, assuming the Mander et al. (1988) stress-strain model for concrete, and elastic-plastic with strain hardening stress-strain relationship for steel.

Test ID	*Experimental*				*Analytical*		*(Anal. - Exp.) / Exp.*	
	V^+_y (kN)	V^-_y (kN)	V^+_{max} (kN)	V^-_{max} (kN)	V_y (kN)	V_{max} (kN)	yielding (%)	peak (%)
P5	86.7	-86.4	108.2	-102.4	80.1	105.3	-7.3%	-2.7%
P6	138.0	-133.6	166.9	-147.1	120.0	158.0	-10.1%	-5.3%

Table 5.4. Yielding and peak lateral load: experimental vs analytical comparison

A moderate underestimation, on average equal to 8%, is observed between

the calculated V_y and the corresponding experimental value (minimum between positive and negative) assumed as corresponding to the attainment of yielding strain in longitudinal reinforcement; a similar underestimation, on average equal to 4%, is observed for V_{max} (maximum between positive and negative). Note that such a comparison should be carried out mainly for test P5, since in test P6 the development of flexural over-strength might have been at least partially prevented by the occurrence of shear failure. On that note, the predicted failure mode can be derived by comparing the analytical value of the yielding (V_y) and peak lateral load (V_{max}) with the maximum (non-degraded) and minimum shear strength values, as reported in Table 5.5.

Test ID	*Analytical*		*FHWA*			*C617*			*EC8/3*			*Exp*
	V_y (kN)	V_{max} (kN)	Max (kN)	Min (kN)	FM	Max (kN)	Min (kN)	FM	Max (kN)	Min (kN)	FM	FM
P5	86	103	147	75	FS	187	101	FS	116	91	FS	F
P6	134	167	155	82	S	195	109	FS	135	107	S	FS

Table 5.5. Predicted and observed lateral loads corresponding to flexural strength at yielding and maximum and failure mode

In Figure 5.19, the comparison between shear strength envelopes and experimental response is reported. In the plots, flexural strength and yielding force are also depicted as black horizontal lines. As observed, neither of the considered models is able to predict the failure mode for test P5. Conversely, only C617 model (Circolare 617, 2009) shows a good capacity of failure mode prediction for test P6, whereas, the FHWA (FHWA, 2006) and EC8/3 model (EC8/3, 2005) show a lower predictive capacity, due to the conservatism in model predictions. Note that the latter model was applied assuming the formulations providing shear strength in the case of diagonal tension failure, which generally controls the shear failure. Strictly speaking, the displacement ductility capacity of RC members failing in shear should not be evaluated from the inverse application of the shear strength model because this would not lead to a reliable evaluation of the drift at shear failure (Biskinis et al., 2004). Vice-versa, it is possible to evaluate the predicted degraded shear strength corresponding to the observed ductility at failure. Therefore, for Tests P6, showing a shear failure following flexural yielding, Table 5.6 reports the failure mode and the shear strength capacity predicted by the considered

models (as described, the latter is evaluated corresponding to the observed ductility at failure if a FS failure is predicted, otherwise as the non-degraded shear strength if a S failure is predicted). The displacement at failure (see Table **5.6**) is evaluated as the displacement corresponding to 20% strength decay on the envelope of the experimental lateral load-drift response, for the EC8/3 model, whereas, for the remaining models, it is assumed as that corresponding to the maximum load. The corresponding ductility values are calculated depending on the displacement at yielding evaluated consisting with each model.

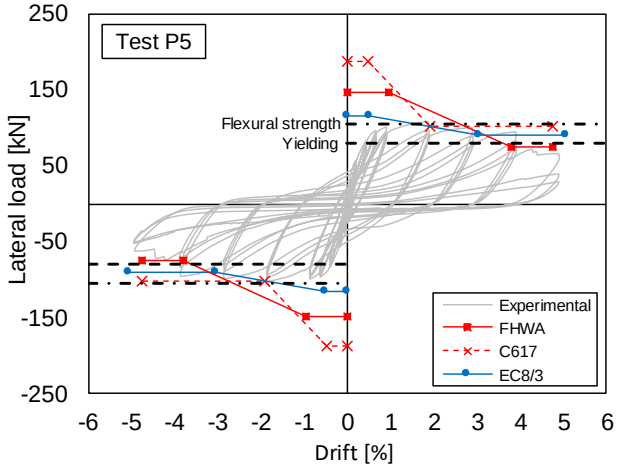

(a)

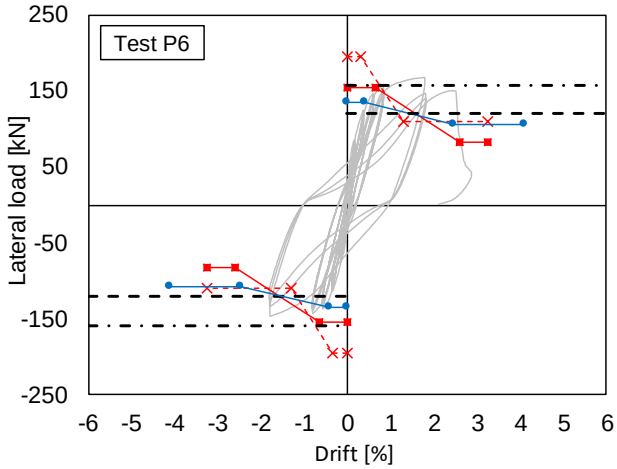

(b)

Figure 5.19. Experimental lateral load-drift responses and shear strength envelopes predicted according to the considered capacity models for tall specimens

Test ID	*Experimental*			*FHWA*			*C617*			*EC8/3*		
	FM	V_u (kN)	D_u (%)	FM	V_R (kN)	E	FM	V_R (kN)	E	FM	V_R (kN)	E
P6	FS	149	2.49	S	121	0.81	FS	109	0.73	S	107	0.72

Table 5.6. Predicted failure mode and shear strength for Tests P6

In Table 5.6 the error (evaluated as the predicted to experimental shear strength ratio) is specified for each of the considered models. A quite large shear strength underestimation (of about 20%) characterizes the FHWA model; the error is higher for both C617 and EC8/3 models, whose underestimation of the experimental shear strength is of about 30%.

5.6 Summary

In this chapter, experimental results of cyclic tests on reduced-scale RC bridge piers with circular hollow cross-section are shown and analyzed. Test units were representative of typical Italian bridge piers constructed prior to 1980s, and they were designed without earthquake provisions (low transverse reinforcement ratio and inadequate seismic details). Given the cross-section and the reinforcement details, different aspect ratios were considered depending on height of the specimens and loading direction.

Depending on the aspect ratio, different failure modes were expected, namely flexure failure for tall pier P5 and shear failure after flexural yielding for short pierP6.

Experimental results, in terms of lateral load versus drift and damage evolution showed that:

- Tests P5, characterized by a higher aspect ratio ($L_V/H = 2.5$), showed flexural failure modes, with an inelastic response controlled by ductile mechanisms. Damage evolution was typical of ductile members, with most of damage consisting of concrete crushing and longitudinal bars buckling.
- Test P6, characterized by an aspect ratio $L_V/H = 2.0$, showed shear failure after flexural yielding. The cyclic response was typical of squat columns, governed by shear mechanisms. In fact, damage evolution was characterized by significant diagonal cracking since linear phase. Shear failure mode was characterized by a large drop in strength (of about 75% respect to maximum reached value) related to evident diagonal cracks opening, inclined of about 42 degrees.

An experimental analysis of deformability contributions to the top displacement was performed, mainly in order to better understand the relevance of taking into account shear deformations for hollow bridge piers assessment. From experimental results, it seems possible to identify a relation between shear contribution to top displacement (Δ_s/Δ) and aspect ratio (L_V/H). In particular, (i) for slenderest specimen P5, maximum value of shear contribution was about equal to 9.4%; (ii) for squat Test unit P3, shear deformability contribution to top displacement was about 15% and 25% respectively at yielding and shear failure conditions.

The energy dissipation capacity was analyzed, evaluating the equivalent damping ratio and its evolution with ductility, which was compared with a

common literature formulation usually used for RC bridge piers, highlighting a slightly lower energy dissipation capacity in large inelastic field for the tested specimens.

The reported comparison between the observed failure modes and shear strength values and the corresponding predictions based on capacity models from literature and/or codes, provided a useful support to the evaluation of the reliability of these models when applied to existing hollow circular RC piers. From this comparison, it seems clear the need to improve the prediction capacity of shear strength models available in codes and literature. This issue will be addressed in the 0.

The tests presented herein can provide a useful contribution to enlarge the relatively limited experimental database on existing hollow circular RC piers. In particular, the experimental analysis of all the sources of deformability characterizing cyclic response can be a valid reference for the proposal/validation of nonlinear modeling approaches and capacity models for seismic assessment of existing bridge structures.

References

Biskinis D., Fardis M. N. (2010). Deformations at flexural yielding of members with continuous or lap-spliced bars. Structural concrete; 11(3): 127-138.

Biskinis D.E., Roupakias G.K., Fardis M.N. (2004). Degradation of shear strength of reinforced concrete members with inelastic cyclic displacement. ACI Structural Journal, 101(6):773–83.

Blandon CA, Priestley MJN. Equivalent viscous damping equations for direct displacement based design. Journal of earthquake Engineering 2005; 9(sup2): 257-278.

Cardone D. Displacement limits and performance displacement profiles in support of direct displacement-based seismic assessment of bridges. Earthquake Engineering & Structural Dynamics 2014; 43(8): 1239-1263.

CEN (2005) European standard EN1998-3. Eurocode 8: design provisions for earthquake resistance of structures – Part 3: assessment and retrofitting of buildings. European Committee for Standardisation, Brussels

CEN [2004a] European Standard ENV 1998-1-1/2/3. Eurocode 8: Design provisions for earthquake resistance of structures – Part I: General rules. Technical Committee 250/SC8, Comité Européen de Normalisation, Brussels, 2004.

Circolare 617. Circolare del Ministero dei Lavori Pubblici n. 617 del 2/2/2009. Istruzioni per l'applicazione delle "Nuove norme tecniche per le costruzioni" di cui al D.M. 14 gennaio 2008. G.U. n. 47 del 26/2/2009, 2009. (in Italian)

Fardis M. N. (2007). LESSLOSS–Risk mitigation for earthquakes and landslides. Guidelines for displacement-based design of buildings and bridges. Report n 5/2007." (2007).

Federal Emergency Management Agency (1997). NEHRP Guidelines for the Seismic Rehabilitation of Buildings. FEMA 273, Washington, D.C.

Kowalsky M. J. and Priestley M. J. N. (2000) Improved analytical model for shear strength of circular reinforced concrete columns in seismic regions. ACI Structural Journal. 97(3), 388–396.

Kowalsky MJ, Priestley MJN, MacRae GA. Displacement-based design of RC bridge columns in seismic regions, Earthquake engineering & structural dynamics 1995; 24(12): 1623-1643.

Mander JB, Priestley MJN, Park R. Theoretical stress-strain model for confined concrete. ASCE Journal of Structural Engineering 1988, 114(8): 1804-1826.

Priestley M. J. N., Seible F., and Calvi G. M. (1996). Seismic design and retrofit of bridges. Wiley, New York.

Priestley M. J. N., Verma R. and Xiao Y. (1994). Seismic shear strength of reinforced concrete columns. ASCEJ. Struct. Engrg, 120 (8) 2310-2329.

Priestley MJN, Calvi GM, Kowalsky MJ. Displacement-based seismic design of structures. Pavia, Italy: IUSS press, 2007.

Priestley MJN. Myths and fallacies in earthquake engineering. Revisited. Pavia, Italy: IUSS press, 2003.

Turmo J., Ramos G., Aparicio A. C. (2009). Shear truss analogy for concrete members of solid and hollow circular cross section. Engineering Structures, 31(2): 455-465.

Chapter 6

SHEAR STRENGTH AND DEFORMABILITY OF RC BRIDGE COLUMNS WITH HOLLOW RECTANGULAR CROSS SECTION

Hollow section piers are a widespread structural solution for highway bridges. While the flexural response of this structural typology can be considered completely defined, their shear capacity assessment is still an open issue. Quite few experimental studies are available in literature focusing on this topic. Moreover, despite their widespread use, none of the current codes addresses specific attention to shear assessment of RC hollow core members, both for design and assessment.

From the results of the preliminary comparison, carried out in the section 4.5 of the present work, between experimental results and main code-based shear strength models, the need to assess the effectiveness and the reliability of these models for hollow rectangular columns has been highlighted. Moreover, the quite recent progress toward displacement-based approaches for design and assessment, requires models able to define the drift value beyond which shear failure is expected. It has been well established that the shear strength models are not adequate for estimating the displacement at shear failure. Consequently, during the last decades, several drift-based methods to evaluate the shear failure have been proposed. The majority of these models has an empirical nature, based on experimental results of buildings columns with solid rectangular section, collected in different databases.

In order to assess the reliability of the existing shear capacity models in

predicting the shear failure, in this chapter an experimental database of tests on hollow rectangular columns will be collected and integrated with the tests presented in this work. Then, a comparison between experimental and predicted shear capacity values will be carried out considering the main capacity models, both in terms of force and displacement. Based on the results of the comparison, some improvements in shear strength assessment are discussed and proposed. Finally, a new empirical drift-capacity model based on the observations from the column database is developed and proposed.

6.1 Experimental database

The assessment of the shear capacity is a crucial issue for existing RC columns. While for ordinary columns with solid cross section several capacity models are available in literature and codes, concerning hollow rectangular columns, none ad-hoc model is suggested in literature and adopted in codes. It is clear the need to investigate the applicability of the existing models to this structural typology, and to develop some improvements or new proposal. To the aim a database of 28 experimental tests is collected, representing the experimental state-of-the-art about RC columns with hollow rectangular cross section and exhibiting a shear failure, occurred with or without flexural yielding. All the considered specimens were tested under unidirectional cyclic lateral load in single curvature. They presented a fixed-end at the bottom (cantilever scheme) and uniform longitudinal details throughout the height (no reinforcement variations, such as bars cut-off).

The main properties of the collected tests are included in the following ranges:

- Concrete cylindrical compressive strength: $17.0 \leq f_c \leq 61.1$ (MPa)
- Yield stress of longitudinal reinforcement: $418 \leq f_y \leq 625$ (MPa)
- Longitudinal reinforcement ratio: $0.88 \leq \rho' \leq 1.88$ (%)
- Yield stress of transverse reinforcement: $363 \leq f_{yw} \leq 655$ (MPa)
- Transverse reinforcement ratio: $0.09 \leq \rho'' \leq 0.52$ (%)
- Axial load ratio: $0.05 \leq P/A_c \cdot f_c \leq 0.22$ (-)
- Tie spacing to depth ratio: $0.08 \leq s/H \leq 0.30$ (-)
- Aspect ratio: $1.50 \leq L_V/H \leq 3.60$ (-)

In the previous list, the axial load ratio is evaluated as the ratio between the applied axial load P and the product between the concrete compressive strength f_c and the concrete area A_c (the gross section area minus the void); the aspect ratio (L_V/H) is defined as the ratio between the shear span L_V and the cross section depth H (assumed as the dimension along the loading direction); the longitudinal reinforcement ratio ρ' is evaluated with respect to the concrete area, namely $\rho' = A_l / A_c$; the transverse reinforcement ratio ρ'' is computed as the ratio between the total area of transverse reinforcement in the loading direction and the product of cross-sectional width (assumed as twice the web thickness $b_w = 2t_w$) times the tie spacing s; f_y and f_{yw} are the yielding stresses for longitudinal and transverse reinforcement, respectively.

The original experimental lateral load-deformation relations for the selected columns are presented in Appendix 6.

Table 6.1 shows geometry and reinforcement details of the test specimens included in the database. In this table, B is the external width of the column cross section, while the remaining terms have been already defined above. Table 6.2 shows material properties, characteristic values of lateral force (V) and drift ratio (DR, defined as displacement to shear span ratio), and failure modes (FM), as defined in the following.

For the specimens failing in shear after flexure yielding (FS-failure mode), the IDR_y corresponding to first flexural yielding (i.e., for which the first bar in tension reaches the nominal yield stress) is assumed equal to the experimental value, if declared. Otherwise, a section analysis is performed, assuming the Mander et al. (1988) stress-strain model for concrete, and elastic-plastic with strain hardening stress-strain relationship for steel. As a result, the moment M_y corresponding to first yielding condition is computed, from which the corresponding lateral load V_y is derived, known the shear span. The DR_y is derived by the intersection between the horizontal line corresponding to V_y and the backbone curve of the global response, namely the force-deformation curve that envelopes the entire cyclic response (Figure 6.1).

The shear strength V_{test} is assumed as the maximum value of the lateral force reached during the test. The corresponding drift ratio (namely, the displacement to shear span ratio) is referred as DR_{max}. The drift ratio at shear failure (DR_s) is determined based on the experimental backbone curve. Shear failure is conventionally defined by the displacement corresponding to a drop in lateral load below 80% of the maximum shear (V_{test}). This definition of the

shear failure occurrence is consistent with that generally used in literature within the context of a displacement-based assessment (Sezen, 2002; Elwood and Moehle, 2004; Pujol et al., 1999; Kato and Ohnishi, 2002).

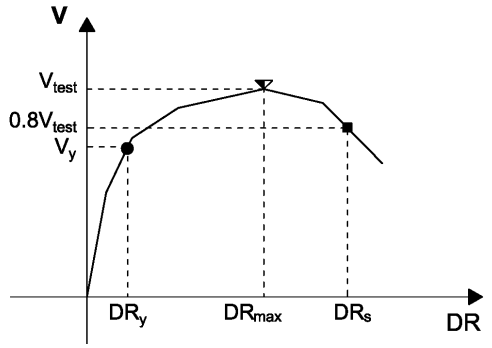

Figure 6.1. Definition of the characteristic points on the experimental envelope

When the shear strength does not drop below the 80% of V_{test}, the DR_s is taken as the maximum-recorded displacement, and thus it somehow represents a lower bound of the true displacement at shear failure. Note that, since all the collected tests were performed under cyclic loadings, two possible values of each characteristic point could be considered, eventually different. In this study, the considered values are those corresponding to the loading direction for which the maximum lateral load is reached.

Regarding the failure mode definition of the specimens of the database, it has been already specified that for all tests, a shear failure occurred, with or without flexural yielding. The failure mode definition (namely, S or FS mode) is not coherent among the various Authors. Some Authors defined the failure mode based on phenomenological aspects (analysis of the damage evolution) and capacity model predictions; some others had adequate instrumentation (strain gauges on longitudinal bars located at the critical section) to check the achievement of yielding. In order to uniform the failure mode definition, an unequivocal definition has been used in this study, based on the above-described values of lateral load (V_y) and drift ratio (DR_y) at first yielding.

Finally, in Table 6.2, the ductility demands (μ), namely the ratios between the DR demand and the DR_y, are reported for the peak and the shear failure conditions, identified as μ_{max} and μ_s respectively.

Table 6.1. Geometry and reinforcement details

ID	Specimen	H (mm)	B (mm)	t_w (mm)	L_V (mm)	s (mm)	ρ' (%)	ρ'' (%)
Calvi et al., (2005)								
1	S250	450	450	75	900	75	1.07	0.13
2	S500	450	450	75	900	75	1.07	0.13
3	S750	450	450	75	900	75	1.07	0.13
4	T250	450	450	75	1350	75	1.79	0.25
5	T500A	450	450	75	1350	75	1.79	0.25
6	T500B	450	450	75	1350	75	1.79	0.25
7	T750	450	450	75	1350	75	1.79	0.25
Delgado, (2009)								
8	PO1-N1	450	450	75	1400	75	1.79	0.20
9	PO1-N2	450	450	75	1400	75	1.79	0.09
10	PO1-N3	450	450	75	1400	75	1.79	0.09
11	PO1-N4	450	450	75	1400	75	1.79	0.09
12	PO1-N5	450	450	75	1400	75	1.79	0.09
13	PO1-N6	450	450	75	1400	75	1.79	0.19
14	PO2-N1	900	450	75	1400	75	1.79	0.20
15	PO2-N2	900	450	75	1400	75	1.79	0.09
16	PO2-N3	900	450	75	1400	75	1.79	0.09
17	PO2-N4	900	450	75	1400	75	1.79	0.09
18	PO2-N5	900	450	75	1400	75	1.79	0.09
19	PO2-N6	900	450	75	1400	75	1.79	0.19
Cassese et al., (2017)								
20	P3	400	600	100	900	120	0.88	0.12
21	P4	600	400	100	900	120	0.88	0.12
Mo and Nien, (2002)								
22	HI-2-a	500	500	120	1800	40	1.88	0.52
23	HI-1-b	500	500	120	1500	40	1.88	0.52
24	HI-0-b	500	500	120	1500	40	1.88	0.52
Yeh, Mo and Yang, (2002)								
25	MI1	1500	1500	300	5400	150	1.29	0.28
26	MI2	1500	1500	300	5400	150	1.29	0.28
Yeh et al., (2002)								
27	PI2	1500	1500	300	3500	200	1.72	0.26
Mo et al., (2004)								
28	NI1-b	500	500	120	1500	50	1.88	0.24

Table 6.2. Material properties, axial load ratio and characteristic values of the experimental response

ID	Specimen	f_c (MPa)	f_y (MPa)	f_{yw} (MPa)	v_a (%)	DR_y (%)	DR_s (%)	V_{test} (kN)	FM (-)	μ_{max} (-)	μ_s (-)
Calvi et al., (2005)											
1	S250	35.0	550	550	0.06	0.65	2.18	217	FS	3.4	3.4
2	S500	23.7	550	550	0.19	0.65	1.48	247	FS	1.2	2.3
3	S750	32.3	550	550	0.21	0.84	1.30	297	FS	1.3	1.5
4	T250	30.3	550	550	0.07	1.20	2.71	217	FS	1.9	2.3
5	T500A	29.7	550	550	0.15	0.95	2.10	209	FS	1.1	2.2
6	T500B	32.7	550	550	0.14	1.02	2.69	226	FS	2.2	2.6
7	T750	30.8	550	550	0.22	1.20	2.00	258	FS	1.7	1.7
Delgado, (2009)											
8	PO1-N1	19.8	625	390	0.11	-	1.72	190	S	-	-
9	PO1-N2	27.9	435	437	0.08	-	2.52	130	S	-	-
10	PO1-N3	27.9	435	437	0.08	-	2.52	130	S	-	-
11	PO1-N4	28.5	560	443	0.08	-	1.79	170	S	-	-
12	PO1-N5	28.5	560	443	0.08	-	1.79	170	S	-	-
13	PO1-N6	28.5	560	443	0.08	1.20	2.14	210	FS	1.4	1.8
14	PO2-N1	19.8	625	390	0.07	-	1.73	240	S	-	-
15	PO2-N2	27.9	435	437	0.05	-	1.79	190	S	-	-
16	PO2-N3	27.9	435	437	0.05	-	1.79	220	S	-	-
17	PO2-N4	28.5	560	443	0.05	-	2.14	190	S	-	-
18	PO2-N5	28.5	560	443	0.05	-	2.14	200	S	-	-
19	PO2-N6	28.5	560	443	0.05	-	2.86	250	S	-	-
Cassese et al., (2017)											
20	P3	17.0	540	655	0.05	0.62	1.35	278	FS	2.0	2.2
21	P4	17.0	540	655	0.05	0.62	2.53	193	FS	3.6	4.1
Mo and Nien, (2002)											
22	HI-2-a	61.1	476	363	0.13	1.06	4.09	350	FS	1.8	3.9
23	HI-1-b	50.5	476	363	0.11	1.05	4.62	364	FS	1.7	4.4
24	HI-0-b	49.7	476	363	0.06	1.01	4.75	302	FS	2.2	4.7
Yeh, Mo and Yang, (2002)											
25	MI1	33.6	476	480	0.09	1.08	4.67	2350	FS	2.4	4.3
26	MI2	29.1	476	480	0.21	1.24	4.30	2610	FS	1.9	3.5
Yeh et al., (2002)											
27	PI2	32.0	418	420	0.08	0.52	2.13	2650	FS	2.6	4.1
Mo et al., (2004)											
28	NI1-b	20.2	476	405	0.14	1.01	4.23	270	FS	2.1	4.2

v_a: axial load ratio, defined as $P/A_c f_c$

6.2 Shear strength evaluation

Seismic bridge design philosophy is to pursue energy dissipation by ductile flexural hinges at the piers base, unlike columns used in building frames that are typically designed following the weak beam-strong column philosophy for seismic resistance (Priestley et al., 1996; Paulay and Priestley, 1992). Brittle shear failure of bridge piers clearly has to be prevented to avoid disastrous collapse, and special attention has to be paid also to shear strength degradation with increasing flexural ductility demand. In fact, shear resisting mechanisms typical of hollow RC columns are very similar to those characterizing tube sections, depending mainly on webs aspect ratio. In particular, in terms of degradation mechanisms, small thickness limits the confined concrete core, crucial to seismic energy dissipation (Kim et al., 2012). As known, reinforced concrete (RC) hollow section piers are a widespread structural solution for bridge structures, due to their economic and structural convenience. Despite their widespread use, none of the current codes addresses specialized attention to shear strength of RC hollow core members, both for design and assessment (Turmo et al. 2009). Recent principal earthquakes around the world have highlighted the inadequate seismic performance of existing hollow piers, generally characterized by poor structural detailing and small web thickness (Kim et al., 2012). It becomes clear the relevance of a thorough investigation about the predictive capability of the models available in literature and codes. In particular, in the following the attention will be focused on the shear strength assessment. First, the main models available in literature, described in detail in the section 2.3.3, are briefly recalled. Then, the experimental shear strengths of the columns reported in the database is compared to the strengths calculated according to the considered models. Finally, a modification to the concrete contribution on the shear strength proposed by Kowalsky and Priestley (2000) is evaluated and proposed.

6.2.1. Considered shear strength models

The main models available in literature for the shear strength assessment are considered with the aim to carry out a comparison with the measured shear strength reported in the collected database (see Table 6.2). The analyzed models have been described and discussed in details in the section 2.3.3. In the

following, these models are recalled, focusing in particular on their formulations, in order to simplify the understanding of the comments derived from the comparison.

Aschheim and Moehle (1992)

The shear strength is calculated as the sum of strength contributions from transverse reinforcement, V_w, and concrete, V_c.

The shear strength degradation influences only the concrete contribution, V_c, through the degradation factor k decreasing with increasing displacement ductility (μ). The contribution of transverse reinforcement, V_w, is computed according to the well-known truss analogy. The corresponding formulations are recalled below:

$$V_c = 0.3\left(k + \frac{P}{13.8A_c}\right)\sqrt{f_c}(0.8A_c) \tag{6.1}$$

$$k = \frac{4-\mu}{3}; 0 \le k \le 1 \tag{6.2}$$

$$V_w = \frac{A_{sw} f_{yw} d}{s \tan(30°)} \tag{6.3}$$

where, A_c is the cross-sectional area, A_{sw} is the area of the transverse reinforcement, d is the effective depth (distance from extreme compression fiber to centroid of longitudinal tension reinforcement), and μ is the ductility demand, assumed here as μ_{max} (see Table 6.2) consistently with the model assumption. All the remaining terms have been defined above.

Kowalsky and Priestley (2000)

The shear strength is calculated as the sum of contributions from concrete, V_c, transverse reinforcement, V_w, and arch mechanism associated with axial load, V_p. The shear strength degradation influences only the contribution due to concrete, through the degradation factor k that decreases with increasing displacement ductility (μ). The corresponding formulations are reported

below:

$$V_c = \alpha\beta k\sqrt{f_c}(0.8A_g) \tag{6.4}$$

$$1 \le \alpha = 3 - \frac{L_V}{H} \le 1.5 \tag{6.5}$$

$$\beta = 0.5 + 20\rho' \le 1 \tag{6.6}$$

$$V_w = \frac{A_{sw}}{s} f_{yw}(d' - c)\cot(\theta) \tag{6.7}$$

$$V_P = P\tan(\alpha) = \frac{H - c}{2L_V} P \tag{6.8}$$

where, c is the neutral axis depth, d' is the distance parallel to the applied shear between centers of peripheral hoop, μ is assumed as μ_{max} (see Table 6.2), consistently with the model assumption. All the remaining terms have been defined above. Note that the effective shear area is assumed here as 0.8 times the cross-sectional area (A_c). The coefficient k, is as assumed equal to 0.29 when the displacement ductility (μ) is less than 2 and 0.05 when μ is more than 8, and decrease linearly between these two values.

Sezen and Moehle (2004)

Shear strength is computed as the sum of strength contributions from transverse reinforcement, V_w, and concrete, V_c. The degradation factor k factor multiplies here both transverse reinforcement and concrete contributions. The corresponding formulations are reported below:

$$V_c = k\left(\frac{0.5\sqrt{f_c}}{L_V/d}\sqrt{1 + \frac{P}{0.5\sqrt{f_c}A_c}}\right)0.8A_c \tag{6.9}$$

$$V_s = k\frac{A_{sw} f_{yw} d}{s} \tag{6.10}$$

where all terms have been already defined. The factor *k* decreases linearly from 1 to 0.7 for μ varying between 2 and 6. The ductility demand (μ), is assumed here as μ_s (see Table 6.2) consistently with the model assumption.

Biskinis et al., (2004)

The shear strength is calculated according to the regression model in equations (6.11) to (6.14) accounting for three contributions: the classical 45-degrees truss model (V_w), the concrete contribution (V_c), and the axial load contribution (V_P).

$$V_R = V_P + k\left(V_c + V_w\right) \tag{6.11}$$

$$V_c = 0.16\max(0.5;100\rho')\left(1 - 0.16\min\left(5;\frac{L_V}{H}\right)\right)\sqrt{f_c}\, b_w d \tag{6.12}$$

$$V_w = \frac{A_{sw}}{s}(d - d_0) f_{yw} \tag{6.13}$$

$$V_N = \frac{(H - c)}{2L_V}\min(P;0.55A_c f_c) \tag{6.14}$$

where, d_0 is the depth of the compression reinforcement layer, and b_w is the width of the section web (for hollow rectangular equal to twice the thickness). Also for this shear model, the coefficient k multiplies both the concrete and the transverse steel contributions. It varies linearly between 1.00 (non-degraded shear strength) and 0.75 for μ between 1 and 6. Consistently with the model assumptions, the ductility demand (μ), is assumed as μ_s.

6.2.2. Comparison of shear strength models with column database

In this section, the selected shear capacity models are applied to all the columns of the database, using the formulations as described above. The results of the comparison are reported in Table 6.3, where, in addition to the predicted to measured shear strengths ratio (labelled as E in the table, i.e. error in the prediction), the failure mode (FM_{pred}) predicted by each of the considered models is shown and compared to the experimental corresponding values, for all the specimens of the collected database.

As discussed in detail in the section 2.3.1, the predicted failure mode (FM_{pred}) is identified through a comparison between the predicted non-degraded and residual values of the shear strength ($V_{R,max}$ and $V_{R,min}$, respectively), with the maximum value of the lateral force reached during the test (V_{test}). When $V_{R,max}$ is lower than V_{test}, shear failure occurs limiting flexural response (S). When $V_{R,min}$ is higher than V_{test}, the flexural response can completely develop (F). In all the other cases, the element fails in FS mode.

The model by Aschheim and Moehle (1992) overestimates the experimental shear strength on average. In fact, it is characterized by a mean trend of the predicted to measured shear strength ratio (E) equal to 1.29 and a coefficient of variation (COV) equal to 0.28. The experimental failure mode is well-predicted for the 54% of the specimens. A similar trend characterizes the prediction of the model by Kowalsky and Priestley (2000), with a mean of 1.36 and a slightly less dispersion (COV = 0.23). In this case, the prediction of the experimental failure mode is obtained for the 50% of the specimens. Vice-versa, for the model by Sezen and Moehle (2004), a considerable underestimation and a substantially lower dispersion are observed. In particular, it is characterized by a mean of E equal to 0.75 and a COV of 0.13. This model is able to predict the 54% of the experimental failure modes. Finally, the model by Biskinis et al. (2004) is characterized by significant underestimation, with a mean of E equal to 0.73, and a quite large dispersion (COV of 0.30). In this case, the 50% of the experimental failure modes are well predicted.

Table 6.3. Shear strength comparison

ID	*Experimental*		*Aschheim and Moehle (1992)*		*Kowalsky and Priestley (2000)*		*Sezen and Moehle (2004)*		*Biskinis et al., (2004)*	
	V_{test} (kN)	FM (-)	E* (-)	FM_{pred} (-)	E* (-)	FM_{pred} (-)	E* (-)	FM_{pred} (-)	E* (-)	FM_{pred} (-)
Calvi et al., (2005)										
1	217	FS	0.45	FS	1.00	FS	0.74	FS	0.59	S
2	247	FS	0.83	S	1.05	FS	0.75	S	0.72	S
3	297	FS	0.85	S	1.09	FS	0.76	S	0.78	S
4	217	FS	0.94	FS	1.35	FS	0.74	S	0.72	S
5	209	FS	1.27	FS	1.53	F	0.85	S	0.93	S
6	226	FS	0.95	FS	1.43	FS	0.78	S	0.84	S
7	258	FS	1.02	FS	1.33	FS	0.77	S	0.85	S
Delgado, (2009)										
8	190	S	0.96	S	1.06	FS	0.61	S	0.60	S
9	130	S	1.45	FS	1.47	FS	0.81	S	0.80	S
10	130	S	1.45	FS	1.47	FS	0.81	S	0.80	S
11	170	S	1.12	FS	1.14	FS	0.62	S	0.62	S
12	170	S	1.12	FS	1.14	FS	0.62	S	0.62	S
13	210	FS	0.93	FS	1.12	FS	0.61	S	0.60	S
14	240	S	1.06	S	1.11	S	0.61	S	0.48	S
15	190	S	1.44	FS	1.39	FS	0.75	S	0.55	S
16	220	S	1.24	FS	1.20	FS	0.65	S	0.48	S
17	190	S	1.45	S	1.39	S	0.76	S	0.55	S
18	200	S	1.38	S	1.32	S	0.72	S	0.52	S
19	250	S	1.20	FS	1.21	FS	0.67	S	0.51	S
Cassese et al., (2017)										
20	278	FS	0.68	FS	1.18	FS	0.86	S	0.56	S
21	193	FS	0.41	FS	1.00	FS	0.70	S	0.48	S
Mo and Nien, (2002)										
22	350	FS	1.81	F	2.22	F	1.00	F	1.29	F
23	364	FS	1.51	FS	1.97	F	0.91	F	1.19	F
24	302	FS	1.42	FS	2.11	F	0.96	FS	1.16	FS
Yeh, Mo and Yang, (2002)										
25	2350	FS	1.06	FS	1.54	F	0.72	S	0.78	S
26	2610	FS	1.21	FS	1.58	F	0.76	FS	0.91	FS
Yeh et al., (2002)										
27	2650	FS	0.77	FS	1.32	FS	0.74	S	0.80	S
Mo et al., (2004)										
28	270	FS	0.96	FS	1.45	FS	0.69	FS	0.84	FS

E*: ratio of predicted to measured shear strengths (V_{pred}/V_{test})

In order to develop some critical comments to these results, it seems crucial to investigate deeply about the experimental basis of the considered shear capacity models. The model by Biskinis et al. (2004) is a regression model calibrated on a very large experimental database including also hollow piers. It is adopted by the Eurocode 8 part 3 (EC8/3, 2005) for existing buildings, and it is suggested by some literature studies for the shear capacity assessment of existing bridge piers (Fardis, 2007; Pinto et al., 2009). Nevertheless, this model confirms the underestimating trend highlighted from the experimental to predicted comparison related to the tests presented in the present work (see section 4.5) also for the comparison with the database.

The model by Sezen and Moehle (2004), adopted in ASCE/SEI 41-06 (2006), is based on experimental data from a database including only RC columns with solid rectangular cross section, inadequate and poorly detailed transverse reinforcement, failing in shear during the inelastic response. This may be the reason of the substantial underestimation in prediction the shear strength.

The model by Kowalsky and Priestley (2000) was developed based on 18 solid circular columns that failed in shear after yielding and 20 solid circular columns failing in shear before yielding. It is adopted by the U.S. Federal Highway Administration (FHWA, 2006) provisions document for seismic retrofitting of bridges. Aschheim and Moehle (1992) calibrated their model on a database of 51 scale models of bridge columns with solid square, rectangular and circular cross section, failing in shear after flexural yielding. The overestimation that characterize these two models may be related to the higher value of the concrete contribution to shear strength contribution deriving from the only solid sections considered.

The results of the comparison are depicted from Figure 6.2 to Figure 6.5, in which the ratio between predicted and experimental shear strength is represented for each capacity model, separately.

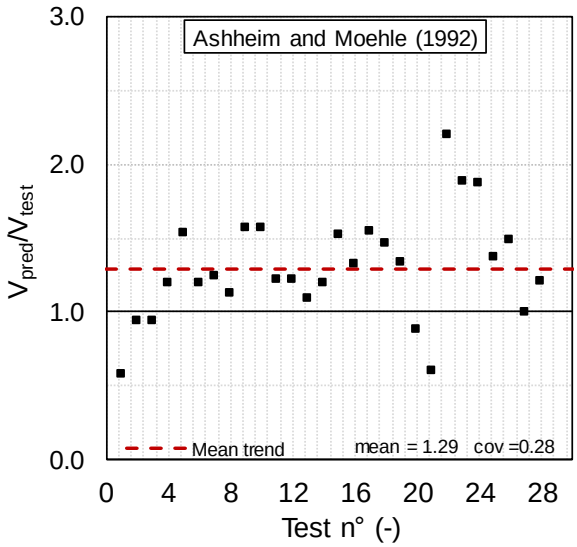

Figure 6.2. Ratio of predicted to measured shear strength - Aschheim and Moehle (1992)

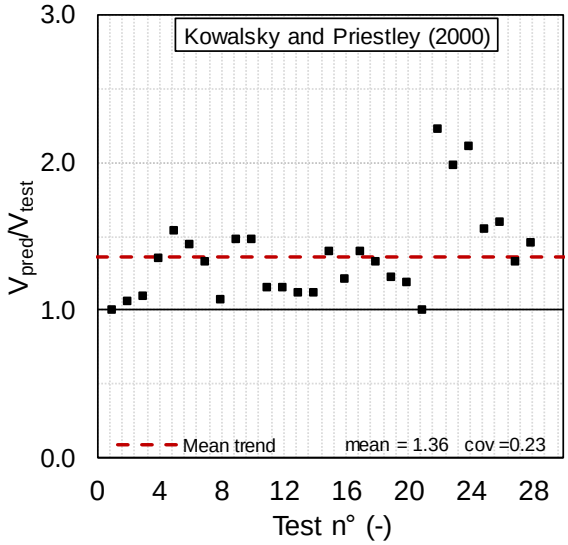

Figure 6.3. Ratio of predicted to measured shear strength - Kowalsky and Priestley (2000)

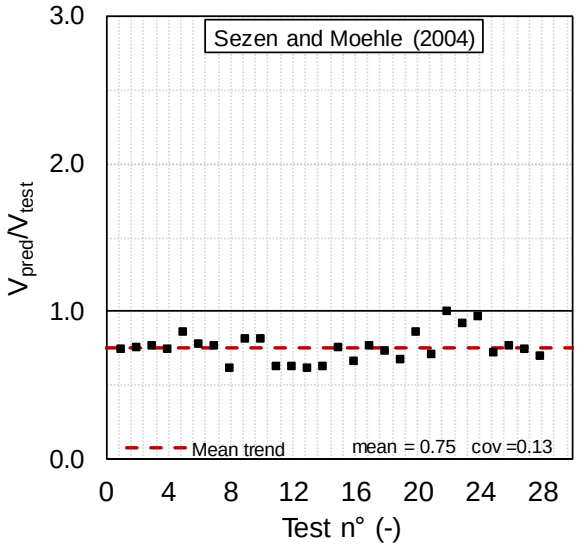

Figure 6.4. Ratio of predicted to measured shear strength - Sezen and Moehle (2004)

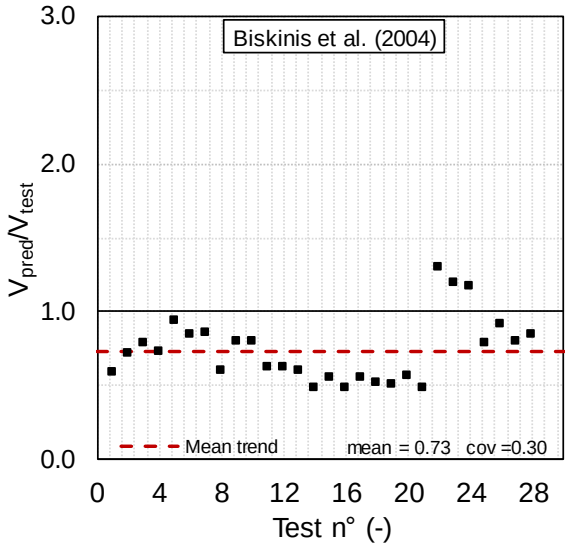

Figure 6.5. Ratio of predicted to measured shear strength - Biskinis et al., (2004)

6.2.3. Proposed modifications to improve shear capacity assessment

The number of experimental tests on hollow rectangular RC columns available in literature is not sufficient to develop a reliable shear capacity model. Nevertheless, it seems interesting to discuss about reasonable improvements of existing models, based on the comments of the comparison results reported in the previous section. In particular, the model by Kowalsky and Priestley (2000) adopts a concrete contribution to shear strength characterized by an effective shear area of $0.8A_c$ and a factor β taking into account the clamping effect of the longitudinal reinforcement (see Equation 6.4). In seems reasonable to modify these two terms in order to apply this model to hollow rectangular columns. As regards the effective shear area for hollow rectangular columns subjected to cyclic shear forces (seismic loading), it is well-known that shear stress distribution is substantially concentrated on the webs, while the flanges are essentially involved in the flexural response. Therefore, for hollow rectangular sections, it can be assumed that only the confined concrete of the webs gives a contribution to the shear strength of the columns (Figure 6.6).

The β factor takes into account the beneficial effect of the dowel action of the longitudinal reinforcement on the shear resisting mechanisms. Its formulation has been calibrated on experimental results of solid circular columns. Considering two RC columns, whose cross sections have the same external dimensions, but one of them solid and the other characterized by a void (hollow section), it is known that the concrete contribution to shear strength is higher for solid section. If the β factor is computed as reported in Equation 6.6, the apparent effect of having a larger concrete contribution is obtained, when, actually, there is less concrete and the same amount of reinforcement. Therefore, it makes more sense to compute β factor on a solid section with the same external dimensions of the actual section (Calvi et al., 2005). By applying these modifications to Equations (6.4) and (6.6), the following equations are obtained:

$$V_c = \alpha\beta k\sqrt{f_c}\cdot(2t_w d) \tag{6.15}$$

$$\beta = 0.5 + 20\rho' \le 1$$
$$\rho' = \frac{A'}{BH} \tag{6.16}$$

where the effective depth of the rectangular webs d is assumed as 0.8 times the gross-section dimension parallel to the applied shear (H), t_w is the thickness of the webs, A' is the total area of longitudinal reinforcement, B and H are the external dimensions of the cross section perpendicular and parallel to the applied shear, respectively (see Figure 6.6)

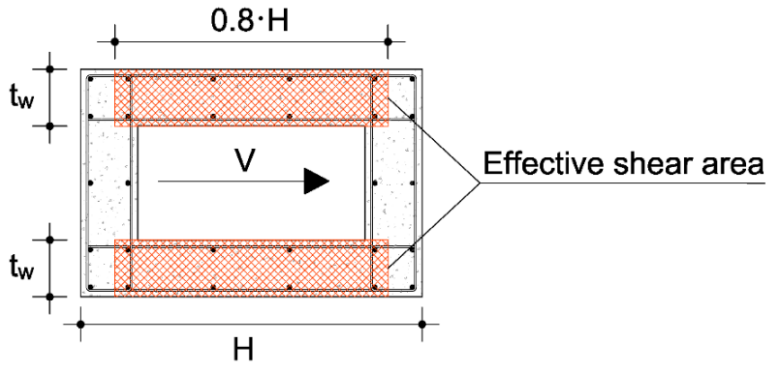

Figure 6.6. Proposed effective shear area

Table 6.4 summarizes the comparison between the predicted shear strength values and failure modes with the corresponding measured ones. The proposed model is characterized by a mean trend of the predicted to measured shear strength ratio equal to 1.01 and a coefficient of variation (COV), of 0.34. Therefore, the capability in prediction of the experimental shear strength is substantially improved through the proposed modifications. A considerable improvement is observed also in terms of experimental failure mode prediction, with an exact prediction for 71% of the specimens.

Table 6.4. Shear strength comparison for the proposed modified version of the model by Kowalsky and Priestley (2000)

ID	*Experimental*		*Proposed modified Kowalsky and Priestley (2000)*		
	V_{test} (kN)	FM (-)	V_{pred} (kN)	V_{pred}/V_{test} (-)	FM_{pred} (-)
Calvi et al., (2005)					
1	217	FS	173	0.80	FS
2	247	FS	217	0.88	S
3	297	FS	273	0.92	S
4	217	FS	229	1.06	FS
5	209	FS	259	1.24	F
6	226	FS	261	1.15	FS
7	258	FS	279	1.08	FS
Delgado, (2009)					
8	190	S	151	0.80	S
9	130	S	131	1.01	S
10	130	S	131	1.01	S
11	170	S	133	0.78	S
12	170	S	133	0.78	S
13	210	FS	173	0.82	FS
14	240	S	153	0.64	S
15	190	S	130	0.68	S
16	220	S	130	0.59	S
17	190	S	128	0.67	S
18	200	S	128	0.64	S
19	250	S	167	0.67	S
Cassese et al., (2017)					
20	278	FS	278	1.00	FS
21	193	FS	149	0.77	FS
Mo and Nien, (2002)					
22	350	FS	658	1.88	F
23	364	FS	607	1.67	F
24	302	FS	531	1.76	F
Yeh, Mo and Yang, (2002)					
25	2350	FS	2997	1.28	F
26	2610	FS	3517	1.35	F
Yeh et al., (2002)					
27	2650	FS	2815	1.06	FS
Mo et al., (2004)					
28	270	FS	322	1.19	FS

Figure 6.7 shows the predicted to measured shear strengths ratio for all the columns of the database, evaluated by applying the proposed modifications to the model by Kowalsky and Priestley (2000).

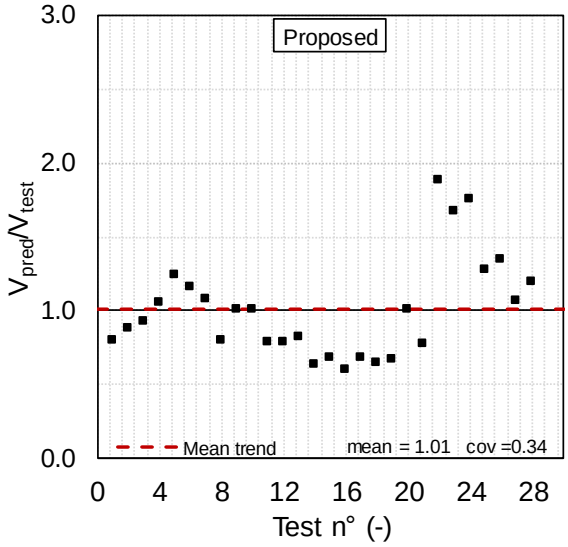

Figure 6.7. Ratio of predicted to measured shear strengths for the proposed modified version of the model by Kowalsky and Priestley (2000)

6.3 Drift at shear failure

As discussed in the previous section, several models have been developed to represent the degradation of shear strength with increasing inelastic deformations. Although these models are useful for estimating the column capacity for conventional force-based design and assessment, the quite recent progress toward displacement-based approaches for design and assessment, requires models able to define the drift value beyond which shear failure is expected. Ideally, a shear strength model could be used to estimate the drift at shear failure, as that at which the idealized backbone curve intercepts the shear-failure curve. Actually, it is well established that the shear strength models are not adequate for estimating the displacement at shear failure. This is because these models have been calibrated in order to obtain the best result in terms of shear strength given a displacement ductility. If the inverse process is performed, a small variation in shear strength, corresponds to a large change in estimated drift ratio at shear failure (Sezen, 2002). This is even truer if the

shear failure occurs after flexural yielding, since an almost horizontal line can generally represent the nonlinear flexural response of a column (Figure 6.8).

Moreover, the degrading shear strength models accounts for the benefic axial load effect on shear capacity. In fact, shear strength increase as compressive axial load increases. Hence, if the shear strength model is used to estimate the drift ratio at shear failure, an increase in axial load will result in an increase in the predicted drift at shear failure (Elwood and Moehle, 2005). This is in contrast with the experimental evidence for which an increase in the axial load may reduce the drift ratio at shear failure, as schematically reported in Figure 6.9 (it is known how, in general, high axial loads tend to increase the strength on one side and to reduce the ductility of the response on the other side).

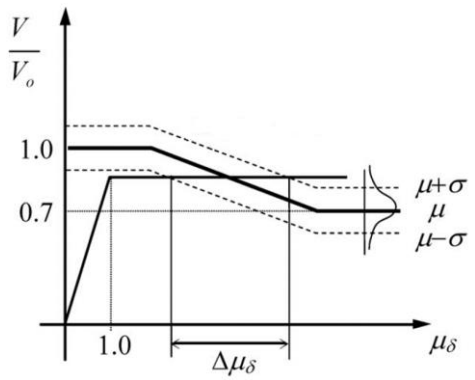

Figure 6.8. Variability of the drift at shear failure using a shear strength model by Sezen (2002) – adapted from Elwood and Moehle (2005)

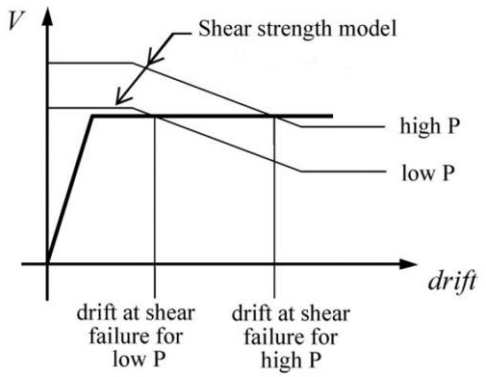

Figure 6.9. Variability of the drift at shear failure due to change of axial load – adapted from Elwood and Moehle (2005)

Consequently, it seems to be clear the reliability of drift-based methods to evaluate the shear failure with respect to force-based approaches. Most models for estimating the drift capacity of reinforced concrete columns are based on the performance of building columns with good seismic detailing. Such models assume that the response is dominated by flexural deformations, and use estimates of the ultimate concrete and steel strains to determine the ultimate curvatures the section can withstand. Generally, these models are not applicable to existing reinforced concrete columns, generally characterized by poor details and materials, since the degradation of the shear strength begins before the flexural deformation capacity can be achieved. In order to assess the shear drift capacity, these models cannot be used, since they does not take into account shear deformations and damages.

Various drift capacity models are available in literature, developed and proposed during the last decades, all developed for solid building columns. The majority of these has an empirical nature, based on experimental results of columns collected in different databases. In the following, the main drift capacity models are described and discussed. Later, their applicability to bridge columns with hollow rectangular sections is investigated. Finally, a new empirical model based on the observations from the column database (defined in the section 6.1) is developed and proposed.

6.3.1. Considered drift-at-shear-failure capacity models

Within the context of a performance-based seismic assessment, it is crucial the definition of displacement-based criteria for the identification of shear failure of RC members. Vertical members, namely columns, in particular, are subjected to higher shear demand during seismic events. Moreover, it is known that existing RC columns are generally characterized by poor details and materials, so they present high shear vulnerability. With the aim to evaluate the drift at shear failure of existing RC columns, various models have been developed during the last decades.

Aslani and Miranda (2005)

Aslani and Miranda (2005) on the basis of 92 cyclic tests of non-ductile RC columns with solid cross-section, defined four damage states for flexure-shear critical RC columns: light cracking, severe cracking, shear failure and loss of

axial carrying capacity. Lognormal fragility functions predict the probability of being in each damage state as a function of the column drift ratio, column axial load ratio and amount of transverse reinforcement. The third damage state (DS3) is used to identify the onset of column shear failure, manifested by the characteristic X-cracking and yielding of transverse reinforcement. The related equation that provides the drift ratio (DR) capacity at DS3 is reported in equation (6.17), where P, A_c, fc, ρ'' represent axial load, concrete area, compressive concrete strength and transverse reinforcement ratio in column, respectively.

$$DR_s = \frac{1}{0.26\frac{P}{A_c f_c \rho''} + 25.4} \geq \frac{1}{100} \tag{6.17}$$

Elwood (2004)

Elwood (2004) introduced an empirical model based on observations from the experimental database of 50 tests collected by Sezen (2002), characterized by observed shear failure after flexural yielding. According to this model, drift at shear failure is defined as that where shear resistance drops below 80%of the maximum shear recorded (V_{test}). When the shear strength does not drop below the 80% of V_{test}, the IDR_s is taken as the maximum displacement.

Author noted that the drift at shear failure depends on axial load ratio, transverse reinforcement ratio and maximum nominal shear stress (ν), the latter assumed as the ratio between the maximum experimental shear and the cross-sectional area (taken equal to $B \cdot d$ for solid and square sections). Drift-capacity model is expressed by the equation (6.18):

$$\mathrm{DR_s} = \frac{3}{100} + 4\rho'' - \frac{1}{40}\frac{\nu}{\sqrt{f_c}} - \frac{1}{40}\frac{P}{A_g f_c} \geq \frac{1}{100} \tag{6.18}$$

Zhu et al., (2007)

Zhu et al. (2007) developed two different drift-capacity models separately for shear-dominated and flexural dominated columns. In fact, a database of

125 columns representative of typical older reinforced concrete buildings was selected. All these columns were characterized by degradation in the lateral load capacity, but for some of them the degradation was due to flexural deformations (flexural dominated columns), for some others the degradation was related to shear failure occurred before or after yielding of the longitudinal reinforcement (shear dominated columns).

In order to determine the column failure mode, therefore the corresponding drift-capacity model to be used, Zhu et al. (2007) proposed an alternative method, called *two-zone classification,* based on three columns parameters: the plastic shear demand to shear strength ratio (V_p/V_R), the aspect ratio (L_V/d), and the transverse reinforcement ratio (ρ''). The plastic shear demand of the column is determined by its maximum moment capacity divided by the shear span, $V_p = M_{max}/L_V$, where the maximum moment capacity, M_{max}, is computed through a moment-curvature analysis for the column's cross section using the Mander concrete constitutive model (Mander et al., 1988) and Burns-Siess steel constitutive model (Burns and Siess, 1962). The column shear strength, V_R, is calculated according to a shear strength model proposed by Sezen and Moehle (2004). The columns of the database were divided into two zones, namely 85 flexure dominated columns (Zone F, i.e. flexural failure mode) and 40 shear dominated columns (Zone S, i.e. flexure-shear or shear failure modes).

The classification was performed according to the flowchart reported in Figure 6.10. Columns with very low transverse reinforcement ratio ($\rho'' \leq 0.002$) were always categorized into Zone S. The columns for which the aspect ratio was less than 2.0 ($L_V/d \leq 2$) or the plastic shear demand to shear strength ratio was higher than 1.05 ($V_p/V_R \geq 1.05$), were classified into Zone S. The remaining were categorized as flexural dominated columns (Zone F).

Since the mechanics leading to a 20% loss in shear capacity is expected to be different for shear-dominated columns and flexure-dominated columns a separate drift capacity model is developed for columns failing in each zone. In particular, for Zone S columns, the drift at shear failure is influenced by transverse reinforcement ratio (ρ''), hoop spacing ratio (s/d), aspect ratio (L_V/d), and axial load ratio ($P/(A_c f_c)$), according to Authors.

The formulation expressing the relation between these parameters and the drift at shear failure is reported in equation (6.19):

$$DR_s = 2.02\rho'' - 0.025\frac{s}{d} + 0.013\frac{L_V}{d} - 0.031\frac{P}{A_c f_c} \quad (6.19)$$

in which, s is the transverse reinforcement spacing. It is noteworthy to observe that the previous equation is referred to the median value of the predicted drift at shear failure.

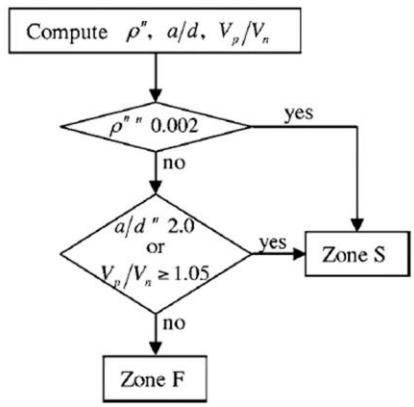

Figure 6.10. Flowchart of two-zone column classification method – adapted from Zhu et al., (2005)

6.3.2. *Comparison of drift capacity models with the column database*

In this section, the selected drift capacity models are applied to all the columns of the database. Before the application of the above-reported formulations, some statements are necessary.

The columns of the databases collected by the Authors described in the previous section are characterized by solid square and rectangular cross-sections. Therefore, with the aim to investigate the applicability of such drift capacity models to hollow rectangular columns, the transverse reinforcement ratio (ρ'') and the maximum nominal shear stress (v) have to be defined in a consistent way.

With regard to the first parameter, two possible definitions of transverse reinforcement will be adopted herein, depending on the assumed width b_w of the section:

- transverse reinforcement ratio is evaluated assuming b_w equal to external width of the hollow section (dimension perpendicular to

the applied shear force):

$$\rho'' = \frac{A_{sw}}{B \cdot s} \tag{6.20}$$

- transverse reinforcement ratio is evaluated assuming b_w equal to twice the thickness of the webs of the hollow section:

$$\rho'' = \frac{A_{sw}}{2 \cdot t_w \cdot s} \tag{6.21}$$

Two possible definitions of the maximum nominal shear stress (ν) (adopted only in the model by Elwood (2004)) will also be adopted, depending on the assumed effective shear area:

- the maximum recorded shear force V_{test} is assumed acting on the whole cross-sectional concrete area:

$$\nu = \frac{V_{test}}{A_c} \tag{6.22}$$

- the maximum recorded shear force V_{test} is assumed acting only on the two webs:

$$\nu = \frac{V_{test}}{2 \cdot t_w d} \tag{6.23}$$

The results of the comparison are depicted from Figure 6.11 to Figure 6.16 in which the measured DRs is reported on the horizontal axis and the DRs predicted by each capacity model, on the vertical axis. In particular, Figure 6.11 and Figure 6.12 show the comparison for the model by Aslani and Miranda (2005), in which transverse reinforcement ratio is computed as reported in equations (6.20) and (6.21), respectively. The comparison for the model by Elwood (2004) is reported in Figure 6.13 and Figure 6.14, where transverse reinforcement ratio is computed as reported in equations (6.20) and (6.21) and

maximum nominal shear stress is evaluated according to equations (6.22) and (6.23), respectively. Finally, Figure 6.15 and Figure 6.16 show the comparison for the model by Zhu et al (2007), assuming transverse reinforcement ratio computed as equations (6.20) and (6.21), respectively. In all the figures, mean value (Mean) and Coefficient of Variation (COV) for the predicted to measured DR_s ratios are specified.

The same results are presented in Table 6.5, where the drift values at shear failure (DR_s) predicted by each of the considered models are summarized and compared to the experimental corresponding values ($DR_{s,exp}$), for all the specimens of the collected database. In this case, the predicted DR_s are evaluated considering all the different definitions expressed from equations (6.20) to (6.23

For the model by Aslani and Miranda (2005), DR_s^1 is computed assuming eq. (6.21) and DR_s^2 assuming eq. (6.20). The same assumptions are adopted for Zhu et al. (2007). As regards the model by Elwood (2004), DR_s^1 is evaluated assuming equations (6.21) and (6.23), whereas DR_s^2 assuming equations (6.20) and (6.22). The predicted to measured ratio of DR_s are labelled as E. Void cells in Table 6.5 represent the cases of inapplicability of the corresponding models. In fact, the model by Elwood (2004) have to be applied, according to Author, only for columns failing in shear after flexural yielding, while the model by Zhu et al. (2007) define the drift at shear failure (DR_s) only for columns classified as shear failing (Zone S).

None of the analyzed models is able to predict the experimental values of drift at shear failure with adequate accuracy.

The model by Elwood (2004) underestimates the experimental drift at shear failure on average, both considering only webs and whole cross section. In fact, in the first case (DR_s^1) the mean of the predicted to measured ratio (E^1) is 0.81, while in the latter case (DR_s^2), the mean of E^2 is equal to 0.88, slightly better. In both the cases high dispersion in the prediction is observed, with a coefficient of variation, evaluated as the ratio between the standard deviation of E and the mean of E, of about 0.30. This model cannot be applied to eleven columns since they are characterized by brittle shear failure (before yielding of longitudinal reinforcement).

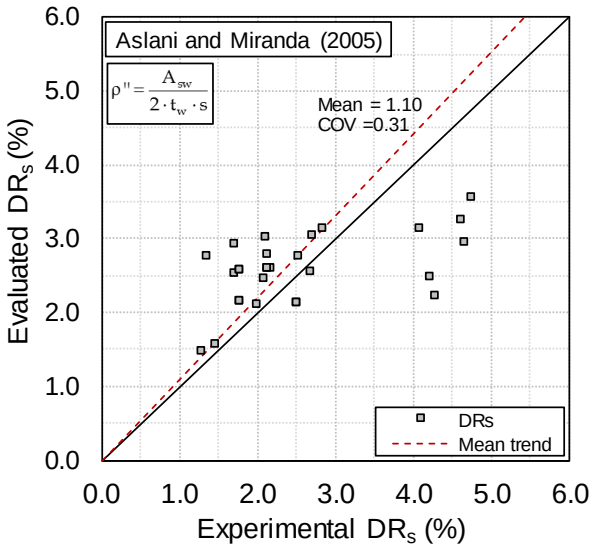

Figure 6.11. Predicted vs measured drift ratio at shear failure (DR_s) - Aslani and Miranda (2005)

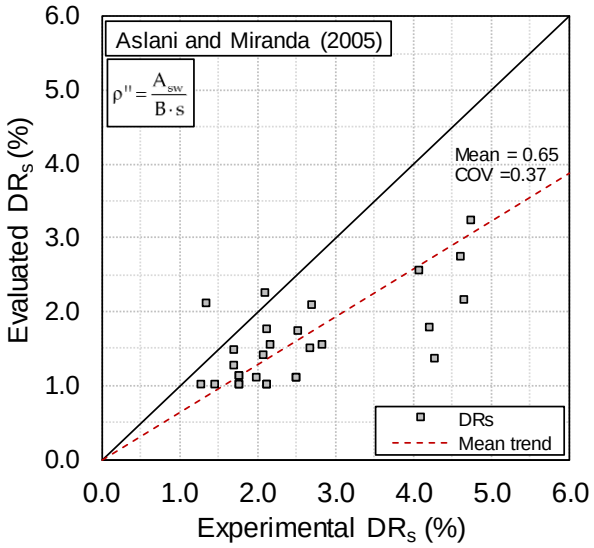

Figure 6.12. Predicted vs measured drift ratio at shear failure (DR_s) - Aslani and Miranda (2005)

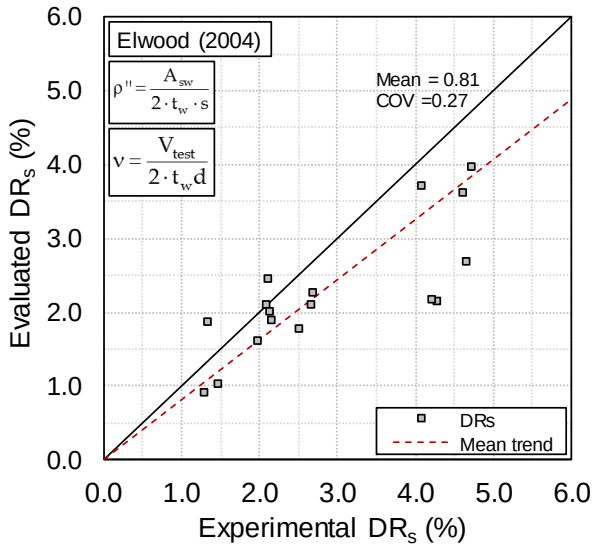

Figure 6.13. Predicted vs measured drift ratio at shear failure (DR_s) – Elwood (2004)

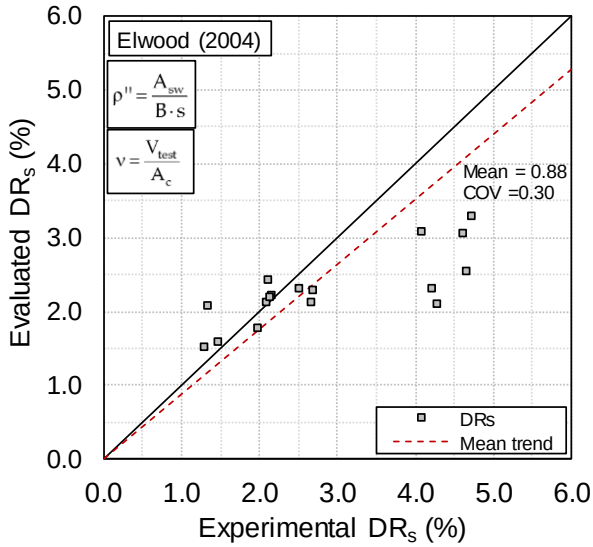

Figure 6.14. Predicted vs measured drift ratio at shear failure (DR_s) – Elwood (2004)

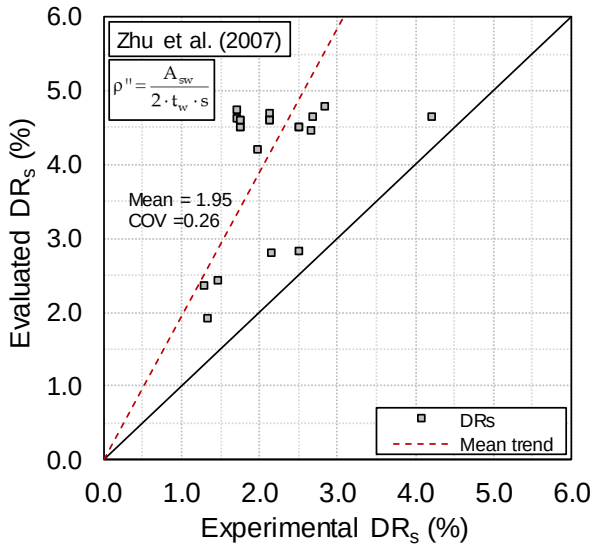

Figure 6.15. Predicted vs measured drift ratio at shear failure (DR_s) – Zhu et al. (2007)

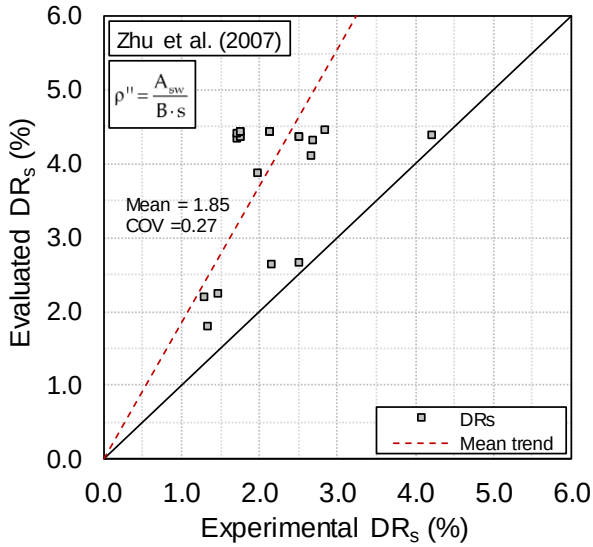

Figure 6.16. Predicted vs measured drift ratio at shear failure (DR_s) – Zhu et al. (2007)

Table 6.5. Drift at shear failure comparison

		Aslani and Miranda (2005)				*Elwood (2004)*				*Zhu et al., (2007)*			
ID	$DR_{s,exp}$ (%)	DR_s^1 (%)	DR_s^2 (%)	E^1 (-)	E^2 (-)	DR_s^1 (%)	DR_s^2 (%)	E^1 (-)	E^2 (-)	DR_s^1 (%)	DR_s^2 (%)	E^1 (-)	E^2 (-)
Calvi et al., (2005)													
1	2.18	2.59	1.54	1.19	0.71	1.88	2.20	0.86	1.01	2.79	2.62	1.28	1.20
2	1.48	1.56	1.00	1.05	0.68	1.00	1.57	0.68	1.06	2.40	2.23	1.62	1.51
3	1.30	1.47	1.00	1.13	0.77	0.89	1.49	0.69	1.15	2.34	2.17	1.80	1.67
4	2.71	3.03	2.08	1.12	0.77	2.24	2.28	0.83	0.84	4.63	4.30	1.71	1.59
5	2.10	2.45	1.39	1.16	0.66	2.09	2.11	1.00	1.00				
6	2.69	2.53	1.48	0.94	0.55	2.08	2.12	0.77	0.79	4.44	4.10	1.65	1.52
7	2.00	2.09	1.08	1.05	0.54	1.60	1.76	0.80	0.88	4.19	3.85	2.10	1.93
Delgado, (2009)													
8	1.72	2.51	1.45	1.46	0.84	-	-	-	-	4.59	4.32	2.67	2.51
9	2.52	2.11	1.10	0.84	0.43	-	-	-	-	4.48	4.35	1.78	1.73
10	2.52	2.11	1.10	0.84	0.43	-	-	-	-	4.48	4.35	1.78	1.73
11	1.79	2.13	1.11	1.19	0.62	-	-	-	-	4.48	4.36	2.51	2.44
12	1.79	2.13	1.11	1.19	0.62	-	-	-	-	4.48	4.36	2.51	2.44
13	2.14	2.77	1.74	1.29	0.81	1.98	2.18	0.93	1.02	4.67	4.42	2.18	2.06
14	1.73	2.90	1.26	1.68	0.73	-	-	-	-	4.72	4.39	2.74	2.54
15	1.79	2.56	1.00	1.43	0.56	-	-	-	-	4.57	4.41	2.56	2.47
16	1.79	2.56	1.00	1.43	0.56	-	-	-	-	4.57	4.41	2.56	2.47
17	2.14	2.58	1.00	1.20	0.47	-	-	-	-	4.57	4.42	2.13	2.06
18	2.14	2.58	1.00	1.20	0.47	-	-	-	-	4.57	4.42	2.13	2.06
19	2.86	3.11	1.52	1.09	0.53	-	-	-	-	4.76	4.45	1.67	1.56
Cassese et al., (2017)													
20	1.35	2.74	2.11	2.03	1.56	1.86	2.06	1.38	1.52	1.90	1.78	1.40	1.32
21	2.53	2.74	1.71	1.08	0.68	1.75	2.30	0.69	0.91	2.80	2.64	1.11	1.04
Mo and Nien, (2002)													
22	4.09	3.12	2.54	0.76	0.62	3.70	3.05	0.90	0.75	-	-	-	-
23	4.62	3.25	2.73	0.70	0.59	3.61	3.03	0.78	0.66	-	-	-	-
24	4.75	3.55	3.21	0.75	0.68	3.94	3.28	0.83	0.69	-	-	-	-
Yeh, Mo and Yang, (2002)													
25	4.67	2.95	2.14	0.63	0.46	2.66	2.52	0.57	0.54	-	-	-	-
26	4.30	2.21	1.34	0.52	0.31	2.12	2.08	0.49	0.48	-	-	-	-
Yeh et al., (2002)													
27	2.13	3.02	2.23	1.42	1.05	2.43	2.41	1.14	1.13	-	-	-	-
Mo et al., (2004)													
28	4.23	2.48	1.77	0.59	0.42	2.16	2.29	0.51	0.54	4.62	4.37	1.09	1.03
			Mean	1.10	0.65		Mean	0..81	0.88		Mean	1.95	1.85
			COV	0.31	0.37		COV	0.27	0.30		COV	0.26	0.27

The model by Zhu et al. (2007) considerably overestimates the experimental drift at shear failure. In fact, both considering only webs and whole cross section, the mean of the predicted DR_s is higher than 1.85, with a relatively high dispersion (COV of about 0.30). Moreover, this model cannot be applied to seven specimens, classified as flexural-dominated. Finally, for the model by Aslani and Miranda (2005) different prediction are obtained depending on the assumed transverse reinforcement ratio (ρ''). When ρ'' is computed according to eq. (6.21), namely considering only the webs of the cross section, a better prediction is obtained, with a mean of 1.10. Conversely, when ρ'' is computed according to eq. (6.20), this model considerably underestimates the experimental DR_s (mean equal to 0.65). In both the cases, high dispersion in prediction is observed, with COV higher than 0.30.

6.3.3. Proposed drift capacity model

The comparison reported in the previous section showed that none of the considered models is able to predict the experimental values of drift at shear failure with adequate accuracy. Moreover, high dispersion in the prediction characterizes all the models. Therefore, in this section, an ad-hoc drift capacity model to predict the shear failure of hollow rectangular columns is developed and proposed. The goal of developing a new model is to reduce the coefficient of variation and mean error prediction, providing a simple relationship that identifies the critical parameters influencing the drift at shear failure for shear-critical hollow bridge columns. First, several structural key parameters, potentially affecting the shear response of hollow rectangular columns, are identified. They are listed below:

- geometrical transverse reinforcement ratio (ρ'')
- mechanical transverse reinforcement ratio ($\omega'' = \rho'' f_{yw}/f_c$)
- geometrical longitudinal reinforcement ratio (ρ')
- aspect ratio (L_V/H)
- tie spacing to depth ratio (s/H)
- axial load ratio ($P/A_c f_c$)
- maximum nominal shear stress ($\nu = V_{test}/2t_w d$)
- width to thickness ratio ($B/2t_w$)
- void to solid area ratio (A_{void}/A_c)

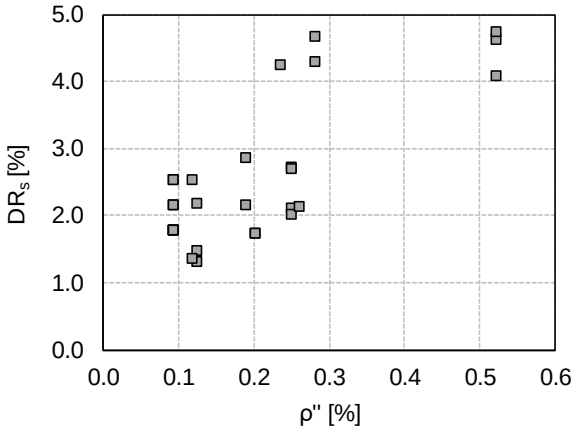

(a)

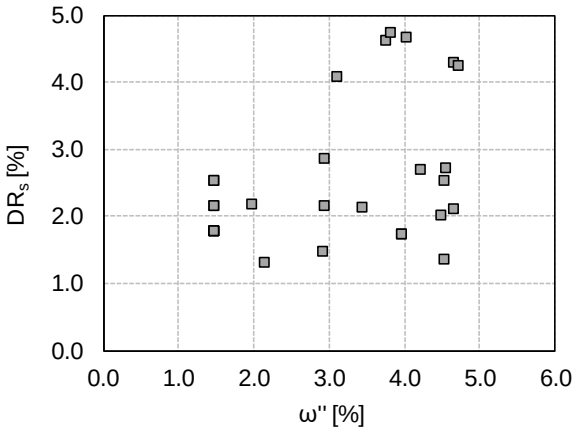

(b)

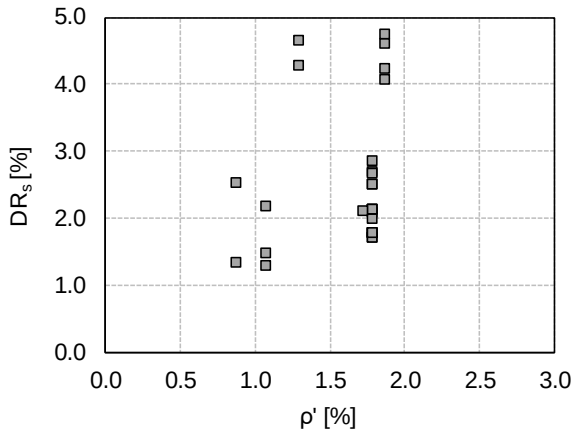

(c)

Figure 6.17. Effect of key parameters on drift at shear failure (DR_s) – (1)

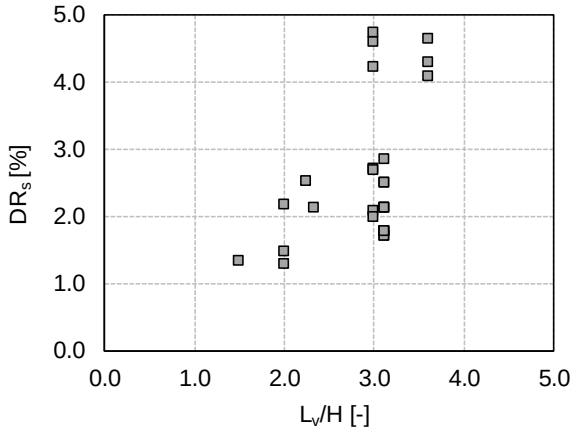

(a)

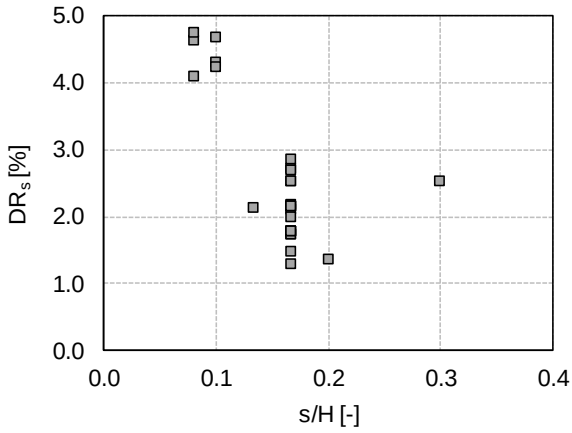

(b)

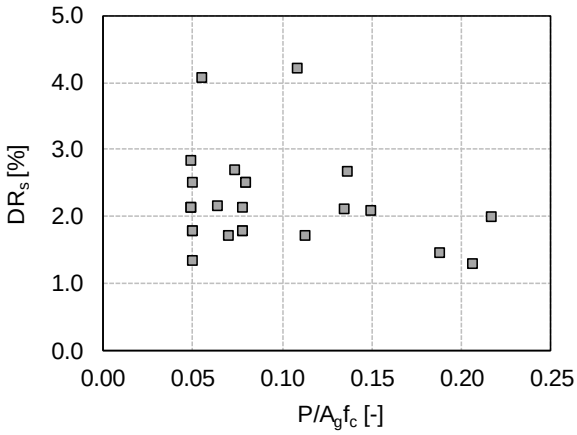

(c)

Figure 6.18. Effect of key parameters on drift at shear failure (DR_s) – (2)

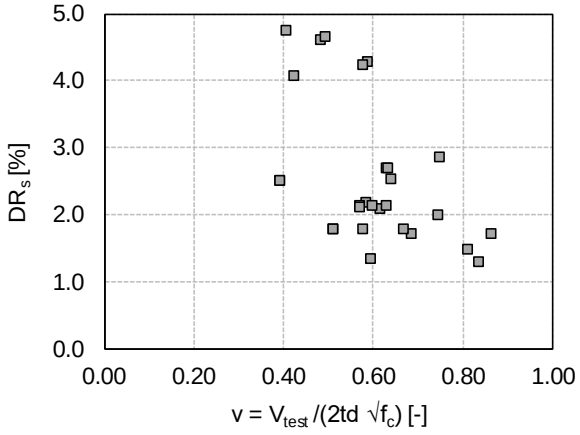

(a)

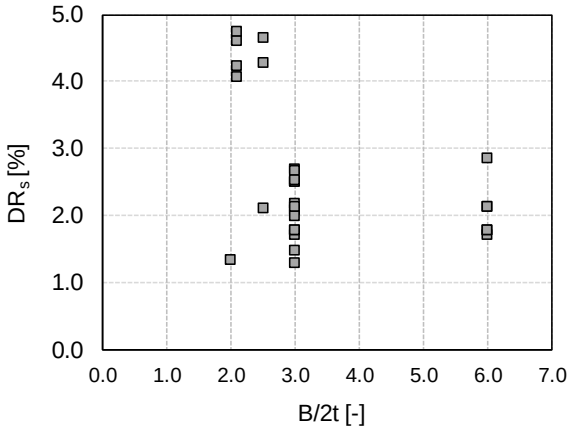

(b)

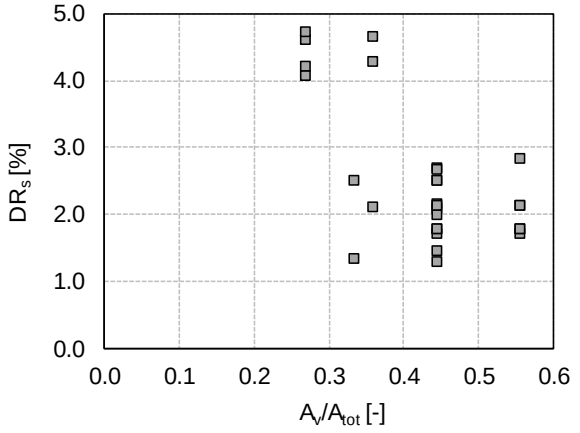

(c)

Figure 6.19. Effect of key parameters on drift at shear failure (DR_s) – (3)

Figure 6.17, Figure 6.18, and Figure 6.19 compare the drift ratio at shear failure (i.e., the displacement at shear failure divided by the height of the column) with the selected key parameters. By observing the plots, considerable variability in the results can be noted and clear relationships can be identified only for some of the analyzed key parameters. The data in Figure 6.17a suggest that columns with higher transverse reinforcement ratios, ρ'', tend to reach larger drifts at shear failure compared with columns characterized by lower transverse reinforcement ratios. In contrast, there is no clear relationship between the mechanical transverse reinforcement ratio, ω'', and the drift at shear failure (Figure 6.17b). Therefore, it seems that for the specimens included in the database, the drift ratio may be better correlated to the amount of transverse steel rather than to the steel strength. The effect of the dowel action of longitudinal reinforcement does not seem to influence the drift at shear failure (Figure 6.17c). Actually, such a result may be related to the limited variability of longitudinal reinforcement ratio, ρ', for the columns in the database. Almost clear relationship can be observed between the aspect ratio and the shear drift capacity (L_V/H) in Figure 6.18a. In fact, the higher the aspect ratio, the lower the drift at shear failure, according to a linear relationship. The identified relationship between transverse reinforcement ratio and drift at shear failure is also confirmed in Figure 6.18b, in which a decreasing trend of DR_s can be identified with increasing tie spacing-to-depth ratio (s/H). Also in this case, the small variability of this parameter within the database leads to a not so clear trend. Between axial load ratio (P/A_cf_c) and drift at shear failure no clear relationship is observable. In fact, the mean trend is almost horizontal. However, a slight tendency of DR_s to reduce with increasing axial load ratio can be identified (Figure 6.18c), as expected. The clearest relationship can be observed in Figure 6.19a, where an almost clear linear decreasing trend of DR_s is identified with increasing maximum nominal shear stress (ν). Finally, no relationship is identified between width to thickness ratio ($B/2t_w$) or void to solid area ratio (A_{void}/A_c), and drift at shear failure (Figure 6.19b and Figure 6.19c).

Then, the key parameters influencing the drift at shear failure are transverse reinforcement ratio (ρ''), aspect ratio (L_V/H), maximum nominal shear stress (ν), and axial load ratio(P/A_cf_c). Based on this observation, two different simple empirical expressions are proposed to estimate the drift ratio at shear failure. The first one is expressed by the following equation:

$$DR_s = \frac{1.78}{100} + 5.1\rho'' + \frac{4.1}{1000}\frac{L_v}{H} - \frac{2.1}{100}\frac{\nu}{\sqrt{f_c}} \tag{6.24}$$

where L_V is the column shear span, and H is the external dimension of the cross section along shear force direction. Transverse reinforcement ratio (ρ'') and maximum nominal shear stress (ν) are evaluated according to the following equations:

$$\rho'' = \frac{A_{sw}}{2 \cdot t_w \cdot s}(-) \tag{6.25}$$

$$\nu = \frac{V_{test}}{2 \cdot t_w d}(MPa^{0.5}) \tag{6.26}$$

The coefficients in Equation (6.24) were chosen based on a least-squares fit of the data. In equations (6.25) and (6.26), d is assumed as 0.8·H. Figure 6.20 compares the drift at shear failure (DR_s) evaluated trough the equation (6.24) with the corresponding experimental value, from the database.

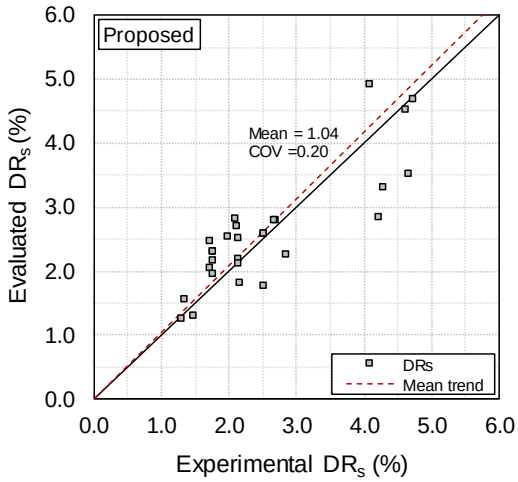

Figure 6.20. Comparison of calculated drift ratio at shear failure using Equation (6.24) with results from the hollow rectangular column database.

The accuracy in the prediction is considerably improved with respect to the models considered in the section 6.3.2. The mean of the calculated drift ratio divided by the measured drift ratio is 1.04, the coefficient of variation (COV) is 0.20. Note that the calculated drift ratio was determined using the maximum experimental shear stress.

In order to use eq. (6.24) for the seismic assessment of existing reinforced concrete columns with hollow rectangular section, it is necessary to define a value of shear strength for the calculation of the maximum nominal shear stress (ν). To this aim, it seems reliable, first, to classify the column by using the model by Kowalsky and Priestley (2000) with the modifications proposed in equations (6.15) and (6.16). Defined as V_p the plastic shear capacity (namely, the flexural capacity M_p divided by the shear span L_V), if V_p is lower than the minimum degraded shear strength ($V_{R,min}$), than no shear distress should be expected, so there is no need to compute DR_s. Otherwise, the DR_s may be computed by assuming in eq. (6.26) V_{test} equal to V_p, if flexure-shear failure is expected, and the maximum non-degraded shear V_p strength, if shear failure is expected. Note that the application of the proposed empirical drift capacity model should be limited to hollow rectangular columns representative of those included in the database, namely, whose properties are included into the variability ranges defined in section 6.1.

Analyzing the relationships between key parameters and measured drift ratios at shear failure, it is possible to develop another empirical expression for the assessment of the drift ratio at shear failure, independent from the maximum nominal shear stress (ν). In this case, in fact, the considered key parameters are transverse reinforcement ratio (ρ''), aspect ratio (L_V/H), and axial load ratio (P/A_cf_c). Based on a least-squares fit to the data, the following empirical expression is proposed:

$$IDR_s = 5.7\rho'' + \frac{5.8}{1000}\frac{L_v}{H} - \frac{1.4}{100}\frac{P}{A_c f_c} - \frac{1.3}{1000} \qquad (6.27)$$

where the transverse reinforcement ratio (ρ'') is evaluated according to eq. (6.25). Figure 6.21 compares the drift at shear failure (DR_s) evaluated trough the equation (6.27) with the corresponding measured, from the database.

The accuracy in the prediction for eq. (6.27) is slightly lower than eq. (6.24), but it can still be considered adequate with respect to the models considered in

the section 6.3.2. In fact, the mean of the calculated drift ratio divided by the measured drift ratio is 1.05; the coefficient of variation (COV) is 0.23.

Eq. (6.27) could be more practice-oriented since only geometrical, reinforcement details and axial load ratio are required to compute the expected drift at shear failure. Engineering judgement suggests that also in this case, before using eq. (6.27) for seismic assessment of existing reinforced concrete columns with hollow rectangular section, it is necessary to carry out a classification by using the model by Kowalsky and Priestley (2000) with the modifications proposed in equations (6.15) and (6.16). If shear failure is expected (with or without flexural yielding), then eq. (6.27) can be applied to compute the drift at shear failure.

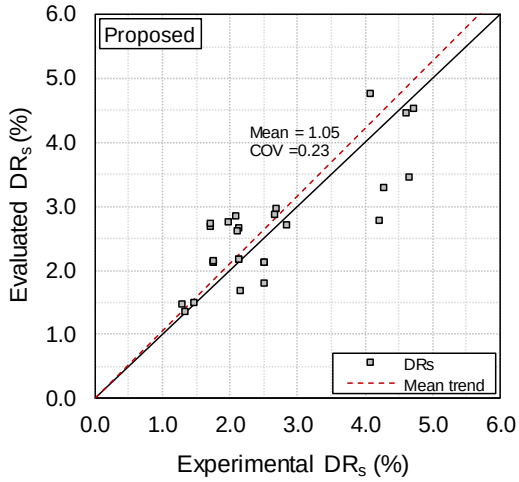

Figure 6.21. Comparison of calculated drift ratio at shear failure using Equation (6.27) with results from the hollow rectangular column database.

6.4 Summary

This chapter has been focused on the assessment of the shear capacity of hollow rectangular columns, both in terms of strength and displacement. To this aim, an experimental database of tests on hollow rectangular columns subjected to shear failure, with or without flexural yielding, has been collected.

Several main shear strength models, described in detail in section 2.3.3, have been selected and applied to all the database columns. Based on the results of the comparison between predicted shear strengths and experimental response, some critical aspects have been identified. Adopting the model by Kowalsky and Priestley (2000), some modifications have been discussed in order to improve the reliability of this model for the applicability to hollow rectangular columns. In particular, the improvements concern the concrete contribution to the shear strength: different definitions of effective shear area and dowel-action contribution have been proposed.

Within the context of a displacement-based approach for design and assessment of bridges, it is crucial to predict the displacement corresponding to shear failure. To this aim, several drift-capacity models have been developed during the last decades. All these models are based on empirical formulations calibrated on experimental results of building columns with solid cross-section. The effectiveness of these models when applied to hollow rectangular columns has been investigated for all the columns of the collected database. The results of this comparison show that existing models are not adequate to assess drift at shear failure of hollow rectangular columns. For this reason, based on the database data, new drift capacity models have been developed, characterized by adequate and less scattered predictions.

Appendix 6: experimental responses of the columns considered in the database

During the last two decades, a number of researchers carried out experiments to investigate the seismic behavior of RC bridge columns with hollow rectangular cross section.

The test parameters included column aspect ratio, material properties, details and amount of longitudinal and transverse reinforcement, axial load ratio. This appendix provides a summary of these experiments, while a detailed description can be found in the section 2.1.

In particular, the recorded lateral load-displacement responses are provided in this appendix, for all the tests considered in the database presented in the section 6.1. The test data reported here represent the basis of comparisons and proposals presented in Chapter 6.

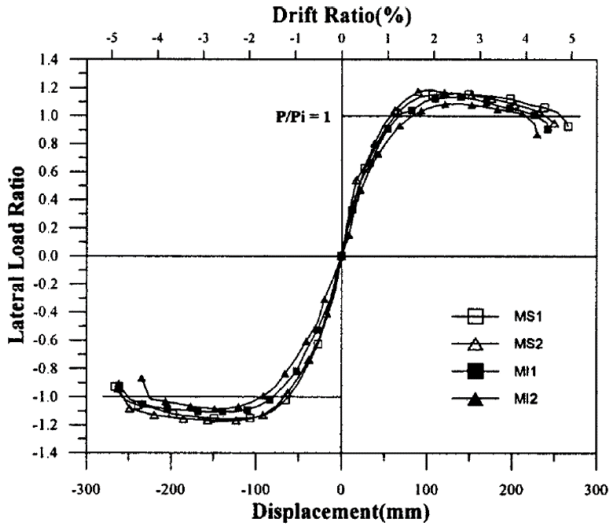

Figure 6.22. Lateral load-displacement relations (Yeh, Mo and Yang, 2002)

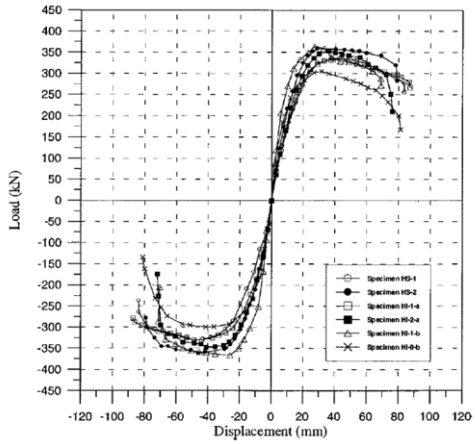

Figure 6.23. Lateral load-displacement relations (Mo and Nien, 2002)

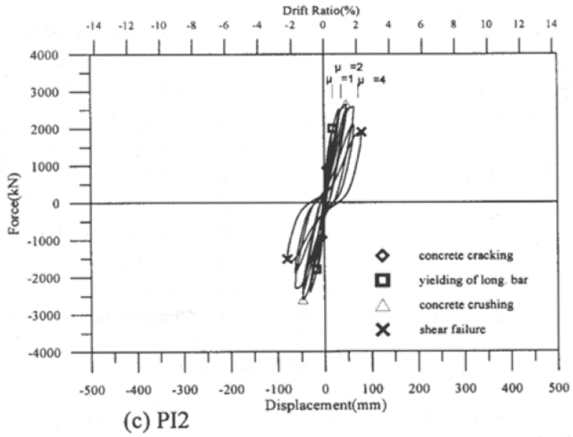

Figure 6.24. Lateral load-displacement relations (Yeh et al., 2002)

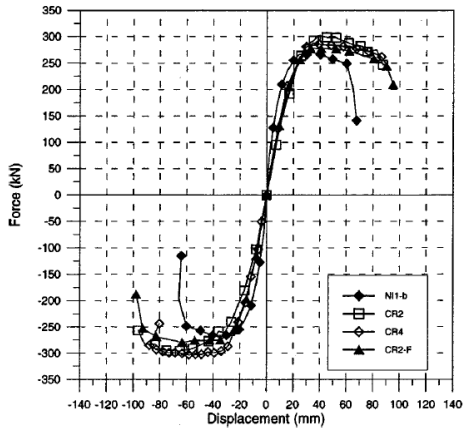

Figure 6.25. Lateral load-displacement relations (Mo et al., 2004)

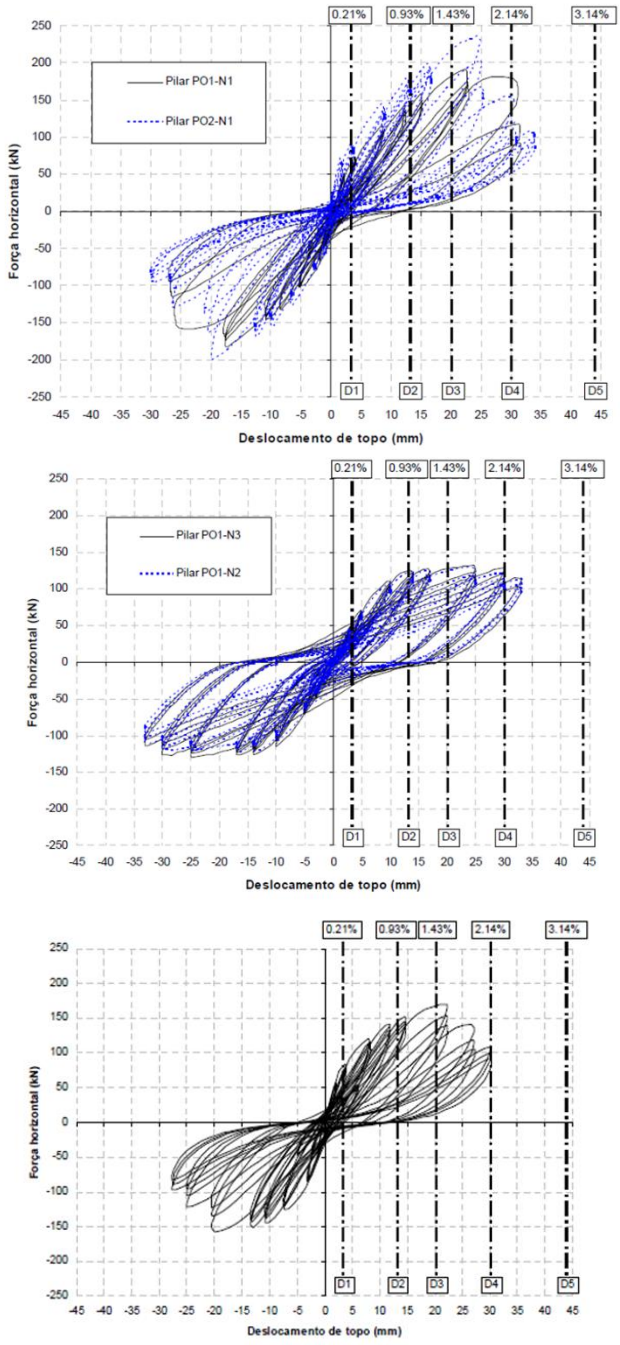

Figure 6.26. Lateral load-displacement relations (Delgado, 2009) – (1)

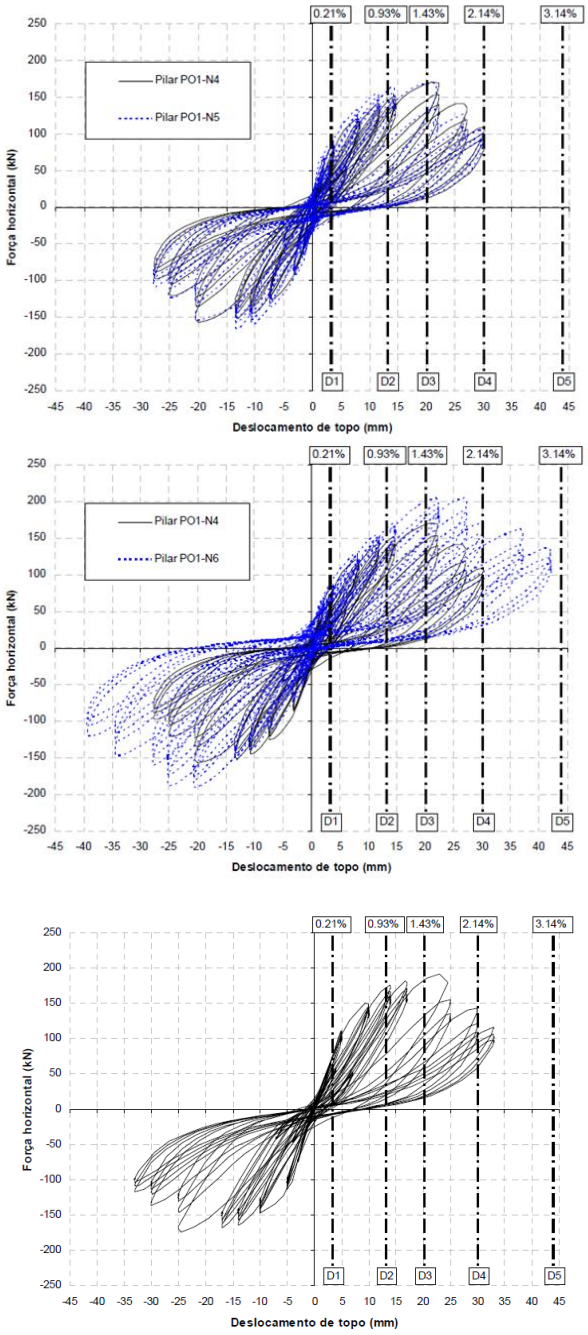

Figure 6.27. Lateral load-displacement relations (Delgado, 2009) – (2)

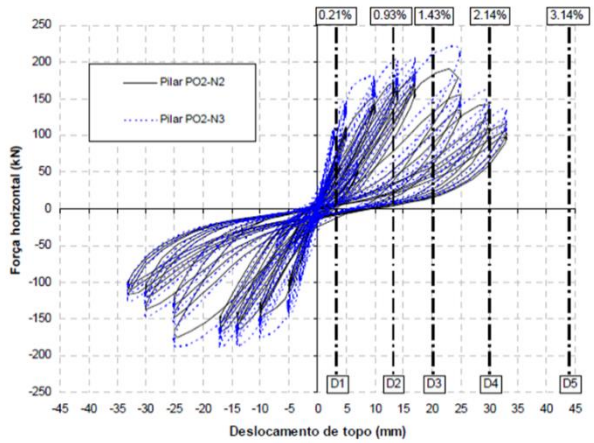

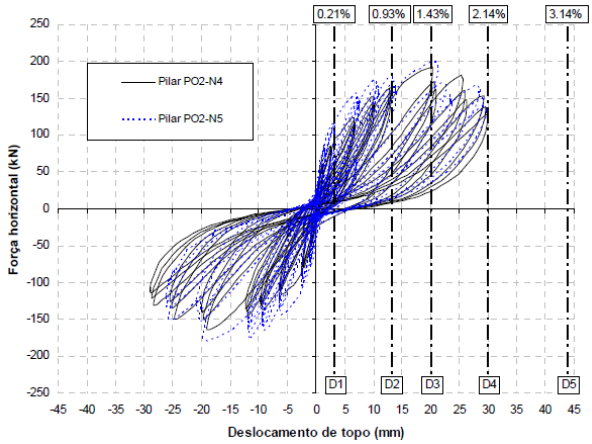

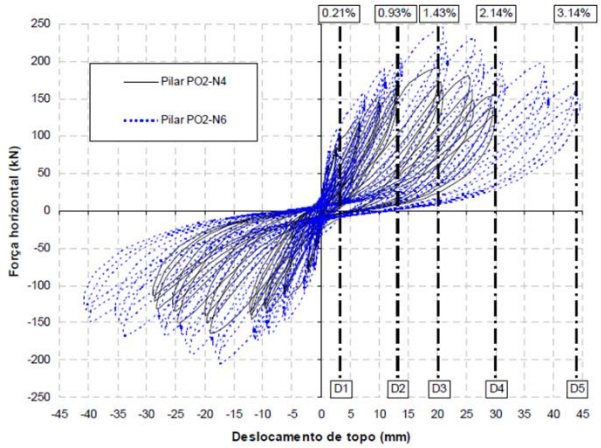

Figure 6.28. Lateral load-displacement relations (Delgado, 2009) – (3)

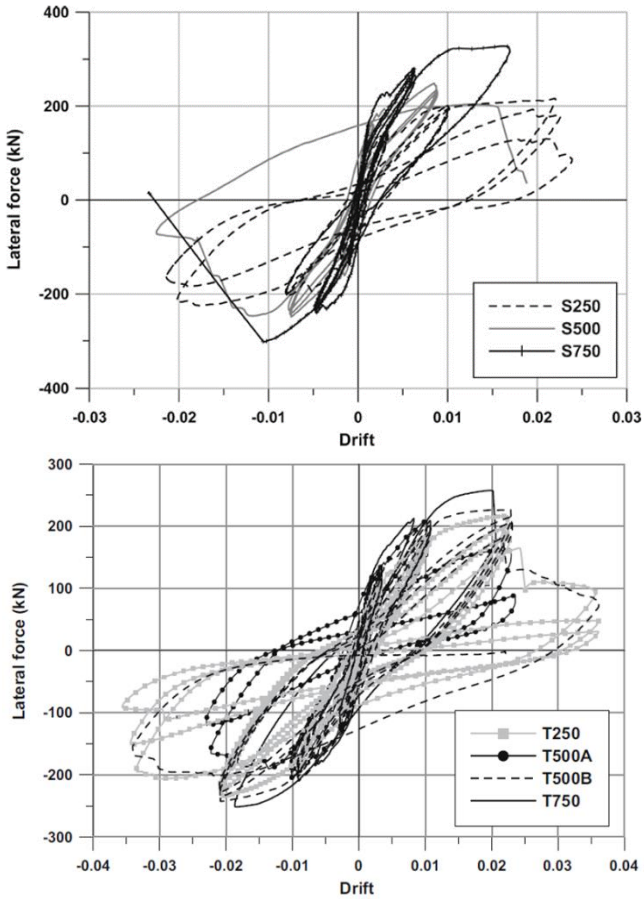

Figure 6.29. Lateral load-displacement relations (Calvi et al., 2005)

Reference

Aschheim M. and Moehle J. P. (1992) Shear strength and deformability of RC bridge columns subjected to inelastic cyclic displacements. Rep. No. UCB/EERC-92/04, Earthquake Engineering Research Centre, University of California at Berkeley, Berkeley, CA, 100 pp.

Aslani H., Miranda E. (2005). Probabilistic Earthquake Loss Estimation and Loss Disaggregation in Buildings, Doctoral Dissertation, Stanford University.

Biskinis D.E., Roupakias G.K., Fardis M.N. (2004). Degradation of shear strength of reinforced concrete members with inelastic cyclic displacement. ACI Structural Journal, 101(6):773–83.

Calvi G. M., Pavese A., Rasulo A., Bolognini D. (2005) Experimental and numerical studies on the seismic response of RC hollow bridge piers. Bulletin of Earthquake Engineering; 3(3): 267-297.

Cassese P., Ricci P., Verderame G.M. (2017). Experimental study on the seismic performance of existing reinforced concrete bridge piers with hollow rectangular section. Engineering Structures (under review).

Delgado, P. (2009). Avaliação da Segurança Sísmica de Pontes (Doctoral dissertation, Ph. D., FEUP, 2009 (in Portuguese) (http://ncrep. fe. up. pt/web/artigos/PDelgado_PhD_Thesis. pdf)).

Elwood K. J. Modelling failures in existing reinforced concrete columns. Canadian Journal of Civil Engineering 31.5 (2004): 846-859.

Elwood K. J., Moehle J. P. (2005). Drift capacity of reinforced concrete columns with light transverse reinforcement. Earthquake Spectra, 21(1), 71-89.

Fardis M. N. (2007). LESSLOSS–Risk mitigation for earthquakes and landslides. Guidelines for displacement-based design of buildings and bridges. Report n 5/2007." (2007).

Kato, D., and Ohnishi, K., 2002. Axial load carrying capacity of R/C columns under lateral load reversals, Third U.S.-Japan Workshop on Performance-Based Earthquake Engineering Methodology for Reinforced Concrete Building Structures, Seattle, WA, PEER Report 2002/02, Pacific Earthquake Engineering Research Center, University of California, Berkeley, CA, pp. 247–255.

Kim IH, Sun CH, Shin M. (2012) Concrete contribution to initial shear strength of RC hollow bridge columns. Structural Engineering and Mechanics; 41(1): 43-65.

Kowalsky M.J. and Priestley M.J.N. (2000) Improved analytical model for shear strength of circular reinforced concrete columns in seismic regions. ACI Structural Journal. 97(3), 388–396.

Mander JB, Priestley MJN, Park R. Theoretical stress-strain model for confined concrete. ASCE Journal of Structural Engineering 1988, 114(8): 1804-1826.

Mo Y. L. and Nien I. C. (2002). Seismic performance of hollow high-strength concrete bridge columns. Journal of Bridge Engineering, 7(6), 338-349.

MoY. L., Yeh Y. K., Hsieh D. M. (2004). Seismic retrofit of hollow rectangular bridge columns. Journal of Composites for Construction, 8(1), 43-51.

Paulay T, Priestley MJN. (1992) Seismic Design of Reinforced Concrete and Masonry Buildings. New York: John Wiley & Sons.

Pinto P. E., Lupoi A., Franchin P. (2009). Valutazione e consolidamento sismico dei ponti esistenti. IUSS Press.(in italian)

Priestley MJN, Seible F, Calvi GM. (1996) Seismic design and retrofit of bridges. New York: John Wiley & Sons.

Pujol, S., Ramirez, J. A., and Sozen, M. A., 1999. Drift capacity of reinforced concrete columns subjected to cyclic shear reversals, Seismic Response of Concrete Bridges, SP-187, American Concrete Institute, Farmington Hills, MI, pp. 255–274.

Sezen H. (2002). Seismic Response and Modeling of Lightly Reinforced Concrete Building Columns, Ph.D. dissertation, Department of Civil and Environmental Engineering, University of California, Berkeley.

Sezen H. and Mohele J.P. (2004). Shear Strength Model for Lightly Reinforced Concrete Columns. ASCE Journal of Structural Engineering, 130(11), 1692-1703.

Turmo J, Ramos G, Aparicio AC. (2009) Shear truss analogy for concrete members of solid and hollow circular cross section. Engineering Structures, 31(2): 455-465.

Yeh Y. K., Mo Y. L., Yang C. Y. (2002). Full-scale tests on rectangular hollow bridge piers. Materials and Structures, 35(2), 117-125.

Yeh, Y. K., Mo, Y. L., & Yang, C. Y. (2002). Seismic performance of rectangular hollow bridge columns. Journal of Structural Engineering, 128(1), 60-68.

Zhu L., Elwood K. J., Haukaa T. (2007). Classification and seismic safety evaluation of existing reinforced concrete columns. Journal of Structural Engineering, 133(9), 1316-1330.

Chapter 7

SHEAR STRENGTH OF RC BRIDGE COLUMNS WITH HOLLOW CIRCULAR CROSS SECTION

Hollow section piers with a circular shape are widespread for highway bridges, because its lateral response under wind and seismic loads is similar in any direction. While the flexural response of this structural typology can be considered completely understood, the shear strength assessment is still an open issue. It can be said that this problem has been more or less ignored, so far, by the experimental literature; in fact, only one experimental study is available in literature focusing on the experimental shear strength assessment of RC bridge columns with hollow circular section.

From the results of the preliminary comparison, carried out in the section 5.5 of the present work, between experimental results and main code-based shear strength models, the need to evaluate the effectiveness and the reliability of these models for hollow circular columns has been highlighted. To this aim, in this chapter an experimental database will be collected and integrated with the tests presented in this work. Then, a comparison will be carried out, between experimental and predicted shear strength values. Finally, some improvements in shear strength assessment are discussed and a new proposal is carried out and assessed.

7.1 Experimental database

Hollow section piers are a very popular structural solution for reinforced concrete (RC) bridge structures, due to their economical higher efficiency with respect to solid sections. In particular, RC piers with hollow circular cross section are widespread for highway bridges, because its lateral response under wind and seismic loads is similar in any direction. This structural typology is in fact extensively used in Europe and in Japan since the early seventies (Priestley et al., 1996). While it seems evident the advantage of using hollow sections in viaducts with very tall piers, where the weight of the vertical members is no longer negligible compared to that of the superstructure, a little less immediate is the case of short piers. Short hollow columns are often used when high stiffness is needed, since section diameter can be increased without causing construction problem related to internal cracking, due to the hydration process (Ranzo and Priestley, 2001). In the past, hollow circular columns were typically designed with two layers of reinforcement and crossties. This aspect represented a significant inconvenience in terms of time needed to place that type of reinforcement, and it was not counterbalanced by significantly improved performance. Therefore, hollow circular columns with a single reinforcement layer started to spread for the construction of bridge piers, chimneys, pipes and other structures (Turmo et al. 2009). Several experimental studies have shown that the performance attainable with only one layer of reinforcement near the outside face is ductile, if moderate axial load is applied and medium-low ratios of longitudinal reinforcement are used (Zahn et al., 1990; Hoshikuma and Priestley, 2001). While the flexural response of this structural typology has been investigated enough through some experimental studies (Zahn et al., 1990; Hoshikuma and Priestley, 2001), the issues related to shear strength mechanisms characterizing hollow circular columns with only one layer of reinforcement in the outside face are still almost unknown. In fact, only one experimental study concerning the above-mentioned topic is available in literature, carried out by Ranzo and Priestley in 2001, and described in detail in the section 2.2.

It becomes clear the relevance of a thorough investigation about the predictive capability of the shear strength models available in literature and codes when applied to this structural typology. To this aim, data from tests on RC columns with hollow circular cross section and a single layer of

reinforcement from literature (see section 2.2) are collected and integrated with the tests presented in this work (see Chapter 5).

All the considered specimens were tested under unidirectional cyclic lateral load in single curvature and were characterized by uniform reinforcement details across the height (no reinforcement variations, such as bars cut-off). The main properties of the selected tests are included in the following ranges:

- Concrete cylindrical compressive strength: $14.0 \le f_c \le 40.0$ (MPa)
- Yield stress of longitudinal reinforcement: $306 \le f_y \le 540$ (MPa)
- Longitudinal reinforcement ratio: $0.85 \le \rho' \le 5.40$ (%)
- Yield stress of transverse reinforcement: $318 \le f_{yw} \le 655$ (MPa)
- Transverse reinforcement ratio: $0.06 \le \rho'' \le 1.14$ (%)
- Axial load ratio: $0.05 \le P/A_c \cdot f_c \le 0.40$ (-)
- Tie spacing to depth ratio: $0.02 \le s/H \le 0.23$ (-)
- Aspect ratio: $2.00 \le L_V/H \le 4.28$ (-)

In the previous list, the axial load ratio is evaluated as the ratio between the applied axial load P and the product of the concrete compressive strength f_c times the concrete area A_c (the gross section area minus the void); the aspect ratio (L_v/D) is defined as the ratio between the shear span L_V and the cross section external diameter D; the longitudinal reinforcement ratio ρ' is evaluated with respect to the concrete area; the transverse reinforcement ratio ρ'' is computed as the ratio between the total area of transverse reinforcement in the loading direction and the product of cross-sectional width (assumed as twice the thickness of the concrete ring $b_w = 2t_w$) times the tie spacing s; f_y and f_{yw} are the yielding strengths for longitudinal and transverse reinforcement, respectively. The original experimental lateral load-deformation relations for the selected columns are reported in section 2.2. Table 7.1 shows geometry, reinforcement details, and material properties of the test specimens included in the database. Note that, except for the tests #12 and #13 (presented in this study), with circular ties (Type s_1), all test specimens are characterized by continuous spiral transverse reinforcement (Type s_2). Some of the terms in Table 7.1 have been defined above; the remaining ones are specified in the legend.

Table 7.1. Geometry, reinforcement details and material properties

Test ID	Specimen ID	D (mm)	t_w (mm)	c (mm)	L_V (mm)	f_c (MPa)	Φ_l[a] (mm)	ρ' (%)	f_y (MPa)	Type[b]	Φ_t[c] (mm)	S[d] (mm)	ρ'' (%)	f_y (MPa)	v[e] (--)
Zahn et al., (1990)															
1	1	400	94	36	1625	29.6	16	3.56	306	s_1	10	75	0.56	340	0.08
2	2	400	94	38	1625	29.6	16	3.56	306	s_1	12	90	0.67	318	0.40
3	3	400	75	36	1625	29.6	16	4.20	306	s_1	10	75	0.70	340	0.10
4	4	400	75	38	1625	29.6	16	4.20	306	s_1	12	90	0.84	318	0.22
5	5	400	55	36	1625	27.3	16	5.40	306	s_1	10	75	0.95	340	0.12
6	6	400	55	38	1625	27.3	16	5.40	306	s_1	12	90	1.14	318	0.12
Hoshikuma and Priestley, (2000)															
7	HF1	1524	140	35	6528	37.4	13	1.42	427	s_1	6	35	0.32	625	0.13
8	HF2	1524	140	38	6528	38.5	19	3.18	444	s_1	6	35	0.32	625	0.13
Ranzo and Priestley, (2001)															
9	HS1	1560	152	26	3880	40.0	13	1.30	450	s_1	6	70	0.15	635	0.05
10	HS2	1524	139	27	3880	40.0	16	2.25	450	s_1	6	70	0.16	635	0.05
11	HS3	1524	139	27	3880	35.0	16	2.25	450	s_1	6	70	0.16	635	0.15
Authors' tests															
12	P5	550	100	17	1650	14.0	8	0.85	540	s_2	3	120	0.06	655	0.05
13	P6	550	100	17	1100	14.0	8	0.85	540	s_2	3	120	0.06	655	0.05

[a] Diameter of longitudinal steel bars equally spaced along a unique external reinforcement layer.

[b] Transverse reinforcement typology: circular ties (s_1) or continuous spiral (s_2).

[c] Cross sectional diameter of circular ties (s_1) or of continuous spiral (s_2), equally spaced along specimens' height.

[d] Spacing between circular ties (s_1) or pitch of the continuous spiral (s_2).

[e] Axial load ratio ($v = P/A_c f_c$)

7.2 Shear strength capacity

Recent principal earthquakes around the world have highlighted the inadequate seismic performance of existing hollow core piers, generally characterized by poor structural detailing and small web thickness (Kim et al., 2012). As known, seismic bridge design philosophy is to pursue energy dissipation by ductile flexural hinges at the piers base (Priestley et al., 1996; Paulay and Priestley, 1992). Therefore, brittle shear failure of bridge piers clearly has to be prevented to avoid disastrous collapse. For hollow RC columns, special attention has to be paid also to shear strength degradation with increasing flexural ductility demand, since their shear resisting mechanisms are very similar to those characterizing tube sections, depending mainly on webs aspect ratio. Small thickness can limit the confined concrete core, crucial to seismic energy dissipation (Kim et al., 2012). Despite their widespread use, none of the current codes addresses specialized attention to shear strength of RC hollow circular members, both for design and assessment, while some code suggests formulations for solid circular columns (Turmo et al. 2009).

For all these reasons, the failure mode prediction and the shear strength evaluation of hollow circular columns assume clear relevance, particularly when the assessment of existing piers is approached. In section 5.5, a comparison between the experimental responses of the specimens presented in this work and the main code-based shear strength models have been carried out. This comparison highlighted a low predictive capacity of the considered models and a trend to underestimate the experimental shear strength.

In order to extend the comparison and to obtain a more reliable evaluation of existing capacity models, thus evaluating their effectiveness in terms of failure mode prediction and shear strength assessment, a database has been developed and integrated with the above-mentioned tests (see section 7.1). As discussed in section 7.1, very few experimental studies are available in literature dealing with the lateral response of RC columns with hollow circular cross section and a single reinforcement layer. Most of these focuses on the flexural behavior, and only two experimental tests failed in shear after flexural yielding. In the following, some of the main models available in literature are briefly described. In particular, the attention will be focused on shear strength

models based on experimental data including also specimens with hollow or solid circular cross section. Then, the measured shear strengths of the columns reported in the database is compared to the values calculated by using the considered models. Finally, some modifications are discussed and a new shear model is proposed.

7.2.1. Considered shear strength models

With the aim to carry out a comparison with the measured shear strength of the collected database specimens, the main models available in literature for the shear strength assessment are analyzed. In particular, only capacity models based on test data including specimens with hollow or solid circular cross section are adopted. Some of the considered models have been described and discussed in details in the section 2.3.3 (Kowalsky and Priestley, 2000; Biskinis et al., 2004). Therefore, they are only recalled in the following, focusing in particular on their formulations, in order to uniform symbols and to simplify the understanding of the comments derived from the comparison. In addition to the above-mentioned models, the specification of the model by Kowalsky and Priestley to hollow circular columns, proposed by Ranzo and Priestley (2001), is also taken into account.

Kowalsky and Priestley (2000)

The shear strength is calculated as the sum of the contributions from concrete, V_c, transverse reinforcement, V_w, and arch mechanism associated with axial load, V_p. The shear strength degradation influences only the concrete contribution, through the degradation factor k decreasing with increasing displacement ductility (μ). The corresponding formulations are reported below:

$$V_c = \alpha\beta k\sqrt{f_c}A_e \tag{7.1}$$

$$A_e = 0.8A_c \tag{7.2}$$

$$1 \le \alpha = 3 - \frac{L_V}{D} \le 1.5 \tag{7.3}$$

$$\beta = 0.5 + 20\rho' \le 1 \tag{7.4}$$

$$V_w = \frac{\pi}{2}\frac{A_{sw} f_{yw} (D - c - x)}{s}\cot(30°) \tag{7.5}$$

$$V_P = P\tan(\alpha) = \frac{H - x}{2L_V}P \tag{7.6}$$

where, x is the neutral axis depth, and A_{sw} is the cross-sectional area of the transverse reinforcement. All the remaining terms have been defined above. The coefficient k, is taken as 0.29 when the displacement ductility (μ) is less than 2 and 0.05 when μ is more than 8, and decrease linearly between these two values. Hereinafter, the displacement ductility (μ) is assumed as that corresponding to the maximum value of the lateral force reached during the test. This model will be identified in the following as "Revised UCSD-A", since it is a review of the original model by Priestley et al. (1994) developed at the University of California San Diego.

Biskinis et al., (2004)

The shear strength is calculated according to the regression model in equations (7.7) to (7.10) accounting for three contributions: the classical 45-degrees truss model (V_w), the concrete contribution (V_c), and the axial load contribution (V_P).

$$V_R = V_P + k(V_c + V_w) \tag{7.7}$$

$$V_c = 0.16\max(0.5;100\rho')\left(1 - 0.16\min\left(5;\frac{L_V}{H}\right)\right)\sqrt{f_c}A_c \tag{7.8}$$

$$V_w = \frac{A_{sw}}{s}(D-2c)f_{yw} \tag{7.9}$$

$$V_N = \frac{(H-x)}{2a}\min(N;0.55A_c f_c) \tag{7.10}$$

where, d_0 is the depth of the compression reinforcement layer, and b_w is the width of the section web (for hollow rectangular equal to twice the thickness). Also for this shear model, the coefficient k multiplies both the concrete and the transverse steel contributions. It varies linearly between 1.00 (non-degraded shear strength) and 0.75 for μ between 1 and 6.

Ranzo and Priestley (2001)

Ranzo and Priestley (2001) carried out an experimental studies aiming to investigate the lateral response of hollow circular columns with one external layer of steel reinforcement and spiral transverse reinforcement. Based on the results of only two tests failing in shear after flexural yielding, Authors proposed some specifications to adapt the model by Kowalsky and Priestley to the hollow circular columns. The modifications concern the concrete contribution to the shear strength, (V_c). In particular, the effective shear area and the position of neutral axis with respect to the inside column face are modified by the coefficients λ and β, respectively defined in equations (7.12) and (7.13):

$$V_c = \alpha\beta k\sqrt{f_c}A_e \tag{7.11}$$

$$A_e = \frac{\left(1+\lambda^2\right)(1-\lambda)}{\left(1+\lambda^3\right)}A_c \tag{7.12}$$

$$\beta = 0.5 + 20\rho' \le 1, \quad \text{if } x \ge t_w \tag{7.13}$$

$$\beta = 0.5 + 20\frac{A_{sw}}{\pi D^2/4} \leq 1, \text{ if } x \geq t_w$$

Moreover, Authors suggest neglecting the axial load contribution (V_p). This model will be identified as "Revised UCSD-B" in the following.

7.2.2. Comparison of shear strength models with column database

Selected shear capacity models are applied herein to all the columns of the database, using the formulations described above. The aim is to investigate about the capability of the considered models in predicting experimental failure modes for the database columns, that is, the reliability of these models in a classification issue typical of seismic assessment.The comparison is summarized in Table 7.2: for each considered shear strength model, the maximum (non-degraded, $V_{R,max}$) and the minimum (degraded, $V_{R,min}$) values of the predicted shear capacity are reported, together with the predicted failure mode (FM_{pred}). These values are compared with the corresponding experimental data. For all the test specimens, the experimental lateral load at yielding is known (V_y). The predicted failure mode (FM_{pred}) is identified through a comparison between the predicted non-degraded and residual values of the shear strength ($V_{R,max}$ and $V_{R,min}$, respectively), and the maximum value of the lateral force reached during the test (V_{test}) and the yielding force (V_y). When $V_{R,max}$ is lower than V_y, brittle shear failure occurs limiting flexural response (S). When $V_{R,min}$ is higher than V_{test}, the flexural response can completely develop (F). In all the other cases, the element fails in FS mode. As observed, all the considered models are able to predict the flexural failure modes for the tests 1-9, characterized by higher transverse geometrical reinforcement ratios and shear span-to-diameter ratios. Conversely, none of the considered models presents an adequate capacity in prediction of flexural failure mode for the test 12 (namely, specimen P5 presented in Chapter 5).

Regarding the tests failing in shear after flexural yielding (FS-mode), Revised UCSD-A (Kowalsky and Priestley, 2000) shows a low prediction capacity of the failure mode, since it is able to catch the experimental failure mode only for test #10, while it is non-conservative for test 11 and very conservative for test #13 (namely, specimen P5 presented in Chapter 5).

Table 7.2. Failure mode prediction

Test ID	*Experimental*			*Revised UCSD-A*			*Revised UCSD-B*			*Biskinis et al., (2004*		
	V_y[a] (kN)	V_{TEST}[b] (kN)	FM_{obs}[c] (-)	$V_{R,max}$[d] (kN)	$V_{R,min}$[d] (kN)	FM_{pred}[e] (-)	$V_{R,max}$[d] (kN)	$V_{R,min}$[d] (kN)	FM_{pred}[e] (-)	$V_{R,max}$[d] (kN)	$V_{R,min}$[d] (kN)	FM_{pred}[e] (-)
Zahn et al., (1990)												
1	74.6	110.8	F	380.0	285.6	F	327.5	260.7	F	300.6	230.2	F
2	119.9	144.0	F	485.5	391.1	F	356.2	289.4	F	397.3	322.0	F
3	75.4	112.0	F	363.8	283.8	F	313.5	258.3	F	301.7	231.4	F
4	91.7	123.7	F	416.9	336.9	F	342.2	287	F	346.1	270.8	F
5	72.7	105.2	F	336.6	276.8	F	295.8	255.3	F	295.0	225.7	F
6	72.5	102.8	F	365.3	305.5	F	324.5	283.9	F	315.0	240.6	F
Hoshikuma and Priestley, (2000)												
7	500.0	730.0	F	2520.6	1961.0	F	2057.9	1682.3	F	1797.7	1408.4	F
8	840.0	1150.0	F	2724.4	1999.2	F	2188.7	1702	F	2139.4	1666.4	F
Ranzo and Priestley, (2001)												
9	700.0	972.0	F	1920.9	1418.5	F	1498.5	1160.8	F	1415.4	1107.8	F
10	900.0	1396.0	FS	2036.2	1334.5	FS	1555.2	1084.2	FS	1656.7	1285.9	FS
11	1200.0	1457.0	FS	2202.6	1546.3	F	1460.1	1007.6	FS	1850.5	1493.0	F
Authors' tests												
12	86.4	108.2	F	147.4	74.6	FS	104.9	54.8	FS	116.2	90.6	FS
13	133.6	166.9	FS	154.9	82.1	S	104.9	54.8	S	131.4	106.6	S

[a] V_y is the value of the shear corresponding to measured first flexural yielding

[b] V_{TEST} is the maximum experimental value of shear force.

[c] FM_{obs} = observed failure mode: "F" = Flexure failure mode; "FS" = Shear failure mode following yielding.

[d] $V_{R,max}$ and $V_{R,min}$ are maximum (non-degrading) and minimum values of shear strength according to the considered capacity model.

[e] FM_{pred} = predicted failure mode according to the considered capacity model.

Revised UCSD-B (Ranzo and Priestley, 2001) is characterized by an adequate predictive capacity of the failure mode for the tests #10-#11 (on which it is calibrated), whereas it provides a very conservative prediction for the test #13. A lower prediction capacity is observed for Biskinis et al. (2004) model, due to the conservatism in prediction for the test #13 and the non-conservatism for the test #11. Note that the latter model was applied assuming the formulations providing shear strength in the case of diagonal tension failure, according to equations (7.7) to (7.10), since such phenomenon governs the shear failure for the columns in the database.

7.2.3. Proposed shear strength model for hollow circular columns

The number of experimental tests on RC columns with hollow circular section and a single external layer of steel reinforcement available in literature is not sufficient to develop a reliable shear capacity model. Nevertheless, it seems interesting to discuss about reasonable improvements of existing models, based on the comparison results reported in the previous section. Among the shear strength models considered in the previous section, the Revised UCSD-B (Ranzo and Priestley, 2001) is characterized by the higher capacity in failure mode prediction. In fact, it is able to predict well the experimental failure modes for all the specimens of the database, except the tests #12 and #13, reported in the present work. The main difference between the latter tests and the remaining tests of the database, which can influence shear-resisting mechanisms, is represented by the different layout of the transverse reinforcement. In fact, the test specimens P5 and P6 are the only ones with isolated circular ties, whereas all the others are characterized by continuous spirals. This because the specimen tests P5 and P6 (corresponding to tests 12 and 13 in the database) are characterized by reinforcement details typical of Italian existing bridges, and therefore isolated circular ties, widespread solution for circular columns in Italy (Cardone et al., 2013).

Based on this observation, a numerical study (Turmo et al. 2009) available in literature has been considered. This study focuses on the steel contribution to shear strength (V_s). In particular, Turmo et al. (2009) focuses their attention on the specification to solid and hollow circular columns of the common shear truss analogy (widely used by main shear strength models available in literature or codes). Authors proposed an analytical model for evaluating the contribution of transverse reinforcement (for both continuous spiral and

circular ties) in concrete members of solid and hollow circular cross section. According to the model by Turmo et al., (2009) the transverse steel contribution on the shear strength of hollow core and solid circular concrete members, reinforced with circular and spiral reinforcement can be computed as reported in equation (7.14):

$$V_s = z\cot(\theta)A_{st}f_{yw}\chi\lambda \tag{7.14}$$

where, z is the lever arm, ϑ is the angle between the inclined strut and the longitudinal axis of the member (it can be assumed as 30°), A_{st} is the area per unit length of the transverse reinforcement. The coefficients χ and λ are efficiency factors taking into account the average inclination of the ties crossing a given crack and the inclination of the spiral respect to the longitudinal axis, respectively. The terms A_{st}, χ, and λ in equation (7.14) are expressed by the following equations:

$$A_{st} = 2\frac{A_{sw}}{s} \quad \text{for circular ties}$$
$$A_{st} = 2\frac{A_{sw}}{p} \quad \text{for continuous spiral reinforcement} \tag{7.15}$$

$$\chi = \int_0^{z\cot(\theta)} \frac{\sqrt{R'^2 - \left(z_0 - x\tan\theta\right)^2}}{R'z\cot(\theta)}dx \tag{7.16}$$

$$\lambda = \frac{1}{\sqrt{\left(\frac{p}{2\pi R'}\right)^2 + 1}} \tag{7.17}$$

In the equation (7.15), A_{sw} is the area of a single rod (cross-sectional area of transverse reinforcement), s and p are the spacing of the circular ties and the pitch of the spiral, respectively. In the equations (7.16) and (7.17), R' is the radius of the circular or helical transverse reinforcement, z_0 is the distance from the centroid of the tensile forces to the center of masses of the member, while

the other terms have already been described above. The integral of equation (7.16) can be solved numerically by a change in variable, in function of the ratios z/D' and z_0/D', with D' equal to the diameter of the circular or helical transverse reinforcement. By assuming a constant value for the lever arm z equal to $0.8 \cdot D$ and the same distance from the center of the cylinder for the resultant forces of compressive and tensile stresses (namely, z_0 equal to 0.5), the product of χ times λ is equal to $\pi/4$. The latter result is that adopted by the Revised UCSD-A and Revised UCSD-B models. For hollow core circular members with circular ties, the product of χ times λ is equal to 1, namely, for this structural solution the maximum efficiency in shear strength is achieved. This apparently surprising result can be easily explained with the examination of Figure 7.1.

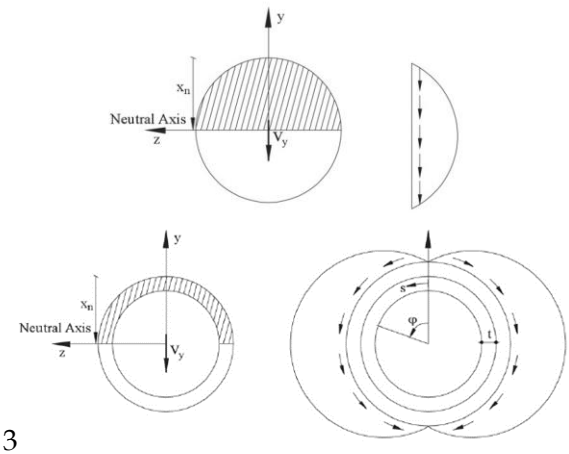

3

Figure 7.1. Elastic shear stresses in solid and hollow core circular cross sections – adapted by Turmo et al., (2009)

Shear stresses in solid circular members are mainly vertical; whereas in annular members, shear stresses have the same orientation as the stirrups. Hence, in annular members, circular stirrups are more effective as their geometry follows the orientation of the shear stresses provided by the Theory of Elasticity. Based on the above-described results, a new method for the shear strength evaluation is identified and proposed. The proposed model evaluates the shear strength as the summation of two contributions, one due to concrete shear resisting mechanisms (V_c), and the other due to transverse steel reinforcement (V_s). The concrete contribution is evaluated according to the

model by Ranzo and Priestley (2001), expressed by the equation (7.11). The transverse reinforcement contribution is computed through the equations (7.14 – 7.17). Note that the contribution of the arch mechanism associated with axial load, V_p, is not considered because such a mechanism for hollow core concrete members seems to be less efficient in enhancing shear strength with respect to solid circular members (as observed, also, by Ranzo and Priestley, 2001). In fact, it is not clear how the arch mechanism could develop along curved struts. Therefore, a conservative assumption can be done by neglecting this contribution in the shear strength assessment. The capability of the proposed method in predict the experimental failure modes is firstly investigated with regard to the results of the database columns. The comparison is summarized in Table 7.3, where the maximum (non-degraded, $V_{R,max}$) and the minimum (degraded, $V_{R,min}$) values of the predicted shear capacity are reported, together with the predicted failure mode (FM_{pred}).

Test ID	*Experimental*			***Proposed model***		
	V_y (kN)	V_{TEST} (kN)	FM_{obs} (-)	$V_{R,max}$ (kN)	V_R (kN)	FM_{pred} (-)
Zahn et al., (1990)						
1	74.6	110.8	F	389.8	323.1	F
2	119.9	144.0	F	427.2	360.5	F
3	75.4	112.0	F	375.9	320.7	F
4	91.7	123.7	F	413.2	358.1	F
5	72.7	105.2	F	358.1	317.6	F
6	72.5	102.8	F	395.5	355.0	F
Hoshikuma and Priestley, (2000)						
7	500.0	730.0	F	2329.7	1954.1	F
8	840.0	1150.0	F	2464.0	1977.2	F
Ranzo and Priestley, (2001)						
9	700.0	972.0	F	1383.4	1045.7	F
10	900.0	1396.0	FS	1521.9	1050.9	FS
Authors' tests						
11	1200.0	1457.0	FS	1485.1	1044.6	FS
12	86.4	108.2	F	178.2	128.1	F
13	133.6	166.9	FS	178.2	128.1	FS

Table 7.3. Failure mode prediction for the proposed model

These values are compared with the corresponding experimental data. The predicted failure mode (FM_{pred}) is identified here again through a comparison between the predicted non-degraded and residual values of the shear strength ($V_{R,max}$ and $V_{R,min}$, respectively), with the maximum value of the lateral force reached during the test (V_{test}) and the measured yielding force (V_y).

As observed, the proposed model shows very good capacity of failure mode prediction for all the considered tests. The reason of this efficiency in prediction seems to be related to the formulation for transverse reinforcement contribution to shear strength, which is able to taking into account the difference of shear reinforcement typology (namely, circular ties and continuous spiral).

In order to investigate further about the prediction capacity of shear strength for the tests characterized by shear failure, a comparison is carried out between the shear strength computed according to all the considered models (see section 7.2.1) and by the proposed model, and the experimental shear strength values. As known, the displacement ductility capacity of RC members failing in shear should not be evaluated from the inverse application of the shear strength model because this would not lead to a reliable assessment of the drift at shear failure (Biskinis et al., 2004). Vice-versa, it is possible to evaluate the predicted degraded shear strength corresponding to the observed ductility at failure. To this aim, the displacement ductility at failure (μ) is computed as the ratio of the displacement corresponding to shear failure to the experimental yielding displacement. The displacement at shear failure is assumed as that where shear resistance drops below 80% of the maximum shear recorded (V_{test}), if measured, otherwise as the maximum recorded displacement.

For the tests #10, #11, and #13, showing a shear failure following flexural yielding (FS-mode), Table 7.4 reports the failure mode and the shear strength predicted by all the considered models and by the proposed model. Note that the shear strength is evaluated corresponding to the observed ductility at failure if FS failure is predicted, otherwise as the non-degraded shear strength if S failure is predicted.

Table 7.4. Shear strength prediction comparison

	Experimental			*Revised UCSD-A*			*Revised UCSD-B*			*Biskinis et al.*			***Proposed Model***		
Test ID	V_u[a]	D_u[a]	μ[a]	V_R[b]	FM_{pred}	V_p/V_t	V_R[b]	FM_{pred}	V_p/V_t	V_R[b]	FM_{pred}	V_p/V_t	V_R[b]	FM_{pred}	V_p/V_t
	(kN)	(%)	(-)	(kN)	(-)	(-)	(kN)	(-)	(-)	(kN)	(-)	(-)	(kN)	(-)	(-)
Ranzo and Priestley, (2001)															
10	1396	2.65%	6.0	1873	FS	1.34	1445	FS	1.04	1479	FS	1.06	1412	FS	1.01
11	1457	2.27%	3.4	2201	FS	1.51	1447	FS	0.99	1484	F	1.22	1778	FS	1.02
Authors' test															
13	149	2.49%	4.8	121	S	0.81	82	S	0.55	114	S	0.76	151	FS	1.01
					Mean	1.22		Mean	0.86		Mean	1.01		Mean	1.01
					COV	0.30		COV	0.31		COV	0.23		Cov	0.01

[a] V_u, D_u, μ, are the value of the shear, drift-ratio and ductility corresponding to the onset of the shear strength decay on the envelope of the experimental response.

[b] V_R is the shear strength evaluated for a ductility μ

[c] V_p/V_t = predicted-to-experimental shear strength.

The very good predictive capacity of the proposed model is confirmed by the results reported in Table 7.4, highlighting an almost exact assessment of the shear strength for all specimens, with a mean of the predicted-to-experimental shear strength ratio equal to 1.01, and a coefficient of variation (COV) technically zero. Revised UCSD-A is characterized by a high overestimation, up to about 50% for members with spiral transverse reinforcement (type s_2); vice-versa, the same model tends to underestimate the shear strength of the test #13 (type s_1), with circular ties. Revised UCSD-B is characterized by a very good predictive capacity only for type s_2 members, with a negligible error, while it underestimates of about 45% the shear strength for the test 13. Finally, the Biskinis et al. (2004) model is characterized by a lower predictive capacity, since it overestimates shear strength for the tests #11 and underestimates shear strength for the test #13.

A graphic comparison is carried out between the shear strength envelopes and the experimental responses, for tests #10, #11, and #13, in Figure 7.2, Figure 7.3, and Figure 7.4. Such a comparison is shown in terms of lateral load versus displacement ductility (μ).

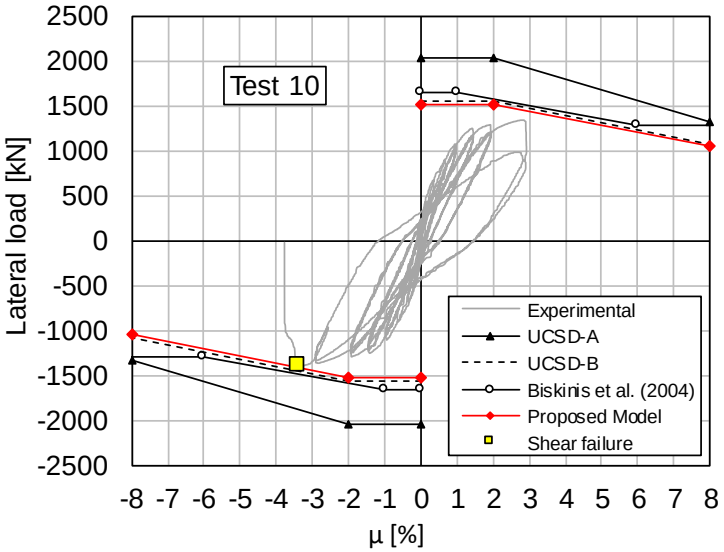

Figure 7.2.Experimental lateral load-drift response and shear strength envelopes predicted according to the considered capacity models for Test 10

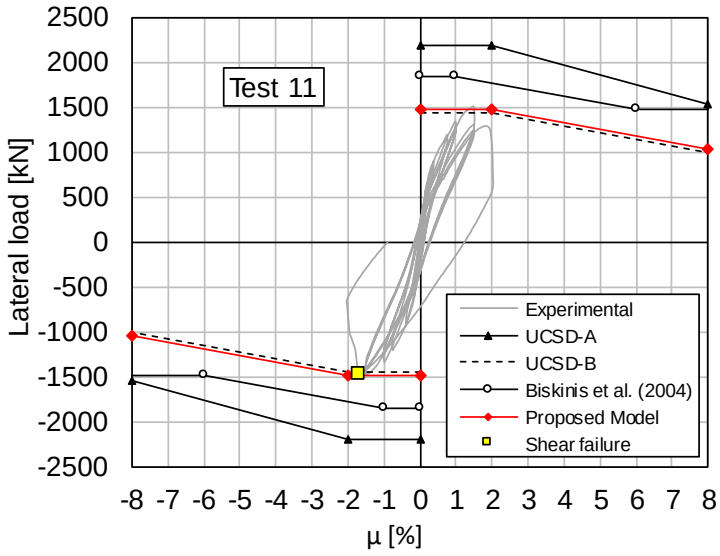

Figure 7.3. Experimental lateral load-drift response and shear strength envelopes predicted according to the considered capacity models for Test 11

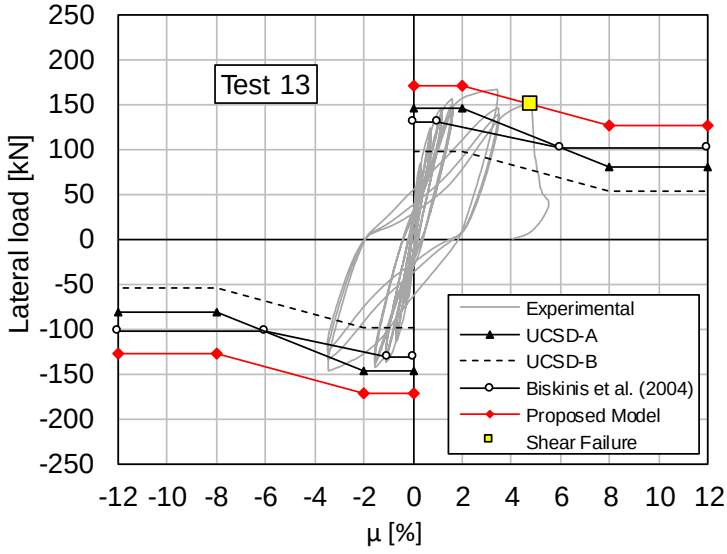

Figure 7.4. Experimental lateral load-drift response and shear strength envelopes predicted according to the considered capacity models for Test 13

The high predictive capacity of the proposed model is confirmed by the results depicted in the above-reported figures. The shear strength is evaluated almost exactly for all tests. It is to be noted that this model certainly needs much more experimental data to be properly validated. In particular, the effect of the axial load has to be experimentally investigated, considering different values of axial load ratio, higher than those characterizing the database columns. However, the proposed model can be considered the most reliable simple shear strength model available in literature for the assessment of shear capacity of RC columns with hollow circular section and one external layer of transverse reinforcement.

7.3 Summary

In this chapter, the shear strength assessment of RC bridge piers with hollow circular section and a single external reinforcement layer has been discussed. The results of a preliminary comparison carried out in the section 5.5, between experimental results and main code-based shear strength models, revealed the need to evaluate the effectiveness and the reliability of existing capacity models when used for the assessment of this structural typology.

To this aim, firstly, an experimental database has been collected and integrated with the tests reported in the present work. Then, a comparison is carried out, between experimental and predicted shear strength values. The results of such comparison revealed that none of the main shear strength models is able to predict the experimental failure mode for hollow circular columns, especially when their transverse reinforcement consists of isolated circular ties, and not continuous spiral. Some improvements in shear strength assessment are discussed, particularly regarding the transverse reinforcement contribution on shear strength. Finally, a new shear strength model is defined and proposed. This new model is characterized by a predictive capacity of failure mode and shear strength almost exact for all the specimens of the database.

Differently from Chapter 6, here an assessment of drift capacity model has not been presented due to the very limited amount of tests available in literature.

References

Biskinis D.E., Roupakias G.K., Fardis M.N. (2004). Degradation of shear strength of reinforced concrete members with inelastic cyclic displacement. ACI Structural Journal, 101(6):773–83.

Cardone D., Perrone G., Sofia S. (2013). Experimental and numerical studies on the cyclic behavior of R/C hollow bridge piers with corroded rebars. Earthquakes Struct, 4(1), 41-62.

Hoshikuma J. I., Priestley M. J. N. (2000) Flexural behaviour of circular hollow columns with a single layer of reinforcement under seismic loading. SSRP 2000; 13. University of California, San Diego.

Kim I. H., Sun C. H., Shin M. (2012) Concrete contribution to initial shear strength of RC hollow bridge columns. Structural Engineering and Mechanics; 41(1): 43-65.

Paulay T., Priestley M. J. N. (1992) Seismic Design of Reinforced Concrete and Masonry Buildings. New York: John Wiley & Sons.

Priestley M. J. N., Seible F., and Calvi G. M. (1996). Seismic design and retrofit of bridges. Wiley, New York.

Priestley M. J. N., Verma R. and Xiao Y. (1994). Seismic shear strength of reinforced concrete columns. ASCEJ. Struct. Engrg, 120 (8) 2310-2329.

Ranzo G., Priestley M. J. N. (2001) Seismic performance of circular hollow columns subjected to high shear. SSRP 2001; 1. University of California, San Diego.

Turmo J., Ramos G., Aparicio A. C. (2009). Shear truss analogy for concrete members of solid and hollow circular cross section. Engineering Structures, 31(2), 455-465.

Zahn F. A., Park R., Priestley M. J. N. (1990) Flexural Strength and Ductility of Circular Hollow Reinforced Concrete column without Confinement on Inside Face. ACI Structural Journal; 87(2): 156-166.

Chapter 8
CONCLUSIONS AND FUTURE DEVELOPMENTS

Among civil structures, highway bridges can be considered as crucial for life and security of the served urban areas. Damages to highway bridges due to earthquake events, may have dramatic impact on the interested area, with or without life threatening consequences. Therefore, the assessment of seismic performance of existing bridge structures is a paramount issue, especially in those countries, such as Italy, where most of existing bridges was constructed before the advancement in earthquake engineering principles and seismic design codes.

Seismic performance of bridges substantially depends on lateral behavior of vertical structural sub-systems, in particular of the bridge piers. To persue sufficient energy dissipation, reinforced concrete bridge piers have to be designed with adequate seismic details, so that ductile flexural hinges at base could develop due to intense seismic demand. Brittle shear failure of bridge piers clearly has to be prevented to avoid disastrous collapse, and special attention has to be paid also to shear strength degradation with increasing flexural ductility demand. The seismic vulnerability of the bridge piers, due to obsolete design, has been highlighted by several major earthquakes occurred throughout the world.

For ordinary shaped reinforced concrete (RC) bridge columns (namely, with solid rectangular or circular cross-section) the seismic assessment issue can be considered as almost resolved, since many experimental and analytical studies are available in literature, from which several analytical assessment formulations have been proposed, and adopted by codes. The same cannot be said for columns with hollow-core cross section. Despite their widespread use,

in fact, none of the current codes addresses specialized attention to RC hollow core members, both for design and assessment. Moreover, only quite recently, attention has been paid to experimental cyclic response of hollow columns: relatively few experimental studies, especially if compared with columns with solid cross section, are available in literature.

A critical, and still open, issue is the assessment of shear capacity of hollow RC columns, special focusing on degradation mechanisms. In fact, shear-resisting mechanisms typical of this structural typology are very similar to those characterizing tube sections, depending mainly on webs aspect ratio and transverse reinforcement details. Another important issue related to existing hollow RC piers is that their seismic response is characterized by high shear deformations, comparable to ones typical of RC walls, which may represent also a considerable portion of global top displacement.

The situation outlined above is sufficient to understand that the state of the art on seismic assessment of hollow bridges piers still needs to be advanced in several areas: proper predictions of nonlinear behavior, failure modes, and shear capacity, in particular.

A contribution towards this direction has been carried out in this work through the investigation of cyclic lateral response of RC existing bridge piers with hollow rectangular and hollow circular cross-section, characterized by not sufficient seismic reinforcement details, therefore susceptible to high shear deformations and, eventually, shear failure. Special attention has been focused on failure mode prediction and shear capacity assessment. For these purposes, both experimental and analytical studies have been carried out and presented herein.

A critical review of the state-of-the-art and of the theoretical background, essential for the development of this work, has been performed. Firstly, the review process has been focused on the past experimental and analytical research on seismic performance of hollow reinforced concrete bridge piers. After a critical description of past experimental tests on RC columns with hollow rectangular cross section, the attention has been moved on the experimental tests available in literature on RC columns with hollow circular section and a single steel reinforcement layer. It has been underlined that very few experimental studies are available in literature, especially on the latter topic. This part of the literature review has been used for the collection of the

databases, presented in the last part of the work.

Several analytical models have been reviewed, too. First, some of the existing models for the evaluation of lateral response of RC column have been briefly discussed. The models have been divided into three main topics: flexural behavior, shear behavior and bar slip. Later, main models for shear strength evaluation from literature and codes have been described and discussed in details.

An experimental campaign was carried out at the Laboratory of the Department of Structures for Engineering and Architecture, University of Naples "Federico II", to address the seismic performance of existing reinforced concrete (RC) bridge piers with hollow cross-sections. The experimental program, realized under the financial support of STRESS S.c.a.r.l. STRIT Project "PON Ricerca e Competitività 2007-2013", comprised tests on six reduced-scale RC bridge piers with hollow cross-section (four rectangular shaped and two circular shaped). All tests were performed in quasi-static way by applying increasing horizontal displacement cycles with constant axial load (equal to 5% of the axial compressive capacity) until collapse.

The main goal of the design procedure was to obtain specimens representative of the existing bridge columns typical of the Italian transport infrastructures realized before 1980. To this aim, the results of an important investigation on a sample of about 400 existing Italian RC beam bridges were considered, taking into account key parameters, such as cross-section shape, slenderness, axial load ratio, geometrical reinforcement ratio, materials strength, among others. Starting from those results, two typical bridge pier cross-sections were designed (hollow rectangular and hollow circular), in terms of geometry and reinforcement details, according with common non-seismic design practice. In order to allow for testing within the capacity of the laboratory, a scaling factor equal to 1:4 was introduced.

The test variable was the aspect ratio (namely, height to depth ratio). Medium-low aspect ratios are considered (between 1.5 and 3.75), since the main goal of the experimental program was to investigate deeply about flexure-shear interaction and failure mode prediction. The representativeness issue was considered also for the material properties definition, resulting into a poor concrete and relatively high strength steel. The construction process, crucial for the success of experimental tests, has been described, focusing on

some critical aspects of the construction procedure. In order to investigate deeply about local deformation components coexisting in the specimens (flexure contribution, shear contribution and fixed end rotation at cantilever base), an appropriate instrumentation was installed. In particular, it was composed of a system of Linear Potentiometers (LPs) and Linear Variable Displacement Transducers (LVDTs), monitoring flexural and shear deformation, and strain gauges (SGs), monitoring axial steel strain of both longitudinal and transverse reinforcement.

Experimental results have been presented for hollow rectangular and hollow circular specimens, separately.

Concerning hollow rectangular specimens, depending on the aspect ratio, different failure modes were expected, namely flexure failure for tall piers and shear failure after flexural yielding for short piers. Experimental results, in terms of lateral load versus drift and damage evolution showed that:

- Tests P1 and P2, characterized by a higher aspect ratio ($L_V/H \geq 2.5$), showed flexural failure modes, with an inelastic response controlled by ductile mechanisms. Damage evolution was typical of ductile members, with most of damage consisting of concrete crushing and longitudinal bars buckling.
- Test P3, characterized by an aspect ratio L_V/H =1.5, showed shear failure after flexural yielding. The cyclic response was typical of squat columns, governed by shear mechanisms. In fact, damage evolution was characterized by significant diagonal cracking since linear phase. Shear failure mode was characterized by a large drop in strength (of about 60% respect to maximum reached value) related to evident diagonal cracks opening, inclined of about 45 degrees.
- Test P4, characterized by an aspect ratio L_V/H=2.25, showed shear failure after flexural yielding. The cyclic response was characterized by flexure-shear interaction. In fact, during non-linear phase damage evolution was characterized initially by flexural cracks at the base, for drift values higher than Test P3, and later by significant diagonal cracks, up to shear failure.

An experimental analysis of deformability contributions to the top displacement was performed, mainly in order to better understand the

relevance of taking into account shear deformations for bridge piers assessment. From experimental results, as expected, a relation between shear contribution to top displacement (Δ_s/Δ) and aspect ratio (L_V/H) has been identified. In particular, (i) for slenderest specimen P2, maximum value of shear contribution was about equal to 11%; (ii) for Test units P1 and P4, characterized by lower similar aspect ratios, about 20% of top displacement corresponding to peak load was due to shear deformations; (iii) for squat Test unit P3, shear deformability contribution to top displacement was about 32% and 45% respectively at yielding and peak load conditions.

The energy dissipation capacity was analyzed, evaluating the equivalent damping ratio and its evolution with ductility, which was compared with a common literature formulation usually used for RC bridge piers, highlighting a slightly lower energy dissipation capacity in large inelastic field for the tested specimens.

The reported comparison between the observed failure modes and shear strength values and the corresponding predictions based on capacity models from literature and/or codes provided a useful support to the evaluation of the reliability of these models when applied to existing hollow rectangular RC piers. From this comparison, a clear need to improve the prediction capacity of shear strength models available in codes and literature has been highlighted.

The global response of test specimens has been modelled through a three-component numerical model, in which flexure, shear and bar slip are considered separately. The numerical results show that the adopted model is able to reproduce the experimental global response and the deformability contributions with adequate accuracy.

As regards hollow circular specimens, depending on the aspect ratio, different failure modes were expected, namely flexure failure for tall pier P5 and shear failure after flexural yielding for short pierP6. Experimental results, in terms of lateral load versus drift and damage evolution showed that:

- Tests P5, characterized by a higher aspect ratio (L_V/H = 2.5), showed flexural failure modes, with an inelastic response controlled by ductile mechanisms. Damage evolution was typical of ductile members, with most of damage consisting of concrete crushing and longitudinal bars buckling.
- Test P6, characterized by an aspect ratio L_V/H = 2.0, showed shear

failure after flexural yielding. The cyclic response was typical of squat columns, governed by shear mechanism: damage evolution was characterized by significant diagonal cracking since linear phase. Shear failure mode was characterized by a large drop in strength (of about 75% respect to maximum reached value) related to evident diagonal cracks opening, inclined of about 42 degrees.

Also in this case, as expected, the experimental analysis of deformability contributions to the top displacement confirmed a relation between shear contribution to top displacement and aspect ratio. In particular, (i) for slenderest specimen P5, maximum value of shear contribution was about equal to 9.4%; (ii) for squat Test unit P3, shear deformability contribution to top displacement was about 15% and 25% respectively at yielding and shear failure conditions.

The analysis of the energy dissipation capacity and the evaluation of the equivalent damping ratio evolution with ductility, highlighted a slightly lower energy dissipation capacity in large inelastic field for the tested specimens with respect to models available in literature.

From the reported comparison between observed failure modes and shear strength values and corresponding predictions based on capacity models from literature and/or codes, also in this case, a clear need to improve the prediction capacity emerged.

The tests presented herein can provide a useful contribution to enlarge the relatively limited experimental database on existing hollow circular RC piers. In particular, the experimental analysis of all the sources of deformability characterizing cyclic response can be a valid reference for the proposal/validation of nonlinear modeling approaches and capacity models for seismic assessment of existing bridge structures.

While for ordinary columns with solid cross section several capacity models are available in literature and codes, concerning hollow rectangular columns, none ad-hoc model is suggested in literature or adopted in codes. It is clear the need to investigate the applicability of the existing models to this structural typology, and to develop some improvements or new proposal. To this aim a database of 28 experimental tests has been collected in this work, representing the experimental state-of-the-art about RC columns with hollow

rectangular cross section and exhibiting a shear failure, occurred with or without flexural yielding. Several main shear strength models have been selected and applied to all the database columns, showing a low predictive capacity of both failure modes and shear strength. Based on the results of the comparison between predicted shear strengths and experimental response, some critical aspects have been identified. Adopting the model by Kowalsky and Priestley (2000), some modifications have been discussed in order to improve the reliability of this model for the applicability to hollow rectangular columns. In particular, the improvements concern the concrete contribution to the shear strength: different definitions of effective shear area and dowel-action contribution have been proposed. The capability in prediction of the experimental failure modes and shear strength is substantially improved through the proposed modifications. In particular, a mean trend of the predicted to measured shear strength ratio equal to 1.01 and a coefficient of variation (COV), of 0.34 has been achieved.

Within the context of a displacement-based approach for design and assessment of bridges, it is crucial to predict the displacement corresponding to shear failure. To this aim, several drift-capacity models have been developed during the last decades. All these models are based on empirical formulations calibrated on experimental results of building columns with solid cross-section. The effectiveness of these models when applied to hollow rectangular columns has been investigated for all the columns of the collected database. The results of this comparison show that existing models are not adequate to assess drift at shear failure of hollow rectangular columns. For this reason, based on the database data, new drift capacity models have been developed. The goal of developing a new drift-capacity model was to reduce the coefficient of variation and mean error predictions characterizing the existing models, through simple relationship depending on some critical parameters influencing the drift at shear failure for shear-critical hollow rectangular bridge columns. These goals have been achieved through the development of two different formulations to compute the drift at the shear failure as a function of some key parameters, identified from the analysis of the experimental database. Both expressions provide accurate prediction of drift at shear failure for the considered columns, with mean of about 1.04 and COV equal to about 0.20, considerably better if compared with existing models.

Finally, the shear strength assessment of RC bridge piers with hollow circular section and a single external reinforcement layer has been discussed. Based on the results of a preliminary comparison between the presented experimental results and main code-based shear strength models, the need to evaluate the effectiveness and the reliability of existing capacity models, when used for the assessment of this structural typology, emerged. To this aim, firstly, an experimental database has been collected and integrated with the tests reported in the present work. Then, a comparison has been carried out, between experimental and predicted shear strength values. The results of such comparison revealed that none of the main shear strength models is able to predict the experimental failure mode for hollow circular columns, especially when their transverse reinforcement consists of isolated circular ties, and not continuous spiral.

Some improvements in shear strength assessment have been discussed, particularly regarding the transverse reinforcement contribution on shear strength. Starting from a critical analyisis of studies available in literature, a new shear strength model is defined and proposed. This new model is characterized by a predictive capacity of failure mode and shear strength almost exact for all the specimens of the database, with mean equal to 1.01 and COV equal to 0.01. It is to be noted that this model certainly needs much more experimental data to be properly validated. However, it can be considered the most reliable simple shear strength model available in literature for the assessment of shear capacity of RC columns with hollow circular section and one external layer of transverse reinforcement. Differently from what is done for hollow rectangular, in this case an assessment of drift capacity model has not been presented due to the very limited amount of tests available in literature.

In the future, a more comprehensive experimental investigation on hollow rectangular and circular RC columns failing in shear after yielding should be carried out, considering different test variables (such as axial load, longitudinal reinforcement, among others), in order to improve the reliability of the provided shear capacity models.

More refined modelling of seismic response of the considered specimen will be developed, taking into account the degradation of flexural and shear mechnisms due to cyclic displacement demand.